

UCL

Department of Chemistry

European Synchrotron Radiation Facility

Dutch-Belgian Beamline

**Formation and Electrocatalysis Studies
of Nickel and Iron Sulfide Catalysts using
in situ XAS**

Thesis submitted for the degree of Doctor of Engineering (EngD) by

Husn-Ubayda Islam

Supervisors

Prof. Richard Catlow, Prof. Gopinathan Sankar, and Dr. Wim Bras

August 2016

Declaration

I, Husn-Ubayda Islam confirm that the work presented in this thesis is my own. Where information has been derived from other sources, I confirm that this has been indicated in the thesis.

Signed:

Date:

Abstract

X-ray absorption spectroscopy (XAS) is an atom specific characterisation technique. It is particularly useful for understanding dilute systems of short range order. When used *in situ* during reaction processes, the technique is a powerful tool to study the evolving local structure of materials. In this thesis, XAS is used to understand the synthesis, stability, and electrocatalytic activity of iron sulfides.

A popular route to the synthesis of nanoparticulate sulfides is the solvothermal decomposition of transition metal dithiocarbamates. These single source precursors are typically dissolved in a coordinating solvent and heated rapidly. The coordinating solvent acts as a heat sink and capping agent but its role in each decomposition process is less understood. Here, it is shown through *ex situ* and *in situ* XAS that the coordinating solvent has significant effect on the starting material and decomposition process through coordination to the transition metal centre and reaction with the dithiocarbamate backbone. Case studies include the decomposition of zinc dimethyl, and nickel and iron diisobutyl dithiocarbamates in oleylamine.

The solvothermal decomposition of iron or iron and nickel diisobutyl dithiocarbamate in the presence of thiuram disulfide results in the formation of Fe_3S_4 or NiFe_2S_4 nanoparticles. These inverse spinel structures are formed as hexagonal sheets with 001 and 111 surfaces which are predicted to be electrocatalytically active. The oxidation of the systems in electrolyte during cyclic voltammetry – a process that is thought to reduce catalytic activity – is investigated by *in situ* XAS.

Acknowledgments

I walked into the department of chemistry about a decade ago and never looked back. It was the warm welcome I received from Saeed, and the relaxed attitude of Dewi Lewis that convinced my otherwise hesitant and unsure self. I would like to thank them for that initial push. Four years later, I met my Masters supervisor Adam McKay. He had an interest in instrumentation and characterisation that I could relate to, and his dedication and determination were inspirational. He also convinced me to continue in research and although I didn't take a PhD with him, the impact he had on my life and the confidence he instilled in me was vast. Thanks Adam.

I was fortunate to work under the supervision of four great researchers over the next four years. I thank Nora de Leeuw for taking me on and giving me opportunities that I could only have dreamed of. She is a woman whom I greatly admire, and I look forward to working with her in the future. I would like to thank Wim Bras for being a brilliant industrial supervisor and an even better guardian when I moved to France three years ago. Wim is the ambassador of political incorrectness but his advice is sound and he has always had my best interests at heart. I would also like to thank Richard Catlow for keeping a keen eye on my work and making sure I was on track. Finally, a special thanks is given to Gopinathan Sankar. I was very lucky to be taken under his wings: his enthusiastic ideas and suggestions formed the pillars of this thesis, and when I realised he could manipulate EXAFS software like a don, I learnt some of that from him too.

Nora's CO₂ consortium was a wonderful group to be a part of. It was designed as a pool of resources and expertise that we could all benefit from in order to produce something significant. Through this group I met Nathan whose passion for scientific research was commendable, and passion for chocolate endearing. I thank him for being my closest ally through these four years with everything that that entailed. I would also like to thank Alberto, Josie, and Maxime, as well as Graeme Hogarth, Katherine Holt, Mariette Wolthers, and Meleke Balk. It becomes evident in following chapters that their contributions to my work are critical. I thank them for their input, extensive discussion, and beamtime assistance. Also, thank you Anna and Siti; as fellow students you should not have been as patient with me as you were. Thank you so much for your help, your presence at beamtimes and your materials.

I thank Sankars and Richard's "old" group at the KLB as they were my mentors during the first EngD year. Speaking technically, Andy, Jon and Martin taught me software basics, and Vlad sat with me through my first ever beamtime. On a personal level, I had the time of my life with these guys and I consider them friends along with Rozie, Jeff, Nazar, and Tiffany. They were and are inspirational.

The second and third year of my EngD were completed at the ESRF. I will never forget the kindness of all the beamline staff, especially Dip who took care of my needs during countless beamtimes, as well as giving me time off the books; Dirk who on a number of occasions quietly scoured the whole synchrotron to find me a tool that I could benefit from; Florian who said "Salut Ooshna" to me every morning; the dubble act Giuseppe and Daniel; my unlikely best friend Alessandro; and the occasional, friendly faces of Halina and Jim. Thanks also to Sergey and Alex. A special acknowledgment is reserved for the CRG liaison officer Murielle; she dealt with an immense out-of-hours workload on my behalf starting with finding me accommodation, a bank, an insurer, becoming my guarantor, and continuing to support me. I am eternally grateful to her because she made life in France that much easier.

When I came back from France in my final year, I met the "new" Sankar group. Huw Glen, Ian, Abdul, Zarrin, and Anastasia were a pleasure to work with. Though young, they are wise, respectful, and intelligent beyond their years. They work very well together, and under the guidance of Sankar, are a formidable team.

A special thanks is given to Tom Daley (not the diver) for always having my back. We started our undergrad and our EngD's at the same time, and are likely to finish together. He has been a loyal and professional colleague. My friends Iman, Meetal, Leila, and Sacha fall into the same category. I am grateful that I got to experience this journey with them.

Finally, I would like to thank my family. I am lucky to belong to this one because it is full of wonderful characters including my three brothers Humza, Yaqoub, and Yusuf, and my cute sister Hufsa, as well as mum, dad, and my gran. They have seen me at my very best and absolute worst but have remained patient and loving. The constant encouragement I get from mum, and her unfaltering conviction, makes impossible things possible. I am a lucky woman who has had opportunities that women from my background do not always have access to, and this is in part due to the progressive attitude of my parents. My family includes my closest and dearest friends Safia, Shazna, and Ateeqa, and my amazing aunts, uncles and cousins. I would like to thank them all for their support and encouragement. I am glad to say I'm almost there thanks to you!

Contents

List of Figures	9
List of Tables	16
List of Equations	17
List of Samples	18
List of Communications	19
Chapter 1 Overview	20
Chapter 1	21
Iron sulfides: structure, synthesis, and applications	21
1.1 Introduction	21
1.1.1 The sulfur cycle	22
1.1.2 Deep sea hydrothermal vents	23
1.1.3 Iron sulfur world theory	24
1.1.4 Iron sulfides in nature	25
1.2 Iron sulfide minerals	26
1.2.1 Iron sulfide clusters.....	26
1.2.2 Mackinawite	27
1.2.3 Greigite	28
1.2.4 Pyrite.....	29
1.2.5 Pyrrhotite	30
1.2.6 Less common iron sulfides	30
1.3 Synthesis of iron sulfides	31
1.3.1 Synthesis of disordered mackinawite from ferrous iron and sulfide salts	31
1.3.2 Synthesis of nanocrystalline iron sulfides from toluene-thermal process	31
1.3.3 Synthesis of magnetic pyrrhotite nanorods and sheets from elemental iron	32
1.3.4 Synthesis of magnetic and non-magnetic pyrrhotite nanowires.....	33
1.3.5 Synthesis of magnetic pyrrhotite and greigite from cubane precursor.....	33
1.3.6 Synthesis of magnetic pyrrhotite and greigite from dithiocarbamate precursor	34
1.3.7 Synthesis of marcasite and pyrite from dithiocarbamate precursor	35
1.4 Applications of iron sulfides	35
1.4.1 Medical imaging	36
1.4.2 Cancer treatment.....	36
1.4.3 Thin film solar cells	36
1.4.4 CO ₂ reduction catalysis.....	37
1.5 Thesis overview	37
1.6 References	41
Chapter 2 Overview	46
Chapter 2	47
X-ray absorption spectroscopy and other experimental techniques	47
2.1 Introduction	47
2.2 X-ray absorption spectroscopy	48
2.2.1 XANES.....	49
2.2.2 EXAFS.....	51
2.2.3 Data acquisition modes	60
2.3 Synchrotron Technology	62
2.3.1 Synchrotron facility design	63
2.3.2 Beamlines	64
2.3.3 Monochromators.....	65
2.3.4 Sample environments.....	66
2.3.5 Detectors.....	66
2.4 DUBBLE at the ESRF	68
2.4.1 European Synchrotron Radiation Facility.....	68
2.4.2 Dutch-Belgian Beamline.....	69
2.5 Other Characterisation Techniques	70
2.5.1 XRD.....	70
2.5.2 TEM.....	71

2.5.3 UV-vis	72
2.5.4 DFT.....	72
2.5.5 Cyclic Voltammetry.....	73
2.5.6 ATR-IR.....	73
2.6 References.....	75
Chapter 3 Overview	79
Chapter 3	80
XAS of the Solvent effects on the local structure of transition metal dithiocarbamates	80
3.1 Introduction.....	80
3.2 Method	82
3.2.1 Samples Synthesis and Preparation	82
3.2.2 Sample Environment	83
3.2.3 Measurements	83
3.2.4 Beamline	83
3.2.5 Data Processing	84
3.3 Results	84
3.3.1 Zinc Dithiocarbamate	84
3.3.2 Nickel Dithiocarbamate	87
3.3.3 Iron Dithiocarbamate	93
3.4 Conclusion	97
3.5 Acknowledgements	98
3.6 References.....	99
Chapter 4 Overview	102
Chapter 4	103
<i>In situ</i> XAS of the solvothermal decomposition of transition metal dithiocarbamate complexes	103
4.1 Introduction.....	103
4.2 Method	105
4.2.1 Sample Synthesis and Preparation	105
4.2.2 Measurements	106
4.2.3 Cell	107
4.2.4 Beamline	108
4.2.5 Processing	109
4.3 Results and Analysis	110
4.3.1 Zinc Dithiocarbamate Decomposition	110
4.3.2 Nickel Dithiocarbamate Decomposition	114
4.3.3 Iron Dithiocarbamate Decomposition	127
4.4 Discussion.....	144
4.5 Acknowledgements	145
4.6 References.....	146
Chapter 5 Overview	149
Chapter 5	150
<i>In situ</i> XAS of Greigite and Violarite during Electrocatalytic Processes with Carbon Dioxide	150
5.1 Introduction.....	150
5.2 Method	154
5.2.1 Sample	154
5.2.2 Electrochemical Cell.....	155
5.2.3 Preparation of Experiment	157
5.2.4 <i>In situ</i> Acquisition.....	158
5.2.5 Beamline	159
5.2.6 Data Analysis.....	159
5.2.7 Sulfur K-edge	159
5.3 Results and Discussion.....	160
5.3.1 Greigite	161
5.3.2 Greigite in phosphate buffer bubbled with N ₂ at pH 6.8.....	163
5.3.3 Greigite in phosphate buffer bubbled with N ₂ at pH 4.5.....	169

5.3.4 Greigite in phosphate buffer bubbled with CO ₂ at pH 6.8	171
5.3.5 Greigite in phosphate buffer bubbled with CO ₂ at pH 4.5	173
5.3.6 Greigite in carbonate buffer bubbled with N ₂ at pH 10.5	176
5.3.7 Bond distances during electrochemical cycle according to EXAFS	178
5.3.8 Violarite in phosphate buffer bubbled with N ₂ at pH 6.8	179
5.4 Conclusion	182
5.5 Acknowledgements	185
5.6 References.....	186
Chapter 6	189
Conclusions and Future Work.....	189
6.1 Summary.....	189
6.2 Future work.....	190
6.3 References.....	192
Appendices.....	193
Appendix 1.....	193
LCF analysis of the solvothermal decomposition of Ni(^tBuNCS₂)₂.....	193
Appendix 2.....	194
The structure of synthetic cubane	194
Method.....	194
Appendix 3.....	197
CV traces of greigite with Ar and CO₂ saturated electrolyte.....	197
Appendix 4.....	203
XRD and XAS of the oxyhydroxide.....	203
Method.....	203
Results	204
Appendix 5.....	206
DFT Calculated bond distances of the greigite surface	206
Appendix 6.....	207
LCF analysis of the greigite during electrochemistry.....	207
Appendix 7.....	210
Coordination numbers for surface and bulk.....	210
Appendix 8.....	211
Surface to bulk ratio of a greigite nanoparticle.....	211
Appendix 9.....	212
Iron Standards and their XANES	212
Appendix 10.....	213
Output parameters of Chapter 5.....	213
Appendix References	216

List of Figures

Figure 1.1: Pictorial diagram demonstrating aspects of the sulfur cycle.

Figure 1.2: a. TEM image of magnetotactic bacterium containing particles of magnetite. Image is taken from www.nature.com/scitable/knowledge/library/bacteria-that-synthesize-nano-sized-compasses-to-15669190. b. Image of enzyme containing Fe_2S_2 active inorganic cluster. The cluster is attached to the organic body of the enzyme by sulfur bridges on cysteine amino acids. Image is taken from www.ebi.ac.uk/training/online/course/introduction-protein-classification-ebi/protein-classification/what-are-sequence-features.

Figure 1.3: Crystalline extended unit cell of mackinawite showing iron(II) (brown) and sulfur(II) (yellow). Iron is tetrahedrally coordinated to four sulfur and the iron arrange in layers of square planar geometries. The layers are held together by van der Waals forces.

Figure 1.4: The 001 surface of mackinawite (left) and greigite (right) showing similarities between the structures. Iron centres are brown and sulfur centres are yellow.

Figure 1.5: Local structure of pyrite showing iron(II) (brown) and sulfur (yellow). The sulfur species, S_2^{2-} , are shaped like dumbbells and arrange at angles to the iron centre causing a distorted octahedral geometry and low symmetry.

Figure 2.1: Graph showing an XAS spectrum of $\chi\mu(E)$ as a function of energy. The spectrum is shown to be divided into two regions. The XANES lies about 20 eV before and 30 eV after the Fermi level manifested as the edge jump, while EXAFS is found after the XANES region at the tail end of the spectrum and contains oscillations which are caused by constructive and destructive interference of the outgoing photoelectron with neighbouring atoms.

Figure 2.2: Features typical of the XANES region arise from unique orbital arrangements and interactions, and are used to identify characteristics of a local environments. Features include a pre-edge, edge, white line intensity, and near-edge. The amplitude of the pre- and near-edge features and white line intensity, and the position of the edge reveal information about coordination geometry and oxidation state.

Figure 2.3: An example of the normalisation process on an X-ray absorption spectrum. For normalisation, the pre-edge polynomial (green) is extrapolated based on two points before the edge, and the post-edge polynomial (purple) is extrapolated from two points after the edge – typically from close to the XANES region to the end of the EXAFS region.

Figure 2.4: An example of background subtraction in the EXAFS region. Background $\mu_0(E)$ is estimated with a spline function and subtracted from the experimental data $\mu(E)$.

Figure 2.5: A schematic diagram showing the shape of the beam emitted from an electron accelerated through a bending magnet and an insertion device. The beam profile resulting from

a bending magnet is fanned, with higher energy closer to the new electron trajectory and lower energy on the far side of the fan. Insertion devices cause far less fanning; the beam is collimated and focussed owing to a succession of alternating magnets.

Figure 2.6: A schematic diagram of a typical synchrotron facility showing basic construction including a booster ring and storage ring as well, and an RF cavity for maintaining electron velocity. The circular structure is actually a polygon made up of a series of hexapoles, quadrupoles, and bending magnets or insertion devices which follow the changing trajectory of the electrons.

Figure 2.7: A schematic diagram showing a double crystal monochromator used for tuning energy.

Figure 2.8: The European Synchrotron Radiation Facility (ESRF) is a central synchrotron facility situated in Grenoble.

Figure 2.9: The layout of the optics hutch of the EXAFS line on the Dutch-Belgian beamline.

Figure 2.10: Diagram describing the derivation of Bragg's law based on incident and elastically scattered waves from a crystal grating.

Figure 3.1: XANES spectra of $\text{Zn}(\text{Me}_2\text{NCS}_2)_2$ solid (12), dissolved in xylene (13), and dissolved in oleylamine (14).

Figure 3.2: a. EXAFS and b. FT of $\text{Zn}(\text{Me}_2\text{NCS}_2)_2$ solid (12), c. EXAFS and d. FT of $\text{Zn}(\text{Me}_2\text{NCS}_2)_2$ dissolved in xylene (13), and e. EXAFS and f. FT of $\text{Zn}(\text{Me}_2\text{NCS}_2)_2$ dissolved in oleylamine (14).

Figure 3.4: XANES spectra of $\text{Ni}(\text{iBu}_2\text{NCS}_2)_2$ solid (1), dissolved in dodecane (2), dissolved in oleylamine (3), and dissolved in hexylamine (4).

Figure 3.5: UV-vis spectra of $\text{Ni}(\text{iBu}_2\text{NCS}_2)_2$ dissolved in hexane (15) and hexylamine (4).

Figure 3.6: Possible conformations of $\text{Ni}(\text{iBu}_2\text{NCS}_2)_2(\text{C}_2\text{H}_4)_2\text{N}$ according to DFT, including two singlet (16a and 16c) and two triplet (16b and 16d) states in *cis* and *trans* geometry.

Figure 3.7: a. EXAFS and b. FT of $\text{Ni}(\text{iBu}_2\text{NCS}_2)_2$ solid (1), c. EXAFS and d. FT of $\text{Ni}(\text{iBu}_2\text{NCS}_2)_2$ dissolved in dodecane (2), e. EXAFS and f. FT of $\text{Ni}(\text{iBu}_2\text{NCS}_2)_2$ dissolved in oleylamine (3), and g. EXAFS and h. FT of $\text{Ni}(\text{iBu}_2\text{NCS}_2)_2$ dissolved in hexylamine (4).

Figure 3.8: XANES spectra of $\text{Fe}(\text{iBu}_2\text{NCS}_2)_3$ solid (7), dissolved in dodecane (8), and dissolved in oleylamine (9).

Figure 3.9: UV-vis spectra of $\text{Fe}(\text{iBu}_2\text{NCS}_2)_3$ dissolved in dodecane (8) and hexylamine (17).

Figure 3.10: a. EXAFS and b. FT of $\text{Fe}(\text{tBu}_2\text{NCS}_2)_3$ solid (7), c. EXAFS and d. FT of $\text{Fe}(\text{tBu}_2\text{NCS}_2)_3$ dissolved in dodecane (8), and e. EXAFS and f. FT of $\text{Fe}(\text{tBu}_2\text{NCS}_2)_3$ dissolved in oleylamine (9).

Figure 3.11: Pictorial representation of 7, and 9.

Figure 4.1: Illustration and specifications of the reaction cell used for solvothermal decomposition reactions. The brass cell is connected to a temperature controller that regulates temperature at the base of the cell. The reaction centre and seal is built with several high boiling point materials for stability during reactions.

Figure 4.2: Set up of experimental hutch at the Dutch-Belgian EXAFS beamline. The beamline is equipped with both ion chambers (I_0 and I_t) and fluorescence detector for transmission and fluorescence measurements. The reaction cell is held at a 20° angle from the perpendicular line to the beam.

Figure 4.3: XRD of the solvothermal decomposition of 14 in oleylamine reveals a good match to the literature structure of wurtzite. The model wurtzite XRD was produced from Crystal Diffract using a wurtzite crystal file available with the software. XRD of the decomposition product of 14 was acquired at the Swiss-Norwegian beamline, station A.²³

Figure 4.4: TEM of ZnS nanoparticles formed during *in situ* measurements of the decomposition of 14 in oleylamine. Particles are shaped nanowires. The nanowires align in rows owing to secondary interactions.

Figure 4.5: *In situ* a. XANES spectra, b. EXAFS and c. FT of the solvothermal decomposition of $\text{Zn}(\text{Me}_2\text{NCS}_2)_2$ in oleylamine (14) up to 94°C at a ramp rate of $1^\circ\text{C}/\text{min}$.

Figure 4.6: Equilibrium demonstrating the dissociation of oleylamine from the zinc centre as a function of increasing temperature.

Figure 4.7: a. EXAFS and b. FT fits for the solvothermal decomposition of $\text{Zn}(\text{Me}_2\text{NCS}_2)_2$ in oleylamine (14) at 25°C (14a), 71°C (14b), 77°C (14c), 83°C (14d), 89°C (14e), and 94°C (14f).

Figure 4.8: XRD of the reaction product of the decomposition of $\text{Ni}(\text{tBu}_2\text{NCS}_2)_2$ in oleylamine (3) up to 150°C in laboratory reaction conditions.

Figure 4.9: *In situ* XANES spectra of the solvothermal decomposition of $\text{Ni}(\text{tBu}_2\text{NCS}_2)_2$ in oleylamine (3) up to 150°C at a ramp rate of $1^\circ\text{C}/\text{min}$.

Figure 4.10: a. EXAFS and b. FT of $\text{Ni}(\text{tBu}_2\text{NCS}_2)_2$ in oleylamine at 118°C (3a), and c. EXAFS and d. FT of $\text{Ni}(\text{tBu}_2\text{NCS}_2)_2$ in oleylamine after decomposition at 150°C (3b).

Figure 4.11: Equilibrium demonstrating the dissociation of oleylamine from the nickel centre as a function of increasing temperature.

Figure 4.12: Linear combination fitting of *in situ* XANES spectra of 3 between 26 and 118° C demonstrating that the fully coordinated structure of 3 at room temperature becomes more like the square planar structure of 2 with increasing temperature.

Figure 4.13: a. *In situ* XANES spectra of the solvothermal decomposition of Ni(ⁱBu₂NCS₂)₂ in dodecane (2) up to 154° C at a ramp rate of 1° C/min, b. *in situ* XANES spectra of the solvothermal decomposition of Ni(Hex(H)NCS₂)₂ in dodecane (5) up to 135° C at a ramp rate of 1° C/min, and c. comparison of spectra of 2 and 5 against spectra of 3a.

Figure 4.14: Predicted structures of 2a and 3a. While 2a contains tertiary amine R groups, 3a is likely to fully or partly contain secondary amine R groups which result in the destabilisation of the complex.

Figure 4.15: DFT modelling of the decomposition of Ni(Ethyl₂NCS₂)(Ethyl(H)NCS₂) (16e) via the loss of ethylisothiocyanate.

Figure 4.16: Reaction products of the side product alkylisothiocyanate which are detected by ¹³C NMR and MS. R = hexyl/oleyl, R' = isobutyl.

Figure 4.17: a. EXAFS and b. FT of Ni(ⁱBu₂NCS₂)₂ in oleylamine at 150° C for an hour (3c), and during cooling at 60° C (3d), 40° C (3e), and 26° C (3f), and c. EXAFS and d. FT of the product of Ni(ⁱBu₂NCS₂)₂ in oleylamine decomposition in laboratory at 150° C (6).

Figure 4.18: a. *In situ* XANES spectra, b. *in situ* EXAFS, and c. and *in situ* FT of the solvothermal treatment of Fe(ⁱBu₂NCS₂)₃ in dodecane (8) up to 154° C at a ramp rate of 1° C/min.

Figure 4.19: a. EXAFS and b. FT of Fe(ⁱBu₂NCS₂)₃ in dodecane.

Figure 4.20: a. *In situ* XANES spectra of the solvothermal decomposition of Fe(ⁱBu₂NCS₂)₃ in oleylamine (9) up to 182° C at a ramp rate of 1° C/min, b. XANES spectra of the same decomposition highlighting temperatures of interest, and c. plot of edge position calculated as value at half spectral maximum against temperature.

Figure 4.21: a. EXAFS and b. FT of Fe(ⁱBu₂NCS₂)₃ in oleylamine at 59° C (9a), c. EXAFS and d. FT of Fe(ⁱBu₂NCS₂)₃ in oleylamine at 67° C (9b), and c. EXAFS and d. FT of Fe(ⁱBu₂NCS₂)₃ in oleylamine at 125° C (9c).

Figure 4.22: Predicted structures of stable intermediates in the decomposition pathway of 9.

Figure 4.23: XANES spectrum of 9 decomposed up to 180° C (9c), and at 230° C (9d). 9c was acquired *in situ* at 180° C, while 9d was acquired *ex situ* at room temperature. Despite different experimental conditions, the significant difference in XANES spectra indicate two different local structures. 9c is suggested to be amorphous FeS as it does not have any diffraction peaks, while 9d is characterised by XRD as pyrrhotite Fe₇S₈.⁴¹

Figure 4.24: a. *In situ* XANES spectra of the solvothermal decomposition of $\text{Fe}(\text{iBu}_2\text{NCS}_2)_3$ at high concentration in oleylamine (11) up to 68° C at a ramp rate of 1° C/min (inhomogeneity after this temperature prevented further successful data acquisition), and b. plot of edge position calculated as value at half spectral maximum against temperature.

Figure 4.25: LCF fit of $\text{Fe}(\text{iBu}_2\text{NCS}_2)_3$ at high concentration in oleylamine (11) at room temperature. The XANES is fit to XANES of 9 (oleylamine interacted $\text{Fe}(\text{iBu}_2\text{NCS}_2)_3$) and 8 (species void of oleylamine interaction, representing here the undissolved constituent of the reaction mixture).

Figure 4.26: Plot of XANES spectra for 9a, 9b, 10a, and 11a, to highlight similarities and differences between the first intermediate structure formed after reduction of the iron centre.

Figure 4.27: a. *In situ* XANES spectra of the solvothermal decomposition of $\text{Fe}(\text{iBu}_2\text{NCS}_2)_3$ with $\text{S}_2(\text{iBu}_2\text{NCS})_2$ in oleylamine (10) up to 129° C at a ramp rate of 1° C/min, b. XANES spectra of the same decomposition highlighting temperatures of interest, c. plot of edge position calculated as value at half spectral maximum against temperature, and d. zoomed image of spectra at pre-edge position showing pre-edge peaks at 68 and 129° C indicating tetrahedral geometry.

Figure 4.28: a. EXAFS and b. FT of $\text{Fe}(\text{iBu}_2\text{NCS}_2)_3$ with $\text{S}_2(\text{iBu}_2\text{NCS})_2$ in oleylamine at 24° C (10), and c. and d. at 129° C (10b).

Figure 4.29: XANES spectrum of 10 decomposed up to 129° C (10b), and at 240° C (18). 10b was acquired *in situ* at 129° C, while 18 was acquired *ex situ* at room temperature.

Figure 4.30: Solved structures of stable intermediates in the decomposition of 10 and 11. While not all structures are solved in either decomposition, a significant similarity is found between them and therefore, the full pathway can be hypothesised.

Figure 5.1: Binding modes of CO_2 onto metals.

Figure 5.2: Insertion of CO_2 into metal-ligand complexes.

Figure 5.3: Electrocatalytic reaction products of CO_2 on carbon loaded greigite at B. pH 4.5, C. pH 6.5, and D. pH 10.5, and A. formation rate of formic acid at the three pH buffer solutions. Figure reproduced produced with permission of Roldan *et al.*³⁴

Figure 5.4: a. Design of electrochemical cell used in laboratory measurements, b. Design of *in situ* electrochemical cell used for XAS measurements (drawn by Mike Sheehy), and c. Labelled image of *in situ* electrochemical cell.

Figure 5.5: EXAFS and FT of greigite nanoparticles.

Figure 5.6: a. *in situ* XANES spectra during two CV loops of carbon loaded greigite in a pH 6.8 buffer solution bubbled with N₂ (18a), and merged b. XANES spectra, c. EXAFS, and d. FT at each potential in the loop.

Figure 5.7: a. Linear combination fitting and b. coordination numbers derived from EXAFS modelling of carbon loaded greigite in a pH 6.8 buffer solution bubbled with N₂ (18a) at each potential in the loop.

Figure 5.8: a. Sulfur k-edge XANES spectra of used (18b) and unused (18) carbon loaded greigite compared against freshly synthesised greigite, natural pyrite (26), iron sulfite, and iron sulfate.

Figure 5.9: a. *in situ* XANES spectra during two CV loops of carbon loaded greigite in a pH 4.5 buffer solution bubbled with N₂ (18c), and merged b. XANES spectra, c. EXAFS, and d. FT at each potential in the loop.

Figure 5.10: a. Linear combination fitting and b. coordination numbers derived from EXAFS modelling of carbon loaded greigite in a pH 4.5 buffer solution bubbled with N₂ (18c) at each potential in the loop.

Figure 5.11: a. *in situ* XANES spectra during two CV loops of carbon loaded greigite in a pH 6.8 buffer solution bubbled with CO₂ (18d), and merged b. XANES spectra, c. EXAFS, and d. FT at each potential in the loop.

Figure 5.12: a. Linear combination fitting and b. coordination numbers derived from EXAFS modelling of carbon loaded greigite in a pH 6.8 buffer solution bubbled with CO₂ (18d) at each potential in the loop.

Figure 5.13: a. *in situ* XANES spectra during two CV loops of carbon loaded greigite in a pH 4.5 buffer solution bubbled with CO₂ (18e), and merged b. XANES spectra, c. EXAFS, and d. FT at each potential in the loop.

Figure 5.14: a. Linear combination fitting and b. coordination numbers derived from EXAFS modelling of carbon loaded greigite in a pH 4.5 buffer solution bubbled with CO₂ (18e) at each potential in the loop.

Figure 5.15: a. *in situ* XANES spectra during two CV loops of carbon loaded greigite in a pH 10.5 carbonate buffer solution bubbled with N₂ (18f), and merged b. XANES spectra, c. EXAFS, and d. FT at each potential in the loop.

Figure 5.16: a. Linear combination fitting and b. coordination numbers derived from EXAFS modelling of the carbon loaded greigite in a pH 10.5 carbonate buffer solution bubbled with N₂ (18f) at each potential in the loop.

Figure 5.17: Evolution of bond distances according to EXAFS of the carbon loaded greigite structure from oxide formation during CV loops in the five buffer solutions.

Figure 5.18: a. *in situ* XANES spectra during a CV loop of violarite on the iron K-edge in a pH 6.8 buffer solution bubbled with N₂ (22), and merged b. XANES spectra, c. EXAFS, and d. FT at each potential in the loop.

Figure 5.19: a. Linear combination fitting, and b. coordination numbers and c. bond distances derived from EXAFS modelling of violarite on the iron K-edge in a pH 6.8 buffer solution bubbled with N₂ (22) at each potential in the loop.

Figure 5.19: a. *in situ* XANES spectra during a CV loop of violarite on the nickel K-edge in a pH 6.8 buffer solution bubbled with N₂ (22), and merged b. XANES spectra, c. EXAFS, and d. FT at each potential in the loop.

Figure 5.20: a. Coordination numbers and b. bond distances derived from EXAFS modelling of violarite on the nickel K-edge in a pH 6.8 buffer solution bubbled with N₂ (22) at each potential in the loop.

List of Tables

Table 3.1: Acquisition mode and k-range details of XAS measurements taken for TM dithiocarbamates in different environments.

Table 3.2: Results of EXAFS fittings for $\text{Zn}(\text{Me}_2\text{NCS}_2)_2$ as a solid and dissolved in xylene and oleylamine.

Table 3.3: Results of EXAFS fittings for $\text{Ni}(\text{tBu}_2\text{NCS}_2)_2$ as a solid and dissolved in dodecane, oleylamine, and hexylamine.

Table 3.4: Results of EXAFS fittings for $\text{Fe}(\text{tBu}_2\text{NCS}_2)_3$ as a solid and dissolved in dodecane, and oleylamine.

Table 4.1: *In situ* experiments carried out on the zinc, nickel, and iron K-edges.

Table 4.2: Results of EXAFS fitting for the *in situ* decomposition of 14.

Table 4.3: Results of EXAFS fitting for the *in situ* decomposition of 3.

Table 4.4: Results of EXAFS fitting for the *in situ* decomposition of 3 (rapid ramp, hold and cool).

Table 4.5: Results of EXAFS fitting for the *in situ* treatment of 8.

Table 4.6: Results of EXAFS fitting for the *in situ* decomposition of 9.

Table 4.7: Results of EXAFS fitting for the *in situ* decomposition of 10.

Table 5.1: Best fit for greigite nanoparticles with fixed coordination numbers.

List of Equations

Equation 2.1: The EXAFS equation.

$$\chi(k) = \sum_j \left(\frac{N_j f_j(k) e^{-2k^2 \sigma_j^2}}{k R_j^2} \sin[2k R_j + \delta_j(k)] \right)$$

Equation 2.2: The Beer-Lambert law of absorption

$$x\mu(E) = -\ln(I_t/I_0)$$

Equation 2.3: Background subtraction to obtain $\chi(E)$ from $\mu(E)$.

$$\chi(E) = \frac{\mu(E) - \mu_0(E)}{\Delta\mu_0(E)}$$

Equation 2.4: Calculation of k (\AA^{-1}) from energy

$$k = \sqrt{\frac{2m(E - E_0)}{\hbar^2}}$$

Equation 2.5: Nyquist equation for EXAFS analysis.

$$N_{idp} = \frac{2 \Delta k \Delta R}{\pi}$$

Equation 2.6: Reduced χ^2

$$\epsilon_v^2 = \frac{1}{(N_{ind} - N_{var}) (N_{ind}/N)} \sum_i w_i (\chi^{exp}(k_i) - \chi^{calc}(k_i))^2$$

Equation 2.6: R-factor in EXAFS

$$R = \sum_i^N \left(\frac{1}{\sigma} \right) (|\chi^{exp}(k_i) - \chi^{calc}(k_i)| \times 100\%)$$

List of Samples

Sample 1: Ni(ⁱBu₂NCS₂)₂ *solid*

Sample 2: Ni(ⁱBu₂NCS₂)₂ dissolved in *dodecane*

Sample 3: Ni(ⁱBu₂NCS₂)₂ dissolved in *oleylamine*

Sample 4: Ni(ⁱBu₂NCS₂)₂ dissolved in *hexylamine*

Sample 5: Ni(Hex(H)NCS₂)₂

Sample 6: Laboratory synthesised nickel sulfide from decomposition of Ni(ⁱBu₂NCS₂)₂ dissolved in *oleylamine*

Sample 7: Fe(ⁱBu₂NCS₂)₃ *solid*

Sample 8: Fe(ⁱBu₂NCS₂)₃ dissolved in *dodecane*

Sample 9: Fe(ⁱBu₂NCS₂)₃ dissolved in *oleylamine*

Sample 10: Fe(ⁱBu₂NCS₂)₃ and S₂(ⁱBu₂NCS₂)₂ (4:1) dissolved in *oleylamine*

Sample 11: Fe(ⁱBu₂NCS₂)₃ (high concentration) dissolved in *oleylamine*

Sample 12: Zn(Me₂NCS₂)₂ *solid*

Sample 13: Zn(Me₂NCS₂)₂ dissolved in *xylene*

Sample 14: Zn(Me₂NCS₂)₂ dissolved in *oleylamine*

Sample 15: Ni(ⁱBu₂NCS₂)₂ dissolved in *hexane*

Sample 16: Ni(ⁱBu₂NCS₂)₂(C₂H₄)₂N

Sample 17: Fe(ⁱBu₂NCS₂)₃ dissolved in *hexylamine*

Sample 18: Laboratory synthesized greigite from decomposition of Fe(ⁱBu₂NCS₂)₃ dissolved in *oleylamine*

Sample 19: FeSO₄·7H₂O (97%, Sigma Aldrich Ltd)

Sample 20: Iron sulfide synthesised from 19 and Na₂S·9H₂O (≥98.0%, Sigma Aldrich Ltd)

Sample 21: Oxidation product of 20, a mixture of γ-FeO(OH) and α-FeO(OH)

Sample 22: Laboratory synthesized violarite from decomposition of Fe(ⁱBu₂NCS₂)₃ and Ni(ⁱBu₂NCS₂)₂ dissolved in *oleylamine*

Sample 23: α-Fe₂O₃ (powder, <5μm, ≥ 99 %, Sigma Aldrich Ltd)

Sample 24: FeCl₃·6H₂O (ACS reagent grade, 97%, Sigma Aldrich Ltd)

Sample 25: Cubane - [NⁿBu₄]₂[Fe₄S₄(SPh)₄], bis(tetra-*n*-butylammonium) tetrakis [benzenethiolato-μ₃-sulfido-iron]

Sample 26: Mineral pyrite from the Huanzala mines donated by Utrecht University Geosciences Department

List of Communications

1. Husn-Ubayda Islam, Anna Roffey, Nathan Hollingsworth, C. Richard A. Catlow, Mariette Wolthers, Nora H. de Leeuw, Wim Bras, Gopinathan Sankar, and Graeme Hogarth; *In Situ XAS of the Solvothermal Decomposition of Dithiocarbamate Complexes*; *Journal of Physics: Conference Series*, **2013**, 430, 012050
2. Nathan Hollingsworth, Anna Roffey, Husn-Ubayda Islam, Maxime Mercy, Alberto Roldan, Wim Bras, Mariette Wolthers, C. Richard A. Catlow, Gopinathan Sankar, Graeme Hogarth, and Nora H. de Leeuw; Active Nature of Primary Amines during Thermal Decomposition of Nickel Dithiocarbamates to Nickel Sulfide Nanoparticles; *Chemistry of Materials*, **2014**, 26 (21), pp 6281–6292
3. Vera P. Santos, Tim A. Wezendonk, Juan José Delgado Jaén, A. Iulian Dugulan, Maxim A. Nasalevich, Husn-Ubayda Islam, Adam Chojecki, Sina Sartipi, Abrar A. Hakeem, Ard Koeken, Matthijs Ruitenbeek, Thomas Davidian, Garry R. Meima, Freek Kapteijn, Gopinathan Sankar, Michiel Makkee, and Jorge Gascon; Metal Organic Framework mediated synthesis of exceptionally stable, highly active Fischer-Tropsch catalysts; *Nature Communication*, **2015**, 6451
4. Anna. Roffey, Nathan. Hollingsworth, Husn-Ubayda Islam, Maxime Mercy, C. Richard A. Catlow, Gopinathan Sankar, Nora H. de Leeuw, Greame Hogarth; Phase control during the synthesis of nickel sulfide nanoparticles from dithiocarbamate precursors; *submitted*, **2015**
5. Alberto Roldan Martinez, Nathan Hollingsworth, Anna Roffey, Husn-Ubayda Islam, Josie Goodall, C. Richard A. Catlow, Jawwad A. Darr, Wim Bras, Gopinathan Sankar, Katherine B. Holt, Graeme Hogarth, Nora H. de Leeuw; CO₂ conversion by greigite under alkaline conditions: Support for Archaeal hydrothermal vents as a niche for early life; *Chem. Commun.* **2015**, 51, 7501–7504.

Chapter 1 Overview

In this thesis, XAS is used to understand the synthesis, stability, and electrocatalytic activity of iron sulfides. The first chapter introduces the role of iron sulfides in nature, including its supposed role in the origin of life. It also provides detail on the structure of different iron sulfides, modern applications for iron sulfides, and popular synthesis techniques to derive various iron sulfide phases. Finally, an overview of this thesis is given.

Chapter 1

Iron sulfides: structure, synthesis, and applications

1.1 Introduction

Iron sulfides are a complex and wide ranging set of materials. The magnetic, conductive, and reactive properties rely heavily on the composition and phase, which in turn are easily interchanged depending on environmental conditions. The oxide analogues of iron sulfides have been studied extensively and are used in a huge variety of applications ranging from Fischer-Tropsch catalysis¹⁻³ and dehydrogenation of ethylbenzene⁴⁻⁶ to magnetic storage^{7,8} and use as semiconductor materials.⁹⁻¹² Iron oxides are also widely used in medical applications; use of magnetic iron oxides in drug delivery for cancer treatment is relatively commonplace.^{13,14} The potential application of iron sulfide materials in some of these areas can be improved significantly if control over the dispersity and stability of iron sulfide particles can be achieved. The use of these materials in electrochemical cells for the electroreduction of carbon dioxide is a prime example of this and will be further investigated in this work.

As it stands, most iron sulfide chemistry is challenging to control. Up to seven iron sulfide phases exist according to the literature.^{15,16} The prevalence of each phase and phase mixtures are dictated by thermodynamic stability which can be significantly different depending on synthesis, storage and operating conditions. As well as isolated solid materials, iron sulfides can exist as dissolved clusters, and similar clusters occur at the active sites of biological enzymes. Iron sulfides play a large role in biogeochemical processes; ancient sulfide sediments provide insight into the evolution of earth's atmosphere, and biological evolution itself.¹⁶

This thesis touches on several aspects of iron sulfide chemistry. First, different methods of iron sulfide synthesis are explored with an interest toward materials that can be used in applications – i.e. stable and phase pure nanoparticulate materials. Characterisation of the synthesized materials is performed using the synchrotron based technique of X-ray absorption spectroscopy (XAS).

The second part of the thesis attempts, via *in situ* XAS, to postulate a synthesis mechanism for the solvothermal decomposition of transition metal (TM)

dithiocarbamate complexes. Of all the synthesis methods, the solvothermal decomposition of TM dithiocarbamates is most successful: decomposition results in nanoparticles with well-defined surfaces and particles are protected by heavy capping agents. In addition dithiocarbamates are versatile and stabilize a range of transition metals; decomposition of a mixture of metal dithiocarbamates is a facile way to form mixed metal sulfides. Here, zinc, nickel, and iron dithiocarbamates are decomposed to form zinc, nickel and iron sulfides respectively, and the mechanisms of each are investigated in an attempt to compare and contrast decomposition processes. To test the quality of a catalytically relevant iron sulfide and mixed iron nickel sulfide made by this method, under realistic electrochemical conditions, the materials were loaded onto a carbon electrode in an electrochemical cell with CO₂ rich electrolyte and monitored by *in situ* XAS.

1.1.1 The sulfur cycle

In order to place iron sulfides in a wider context, a basic grasp of the sulfur cycle is necessary. Sulfur is defined by its wide ranging redox properties. The sulfur cycle explains the sources, sinks, and movement of sulfur species, via redox processes, in nature (Figure 1.1). Iron sulfide minerals are the earth's original sulfur pool. They were introduced to the earth's surface primarily through hydrothermal vents.^{17,18} The world sulfur content is increasingly composed of mobile sulfur species released from the sulfide pool through release of hydrogen sulfide from volcanic activity, and weathering of the earth's crust by an increasingly more oxygenated atmosphere. Processes within the cycle include the uptake of sulfur by organisms to form amino acids and enzyme active centres and release of sulfur from biological matter to sediment by biomineralisation.

The sulfur cycle also defines non-biological and man-made processes that aid the reduction and oxidation of sulfur species, and the processes by which species are distributed including atmospheric movement and absorption by soil and seawater. Figure 1.1 provides a basic overview of the sulfur cycle. Iron sulfide chemistry is most pronounced in anoxic conditions. While this is less common in today's oxygen rich atmosphere, some marine environments exist in a permanently anoxic condition including the deep waters of the Black sea¹⁹, Cariaco Trench²⁰, Framvaren Fjord²¹, and Chesapeake Bay.^{16,22}

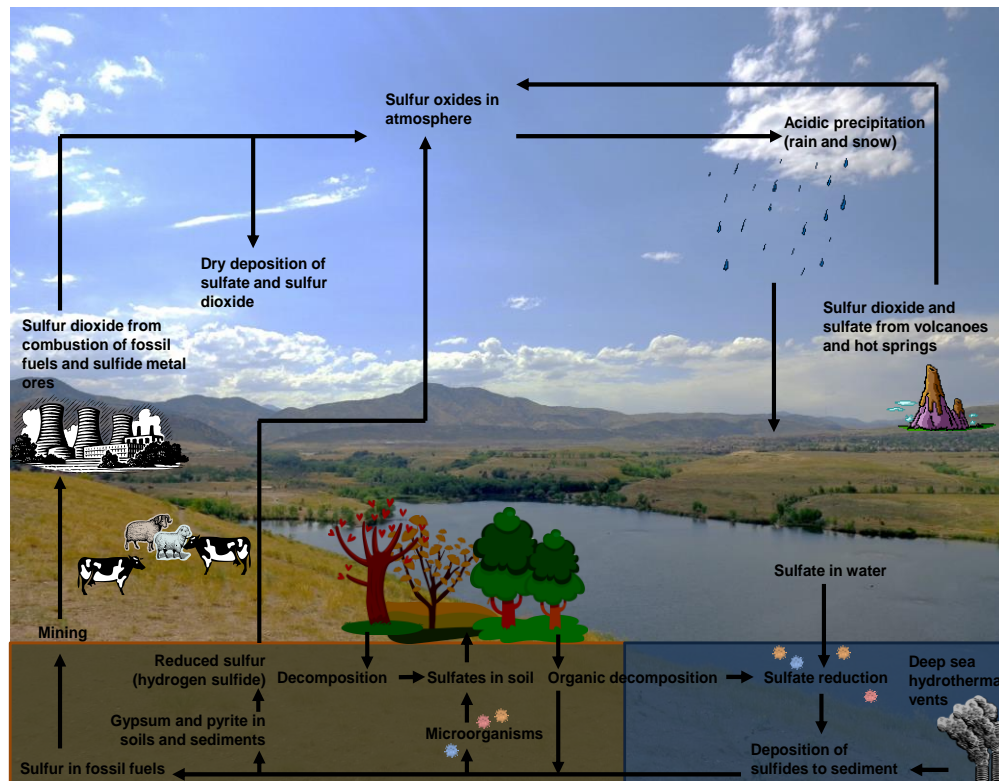


Figure 1.1: Pictorial diagram demonstrating aspects of the sulfur cycle.

1.1.2 Deep sea hydrothermal vents

Deep sea hydrothermal vents are the primary source of iron sulfides on earth. Hydrothermal vents are holes in the earth's mantle that release geothermally heated water from within the earth's crust. They form both on land and sea, although naturally the prevalence at sea is far greater as there is more water than land surface. Vents are found at the border of tectonic plates near volcanic activity. The water released from hydrothermal vents contain high concentrations of small molecules. Unique environments that are rich in organic life forms surround deep sea vent systems, supported by the nutrient rich waters; chemosynthetic bacteria utilise chemicals in the water for energy, building whole, very localised ecosystems. Due to the solitary nature of vents, the ecosystems evolve in isolation and often display unexampled lifeforms.

Water bodies within vents are also supercritical, with respect to temperature and pressure, in nature, with temperatures reaching above 400° C. When the supercritical water is rapidly introduced to the typically near freezing temperatures of the ocean floor, it causes minerals to precipitate out of solution. 'Black smokers' are hydrothermal vents rich in sulfur species that precipitate a range of transition metal

sulfides including iron, zinc, and copper sulfides.^{17,18} The dynamic nature of the sulfide formation results in structures that are porous and metastable.^{23–25}

1.1.3 Iron sulfur world theory

The vast and complex ecosystems that occur around vents add weight to the iron sulfur world theory which hypothesises that deep sea hydrothermal vents were the geological origin of living organisms, and that the development of living organism was catalytically assisted by sedimentary iron sulfides.^{26–35}

While iron sulfur world theories vary in detail, the central theme is that fixation of small inorganic molecules - particularly CO_2 - on sulfide surfaces and the subsequent catalytically activated reaction to small organic compounds, resulted in the first organic lifeforms. The low entropy mechanism would have seen freshly formed organic molecules remain attached to the surface of iron sulfides depending on dissociation energies, and further catalyse to longer chain molecules. Eventually through millions of years of autocatalytic reactions aided by constant availability of reactants and iron sulfide catalysts, the organic complexes would have become more complex thus forming the first self-sufficient respiring biological entity.

Wächtershäuser first suggested the idea of CO_2 capture and conversion to useful organic compounds^{26–31} and went on to further suggest that the driving force of reactions, and source of electrons for the reduction of CO_2 , was obtained from the oxidation of sulfides to produce pyrite. Pyrite formation is a known process that takes place very close to black smokers at high temperatures and acidic conditions. Russel, Hall, and Martin suggested an alternative approach which saw CO_2 capture take place in more alkaline environments and at low temperatures.^{32–35} Here the driving force is the ionic gradient formed between the interconnecting networks of highly porous iron sulfide sediments, and the surrounding alkaline ocean environment which causes a natural circuit to be created and hence an electrochemical cell providing external electrons for CO_2 reduction. Greigite is a popular choice in the Russel, Hall, and Martin hypothesis on account of its distinctive cubane building blocks that share similarity with modern day biological enzymatic structures.

1.1.4 Iron sulfides in nature

There are multiple examples of the intimate relationship between sulfides and biological complexes, and in particular the use of sulfides in some organisms specifically for mediating energy transfer. Some of these examples are highlighted below.

It was discovered by Blakemore³⁶ that some bacteria could perform magnetotaxis; a phenomenon whereby bacteria orientate and navigate towards the earth's natural magnetic field. The bacteria which had high mobility would move in the direction of the north pole and change direction when in close proximity to a bar magnet. Blakeman attributed the magnetism to "novel structured particles rich in iron". Mössbauer experiments revealed the presence of magnetite, Fe_3O_4 within the magnetotactic bacteria,³⁷ and later, Fe_3S_4 nanocrystals were also found.³⁸ The particles have been shown to be synthesized by the bacteria. This is one of the many examples of biologically assisted formation of iron sulfides.

Ferredoxins are a group of proteins that mediate electron transfer in a range of metabolic reactions in plants and bacteria. They contain iron sulfur clusters that can accept or donate electrons through the interconversion of iron(II) and iron(III). There are two groups of ferredoxins. Planar Fe_2S_2 clusters are found mainly in plants^{39,40} while the cubane Fe_4S_4 is found in bacteria.⁴¹ Fe_3S_4 is a variant of Fe_4S_4 with an open cage structure. Iron sulfide clusters are attached to peptide chains through cysteine amino acid residues that create sulfur bridges with the cluster.⁴²

An example of a ferredoxin being used for respiration in anaerobic bacteria is found in the enzyme carbon monoxide dehydrogenase/acetyl coenzyme-A synthase, CODH/ACS. This is a dimeric enzyme used for the acetylation of coenzyme-A. The process is vital to the ATP cycle used in cellular respiration. Carbon monoxide dehydrogenase (CODH) is responsible for the reduction of CO_2 and conversion to CO. The active complex at the centre of the enzyme is an NiFe_3S_4 cubane. The CO is then transported to the active site of acetyl coenzyme-A synthase (ACS) where it is methylated by addition of a $-\text{CH}_3$ group to form thio-acetic acid before release. The active site of this enzyme is also an iron sulfide cubane Fe_4S_4 with a nickel atom attached.⁴³

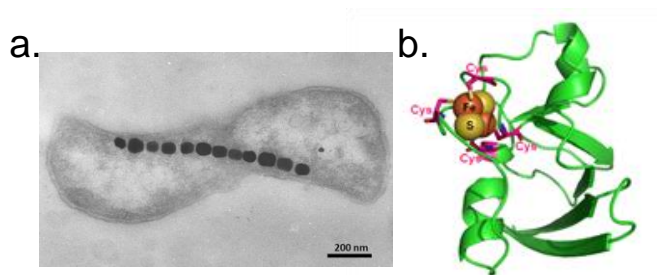


Figure 1.2: a. TEM image of magnetotactic bacterium containing particles of magnetite. Image is taken from www.nature.com/scitable/knowledge/library/bacteria-that-synthesize-nano-sized-compasses-to-15669190. b. Image of enzyme containing Fe₂S₂ active inorganic cluster. The cluster is attached to the organic body of the enzyme by sulfur bridges on cysteine amino acids. Image is taken from www.ebi.ac.uk/training/online/course/introduction-protein-classification-ebi/protein-classification/what-are-sequence-features.

1.2 Iron sulfide minerals

In order to appreciate the full complexity of iron sulfides, natural sulfide structures are reviewed here. Iron sulfides exist as solids and dissolved complexes. On the earth's surface, there are at least seven distinct iron sulfide phases.¹⁶ As sulfur is considered a soft ligand, iron prefers to be in 2+ rather than 3+ oxidation state; greigite is the only iron sulfide to stabilise iron(III) centres. This is in contrast to oxides which are by far more stable as iron(III) complexes. Wüstite, the only fully iron(II) oxide, is unstable in air and readily oxidises to iron(III) oxide materials. Since iron ions are hard (small, highly charged and weakly polarisable), it prefers coordination to oxygen, another hard ion, rather than sulfur which is soft (large and strongly polarisable). This is why many sulfides are easily transformed to oxides in aerobic conditions.

1.2.1 Iron sulfide clusters

Dissolved iron sulfide molecular complexes exist as Fe₂S₂·4H₂O, Fe₄S₄·4H₂O, and [Fe₄S₄(SH)₄]^{x-}, where x is a number between 1 and 4. The first two are stabilised in aqueous environments while the latter is prevalent in non-aqueous systems. In aqueous solutions, iron only exists in a 2+ oxidation state, however, the same clusters stabilised within enzymes can interchange between 2+ and 3+ oxidation states, giving the electron transfer capabilities.^{39–43}

Iron sulfide complexes ligated directly to water were first discovered by Buffle⁴⁴ while the non-aqueous analogues, comprising of iron in varied oxidation states and

containing counter ions such as tetrabutyl-ammonium, were synthesised by Holm *et al.*^{45–47}

1.2.2 Mackinawite

The smallest cluster to contain the distinctive structure of the mackinawite phase exists at 2.2nm.^{15,48,49} Before its discovery, mackinawite was suggested to form amorphous systems that would either crystallise and become more prominent in XRD traces, or go on to form other stable iron sulfide phases.¹ The density of the nanoparticle is less than bulk values, and expanded cell parameters are attributed to water infiltration into the mackinawite layers as well as general nano size effects.

Bulk mackinawite has tetragonal symmetry and a stoichiometric 1:1 ratio of iron(II) and sulfur(II).⁵⁰ The bulk is arranged in a layered structure: typically, $a = b = 3.67 \text{ \AA}$ while $c = 5.03 \text{ \AA}$ (Figure 1.3). The iron(II) is tetrahedrally coordinated to four equidistant sulfur atoms to form a perfect square planar arrangement perpendicular to the c axis with Fe-Fe distances of about 2.60 \AA , similar to distances observed in α -iron. Some level of metallic character and delocalisation of electron density is expected along the c axis. Van der Waals forces exist between the stacks through sulfur ions.⁵¹

Mackinawite is considered the precursor of many other iron sulfides. It shares characteristics with the crystallographic structure of greigite in particular. Natural mackinawite is widespread, it is particularly abundant in low temperature aqueous environments.¹⁶

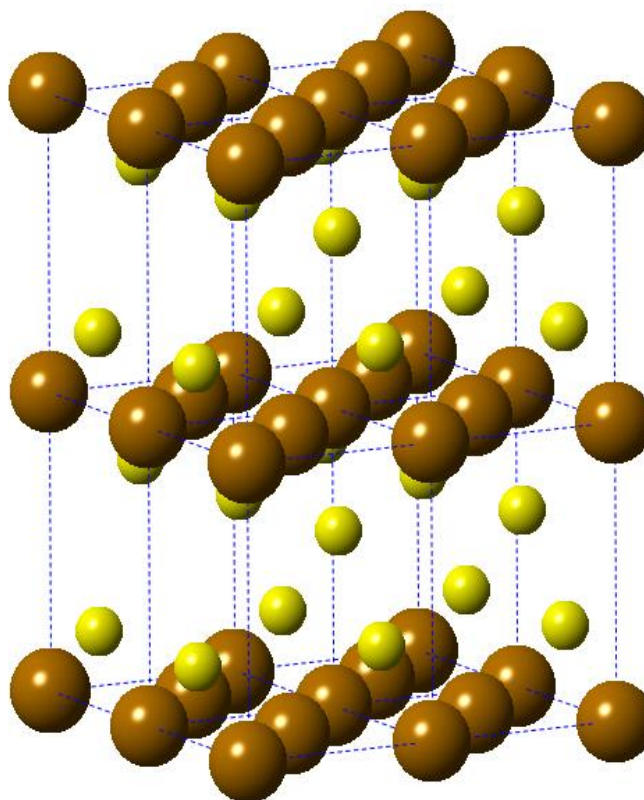


Figure 1.3: Crystalline extended unit cell of mackinawite showing iron(II) (brown) and sulfur(II) (yellow). Iron is tetrahedrally coordinated to four sulfur and the iron arrange in layers of square planar geometries. The layers are held together by van der Waals forces.

1.2.3 Greigite

Greigite, Fe_3S_4 , is the sulfide analogue of magnetite Fe_3O_4 . It adopts an inverse spinel structure of cubic close packed symmetry with the formula $\text{A}(\text{AB})_2\text{S}_4$ where A is the symbol for iron(II) and B for iron(III). In a unit cell of greigite there are eight tetrahedral and sixteen octahedral sites.¹⁶ Iron(III) occupy purely octahedral sites while iron(II) is present in both coordinations. Bond distances of the two sites differ significantly, with octahedral Fe-S distances listed at 2.46 Å and tetrahedral distances at the much shorter value of 2.16 Å.^{52,53}

Greigite and mackinawite have related structures (Figure 1.4) and conversion from mackinawite to greigite can be achieved through the oxidation of a third of the iron(II) sites to iron(III) - the iron(III) adopts octahedral coordination thus forces structural change.¹⁶

Greigite is known to be ferromagnetic and is associated with magnetotactic bacteria.³⁸ Greigite is also commonly found in the presence of other transition

metals, notably copper, cobalt, and nickel, to form doped greigite in fresh water systems.⁵⁴ The replacement of half the octahedral iron sites by nickel results in the formation of a stable mixed metal inverse spinel structure known as violarite.⁵⁵ Building blocks of violarite bare strong resemblance to the cubane structures found in iron sulfide containing enzymes including CODH/ACS mentioned in section 1.1.4.⁵⁶ Greigite and violarite are implicated in Origins of Life theories, and are both investigated in Chapter 6.³²⁻³⁵

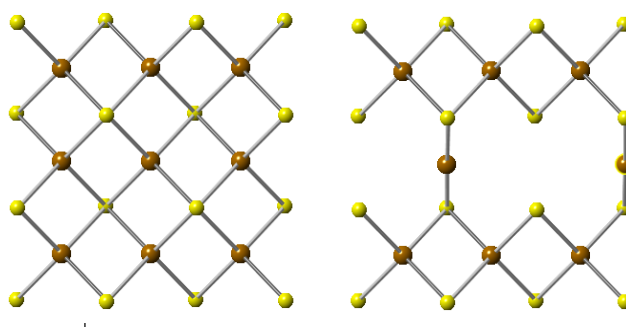


Figure 1.4: The 001 surface of mackinawite (left) and greigite (right) showing similarities between the structures. Iron centres are brown and sulfur centres are yellow.

1.2.4 Pyrite

Pyrite is the most stable iron sulfide structure on earth. It is commonly called “Fool’s Gold” owing to its seemingly inert chemistry and, when weathered, has a slight golden hue in the bulk form. Like gold, nanoparticulate pyrite is less inert.⁵⁷ Stability of the structure means that it is long lasting and geochemists often use the profile of ancient pyrite to determine major environmental events on the earth.¹⁶

The structure of pyrite is similar to that of NaCl with S_2^{2-} anionic species. There is a low symmetry and mineral chirality associated with the material despite cubic geometry due to the number of arrangements the non-spherical anion can adopt (Figure 1.5).⁵⁸ The structure of pyrite was first solved by Bragg in 1914,⁵⁹ and values were updated through the years with improved characterisation capabilities. Bond distances of pyrite are reported at 2.27 Å, and 3.46 Å for the six short and six long interactions.⁶⁰ Pyrite doping results in both p-type and n-type conductivity⁶¹ which makes the material of interest for photovoltaics.

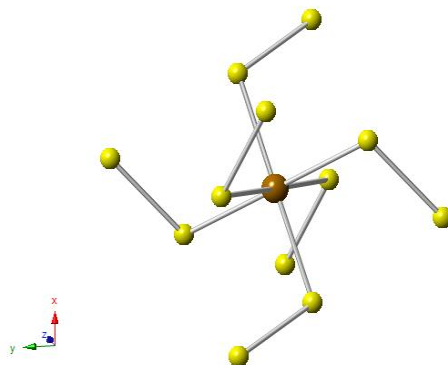


Figure 1.5: Local structure of pyrite showing iron(II) (brown) and sulfur (yellow). The sulfur species, S_2^{2-} , are shaped like dumbbells and arrange at angles to the iron centre causing a distorted octahedral geometry and low symmetry.

1.2.5 Pyrrhotite

Owing to the wide range of metastable defect structures under the classification of pyrrhotites, this group of iron sulfides are probably the most abundantly produced form of iron sulfide on the earth's surface although it tends to be rare in marine systems.¹⁶ Pyrrhotite has the non-stoichiometric composition of $Fe_{1-x}S$ where $x > 0.2$. It is a stable material that can be found as either monoclinic^{62,63} or hexagonal⁶⁴ form depending on composition; monoclinic pyrrhotite has a formula close to Fe_7S_8 and is magnetic in nature while hexagonal pyrrhotite is approximately $Fe_{10}S_{11}$ and non-magnetic.

1.2.6 Less common iron sulfides

Cubic FeS is a stoichiometric iron sulfide similar to the structure of sphalerite. The material is not found naturally and is highly unstable, rapidly forming mackinawite.⁶⁵ Troilite is another FeS structure containing a stoichiometric 1:1 ratio of iron and sulfur. It is related to pyrrhotite, but differs in the fact that it is non-magnetic due to lack of iron vacancy. The structure is hexagonal phase, and it is usually found in meteorites.⁶⁶ Smythite is a metastable structure also related to pyrrhotite with a hexagonal phase. The formula for smythite is Fe_9S_{11} . The structure is rare and is normally found in hydrothermal systems usually in conjunction with carbonates although it was first discovered inland.⁶⁷ Marcasite, FeS_2 , an orthorhombic phase is a metastable disulfide structure related to pyrite.⁶⁸ It is a common mineral found in hydrothermal systems and within sedimentary rocks.

1.3 Synthesis of iron sulfides

The work described in this thesis is based on the investigation of a geochemical system from a materials chemistry perspective and especially in catalysis. This includes laboratory based synthesis of iron sulfides. In keeping with the theme, published synthesis techniques for the production of iron sulfide nanoparticles have been discussed here. Emphasis has been made on nanoscale particles owing to the importance of high surface area in catalysis.

1.3.1 Synthesis of disordered mackinawite from ferrous iron and sulfide salts

The most common method of iron sulfide synthesis is the mixing of iron and sulfide salts which results in a displacement reaction. Without capping agent, these syntheses are performed under strict anaerobic conditions. A report by Wolthers *et al.* suggests the use of Mohr's salt $\text{Fe}(\text{NH}_4)_2(\text{SO}_4)_2 \cdot 4\text{H}_2\text{O}$ owing to its relatively high resistance to oxidation.⁴⁹ According to the report, solutions are prepared from milli-Q water purged with purified oxygen-free nitrogen gas. Mackinawite nanoparticles are formed by mixing a solution of Mohr's salt with a sodium sulfide solution of equivalent molarity under nitrogen. The freshly formed particles are filtered from the suspension and freeze dried for three to four days.

For the characterisation X-ray diffraction (XRD) of the freeze-dried material is acquired under a flow of nitrogen. While the pattern matches mackinawite, broad peaks suggest a disordered phase or nanoparticulate particle size. A Transmission electron microscopy (TEM) mesh loaded in air using freeze-dried nanoparticles dispersed in acetone reveals micrometre-sized aggregated structures consisting of smaller particles. Aggregation is suggested to result from filtration and the subsequent freeze-drying process. The average particle sizes are estimated to be between 20 and 400 nm in diameter.

1.3.2 Synthesis of nanocrystalline iron sulfides from toluene-thermal process

A reoccurring theme in iron sulfide synthesis is the use of non-polar solvents since polar environments tend to create conditions with rather unfavourable conversion kinetics. In a report by Qian *et al.* a solvothermal technique is used to synthesise iron sulfide nanoribbons.⁶⁹ The first step of the reported process is the synthesis of a Na_2S_3 precursor. This is done by reacting Na and S in toluene at 120 to 150° C for 4 hrs. To form the iron sulfide nanoribbons, $\text{FeSO}_4 \cdot 7\text{H}_2\text{O}$ is typically mixed with a

50% excess of Na_2S_3 and added to a Teflon-lined autoclave containing 75% toluene. The reactants are heated to a range of temperatures between 80 and 170° C for 24 hrs. The resulting precipitates are collected and dried in vacuum at 80° C for 4 hrs.

XRD patterns show that the purest products are found when reaction temperatures of 80° C (cubic Fe_3S_4 , greigite) and 170° C (monoclinic FeS_2 , pyrite) are used with a reaction time of 24 hrs. Intermediate reaction conditions produce a mixture of phases. At 120° C, a mixture of greigite and marcasite (orthorhombic FeS_2) is formed. Between 150 and 170° C with a reaction time of 12 hrs, a mixture of marcasite and pyrite is observed.

TEM reveals an average grain size of 25 nm for greigite particles formed at 80° C – a size distribution is not provided in the report. The size distribution of pure phase pyrite ranges from 20 nm to 60 nm.

1.3.3 Synthesis of magnetic pyrrhotite nanorods and sheets from elemental iron

Elemental iron is the second most popular reactant for the synthesis of iron sulfides after ferrous iron. A report by Kong *et al.* describes the synthesis of nanorods and nanosheets of pure magnetic pyrrhotite using elemental iron.⁷⁰ The synthesis involves grinding iron powder and potassium iodide together and loading the mixture into a crucible placed at the centre of a quartz tube furnace with a second crucible upstream containing elemental sulfur. Reactants are typically heated to between 750 and 800° C for 3 hrs under a constant argon flow. After cooling naturally, the product is washed with distilled water and dried at 60° C for 5 hrs.

XRD reveals the synthesis of magnetic pyrrhotite Fe_7S_8 . For the reaction at 750° C, Scanning electron microscopy (SEM) images reveal well aligned nanorods with 200 nm diameters and 1.5-2 μm lengths. Selected Area Electron Diffraction (SAED) of the nanorods shows that the (012) direction is parallel to the rod axis, strongly suggesting growth of the rods along the [012] direction. At 850° C, nanosheets are formed with faces parallel to the growth axis.

The report explains that the presence of potassium iodide is vital to the formation of the rods and sheets. A suggested mechanism involves potassium iodide reacting with sulfur and trace amounts of molecular oxygen to form iodine which in turn acts as a catalyst for the production of Fe-S bonds: elemental iron reacts with iodine to form

FeI₂ which is displaced by sulfur to form FeS and I₂. It is suggested that at the higher temperatures, iodine is produced more easily thus resulting in greater quantities of Fe-S which agglomerate and grow upwards in sheet formation.

1.3.4 Synthesis of magnetic and non-magnetic pyrrhotite nanowires

A report by Nath *et al.* describes the synthesis of iron sulfide nanowires of magnetic and non-magnetic pyrrhotite.⁷¹ Control is achieved over nanowire length and magnetism, both qualities beneficial in the area of magnetic information storage. The nanowires are synthesised in a two-step process. The first step involves the solvothermal synthesis of a capped iron sulfide precursor, and the second step uses a flux method to remove amine capping agents and aid crystallisation. In the first step, FeCl₂.H₂O mixed with thioacetamide CH₃CSNH₂ is added to a Teflon-lined autoclave with ethylenediamine and heated to 180° C for 4 days. The resulting product is immediately extracted by dispersion in methanol and filtering. The composite is then deposited onto a quartz boat in a quartz tube and placed in a horizontal tubular furnace and heated under a flow of argon to 200° C for 20 hrs or 300° C for 30 hrs.

According to X-ray Diffraction data, the removal of amine groups from the precursor at 200° C and 300° C results in characteristic magnetic and non-magnetic pyrrhotite phases respectively. For the sample produced at 200° C, SEM shows the formation of micrometer length nanowires and TEM reveals diameters of between 40 and 180 nm. The SEM of the sample formed at 300° C shows the formation of shorter nanowires while TEM reveals diameters between 80 and 100 nm. Although there seems to be higher monodispersity at 300° C, the product contains significant amounts of a secondary structure unrelated to the nanotube.

1.3.5 Synthesis of magnetic pyrrhotite and greigite from cubane precursor

The formation of monodisperse spherical nanocrystals of magnetic pyrrhotite and greigite using a novel cubane-type single-source precursor, [NnBu₄]₂[Fe₄S₄(SPh)₄], bis(tetra-*n*-butylammonium) tetrakis[benzenethiolato- μ 3-sulfido-iron] was reported by O'Brien *et al.*⁷²

The cubane precursor contains twelve pre-formed Fe-S bonds that contribute to the resultant nanocrystals. As mentioned in section 1.1.4, iron sulfide cubanes are

abundant in nature, forming active sites of ferredoxin enzymes where they are involved in electron-transfer processes.

The synthesis of the iron sulfide cubane is well established.⁴⁵⁻⁴⁷ In the most practical synthesis method, lithium is dissolved in methanol and treated with benzenethiol. Anhydrous iron(III) chloride in methanol is added to the solution. Elemental sulfur is then added to form $[\text{Fe}_4\text{S}_4(\text{SPh})_4]^{2-}$. This is stirred overnight before filtering into a solution of tetra-n-butylammonium iodide in methanol to form the final salt.⁴⁷ Larger crystals are made by dissolving the product in warm acetonitrile, filtering, and adding methanol. The synthesis of the iron sulfide nanocrystals involves pyrolysis of the cubane in alkylamines at temperatures between 180 and 230° C. The dissolved cubane is rapidly injected into hot amine and held at given temperatures for an hour. Products are precipitated and filtered.

Products of the syntheses are monodisperse spherical nanocrystals. XRD patterns indicated that monoclinic pyrrhotite, Fe_7S_8 , is formed at 180° C while cubic greigite, Fe_3S_4 , is formed at higher temperatures. Variations in size are determined using TEM: the pyrrhotite structure has an average diameter of 5.6 nm while the cubic greigite decreases from ~4.5 nm to ~2.5 nm with increasing temperature. An explanation for decreased particle size with increasing temperature is attributed to higher efficiency in nucleation according to the report.

1.3.6 Synthesis of magnetic pyrrhotite and greigite from dithiocarbamate precursor

The transition metal dithiocarbamate complex is a versatile single-source precursor for the synthesis of sulfide nanoparticles. A report by Han *et al.* demonstrates the use of the precursor for the synthesis of pyrrhotite and greigite nanosheets.⁷³ The dithiocarbamate complexes used in the report are $\text{Fe}(\text{Et}_2\text{NCS}_2)_3$ (Et=ethyl) and $\text{Fe}(\text{Et}_2\text{NCS}_2)_2(\text{Phen})$ (Phen=1,10-phenanthroline). $\text{Fe}(\text{Et}_2\text{NCS}_2)_3$ is synthesised by the addition of $\text{Na}(\text{Et}_2\text{NCS}_2) \cdot 3\text{H}_2\text{O}$ to aqueous $\text{FeCl}_3 \cdot 6\text{H}_2\text{O}$. The solution is stirred vigorously until precipitated. The precipitate is then washed with water and dried in vacuum. $\text{Fe}(\text{Et}_2\text{NCS}_2)_2(\text{Phen})$ is synthesised in two steps. First, $(\text{Phen}) \cdot 3\text{H}_2\text{O}$ (5mmol) is added to boiling water and introduced to aqueous $\text{FeSO}_4 \cdot 7\text{H}_2\text{O}$, and then aqueous $\text{Na}(\text{Et}_2\text{NCS}_2) \cdot 3\text{H}_2\text{O}$ is added dropwise to the solution. The precipitate is washed and filtered until dry. The iron sulfide nanosheets are formed by dissolving

each precursor in oleylamine, purging with nitrogen, and heating to temperatures between 240 and 320° C for five minutes. The reaction product is cooled, centrifuged, washed in acetone, and filtered.

The iron sulfide made at 240° C from $\text{Fe}(\text{Et}_2\text{NCS}_2)_2(\text{Phen})$ is amorphous according to TEM and XRD. From 260° C, monoclinic pyrrhotite is formed, this is most crystalline at 280° C. Higher temperatures result in a phase change to hexagonal FeS troilite. The nanosheets formed from the solvothermal decomposition $\text{Fe}(\text{Et}_2\text{NCS}_2)_3$ have defined crystal structures over the whole temperature range. Between 240° C and 300° C, greigite particles are formed with traces of hexagonal pyrrhotite according to XRD. At 320° C, phase change occurs and pure hexagonal pyrrhotite is formed.

1.3.7 Synthesis of marcasite and pyrite from dithiocarbamate precursor

Dithiocarbamate complexes are also reported as single source precursors in hydrothermal syntheses. Chen *et al.* reported the hydrothermal decomposition of $\text{Fe}(\text{Et}_2\text{NCS}_2)_3$ to marcasite and pyrite nanoparticles.⁷⁴ The synthesis proceeds by dissolving $\text{Fe}(\text{Et}_2\text{NCS}_2)_3$ into distilled water and heating at 180° C for 12 hrs in a Teflon-lined stainless steel autoclave. The resultant precipitate is filtered and washed using distilled water and absolute ethanol and dried in vacuum at 50° C for 6 hrs.

Amorphous products are synthesised at autoclave temperatures of 120 ° C and 140° C. At 160° C, a mixture of pyrite and orthorhombic FeS_2 (marcasite) is produced. At 180° C, XRD reveals the formation of pure pyrite. According to field emission scanning electron microscopy (FESEM) images, the pyrite synthesised at 180° C exist as cubes with an average diameter of about 500nm.

1.4 Applications of iron sulfides

Capping iron sulfide nanoparticles using solvothermal synthesis methods has increased the general stability of these materials in aerobic environments. This has meant that sulfides are starting to feature more prominently in the arena of applied materials chemistry. The following text describes possible iron sulfide applications. A number of these applications already use iron oxides in established methodology.

1.4.1 Medical imaging

The magnetic properties of ferro materials play an increasingly important role in bio-imaging. Biocompatible Fe_3O_4 nanocrystals are a popular material for use as contrast agents in MRI. For example, Fe_3O_4 materials have been successfully coupled to specific cancer targeting antibodies thus allowing contrast of cancerous cells for imaging.⁷⁵ While the use of magnetite is currently popular, possible application of the thio-analogue greigite is recognised.^{76,77}

1.4.2 Cancer treatment

Magnetic hyperthermia is a cancer treatment based on subjecting an alternating magnetic field onto magnetic nanoparticles to produce heat. The treatment is in research phase but has shown promising signs; when applied alongside other cancer treatments such as chemotherapy, the combination of treatments has shown significantly increased efficiencies.⁷⁸ A balance must be struck in order to avoid heat damage to normal cells. The ability to heat only affected areas is difficult to achieve if cancerous cells are embedded in delicate areas such as in brain tissue. Several studies have been carried out to develop “thermoseeds” that selectively embed into cancer cells. Iron oxide nanoparticles appear to be successful thermoseeds on account of their magnetic properties and ability to be functionalised to target cancer cells.^{13,14,76,77,79} Recently, an attempt was made to synthesise greigite nanoparticles for use in magnetic hyperthermia.⁸⁰

1.4.3 Thin film solar cells

Pyrite has gained considerable attention as a potential absorber material for thin-film solar cells.^{9-12,81} The material is a semiconductor with an energy bandgap of 0.95 eV, comparable to the bandgap of silicon at 1.1 eV,⁸² and exhibits a high absorption coefficient. These two characteristics, coupled with good electronic properties including long lifetime and sufficient mobility of the light-generated charge carriers, means it is possible to use thin pyrite absorption layers in solar cells. In reality, the pure pyrite structure is a poor solar cell material. Instead, pyrite with a high proportion of defects (usually manifesting in the form of sulfur deficiency), and dopants, are more successful.⁹⁻¹² A recent report suggests the use of iron silicon disulfide and iron gallium disulfide in place of pure pyrite to markedly improve the solar cell efficiency compared to pure iron disulfide.⁷⁷

1.4.4 CO₂ reduction catalysis

The iron sulfide world hypothesis postulates the use of iron sulfide materials as catalysts for the activation of CO₂. Research into materials that catalytically activate CO₂ are of great interest. CO₂ is not only the most common product in the oxidation processes of hydrocarbons, but its increasing presence in the atmosphere presents a problem for global atmospheric temperatures.

Evidence of the electrocatalytic reduction of CO₂ on iron sulfide surfaces in ambient conditions was obtained recently.⁸³ The use of solvothermal decomposition methods permitted the synthesis of heavily protected carbon loaded greigite nanoparticles. Electrocatalytic measurements of carbon loaded greigite, in a CO₂-rich electrolyte, resulted in the formation of small organic molecules. The highest rate of productivity was shown to occur in a pH 6.5 buffer solution; formic acid, acetic acid, methanol, and even pyruvic acid were all formed at this pH. Formic acid and methanol are common CO₂ catalysis products seen elsewhere.^{84–88} Acetic acid is more complex and requires two activated carbon dioxide molecules in close proximity to each other, and pyruvic acid, with its three-carbon chain, points to the possible existence of an autocatalytic process.

1.5 Thesis overview

The EngD project detailed in the following chapters was undertaken as part of a wider consortium whose aim was to develop and test iron sulfide, and doped iron sulfide systems for carbon dioxide capture and conversion. The consortium took inspiration from origins of life hypotheses, and with a strong chemistry background, approached the question as an energy and materials challenge – proving carbon dioxide capture and conversion on iron sulfides could potentially place iron sulfides on the green catalyst platform. Within the consortium, several sub-groups existed. These were in the fields of synthesis, computation, and characterisation.

The synthesis group used the decomposition of single source precursors, in particular transition metal dithiocarbamates, in organic solvents, to synthesise iron and doped iron and nickel sulfides. The pre-existing metal-sulfur bonds, and the range of stabilised metals of varying oxidation states in dithiocarbamate complexes, made this family of syntheses versatile. The main dopant investigated in the project was nickel – this is widely thought to be a significant contributor to catalytic activity according

to ORL theory. The first catalyst test setup was an electrocatalytic one involving the use of a three electrode cell with a working electrode drop-coated in sulfide, and immersed in deionised and degassed buffer solution pumped with CO₂. This setup yielded results showing products of formic acid, methanol, acetic acid, and pyruvic acid, albeit in small yields. The computational group was formed in order to model and understand the process of carbon dioxide reduction on a sulfide surface. In order to do this, surfaces of the sulfides had to be modelled. This was done to a remarkable degree of accuracy, when compared to high resolution TEM of the surfaces. Once surfaces were formed, CO₂, H₂, H₂O, O₂, and N₂ were introduced to the computational model. While experimental work provided proof of catalytic products, modelling provided reasoning for the observed results.

The final aspect of the consortium was advanced characterisation. This was set up in collaboration with the Dutch-Belgian beamline and was intended to be based at DUBBLE, using synchrotron techniques – especially EXAFS - to probe mechanisms of important processes. The thesis presented here is the product of this research. Over four years, two sets of investigations were performed, naturally evolving from the wider interests of the group. The first was probing the solvothermal synthesis of sulfides from decomposition of dithiocarbamate complexes *in situ*. It was here that the strong interaction of the solvent with the single source precursor was first discovered. The solvent was shown to be crucial to the whole reaction mechanism – a phenomenon that was not fully appreciated before these investigations were performed. Decomposition of three metal dithiocarbamates was investigated: zinc, nickel, and iron dithiocarbamates were decomposed to form various sulfide phases. The iron system began as the primary interest since there are several phases that could be synthesised, and structure determination is in itself a highly relevant investigation. It fast became apparent that this “real system” was much more complex and interesting than originally anticipated with oxidation state changes, spin cross-over, and major structural changes prior to decomposition. Incompatibility of the system with other probing techniques meant that XAS was the only obvious means by which evidence could be gathered. Nickel dithiocarbamate was investigated for its role as a dopant in iron sulfide. The simplicity of the nickel system and the ease with which it could be studied with many techniques including UV-vis and DFT meant that this system soon became the focus of the group as an

ideal model; results were then used to explain similar trends in the zinc and iron dithiocarbamate decompositions. Zinc dithiocarbamate was also investigated for its decomposition into zinc sulfide. The initial justification for investigating a third system was the difficulty of identifying trends based on two datasets. Zinc dithiocarbamate was ideal owing to existing studies of zinc dithiocarbamate amine complexes and zinc sulfide formation mechanisms. Zinc sulfides are also popular in semiconductor research.

Discussion is then turned to the main objective of the wider consortium concerning the use of electrochemistry for carbon dioxide reduction using iron sulfides. The group showed that greigite aided the formation of formic acid, methanol, acetic acid and pyruvic acid electrochemically from carbon dioxide. DFT explained the mechanism by which this could occur. XAS was meant to probe the structural changes of the local environment of the iron during electrochemistry. *In situ* characterisation was also performed by IR to probe sulfur species, carbonates, phosphates, and water bands. The latter is the work of another PhD and is as of yet unpublished, but alluded to here. In order to perform the *in situ* XAS measurements, an electrochemical cell was designed and built. In the study it was quickly found that although a bulk technique, XAS provided significant information of the surface structure of the nanoparticles. It was found that iron sulfides transformed into iron oxyhydroxides over time. The oxidation was attributed to hydration of the surface by water, and subsequent water dissociation by applied potential. The study highlighted the complexity of the surface chemistry in the electrochemical setup: species present, including water, CO₂, phosphates, and eventually different sulfur species were highly influenced by pH.

In summary, the questions asked in this thesis are as follows:

1. What is the decomposition mechanism of a metal dithiocarbamate complex in solvent which leads to the formation of metal sulfide (Chapter 4)?

This leads to questions about the role of the solvent, and the trends across the first row transition metals:

2. How does the solvent in the decomposition process interact with the dithiocarbamate complexes prior to decomposition (Chapter 3), and during decomposition (Chapter 4)?
3. What are the similarities and differences between the decomposition of three metal dithiocarbamate complexes (zinc, nickel, and iron are used as the case studies)?

Tweaking the iron dithiocarbamate decomposition results in the synthesis of different phases. One of these phases is the catalytically relevant greigite phase.

4. What is the mechanism by which phase is determined (Chapter 4)?

The greigite is used electrocatalytically for the reduction of CO₂ to produce small organic molecules. The process is inefficient, possibly as a result of greigite structural change in the electrochemical set up.

5. What happens to the structure of greigite during the electrochemical process (chapter 5)?

These questions were answered primarily by *in situ* XAS.

1.6 References

- (1) Lei, Y.; Cant, N. W.; Trimm, D. L. *Catal. Letters* **2005**, *103*, 133–136.
- (2) Storch, H. H.; Golumbic, N.; Anderson, R. B. *John Wiley Sons, Inc, New York* **1951**.
- (3) Xu, L.; Bao, S.; O'Brien, R. J.; Houpt, D. J.; Davis, B. H. *Fuel Sci. Technol. Int.* **1994**, *12*, 1323–1353.
- (4) Chang, J.-S.; Park, S.-E.; Park, M. S. *Chem. Lett.* **1997**, *26*, 1123–1124.
- (5) Huang, W.; Ranke, W.; Schlögl, R. *J. Phys. Chem. B* **2005**, *109*, 9202–9204.
- (6) Zscherpel, D.; Weiss, W.; Schlogl, R. *Surf. Sci.* **1997**, *382*, 326–335.
- (7) Suber, L.; Imperatori, P.; Ausanio, G.; Fabbri, F.; Hofmeister, H. *J. Phys. Chem. B* **2005**, *109*, 7103–7109.
- (8) Xiong, Y.; Ye, J.; Gu, X.; Chen, Q. *J. Magn. Magn. Mater.* **2008**, *320*, 107–112.
- (9) Ennaoui, A.; Fiechter, S.; Pettenkofer, C.; Alonso-Vante, N.; Büker, K.; Bronold, M.; Höpfner, C.; Tributsch, H. *Sol. Energy Mater. Sol. Cells* **1993**, *29*, 289–370.
- (10) Ennaoui, A.; Tributsch, H. *Sol. Cells* **1984**, *13*, 197–200.
- (11) Jaegermann, W.; Tributsch, H. *J. Appl. Electrochem.* **1983**, *13*, 743–750.
- (12) Fujishiro, Y.; Uchida, S.; Sato, T. *Int. J. Inorg. Mater.* **1999**, *1*, 67–72.
- (13) Dobson, J. *Gene Ther.* **2006**, *13*, 283–287.
- (14) Dobson, J.; Å, J. D. *Drug Dev. Res.* **2006**, *67*, 55–60.
- (15) Morse, J. W.; Millero, F.; Cornwell, J.; Rickard, D. *Earth-Science Rev.* **1987**, *24*, 1–42.
- (16) Rickard, D.; Luther, G. W. *Chem. Rev.* **2007**, *107*, 514–562.
- (17) Walker, J. C. *Mar. Geol.* **1986**, *70*, 159–174.
- (18) Edmond, J. M.; Measures, C.; McDuff, R. E.; Chan, L. H.; Collier, R.; Grant, B.; Gordon, L. I.; Corliss, J. B. *Earth Planet. Sci. Lett.* **1979**, *46*, 1–18.
- (19) Murray, J. W.; Jannasch, H. W.; Honjo, S.; Anderson, R. F.; Reeburgh, W. S.; TOP, Z.; Friederich, G. E.; Codispoti, L. A.; Izdar, E. *Nature* **1989**, *338*, 411–413.

- (20) Hastings, D.; Emerson, S. *Limnol. Oceanogr.* **1988**, *33*, 391–396.
- (21) Skei, J. M. *Mar. Chem.* **1988**, *23*, 209–218.
- (22) Officer, C. B.; Biggs, R. B.; Taft, J. L.; Cronin, L. E.; Tyler, M. A.; Boynton, W. R. *Science* **1984**, *223*, 22–27.
- (23) Berner, R. A. *Am. J. Sci.* **1970**, *268*, 1–23.
- (24) Butler, I. B.; Rickard, D. *Geochim. Cosmochim. Acta* **2000**, *64*, 2665–2672.
- (25) Wilkin, R. T.; Barnes, H. L.; Brantley, S. L. *Geochim. Cosmochim. Acta* **1996**, *60*, 3897–3912.
- (26) Wächtershäuser, G. *Syst. Appl. Microbiol.* **1988**, *10*, 207–210.
- (27) Wächtershäuser, G. *Proc. Natl. Acad. Sci. U. S. A.* **1990**, *87*, 200–204.
- (28) Wächtershäuser, G. *Proc. Natl. Acad. Sci. U. S. A.* **1994**, *91*, 4283–4287.
- (29) Keller, M.; Blöchl, E.; Wächtershäuser, G.; Stetter, K. O. *Nature* **1994**, *368*, 836–838.
- (30) Drobner, E.; Huber, H.; Wächtershäuser, G.; Rose, D.; Stetter, K. O. *Nature* **1990**, *346*, 742–744.
- (31) Blöchl, E.; Keller, M.; Wächtershäuser, G.; Stetter, K. O. *Proc. Natl. Acad. Sci. U. S. A.* **1992**, *89*, 8117–8120.
- (32) Russell, M. J.; Daniel, R. M.; Hall, A. J.; Sherringham, J. A. *J. Mol. Evol.* **1994**, *39*, 231–243.
- (33) Russell, M. J.; Hall, A. J. *J. Geol. Soc. London.* **1997**, *154*, 377–402.
- (34) Russell, M. J.; Martin, W. *Trends Biochem. Sci.* **2004**, *29*, 358–363.
- (35) Milner-White, E. J.; Russell, M. J. *Orig. Life Evol. Biosph.* **2005**, *35*, 19–27.
- (36) Blakemore, R. *Science (80-)*. **1975**, *190*, 377–379.
- (37) Frankel, R. B.; Blakemore, R. P.; Wolfe, R. S. *Science* **1979**, *203*, 1355–1356.
- (38) Mann, S.; Sparks, N. H. C.; Frankel, R. B.; Bazyliński, D. A.; Jannasch, H. W. *Nature* **1990**, *343*, 258–261.
- (39) Fukuyama, K. *Photosynth. Res.* **2004**, *81*, 289–301.
- (40) Holden, H. M.; Jacobson, B. L.; Hurley, J. K.; Tollin, G.; Oh, B. H.; Skjeldal, L.; Chae, Y. K.; Cheng, H.; Xia, B.; Markley, J. L. *J. Bioenerg. Biomembr.* **1994**, *26*, 67–88.

- (41) Bruschi, M.; Guerlesquin, F. *FEMS Microbiol. Rev.* **1988**, *4*, 155–175.
- (42) Stephan, D. W.; Papaefthymiou, G. C.; Frankel, R. B.; Holm, R. H. *Inorg. Chem.* **1983**, *22*, 1550–1557.
- (43) Doukov, T. I.; Iverson, T. M.; Seravalli, J.; Ragsdale, S. W.; Drennan, C. L. *Science* **2002**, *298*, 567–572.
- (44) Buffle, J.; Vitre, R.; Perret, D.; Leppard, G. In *Metal Speciation: Theory, Analysis and Application*; Kramer, J. R.; Allen, H. E., Eds.; Lewis Publishers Inc.: London, 1988; pp. 99–124.
- (45) Que, L.; Holm, R. H. *J. Am. Chem. Soc.* **1975**, *97*, 463–464.
- (46) Rao, P. V.; Holm, R. H. *Chem. Rev.* **2004**, *104*, 527–559.
- (47) Christou, G.; Garner, C. D. *J. Chem. Soc. Dalton Trans.* **1979**, *6*, 1093–1094.
- (48) Ohfuji, H.; Rickard, D. *Earth Planet. Sci. Lett.* **2006**, *241*, 227–233.
- (49) Wolthers, M.; Van Der Gaast, S. J.; Rickard, D. *Am. Mineral.* **2003**, *88*, 2007–2015.
- (50) Kouvo, O.; Vuorelainen, Y.; Long, J. *Am. Mineral.* **1963**, *48*.
- (51) Lennie, A. R. *Mineral. Mag.* **1995**, *59*, 677–683.
- (52) Uda, M. *Sci. Pap. Inst. Phys. Chem. Res.* **1968**, *62*, 14.
- (53) Skinner, B. J.; Erd, R. C.; Grimaldi, F. S. *Am. Mineral.* **1964**, *49*, 543–555.
- (54) Pósfai, M.; Buseck, P. R. *Am. Mineral.* **1998**, *83*, 373–382.
- (55) Kesler, Y. A.; Smirnov, S. G.; Pokholok, K. V.; Viting, B. N. *Neorg. Mater.* **1991**, *27*, 1162–1165.
- (56) Yamaguchi, S.; Katsuri, T. *Kolloid Z.* **1960**, *170*, 147.
- (57) Rickard, D. *Sulfidic Sediments and Sedimentary Rocks*; van Loon, A. J., Ed.; Elsevier B.V., 2012.
- (58) Guevremont, J. M.; Strongin, D. R.; Schoonen, M. A. A. *Am. Mineral.* **1998**, *83*, 1246–1255.
- (59) Bragg, W. L. *Proc. R. Soc. A Math. Phys. Eng. Sci.* **1914**, *89*, 468–489.
- (60) Will, G.; Lauterjung, J.; Schmitz, H.; Hinze, E. *Mater. Res. Soc. Symp. Proceedings* **22** **1984**, 49–52.
- (61) Agaev, Y.; Emujazov, K. *Izv. Akad. Nauk. Turkm. SSR* **1963**, *F12*, 104.

- (62) Keller-Besrest, F.; Collin, G. *Acta Crystallogr. Sect. B - Struct. Crystallogr. Cryst. Chem.* **1982**, *39*, 269–303.
- (63) Powell, A. V.; Vaqueiro, P.; Knight, K. S.; Chapon, L. C.; Sánchez, R. D. *Phys. Rev. B - Condens. Matter Mater. Phys.* **2004**, *70*.
- (64) Morimoto, N.; Nakazawa, H.; Nishigucmi, K.; Tokonami, M. *Science* **1970**, *168*, 964–966.
- (65) De Médicis, R. *Sci.* **1970**, *170*, 1191–1192.
- (66) McCall, G. J. H.; Bowden, A. J.; Howarth, R. J. *Geol. Soc.* **2006**, 206–207.
- (67) Erd, R. C.; Evans, H. T. J.; Richter, D. H. *Am. Mineral.* **1957**, *42*, 309–333.
- (68) Brostigen, G.; Kjekshus, A. *Acta Chem. Scand.* **1970**, *24*, 1925–1940.
- (69) Qian, X. F.; Zhang, X. M.; Wang, C.; Xie, Y.; Wang, W. Z.; Qian, Y. T. *Mater. Sci. Eng. B* **1999**, *64*, 170–173.
- (70) Kong, X.; Lou, T.; Li, Y. *J. Alloys Compd.* **2005**, *390*, 236–239.
- (71) Nath, M.; Choudhury, a.; Kundu, a.; Rao, C. N. R. *Adv. Mater.* **2003**, *15*, 2098–2101.
- (72) Vanitha, P. V.; O'Brien, P. *J. Am. Chem. Soc.* **2008**, *130*, 17256–17257.
- (73) Han, W.; Gao, M. *Cryst. Growth Des.* **2008**, *8*, 1023–1030.
- (74) Chen, X.; Wang, Z.; Wang, X.; Wan, J.; Liu, J.; Qian, Y. *Inorg. Chem.* **2005**, *44*, 951–954.
- (75) Huh, Y.-M.; Jun, Y.; Song, H.-T.; Kim, S.; Choi, J.; Lee, J.-H.; Yoon, S.; Kim, K.; Shin, J.-S.; Suh, J.-S.; Cheon, J. *J. Am. Chem. Soc.* **2005**, *127*, 12387–12391.
- (76) Yang, K.; Yang, G.; Chen, L.; Cheng, L.; Wang, L.; Ge, C.; Liu, Z. *Biomaterials* **2015**, *38*, 1–9.
- (77) Jun, Y.; Huh, Y.-M.; Choi, J.; Lee, J.-H.; Song, H.-T.; KimKim; Yoon, S.; Kim, K.-S.; Shin, J.-S.; Suh, J.-S.; Cheon, J. *J. Am. Chem. Soc.* **2005**, *127*, 5732–5733.
- (78) Maier-Hauff, K.; Ulrich, F.; Nestler, D.; Niehoff, H.; Wust, P.; Thiesen, B.; Orawa, H.; Budach, V.; Jordan, A. *J. Neurooncol.* **2011**, *103*, 317–324.
- (79) Kievit, F. M.; Zhang, M. *Acc. Chem. Res.* **2011**, *44*, 853–862.
- (80) Chang, Y. S.; Savitha, S.; Sadhasivam, S.; Hsu, C. K.; Lin, F. H. *J. Colloid Interface Sci.* **2011**, *363*, 314–319.

- (81) Yu, L.; Lany, S.; Kykyneshi, R.; Jieratum, V.; Ravichandran, R.; Pelatt, B.; Altschul, E.; Platt, H. A. S.; Wager, J. F.; Keszler, D. A.; Zunger, A. *Adv. Energy Mater.* **2011**, *1*, 748–753.
- (82) Ferrer, I. J.; Nevskaja, D. M.; de las Heras, C.; Sánchez, C. *Solid State Commun.* **1990**, *74*, 913–916.
- (83) Roldan Martinez, A.; Hollingsworth, N.; Roffey, A.; Islam, H. U.; Goodall, J. B. .; Catlow, C. R. A.; Darr, J. A.; Bras, W.; Sankar, G.; Holt, K. B.; Hogarth, G.; de Leeuw, N. H. *Chem. Commun.* **2015**, *51*, 7501–7504.
- (84) Ahmed, N.; Morikawa, M.; Izumi, Y. Photocatalytic conversion of carbon dioxide into methanol using optimized layered double hydroxide catalysts. *Catalysis Today*, 2012, *185*, 263–269.
- (85) Ganesh, I. *Renew. Sustain. Energy Rev.* **2014**, *31*, 221–257.
- (86) Graciani, J.; Mudiyansele, K.; Xu, F.; Baber, A. E.; Evans, J.; Senanayake, S. D.; Stacchiola, D. J.; Liu, P.; Hrbek, J.; Sanz, J. F.; Rodriguez, J. A. *Science (80-.)*. **2014**, *345*, 546–550.
- (87) Moret, S.; Dyson, P. J.; Laurency, G. *Nat. Commun.* **2014**, *5*, 4017.
- (88) Jin, F.; Gao, Y.; Jin, Y.; Zhang, Y.; Cao, J.; Wei, Z.; Smith Jr, R. L. *Energy Environ. Sci.* **2011**, *4*, 881.

Chapter 2 Overview

X-ray absorption spectroscopy (XAS) is an atom specific characterisation technique. It is particularly useful for understanding dilute systems of short range order. When used *in situ* during reaction processes, the technique is a powerful tool to study the evolving local structure of materials. In this chapter, a theoretical understanding of the technique is shown. As well as this, practical information for XAS data acquisition and analysis is given. Other techniques used in this thesis are also described briefly.

Chapter 2

X-ray absorption spectroscopy and other experimental techniques

2.1 Introduction

X-ray absorption spectroscopy (XAS) is the primary characterisation technique used for experiments described in this text. The technique is element specific, providing information on average local environment. It is popular for characterisation of systems with little or no long range order including amorphous materials,⁴⁻⁶ liquids,⁷ and nanoparticles⁸ although the presence of long range order does not inconvenience the technique either. The element specific nature of the technique combined with the fact that the technique does not require a high concentration of probe elements makes it ideal for investigation of doped materials from the perspective of the dopant.⁹⁻¹²

In its simplest form, XAS is the measure of an absorption coefficient as a function of X-ray photon energy in an energy band straddling an atomic X-ray absorption edge. An XAS spectrum is divided into two regions, the first is the X-ray absorption near edge structure (XANES), or the Near edge x-ray absorption fine structure (NEXAFS) – the latter term is generally used for a low energy scheme (Figure 2.1). XANES provides insight into the nature of bound and unbound states near to the Fermi level (i.e. the highest occupied and lowest unoccupied molecular orbitals [HOMO and LUMO]) and the symmetry of the local structure.¹³

The second region is the Extended x-ray absorption fine structure (EXAFS). When EXAFS data is fully characterised, information is revealed about nearest neighbours, their bond distances, disorder, and coordination. While the XANES and EXAFS regions are experimentally probed in a nearly identical way the theoretical approaches used to tackle them differ, and the information that is derived from them are complimentary.¹³

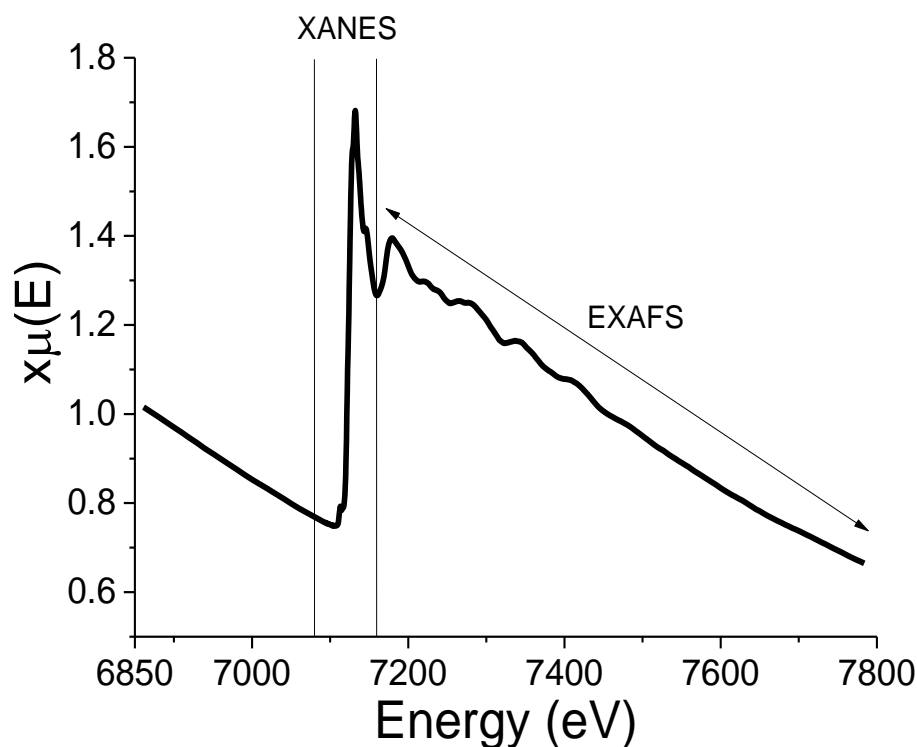


Figure 2.1: Graph showing a typical XAS spectrum of $x\mu(E)$ as a function of energy. The spectrum is shown to be divided into two regions. The XANES lies about 20 eV before and 30 eV after the Fermi level manifested as the edge jump, while EXAFS is found after the XANES region at the tail end of the spectrum and contains oscillations which are caused by constructive and destructive interference of the outgoing photoelectron with neighbouring atoms.

Development of XAS, and particularly EXAFS as an experimental technique^{14–17} is synchronous with the development of synchrotron radiation technology¹⁸ since it requires a high intensity and energy tuneable X-ray source. Moreover, improvements in beamline and detector technology have allowed access to important *in situ time-resolved* studies in physics and chemistry.^{19–21}

In this chapter, the basic theory of XAS and practical steps to modelling EXAFS is provided. Other experimental techniques featured in the text are also described here. These include X-ray diffraction (XRD), Transmission electron microscopy (TEM), UV-Visible spectroscopy, and Density functional theory (DFT).

2.2 X-ray absorption spectroscopy

X-ray absorption spectroscopy is a technique that provides information on the local structure of a specific element within a system. XAS is a measure of $\mu(E)$, the X-ray

mass absorption coefficient as a function of energy (eV). The relationship between the absorption coefficient and energy is described by the Beer-Lambert law shown in Equation 1, where x is the sample depth, I_0 is the intensity of the incident beam, and I_t is the intensity of the transmitted beam. $\mu(E)$ decreases with increasing photon energy, following the function $1/E^3$. When the incident beam is equivalent to the energy required to excite a core electron to an allowed valence orbital at the Fermi level, a strong increase in absorption is observed. This energy dependent increase is known as an X-ray absorption edge and defines the edge positions unique to each element.

Equation 2.1: The Beer-Lambert law of absorption

$$x\mu(E) = -\ln(I_t/I_0)$$

2.2.1 XANES

When measured with a small enough step size, it becomes apparent that the edge is not a simple increase in absorption, and there are many features in this region. These features are related to the variations in absorption due to other orbital transitions, which are dictated by transition rules and ligand interactions – they are also influenced by multiple scattering events which occur as a result of high symmetry in the local geometry of a system. This area of the XAS spectrum is coined the XANES, it lies approximately 20 eV below and 30 eV above the primary absorption edge, and provides information on the atomic geometry, and oxidation state.

XANES can be interpreted and compared with results from computer modelling, usually involving complex quantum mechanical calculations.^{22–24} The XANES spectrum is a fingerprint region for a material. Various features are used as markers. These are the pre-edge, edge, white line, and near-edge intensities (Figure 2.2). The absorption edge is related to the first fully allowed transition of a core electron to an unoccupied bound state based on the selection rule $\Delta l = \pm 1$. The pre-edge peak is classically disallowed as it does not follow the selection rule $\Delta l = \pm 1$, but arises due to orbital overlap. For example, in first row transition metals, a pre-edge peak is observed for metal-ligand systems in tetrahedral geometry. The peak arises due to orbital mixing between the transition metal 3d orbitals and p-orbitals from the ligands; the p-orbital interactions provide p-character to the 3d orbitals thus relaxing the $\Delta l = \pm 1$ selection rule.^{25,26} The intensity of the pre-edge peak depends on the

number of vacancies in the 3d orbital; zinc complexes in tetrahedral geometry do not demonstrate a pre-edge peak owing to fully occupied 3d orbitals. As a result of the poor orbital overlap between the $d_{x^2-y^2}$ and d_z^2 of first row transition metals with ligands in a perfect octahedral geometry, a pre-edge peak is less likely to be observed. The white line intensity arises from coordination to ligands and is related to the density of unoccupied states, it is intensified by multiple scattering and high coordination number, and is observed for octahedral complexes.^{27,28} Similarly, an edge shoulder may arise from interaction of a metal centre with softer ligands²⁹ owing to greater overlap between ligand p-orbitals and the s orbital of the metal centre, thus increasing p-character and relaxing the $\Delta l = \pm 1$ rule. Finally, the near-edge arises due to strong influence from multiple scattering.³⁰

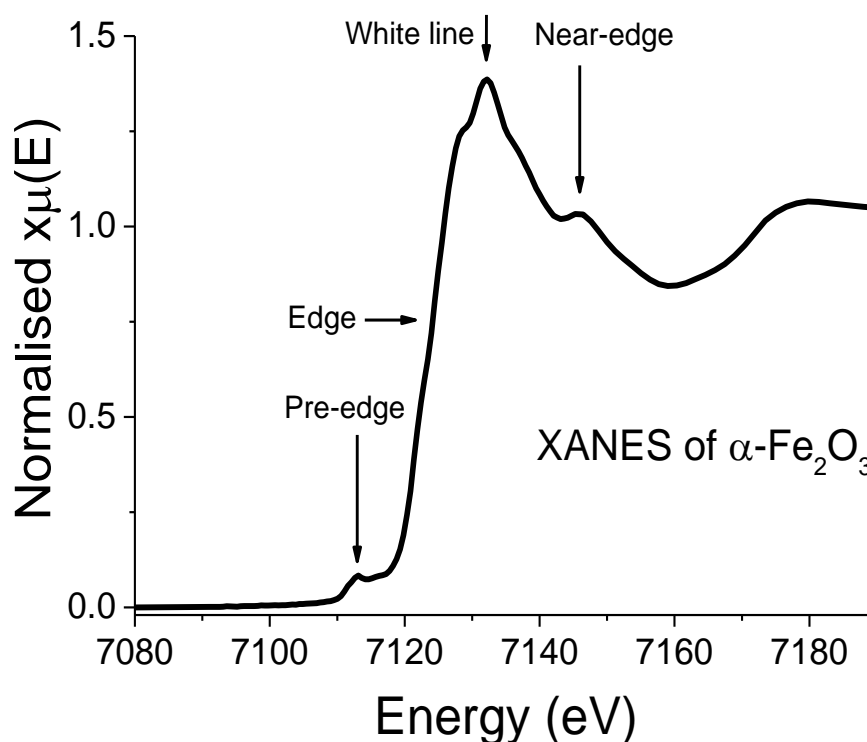


Figure 2.2: Features typical of the XANES region arise from unique orbital arrangements and interactions, and are used to identify characteristics of a local environments. Features include a pre-edge, edge, white line intensity, and near-edge. The amplitude of the pre- and near-edge features and white line intensity, and the position of the edge reveal information about coordination geometry and oxidation state.

XANES is an average of contributions from the different oxidation state and coordination environments present in a system. Therefore, by performing Linear

combination fitting (LCF) using suitable standard structures, i.e. reference samples, it is in principle possible to calculate the percentage contribution from each known structure within the real system, thus making the technique semi-quantitative. As all X-ray absorption spectra are an average of the signal from the excited atoms, the LCF approach is not limited to XANES but can be applied to EXAFS as well.^{29,31,32}

2.2.2 EXAFS

The edge position defines the excitation energy of a core electron to the lowest allowed valence orbital. At greater energies, absorption results in the core electron being expelled from the central atom as an excited photoelectron. In this higher energy region, oscillations are observed along the spectrum for materials other than monatomic gasses. The oscillations arise from constructive and destructive interference of the photoelectron wave function with itself when it is scattered back from neighbouring atoms. The oscillations are known as the EXAFS. In order to participate in EXAFS, the photoelectron which is better described as a spherical wave, must scatter from the neighbouring atoms and return to the absorbing atom elastically, i.e. without energy loss. The absorption probability depends on the frequency, i.e. energy, of the photoelectron and the characteristics of the scatterer. When fully analysed, information gleaned from the EXAFS includes the neighbouring scatterers, bond distance, coordination number, and thermal and static disorder of the nearest neighbours. The following text attempts to lay down the theoretical and practical landscape of EXAFS analysis as described in a number of textbooks including “Introduction to XAFS” (Bunker, G)¹³ and “XAFS for Everyone” (Calvin, S).³³

2.2.2.1 EXAFS theory

EXAFS can be fully characterised using the EXAFS equation (Equation 4). The equation is derived from quantum mechanics describing the transition between two allowed quantum states. It takes into account the isolated initial state, and the final state which is affected by neighbouring atoms. A detailed derivation of the EXAFS equation can be found elsewhere.^{13,33,34}

Equation 2.2: The EXAFS equation.

$$\chi(k) = \sum_j \left(\frac{N_j f_j(k) e^{-2k^2 \sigma_j^2}}{k R_j^2} \sin[2k R_j + \delta_j(k)] \right)$$

The EXAFS equation is derived from the theory describing the quantum mechanical transitions between the ground and excited states of an atom. While the core electron in the ground state is isolated and therefore in an unperturbed orbit, the excited state orbitals are influenced by nearest neighbours. Therefore, the equation encompasses a number of variables related to the central atom and its interaction with nearest neighbours. The sensitivity due to neighbours is reflected in the inclusion of the atomic scattering factors $f_j(k)$ and phase shifts $\delta_j(k)$, which detail the scattering properties for the excited central atom and neighbouring atoms. These atomic scattering factors depend on atomic numbers Z . $\delta_j(k)$ is the phase shift that occurs when the outgoing photoelectron scatters back towards the excited central atom. Phase shifts were once determined experimentally, but with increasingly more accurate computational potential calculations, they can now be approximated prior to data modelling. Calculations are inclusive in the EXAFS modelling software mentioned in section 2.2.3.2. Parameters that can be determined by the EXAFS equation are N_j , the number of neighbouring atoms, R_j , the bond distance of neighbouring atoms, and σ^2 , the static and thermal disorder of neighbouring atoms, also known as the Debye-Waller factor. The EXAFS is formed from a sum of all scattering paths j . $\chi(k)$ is inversely proportional to R_j^2 and therefore the amplitude function quickly decreases with bond distance – this makes EXAFS an inherently short range technique that is effective up to about 6 Å. In addition, EXAFS at higher distances (above 4 Å) are further complicated by multiple scattering events that occur when the photoelectron scatters back and forth along highly symmetric paths.³⁵ Typically, EXAFS data are k^2 or k^3 weighted in order to enhance higher k oscillations.^{13,33,34,36,37}

Experimentally obtained EXAFS data can be Fourier transformed to real space R (Å). The Fourier Transform is derived from a complex function containing real and imaginary parts, but the apparent partial radial distribution of shells depending on sets of scatter paths in real space makes it a more intuitive when rationalising the local structure. The Fourier transform is a useful tool to visualise nearest neighbours

although since it is not an actual partial distribution function, phase cancellations can have unusual effects on the R-space which must be treated with caution.¹⁴

XAS is best defined in terms of $\mu(E)$ while the EXAFS is defined as $\chi(k)$. The first step to achieving this is obtaining $\chi(E)$ through a background subtraction (Equation 2.3); the theoretical spectrum of an isolated atom $\mu_0(E)$ is subtracted from the real spectrum $\mu(E)$, and divided by the edge jump $\Delta\mu_0(E)$.

Equation 2.3: Background subtraction to obtain $\chi(E)$ from $\mu(E)$.

$$\chi(E) = \frac{\mu(E) - \mu_0(E)}{\Delta\mu_0(E)}$$

The next step is conversion of photon energy to reciprocal space k (\AA^{-1}). The conversion of E to k is accomplished using Equation 2.4 where E_0 is the energy of the edge position, and m is the mass of an electron. There are several advantages to having EXAFS expressed as a function of k . The main advantage is the inter-conversion between k and R space which is a direct indicator of bond distance.

Equation 2.4: Calculation of k (\AA^{-1}) from energy

$$k = \sqrt{\frac{2m(E - E_0)}{\hbar^2}}$$

2.2.2.2 EXAFS modelling software

EXAFS analysis can be performed using a number of established software packages. For instance Athena³⁸ and VIPER³⁹ are XAS data processing software. Athena is commonly used for multiple data processing, the software's strength lies in data comparison and basic XANES analysis by linear combination fitting or multiple component analysis. Usual processing functions are available including normalisation and background subtraction. The software also allows data to be saved in useful formats including $x\mu(E)$, Normalized $x\mu(E)$, $\chi(E)$, $\chi(k)$, and $\chi(R)$. VIPER allows a more visual control of normalisation and background subtraction. Owing to its flexibility, VIPER is particularly useful for processing more challenging datasets including those containing low frequency oscillations and data sets containing 'glitches', i.e. strong intensity maxima caused by higher order beam line monochromator reflections. After data processing, scatter paths are calculated. The FEFF program is used for multiple scattering calculations.³⁶ It yields a list of scattering amplitudes and phases from crystallographic database (.cif) files and is

used as a starting point in many software packages that deal with EXAFS modelling. The Artemis program belongs to the same software package as Athena and is used for EXAFS modelling.³⁸ The software also uses FEFF to calculate theoretical scatter paths although adding scattering paths to calculations without a .cif file is also possible for non-crystalline or unknown structures limited to first shell analysis. Artemis is proficient in including multiple scattering paths for fits. EXCURVE is another EXAFS modelling software.⁴⁰ Scatter paths, known as shells, are either manually inserted by a user, or can be imported from protein data bank (.pdb) files. These files contain three-dimensional structures void of symmetry operations. Basic symmetry operations can be implemented on the program in order to enable multiple scattering calculations, although this is not commonly used. The software allows a greater control over variable and fixed parameters and is ideal for modelling non-crystalline structures. During the modelling process in both Artemis and EXCURVE, restraints and constraints can be added to parameters and secondary bond distances of the theoretical model.

2.2.2.3 XAS data reduction

In this thesis, Horae Athena was used as the primary means of data reduction for XANES analysis and conversion to $\chi(k)$ for EXAFS analysis. This software is therefore discussed here. The increase in absorption around the edge region is proportional to the concentration of absorbing atom. Normalisation of the absorption by the edge jump is therefore necessary to eliminate the dependency of the absorption on sample concentration and thickness. The normalisation is done using polynomials that are extrapolated from the pre-edge and post-edge. Particular attention must be paid to the white line and near edge region which can change substantially depending on the normalisation process. Typically, the two points for the pre-edge polynomial are taken from the beginning of the scan, and about 30 eV before the edge. The post-edge polynomial is extrapolated here from the first oscillation and the tail end of the spectrum (Figure 2.3). Both polynomials are affected by the point chosen as the edge position. This position also affects EXAFS, and is therefore considered carefully. Typically, the inflection point, or when this is difficult to find, the halfway point is selected as the edge. For EXAFS, the value is considered appropriate as long as it is approximately in the correct region (± 10 eV) as this parameter is refined during EXAFS analysis. The accuracy of the edge

position is far more important when extracting oxidation state information from it. Furthermore, normalisation parameters play an important role in Linear combination fitting. A useful feature of the software is the transfer of parameters to a set of data, when this is done, data sets must be evaluated see if the transferred parameters are good for a spectrum, or if new parameters should be used – an example of this is when an edge position is shifted as a result of oxidation state change in a set of *in situ* data; using the same point for edge position is no longer acceptable.³⁸

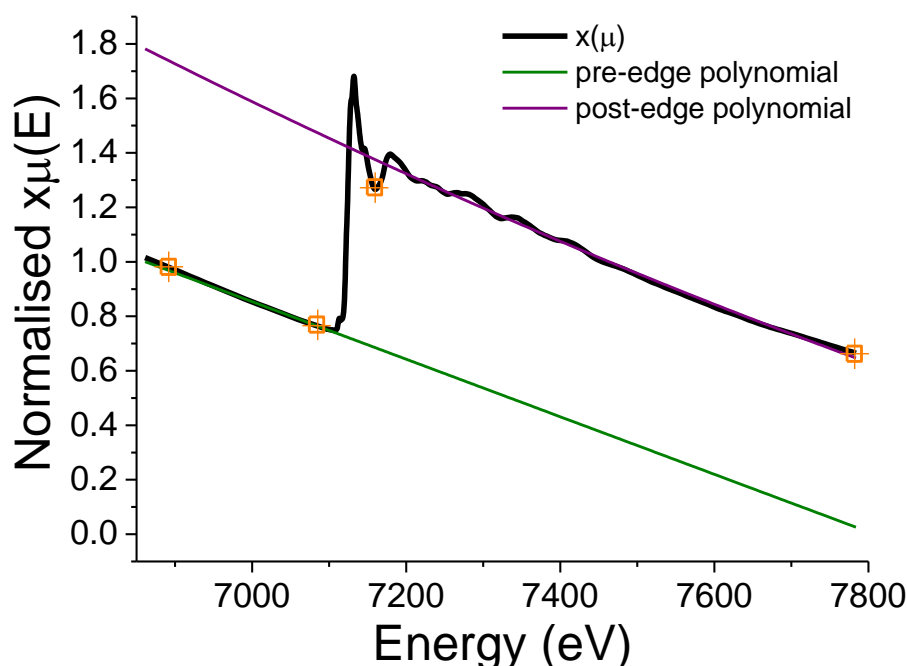


Figure 2.3: An example of the normalisation process on an X-ray absorption spectrum. For normalisation, the pre-edge polynomial (green) is extrapolated based on two points before the edge, and the post-edge polynomial (purple) is extrapolated from two points after the edge – typically from close to the XANES region to the end of the EXAFS region.

Removal of the background $\mu_0(E)$ from the absorption coefficient $\mu(E)$ is the next step of data reduction (Equation 2.3). For practical purposes, $\mu_0(E)$ is determined using a cubic spline function and removed using least squares fitting (Figure 2.4). $\mu_0(E)$ must be fit to $\mu(E)$ without removing or reducing any oscillations in the EXAFS region. The background subtraction can be k^n weighted ($n = 1-3$) in order to improve the fit of the lower energy region (k^1) or higher energy region (k^3). Other tools to improve background subtraction include spline clamps and the Rbkg parameter. Extraction of the EXAFS is then finally performed by the software by following the remainder of Equation 2.3.³⁸

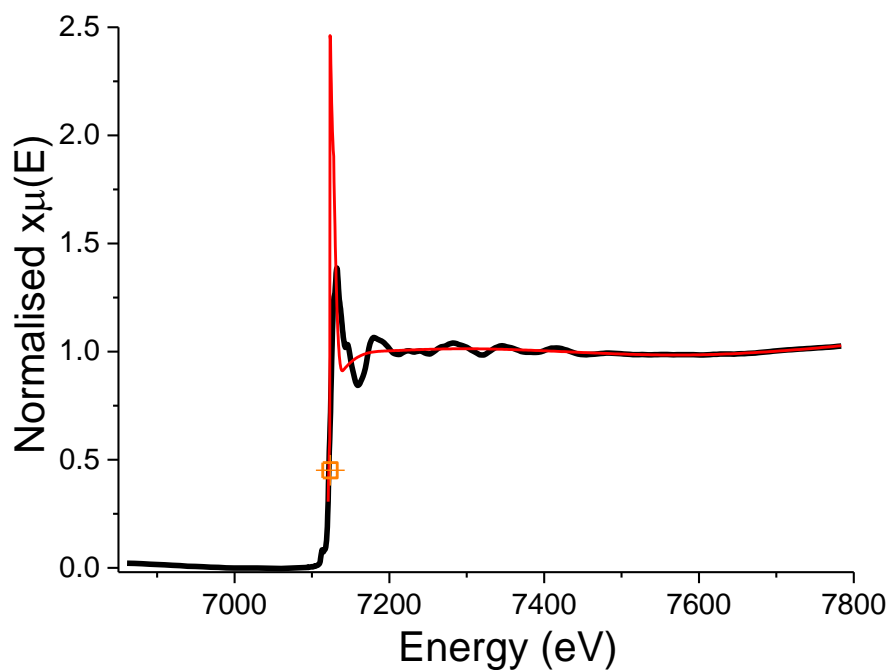


Figure 2.4: An example of background subtraction in the EXAFS region. Background $\mu_0(E)$ is estimated with a spline function and subtracted from the experimental data $\mu(E)$.

EXAFS data is presented with a k^n weighting ($k = 1-3$) and can also be displayed as a Fourier Transform (Figure 2.5).³⁸

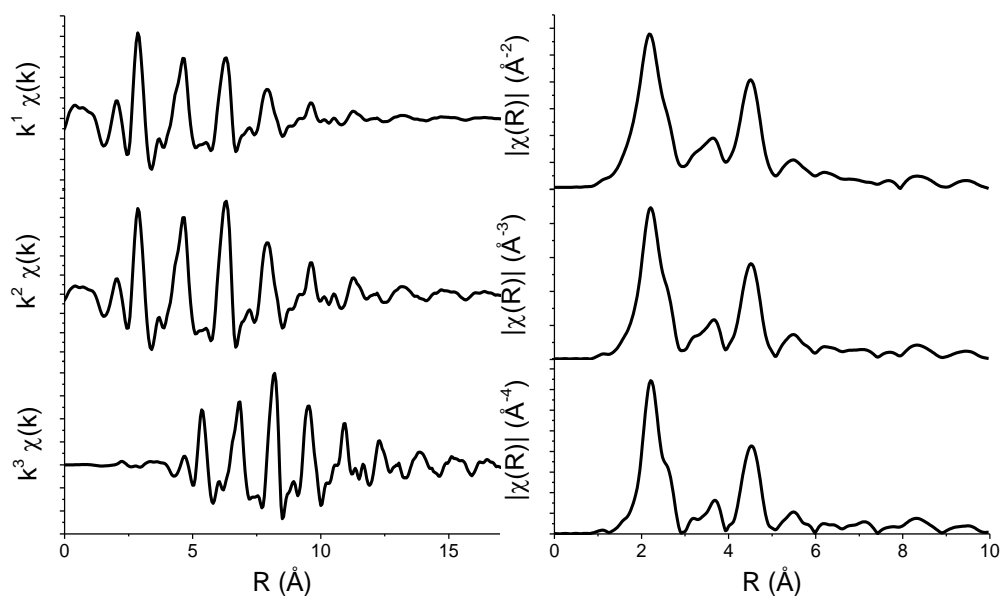


Figure 2.5: Example of EXAFS and Fourier Transforms at k -weighting 1-3 (top to bottom). With increased k -weighting, higher oscillations have more contribution. EXAFS of k^1 is magnified by $\times 45$, and k^2 is magnified by $\times 8$ on the y -axis. FT of k^1 is magnified by $\times 65$, and k^2 is magnified by $\times 9$ on the y -axis.

2.2.2.4 XANES analysis

XANES analysis in this text was performed qualitatively by identification of XANES features, and semi-quantitatively through linear combination fitting. Linear combination fitting is performed in order to determine the exact components of a material using reference materials containing these components. The XANES region is made up of the weighted sum of all local environments present in a sample. The normalised spectrum can therefore be fit with spectra of each individual local environment in order to calculate component ratios. This forms an important tool for sample characterisation, particularly for characterisation of systems that transform *in situ* as is demonstrated later. For acceptable results, it is important to use a complete set of reliable reference materials which are an accurate description of components likely to exist within the sample. The analysis is evaluated by R-factor, reduced chi square, standard deviation of each calculated component, as well as visually.

2.2.2.5 EXAFS analysis

EXAFS analysis in this text was performed using the EXCURVE software package. The main reason for choosing this software over others is the flexibility of the software for analysis of unknown and non-crystalline materials, and mixtures.

The aim of EXAFS analysis is to extract structural parameters of a material including nearest neighbours, interatomic distance, and the Debye-Waller factor (interatomic distance variation due to thermal and static disorder), and coordination numbers. The program uses EXAFS equation (equation 2.2) to extract these parameters from the EXAFS data using a least squares fitting process. These standard curve fitting procedures involve minimizing the mean square error between experimental data and the theoretical fit.

The experimental data is loaded into the software first as $\chi(E)$ and k-weighting is set. Throughout this text, k^3 weighting was chosen. A decision must then be made as to the atom types that will be used within the calculations in order to calculate atomic potentials and phases shifts.

The theoretical model used to fit the experimental EXAFS data in k-space is either taken from .pdb input files or added as single scattering paths at the users discretion. In order to achieve the global minimum, input parameters are estimated to as close to

the real values as possible. The scattering paths added manually can be given coordinates in order to create three dimensional structures, although it is also possible to perform the analysis using just bond distances. Symmetry can also be applied to individual shells or whole .pdb structures for a more detailed analyses including coordinate optimisation and multiple scattering effects. Bond distances and angles can be restrained to introduce rigidity to a theoretical structure.

The definition of a shell is interchangeable: the visible peaks in the Fourier transform of an EXAFS data set, i.e. the radial distribution function, are known as shells and can contain a number of scatter paths of similar distances. The individual scatter paths defined on EXCURVE are also known as shells within the software.

The amplitude reduction factor is essentially a term added to the EXAFS equation to account for lower amplitude than theoretical values. Amplitude reduction is typically the same value for each element, the numbers vary slightly between experiments owing to beamline optics but have established approximate values, for example amplitude reduction for iron is approximately 0.7. The amplitude reduction factor, known as *afac* in EXCURVE, can be a variable parameter but is usually fixed at a value that is solved by refining a well-known structure at the same edge such as a pure metal foil. During refinement, the value of the Fermi Energy E_0 (known in the program as *EF*) is allowed to float but kept between $\pm 10\text{eV}$. It is dependent on the edge position chosen during data reduction on Athena. This parameter is always refined. R is the parameter used to determine interatomic distances. Error for R is low at a minimum of 0.01 \AA . In EXCURVE, R of shells are refined as absolute terms whereas in other programs, grouping R values allows them to expand or contract by the same value. The parameter a is the Debye-Waller factor multiplied by 2, and in this report, is written as $2\sigma^2$. N , the coordination number can also be refined with ease. Parameters are grouped for similar scatter paths. For example, in a mixed phase structure, for different bond distances in the first shell, the Debye-Waller factor can be grouped in order to reduce the number of independent parameters. It must be decided whether the groupings are chemically viable by the user. The error associated with coordination number and Debye-Waller factor are typically high at 10 %. For this reason, where possible, coordination is kept unrefined at expected

values. Finally, the refinement of Debye-Waller factor and coordination number is avoided in tandem owing to strong correlation.

Given that each scattering path is subject to up to 4 independent variables, and there is often more than one scatter path, the number of variables can increase rapidly. With too many independent parameters, it is possible to fit an elephant. The Nyquist equation (Equation 4) is a measure of the number of parameters by defining upper ranges for the product of k and R space. Here, N_{idp} is the number of independent parameters, Δk is the k -range and ΔR is the R -range used in the fit. This Nyquist number should be kept within an acceptable limit.

Equation 2.5: Nyquist equation for EXAFS analysis.

$$N_{idp} = \frac{2 \Delta k \Delta R}{\pi}$$

The maximum resolution of bond distance is also limited by the k -range by the relationship $\pi/2\Delta k$, this is important when considering several similar bond distances within a system.

Methods to determine goodness of fit are important to evaluate output structural models. Individual output parameters obtained from the fit are produced with error bars and information on correlations with other parameters. Coordination number is typically calculated with a 10% error, the error of bond distance is far smaller, with a maximum resolution of 0.01 Å.¹³ Debye-Waller factors are associated with errors of up to 20%. Correlations can occur between parameters associated with amplitude. It is a regular problem when coordination numbers and Debye-Waller factors are refined together. Correlations should be kept below ± 0.85 , and where correlations are a problem, parameters can be refined separately.

The most effective way to evaluate the goodness of a fit on excurve – including comparison against other fits - is to use reduced χ^2 or ϵ^2_v . This is calculated from Equation 2.6 where N_{ind} and N_{var} are the number of independent data points and the number of variable parameters respectively, $\chi^{calc}(k_i)$ and $\chi^{exp}(k_i)$ are the theoretical and experimental EXAFS respectively, N is the number of data points (a value usually more than N_{ind}) while w_i is the weighting which allows a constant amplitude over the data range.

Equation 2.6: Reduced χ^2

$$\epsilon_v^2 = \frac{1}{(N_{ind} - N_{var}) (N_{ind}/N)} \sum_i w_i (\chi^{exp}(k_i) - \chi^{calc}(k_i))^2$$

Alternatively, R-factor is often quoted which is the measure of the difference between the experimental and calculated data. R-factor is calculated using Equation 2.7 where σ is standard deviation of each point. A small R-factor indicates a good fit. The limitation of R-factor is that it does not take number of variables or number of independent data points into account and it is therefore limited for the evaluation of multiple fits where these two values vary. Throughout the work presented here, both R-factor and reduced χ^2 was used and have been quoted.

Equation 2.6: R-factor in EXAFS

$$R = \sum_i^N \left(\frac{1}{\sigma} \right) (|\chi^{exp}(k_i) - \chi^{calc}(k_i)| \times 100\%)$$

2.2.3 Data acquisition modes**2.2.3.1 Transmission**

The standard mode of XAS data acquisition is in a transmission geometry. For this the sample is placed between two detectors, aligned to the synchrotron beam. Signals from the incoming beam, I_0 , and transmitted beam, I_t , detectors provide a direct measurement of $x\mu(E)$. The sample in the beam must be homogeneous so that the whole beam is interacted uniformly. Non-linearity in the spectrum arises as a result of inhomogeneity or beam clipping – this is further exacerbated if the position of the beam migrates along the z axis as a function of energy due to the design of the beamline optics. Sample thickness also affects spectra as a very thick sample can severely attenuate the beam, particularly at the XANES region. An optimum edge jump ($x\Delta\mu(E)$) of between 0.2 and 2 - calculated using software such as XAFSMass⁴¹ - and careful sample preparation, are applied to overcome these issues.

2.2.3.2 Fluorescence

Decay of the excited state of an atom occurs by two mechanisms. The first is by the filling of the core hole with an electron from a higher orbital. This causes a photon with an energy equivalent to the energy difference between the core hole and higher orbital to be emitted. The photon provides analogous information to transmission

data as a function of energy. Therefore, as an alternative to transmission, I_f/I_0 is also used to obtain $\mu(E)$.¹³ Fluorescence data is generally noisier. This is because of the presence of other scattering events, and also the fact that the small solid angle measured by a fluorescence detector results in less than 1% photon detection compared to 100% photon detection in transmission. This acquisition mode is preferred for measurements of dilute samples, inhomogeneous samples, and thin films owing to greater sensitivity and versatility. There are a number of considerations when acquiring fluorescence data including detector dead time which is described later. A common challenge is self-absorption which occurs when the fluorescence intensity is not proportional to the absorption coefficient resulting in the modulation of $\mu(E)$ so that the absorption spectrum seems distorted and amplitude of the oscillations in the EXAFS region are suppressed. The most common sign of self-absorption is lower white line intensity and low scattering amplitude values. Self-absorption is prevented by diluting samples or having very thin concentrated samples, or alternatively acquiring total electron yield (TEY) EXAFS spectra. Where self-absorption is unavoidable, other analytical methods are used to reduce the effects.⁴²⁻⁴⁵

2.2.3.3 Electron Yield

The second decay mechanism involves excitation of a secondary (Auger) electron as a result of relaxation of the first electron to the core hole. The second electron is emitted as a photoelectron and can be detected using standard electron detectors which must be operated in vacuum. Like fluorescence, the electron yield is proportional to absorption and can therefore be used as a measure of XAS. TEY is used as an alternative acquisition method for low energy XAS where transmission is not possible, and self-absorption is a greater issue. TEY is used primarily in vacuum to prevent absorption by air. Absorption of Auger electrons within the bulk of the system means that only excitations on the surface of materials are detected, and the technique is therefore surface sensitive.

2.3 Synchrotron Technology

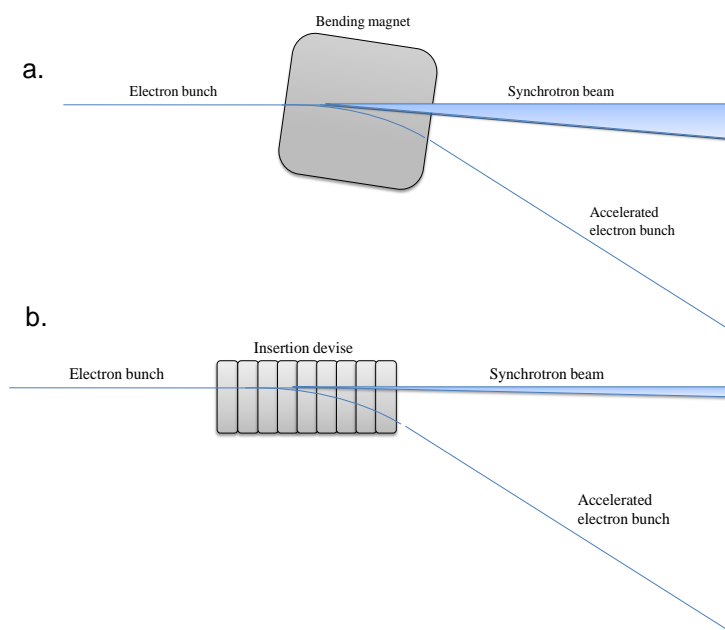


Figure 2.6: A schematic diagram showing the shape of the beam emitted from an electron accelerated through a bending magnet and an insertion devise. The beam profile resulting from a bending magnet is fanned, with higher energy closer to the new electron trajectory and lower energy on the far side of the fan. Insertion devises cause far less fanning; the beam is collimated and focussed owing to a succession of alternating magnets.

Development of XAS is synonymous with the development of synchrotron radiation technology and in present day XAS is rarely performed without the use of synchrotron radiation. The finely tuneable and high flux energy required for the technique is readily available at synchrotron radiation laboratories which are often operated as user facilities.

Synchrotron radiation (SR) is the radiation emitted from particles travelling at near relativistic speeds: when the particle trajectory is bent by a magnetic field, the particle accelerates in the radial direction but decelerates in the direct path and in doing so releases a powerful polychromatic fan of radiation at a tangent to the beam path (Figure 2.6a). The emitted beam is highly directional and can be harnessed using specialised X-ray optics. It is defined by characteristics including high flux (photons/second/area) and high brilliance (flux/angular divergence) which make it an ideal electromagnetic beam source for analytical experiments.¹³ Synchrotron technology was originally developed for particle physics and the synchrotron radiation that was emitted from the accelerated particles was seen as a loss of energy

rather than anything useful. It was only upon the development of storage rings specifically designed for the emission of synchrotron radiation, i.e. second generation SR laboratories, where beams emitted at bending magnets could be used on an industrial scale, that synchrotron radiation could truly be harnessed.¹⁸ Third generation synchrotron sources, including the ESRF, were designed to enable the routine use of insertion devices. These devices offer a higher collimated and less divergent X-ray beam at the expense of the continuity of the emitted X-ray spectrum. In these laboratories, both bending magnet and insertion device radiation is available. (Figure 2.6b).

2.3.1 Synchrotron facility design

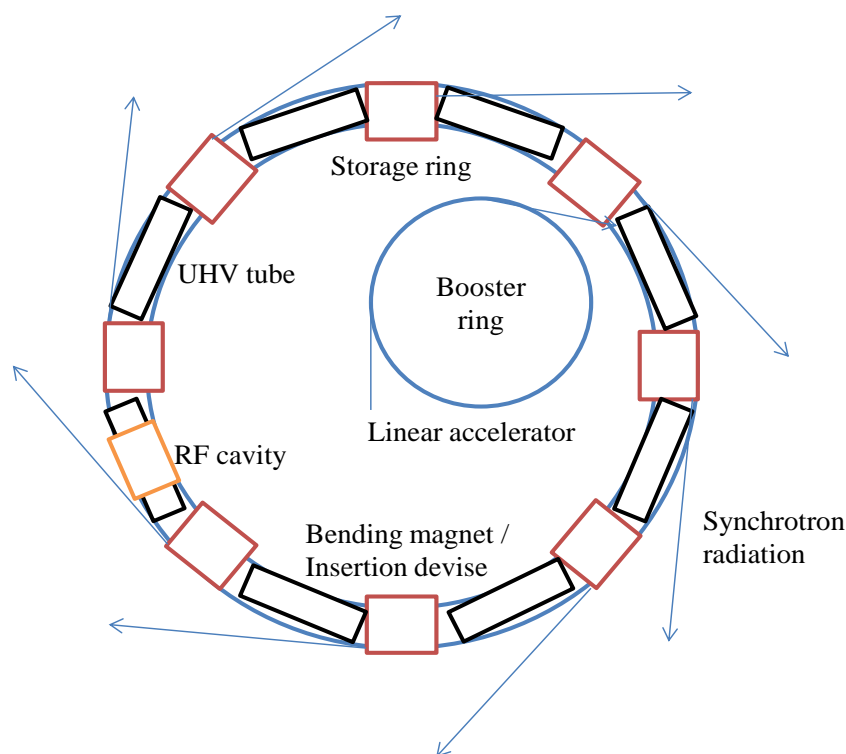


Figure 2.7: A schematic diagram of a typical synchrotron facility showing basic construction including a booster ring and storage ring as well, and an RF cavity for maintaining electron velocity. The circular structure is actually a polygon made up of a series of hexapoles, quadrupoles, and bending magnets or insertion devices which follow the changing trajectory of the electrons.

Modern synchrotron radiation sources follow the same basic framework shown in Figure 2.7. Typically, bunches of electrons are accelerated first in a linear accelerator followed by a booster synchrotron ring and then injected into a storage ring. The placement of many bending magnets and insertion devices along the path of the electron bunches result in the closing of a loop into a polygon. In this way, the same

electron bunch circles the ring emitting energy for up to a day. Radio frequency cavities may be used to re-energise electrons while quadrupoles and hexapoles keep the beam in its intended path between bends. The whole ring is kept under ultra-high vacuum. The radiation output is not a continuum in time, rather there is a defined pulsed time structure in the order of picoseconds. Fourth generation light sources are currently emerging. These use free electron laser technology and will change the pulsed time structure. Instead of small bunches spaced at picosecond intervals, larger bunches will be produced with shorter bunch length but larger intervals. While this is useful for probing ultra-fast processes in a pump-probe configuration, the very high intensity pulses destroy the samples making it incompatible with EXAFS. Synchrotron radiation sources are generally government funded shared research facilities. A list of current working sources is found on www.lightsources.org.

2.3.2 Beamlines

A custom beamline is built along each X-ray beam in order to filter, tune, and utilise the beam in controlled experiments. A typical beamline is split into three sections: the optics hutch, the experimental hutch, and the control cabin.

The beamline is made of a succession of shutters connected by an interlock system that is operated under strict safety conditions. The raw synchrotron radiation enters into the optics hutch of a beamline where a combination of mirrors and monochromators are used for harmonic rejection, collimation, monochromation and focussing before entering the experimental hutch.

2.3.3 Monochromators

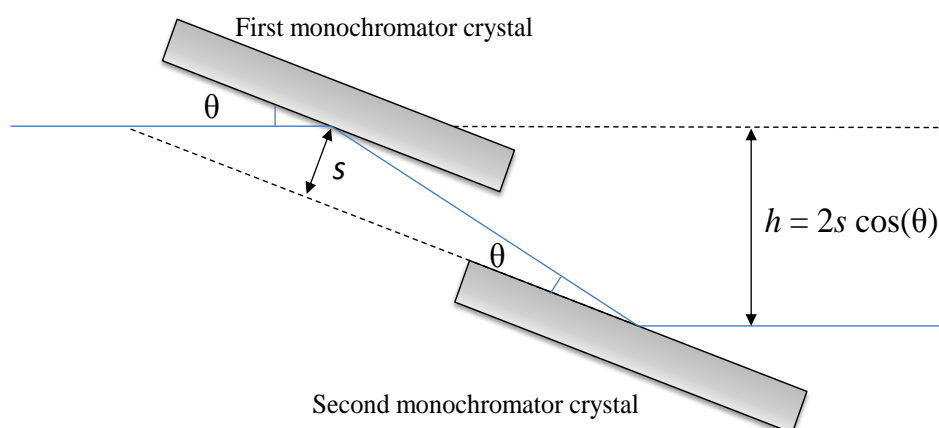


Figure 2.8: A schematic diagram showing a double crystal monochromator used for tuning energy.

The heart of an XAS line is the monochromator which tunes the beam to the desired wavelengths. The monochromator is commonly constructed from silicon single crystals and exploits Bragg's law $\lambda x = 2d\sin\theta$ to set the desired beam energy – the angle of the incident beam to the silicon crystal surface dictates the diffracted wavelength. A second crystal is held parallel to the first in order to keep the outgoing beam parallel to the incident beam and sharpen the transmitted energy bandwidth, also known as the rocking curve (Figure 2.8). Most of the energy in the white beam is not diffracted. Instead, it is absorbed by the first monochromator crystal. This monochromator crystal is continuously cooled in order to prevent crystal distortion from the effects of overheating. The monochromator is also kept under vacuum to prevent the formation of ozone from destroying the crystal surfaces, and to reduce beam absorption and scatter.

The angle of the double crystal with respect to the incoming beam is controlled by precision goniometers or rotation stages which maintain high accuracy and allow the required resolution (step size) to be met. The higher order harmonics must also be considered, and usually a slight misalignment between the first and second crystal, in combination with the mirror position, can be used to reduce the intensity of these higher harmonics (harmonic rejection). The angle of the monochromator affects the height (d or h) of the beam by $h = 2s\cos\theta$ where s is the perpendicular distance between two crystals. The shift is more apparent at low x-ray energy and can cause

distortions in measurements of inhomogeneous samples. One of the best ways to prevent this, apart from moving the whole sample stage with the beam, is to change s with changing θ in order to maintain a constant h . This is known as a fixed exit monochromator. The monochromator crystals can also be slightly bent in order to focus the beam as well as tune to the desired wavelength. Sagittal focussing is used to focus the x-ray beam horizontally while meridional focus is used for vertical beam focussing. However, due to bandwidth deterioration issues the latter is hardly used successfully in XAS beamlines.

Different crystal planes can be used in monochromators: 111 is most common and allows wavelengths between 2 and 22 keV to be achieved. With a 311 crystal, higher energies are possible.¹³

2.3.4 Sample environments

In the experiments hutch, sample environments are tailored to the requirements of the system on a flexible sample stage. Typical sample environments include furnaces and cryostats as well as controlled gas atmospheres.

2.3.5 Detectors

2.3.5.1 Ionisation Chambers

Detectors follow the same design principle – photon interaction with a detector material results in photoionisation which is converted into electrical signals ready for interpretation. The simplest detectors are gas filled proportional ion chambers. An ionisation chamber is a pair of electrodes with a gas in between them. A constant voltage is placed between the electrodes thus producing an electric field. Without x-rays, the gas acts as an insulator, but when x-rays are present, gas excitation results in electron-positive ion pairs. The positively charged ions migrate to the cathode and electrons migrate to the anode. The resulting current signal is amplified and then integrated over a time interval after which it is converted to produce a voltage signal. This voltage is easily digitised. The gasses are sealed within the ionisation chamber using x-ray transparent windows such as Kapton. Inert noble gasses are used and include, helium, argon, krypton, and xenon. Gas mixtures are calculated for each energy range in order to optimise beam absorption – the beam absorption has a direct consequence of number of electron-positive ion pairs created, and therefore current, and ultimately signal. Ion chambers are usually the detector of choice for XAS

transmission experiments. The gas fill for the first ion chamber used to detect I_0 is optimised to 10% absorption, and the second ion chamber used to detect I_t is optimised for 30% absorption – this is under the assumption that a sample placed between the first and second chambers with optimum depth is likely to absorb 20% of flux. While photon energy is not conventionally measured using ion chambers, pure element foils with known absorption edges are used to calibrate the monochromator. A third ion chamber is often placed after the first two with a reference foil in front of it, in order to monitor the energy. Ion chambers must be exactly aligned with each other so that each ion chamber experiences the same beam.¹³

2.3.5.2 Fluorescence detectors

Solid state fluorescence detectors work essentially like ionisation chambers. However, the inert gas is replaced by a solid semi-conductor that produces electron–hole pairs upon contact with x-ray photons. When the electron–hole pairs diffuse through the semi-conductor, they are split at junctions and the resultant current is detected in a similar fashion to above. The semiconductor materials used in solid state detectors are usually silicon, for lower photon energies, or germanium based for higher energies. The detector surface covers as wide a solid angle as possible in order to capture fluorescence effectively, with multi-channel detectors commonly available.

Before XAS measurements, the fluorescence emitted from a choice element must be identified and manually isolated – this is done by looking at photon intensity before and after an edge and windowing the peak which disappears before and edge (before excitation energy of the core electrons in an element is reached) and appears after the edge. The fluorescence detector is optimally placed 90° to the incident beam in the horizontal plane, with the sample at 45° in order to retrieve the maximum inelastic scatter. Charge pile up results in detector saturation: there is a minimum pulse processing time required to detect a single event during which the detector is inactive (dead time). During this time no other event should occur otherwise both events must be rejected. This is a common problem caused by high flux and concentrated sample and solved by sample dilution as well as misaligning the detector from its optimum angle or increasing distance between detector and sample.

2.4 DUBBLE at the ESRF

This thesis project was undertaken and written at the European Synchrotron Radiation Facility (ESRF) with the project student's industrial sponsor, the Dutch-Belgian Beamline (DUBBLE). A brief introduction to both is given in this section.

2.4.1 European Synchrotron Radiation Facility



Figure 2.9: The European Synchrotron Radiation Facility (ESRF) is a central synchrotron facility situated in Grenoble.

The ESRF is the largest synchrotron source in Europe. As a joint research facility, it is supported by twenty countries, and is based in Grenoble, France (Figure 2.9). ESRF forms part of the Polygone Scientifique in Grenoble; the site is shared by the Institut Laue-Langevin (ILL) and the European Molecular Biology Laboratory (EMBL). In addition to this, several large research and development institutes and universities are based in the area, making Grenoble a strongly science oriented city.

The ESRF houses forty specialized beamlines for use by the international scientific community. These beamlines are designed for research in the areas of structural biology, structure of materials, electronic structure and magnetism, dynamics and extreme conditions, structure of soft matter, and x-ray imaging. Several beamlines are built and operated by Collaborating Research Groups (CRGs) who are institutes from countries that participate in the ESRF. The Dutch Belgian Beamline (DUBBLE) falls into this category, as do the Swiss-Norwegian (SNBL), Italian (GILDA), German (RoBL), Spanish (SpLine), British (XMaS), and several French

(D2AM, IF, FAME) lines. All the information provided above, and further information is available at the ESRF website at www.esrf.eu/UsersAndScience.

2.4.2 Dutch-Belgian Beamline

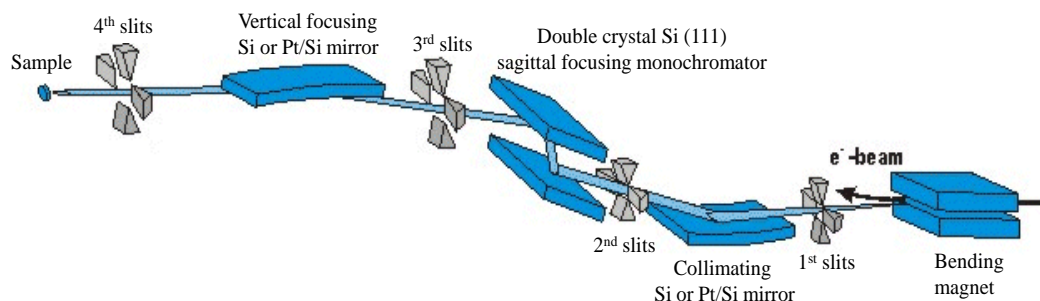


Figure 2.10: The layout of the optics hutch of the EXAFS line on the Dutch-Belgian beamline.

The Dutch-Belgian Beamline, DUBBLE or BM26, at the ESRF is a bending magnet beamline sponsored by Dutch and Belgian research councils NWO and FWO.^{46–49} DUBBLE is actually a double beamline offering users two sets of experimental and control hutches for two distinct techniques. BM26B is the name given to the small and wide angle x-ray scattering (SAXS/WAXS) experiments hutch,⁴⁹ while BM26A is designed for XANES/EXAFS measurements.⁴⁷ The two lines share the same optics hutch, and the BM26B beam shares space with users in the BM26A control hutch. The beamline design takes advantage of the horizontal fan produced by the bending magnet. A simple beam splitter divides the beam so that the hardest x-rays (closest trajectory to the storage ring) feed into BM26B while the softer x-rays are directed into BM26A. The beams are directed through their own set of focussing mirrors and monochromator. The layout of the BM26A beam is shown in Figure 2.10. The beam is shaped by a succession of slits. Before monochromating using a silicon [111] double crystal monochromator, the beam is collimated on a platinum/silicon coated mirror. Collimation involves parallelising the beam in order to reduce divergence and therefore reduce the bandwidth transmitted by the monochromator. The second crystal of the monochromator can be bent in order to create sagittal focussing, and a platinum/silicon coated focussing mirror after the monochromator is responsible for meridional focussing. Transmission experiments at BM26A are detected using two ion chambers before and after the sample. Fluorescence is detected using a 9 element monolithic germanium solid state

detector. The detector used at BM26A is of an unusual design; rather than using discrete elements, a solid germanium detector head is used in order to maximize the detected solid angle. The beamline is particularly suited to *in situ* catalysis characterisation experiments. It is fitted with a gas rig system which allows control of gas flows and mixtures from up to 4 feeds.⁵⁰ As well as this, a number of furnaces for pelleted, powdered, and liquid samples are compatible with the beamline, with sealed sample environments, heat sources and temperature controllers, and a cryostat is also available. The beamline can also be used to perform basic XRD acquisition using a MAR area detector. More information can be found on the beamline website at www.esrf.eu/UsersAndScience/Experiments/CRG/BM26.

2.5 Other Characterisation Techniques

2.5.1 XRD

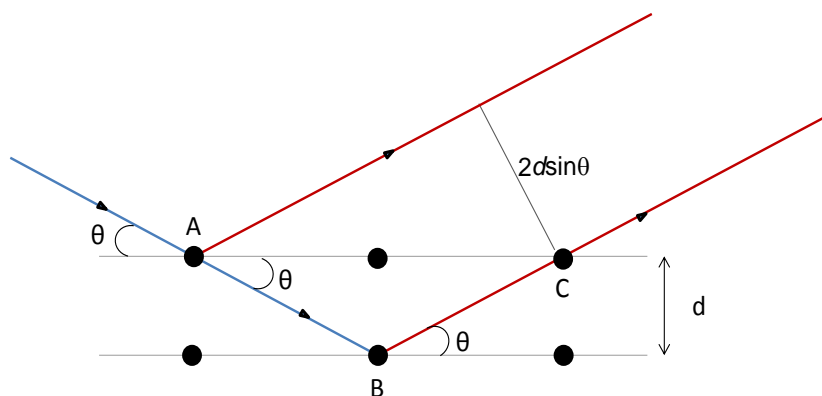


Figure 2.11: Diagram describing the derivation of Bragg's law based on incident and elastically scattered waves from a crystal grating.

X-ray diffraction is a popular method for crystallographic characterisation. The technique utilises Bragg's law $2d\sin\theta = x\lambda$ to determine d , the distance between crystallographic planes. In most experiments a fixed wavelength is used during acquisition, and elastic scattering is detected as a function of 2θ . Intensity maxima occur when the reflected wavelength from A and B in Figure 2.11 interfere constructively. This is only possible when the wavelength value is $x\lambda$ where x is an integer number. Single crystal XRD is used to obtain unit cell dimensions, bond-lengths, bond-angles, and details of site-ordering. Essentially, data generated from the single crystal x-ray analysis is interpreted and refined to obtain the crystal structure. When diffraction data is acquired from powders, some of this detail is lost;

the averaging of orientation causes the three-dimensional reciprocal space that is studied in single crystal diffraction to be projected onto a single dimension. The most widespread use of powder diffraction is in the identification and characterization of crystalline phases – selection rules determine peak patterns for each lattice type and data is often compared to diffraction patterns of known standards from databases including Inorganic Cambridge Structural Database (ICSD). In order to obtain an XRD pattern, materials must be crystalline. Laboratory x-ray sources are generated from cathode ray tubes; X-rays are produced through bombardment of a metal target (typically copper or molybdenum) with a beam of electrons emitted from a hot filament (usually tungsten). The incident beam ionizes electrons from the core 1s orbital of the target atom. Fluorescence x-rays are emitted as the result of relaxation of the excited electron back to the core shell. Synchrotron sources are highly advantageous for XRD measurements owing to the quality of the beam, i.e. very low divergence, and also flexibility in choosing wavelength. Wavelengths can be chosen to avoid sample fluorescence, and exploited for related techniques. Statistics are greatly improved with higher resolution and lower noise levels. In this text, XRD data was used as the base identification of laboratory synthesised structures using a Bruker D4 with copper source. Although not demonstrated here, the combined *in situ* XAS/XRD method is an extremely powerful technique to identify long and short range changes in a reactive system.⁵¹

2.5.2 TEM

Transmission electron microscopy (TEM) is a microscopy technique in which a beam of electrons is transmitted through an ultra-thin layer of material, the interacted beam transmitted through the material creates an image which is magnified and focussed onto an image device such as a fluorescent screen or CCD detector. Imaging resolution is limited only by the de Broglie wavelength of an electron and therefore atomic resolution imaging can be achieved. Interchanging between low and high resolution allows TEM to be a versatile tool for the characterisation of particle shapes as well as detailed surface analysis. The largest part of the electron path in an Electron Microscope has to be evacuated to a high level in order to avoid electron scatter and absorption. Although environmental microscopes have become available in recent years it is still most common practice to keep the samples in a high ($< 10^{-7}$ mbar) vacuum. The sample stage is interlocked to allow insertion of the sample holder without compromising vacuum quality in other areas of the microscope. The

sample holders are small grid meshes upon which the sample is dispersed. Usual grid materials are copper, molybdenum, gold or platinum. Although a slightly subjective characterisation technique, TEM is useful in the area of nanoparticle synthesis to identify particle shapes and surfaces. In the work described in this thesis TEM was used for morphology characterisation of transition metal sulfides formed from solvothermal decompositions using a standard JEOL 100keV system.

2.5.3 UV-vis

Ultraviolet–visible (UV-Vis) spectroscopy refers to absorption spectroscopy in the ultraviolet-visible spectral region. Like XAS, this technique is based on the Beer-Lambert law of absorption, $A = \ln(I_0/I_t) = \epsilon cL$. Here terminology is slightly different: L refers to sample depth, and ϵ is the absorption coefficient while c refers to the sample concentration. The energy range used in this technique is similar to that needed to excite electrons in d-orbitals of transition metals – the same orbital transitions that are responsible for colouring of transition metal complexes. The higher energy excitations reveal information about band gaps, metal to ligand charge transfers, and solvent effects on a complex. In this text, UV-Vis spectroscopy was used to confirm coordination changes of dithiocarbamate complexes using a Shimadzu 204 1PZ UV-vis spectrometer with a range of 1100 – 190 cm^{-1} .

2.5.4 DFT

Density functional theory (DFT) is a computational modelling method used to investigate the electronic structure of many-body systems, including atoms, molecules, and crystal phases. The name density functional theory comes from the use of functionals of the spatially dependent electron density from which the properties of a many-electron system can be determined.^{52,53} DFT is among the most popular and versatile methods available in computational chemistry. In many cases the results of DFT calculations for solid-state systems agree well with experimental data. Computational costs are relatively low when compared to traditional methods, such as Hartree–Fock theory based on many-electron wavefunctions. Despite continuous improvements some challenges still exist including properly accounting for intermolecular forces including van der Waals forces. Newer DFT methods are designed to overcome the van der Waals problem by the inclusion of additional terms.^{54–57} Calculations reported here are published⁵⁸, and were performed with the

B3PW91 hybrid functional⁵⁹ with a Pople basis set 6-31G(d,p),⁶⁰ and the PCM model⁶¹ using the Gaussian 09 Rev C suite of programs.⁶²

2.5.5 Cyclic Voltammetry

The use of electrochemistry, in particular cyclic voltammetry, features heavily in Chapter 5 of this thesis. The potentiostat used for electrochemical measurements featured in this thesis was an Autolab N series from eco-chemie. Cyclic voltammetry (CV) is a type of electrochemical measurement. In a CV experiment the potential of the working electrode is ramped as a function of time and after the set potential is reached, the potential is returned to the initial potential by ramping in the opposite direction. These cycles can be repeated as many times as is needed. In a CV trace, current is plotted against the applied voltage, or the potential. Cyclic voltammetry is generally used to study the electrochemical properties of an analyte in solution.⁶³ Cyclic voltammetry is a widely used electroanalytical technique in chemistry. It can be used to study redox processes, including the study of intermediates in redox reactions,⁶⁴ electron transfer kinetics,⁶⁵ the reversibility of a reaction.⁶⁶ It can also be used to determine stability of reaction products.⁶⁴

2.5.6 ATR-IR

Attenuated total reflectance Infrared, ATR-IR, is an IR technique that is mentioned in Chapter 5 as an *in situ* method for investigating CV experiments. Infrared (IR) spectroscopy is a very effective fingerprinting method for characterisation of liquids, solids, and gasses. In many cases however, sample preparation required for traditional transmission IR limit flexibility of the technique. Attenuated total reflectance (ATR) is a technique that has revolutionized solid and liquid sample analyses because it alleviates the issue of sample preparation. An attenuated total reflection setup uses a crystal with high refractive index to totally internally reflect the infrared beam once it comes into contact with a sample. The internal reflectance through the optically dense crystal creates an evanescent wave that extends beyond the surface of the crystal into the sample; the wave protrudes a 0.5 - 5 microns beyond the crystal surface. The IR beam then exits on the opposite end of the crystal and is passed to the IR detector to generate an infrared spectrum. The sample is typically pressed against the surface of the crystal.⁶⁷ Several groups including the Holt research group at the Department of Chemistry at UCL have an *in situ* ATR-IR setup built onto a Bruker Tensor 27

spectrometer with DLa TGS detector, to measure changes on a working electrode during electrochemistry. Details of the in situ ATR-IR setup is provided in the Chapter 5.

2.6 References

- (1) Beamline specs
<http://www.esrf.eu/UsersAndScience/Experiments/CRG/BM01/bm01-a>.
- (2) Roffey, A. Dithiocarbamate Complexes as Single Source Precursors to Metal Sulfide Nanoparticles for Applications in Catalysis, University College London, 2014.
- (3) Roldan Martinez, A.; Hollingsworth, N.; Roffey, A.; Islam, H. U.; Goodall, J. B. .; Catlow, C. R. A.; Darr, J. A.; Bras, W.; Sankar, G.; Holt, K. B.; Hogarth, G.; de Leeuw, N. H. *Chem. Commun.* **2015**, *51*, 7501–7504.
- (4) Cargill III, G. S. *J. Non. Cryst. Solids* **1984**, *61-62*, 261–272.
- (5) Hayes, T. M. *J. Non. Cryst. Solids* **1978**, *31*, 57–79.
- (6) Dalba, G.; Grisenti, R. *J. Non. Cryst. Solids* **2004**, *338-340*, 201–205.
- (7) Filipponi, A. *J. Phys. Condens. Matter* **2001**, *13*, 23–60.
- (8) Chadwick, A. V. *Solid State Ionics* **2006**, *177*, 2481–2485.
- (9) Chadwick, A. V. *Solid State Ionics* **1993**, *63-65*, 721–727.
- (10) Knauth, P.; Chadwick, A. V.; Lippens, P. E.; Auer, G. *ChemPhysChem* **2009**, *10*, 1238–1246.
- (11) Catlow, C. R. A.; Chadwick, A. V.; Greaves, G. N.; Moroney, L. M. *Nature* **1984**, *312*, 601–604.
- (12) Jupe, A. C.; Cockcroft, J. K.; Barnes, P.; Colston, S. L.; Sankar, G.; Hall, C. J. *Appl. Crystallogr.* **2001**, *34*, 55–61.
- (13) Bunker, G. *Introduction to XAFS*; Cambridge University Press, 2010.
- (14) Sayers, D. E.; Stern, E. A.; Lytle, F. W. *Phys. Rev. Lett.* **1971**, *27*, 1204–1207.
- (15) Stern, E. A. *Phys. Rev. B* **1974**, *10*, 3027–3037.
- (16) Lytle, F. W.; Sayers, D. E.; Stern, E. A. *Phys. Rev. B* **1975**, *11*, 4825–4835.
- (17) Stern, E. A.; Sayers, D. E.; Lytle, F. W. *Phys. Rev. B* **1975**, *11*, 4836–4846.
- (18) <http://www.lightsources.org/history>.
- (19) Dent, A. J.; Cibin, G.; Ramos, S.; Smith, A. D.; Scott, S. M.; Varandas, L.; Pearson, M. R.; Krumpa, N. A.; Jones, C. P.; Robbins, P. E. *J. Phys. Conf. Ser.* **2009**, *190*, 012039.

- (20) Kong, Q.; Baudelet, F.; Han, J.; Chagnot, S.; Barthe, L.; Headspith, J.; Goldsbrough, R.; Picca, F. E.; Spalla, O. *Sci. Rep.* **2012**, *2*.
- (21) Milne, C. J.; Pham, V.-T.; Gawelda, W.; Veen, R. M. van der; Nahhas, A. El; Johnson, S. L.; Beaud, P.; Ingold, G.; Lima, F.; Vithanage, D. A.; Benfatto, M.; Grolimund, D.; Borca, C.; Kaiser, M.; Hauser, A.; Abela, R.; Bressler, C.; Chergui, M. *J. Phys. Conf. Ser.* **2009**, *190*, 012052.
- (22) Schöll, A.; Fink, R.; Umbach, E.; Mitchell, G. E.; Urquhart, S. G.; Ade, H. *Chem. Phys. Lett.* **2003**, *370*, 834–841.
- (23) Stöhr, J. *NEXAFS Spectroscopy*; Ertl, G.; Gomer, R.; Mills, L.; Lotsch, H. K., Eds.; Springer-Verlag, 2003.
- (24) Te Velde, G.; Bickelhaupt, F. M.; Baerends, E. J.; Fonseca Guerra, C.; van Gisbergen, S. J. A.; Snijders, J. G.; Ziegler, T. *J. Comput. Chem.* **2001**, *22*, 931–967.
- (25) Westre, T. E.; Kennepohl, P.; Dewitt, J. G.; Hedman, B.; Hodgson, K. O.; Solomon, E. I.; V, S. U. *J. Am. Chem. Soc.* **1997**, *7863*, 6297–6314.
- (26) George, S. D.; Brant, P.; Solomon, E. I.; Radiation, S.; V, S. U.; Company, E. *C. J. Am. Chem. Soc.* **2005**, 667–674.
- (27) De Groot, F.; Vankó, G.; Glatzel, P. *J. Phys. Condens. Matter* **2009**, *21*, 104207.
- (28) McBreen, J. In *Electrochemistry in Transition: From the 20th to the 21st Century*; Conway, B. E.; Murphy, O. J.; Srinivasan, S., Eds.; 1992; p. 606.
- (29) Colpas, G. J.; Maroney, M. J.; Bagyinka, C.; Kumar, M.; Willis, W. S. *Inorg. Chem.* **1991**, 920–928.
- (30) Ankudinov, A. L.; Ravel, B.; Rehr, J. J.; Conradson, S. D. *Phys. Rev. B* **1998**, *58*, 7565.
- (31) cars9.uchicago.edu/~ravel/software/doc/Athena/html/examples/aucl.html.
<http://cars9.uchicago.edu/~ravel/software/doc/Athena/html/examples/aucl.html>.
- (32) Kim, W. B.; Choi, S. H.; Lee, J. S. *J. Phys. Chem.* **2000**, 8670–8678.
- (33) Calvin, S. *XAFS for Everyone*; CRC Press, 2013.
- (34) Newville, M. *ReVision* **2004**, 43.
- (35) Rehr, J. J.; Albers, R. C.; Zabinsky, S. I. *Phys. Rev. Lett.* **1992**, *69*, 3397.
- (36) Rehr, J. J. *Rev. Mod. Phys.* **2000**, *72*, 621–654.

- (37) Koningsberger, D. C.; Mojet, B. L.; Dorssen, G. E. Van; Ramaker, D. E. *Top. Catal.* **2000**, *10*, 143–155.
- (38) Ravel, B.; Newville, M. *J. Synchrotron Radiat.* **2005**, *12*, 537–541.
- (39) Klementev, K. V. *J. Phys. D Appl. Phys.* **2001**, *34*, 209–217.
- (40) Binsted, N. EXCURV98: CCLRC Daresbury Laboratory Computer Program, 1998.
- (41) Klementiev, K. V. XAFSmass, freeware:
www.cells.es/Beamlines/CLAESS/software/xafsmass.html.
- (42) Tröger, L.; Arvanitis, D.; Baberschke, K.; Michaelis, H.; Grimm, U.; Zschech, E. *Phys. Rev. B* **1992**, *46*, 3283–3289.
- (43) Booth, C. H.; Bridges, F. *Phys. Scr.* **2005**, *202*.
- (44) Pfalzer, P.; Urbach, J.-P.; Klemm, M.; Horn, S.; DenBoer, M.; Frenkel, A.; Kirkland, J. *Phys. Rev. B* **1999**, *60*, 9335–9339.
- (45) Tröger, L.; Zschech, E.; Arvanitis, D.; Baberschke, K. *Japanese J. Appl. Phys.* **1993**, *32*.
- (46) Beale, A. M.; Van Der Eerden, A. M. J.; Jacques, S. D. M.; Leynaud, O.; O'Brien, M. G.; Meneau, F.; Nikitenko, S.; Bras, W.; Weckhuysen, B. M. *J. Am. Chem. Soc.* **2006**, *128*, 12386–12387.
- (47) Nikitenko, S.; Beale, A. M.; van der Eerden, A. M. J.; Jacques, S. D. M.; Leynaud, O.; O'Brien, M. G.; Detollenaere, D.; Kaptein, R.; Weckhuysen, B. M.; Bras, W. *J. Synchrotron Radiat.* **2008**, *15*, 632–640.
- (48) Borsboom, M.; Bras, W.; Cerjak, I.; Detollenaere, D.; Glastra Van Loon, D.; Goedtkindt, P.; Konijnenburg, M.; Lassing, P.; Levine, Y. K.; Munneke, B.; Oversluizen, M.; Van Tol, R.; Vlieg, E. *J. Synchrotron Radiat.* **1998**, *5*, 518–520.
- (49) Bras, W.; Dolbnya, I. P.; Detollenaere, D.; Van Tol, R.; Malfois, M.; Greaves, G. N.; Ryan, A. J.; Heeley, E. *J. Appl. Crystallogr.* **2003**, *36*, 791–794.
- (50) Martis, V.; Beale, A. M.; Detollenaere, D.; Banerjee, D.; Moroni, M.; Gosselin, F.; Bras, W. *J. Synchrotron Radiat.* **2014**, *21*, 462–463.
- (51) Sankar, G.; Thomas, J. M.; Catlow, R. *Top. Catal.* **2000**, *10*, 255–264.
- (52) Dreizler, R. M.; Engel, E. *Density Functional Theory: An Advanced Course*; Springer: Berlin, 2011.
- (53) Eschrig, H. *The Fundamentals of Density Functional Theory*; Springer, 1996.

- (54) Grimme, S. *Wiley Interdiscip. Rev. Comput. Molecular Sci.* **2011**, *1*, 211–228.
- (55) Xu, X.; Goddard III, W. A. *Proc. Natl. Acad. Sci. U. S. A.* **2003**, *101*, 2673–2677.
- (56) Himmetoglu, B.; Floris, A.; Gironcoli, S.; Cococcioni, M. *Int. J. Quantum Chem.* **2013**, *114*, 14–49.
- (57) Hafner, J. *Comput. Phys. Commun.* **2007**, *177*, 6–13.
- (58) Hollingsworth, N.; Roffey, A.; Islam, H.; Mercy, M.; Roldan, A.; Bras, W.; Wolthers, M.; Catlow, R.; Sankar, G.; Hogarth, G.; de Leeuw, N. *Chem. Mater.* **2014**, *26*, 6281–6292.
- (59) Becke, A. D. *J. Chem. Phys.* **1993**, 5648.
- (60) Ditchfield, R.; Hehre, W. J.; Pople, J. A. *J. Chem. Phys.* **1971**, *54*, 724.
- (61) Scalmani, G.; Frisch, M. J. *J. Chem. Phys.* **2010**, *132*.
- (62) Frisch, M. J.; Trucks, G. W.; Schlegel, H. B.; Scuseria, G. E.; Robb, M. A.; Cheeseman, J. R.; Montgomery Jr., J. A.; Vreven, T.; Kudin, K. N.; Burant, J. C.; Millam, J. M.; Iyengar, S. S.; Tomasi, J.; Barone, V.; Mennucci, B.; Cossi, M.; Scalmani, G.; Rega, N.; Petersson, G. A.; Nakatsuji, H.; Hada, M.; Ehara, M.; Toyota, K.; Fukuda, R.; Hasegawa, J.; Ishida, M.; Nakajima, T.; Honda, Y.; Kitao, O.; Nakai, H.; Klene, M.; Li, X.; Knox, J. E.; Hratchian, H. P.; Cross, J. B.; Bakken, V.; Adamo, C.; Jaramillo, J.; Gomperts, R.; Stratmann, R. E.; Yazyev, O.; Austin, A. J.; Cammi, R.; Pomelli, C.; Ochterski, J. W.; Ayala, P. Y.; Morokuma, K.; Voth, G. A.; Salvador, P.; Dannenberg, J. J.; Zakrzewski, V. G.; Dapprich, S.; Daniels, A. D.; Strain, M. C.; Farkas, O.; Malick, D. K.; Rabuck, A. D.; Raghavachari, K.; Foresman, J. B.; Ortiz, J. V.; Cui, Q.; Baboul, A. G.; Clifford, S.; Cioslowski, J.; Stefanov, B. B.; Liu, G.; Liashenko, A.; Piskorz, P.; Komaromi, I.; Martin, R. L.; Fox, D. J.; Keith, T.; Al-Laham, M. A.; Peng, C. Y.; Nanayakkara, A.; Challacombe, M.; Gill, P. M. W.; Johnson, W.; Chen, B.; Wong, M. W.; Gonzalez, C.; Pople, J. A. *Gaussian 09, Revision C 01*, Gaussian Inc., Pittsburgh PA, 2009.
- (63) Bard, A. J.; Faulkner, L. R. *Electrochemical Methods: Fundamentals and Applications*; Wiley, Ed.; (2 ed.); 2000.
- (64) Nicholson, R. S. *Anal. Chem.* **1965**, *37*, 1351–1355.
- (65) DuVall, S. H.; McCreery, R. L. *Anal. Chem.* **1999**, *71*, 4594–4602.
- (66) Bond, A. M.; Feldberg, S. *J. Phys. Chem.* **1998**, *102*, 9966–9974.
- (67) PerkinElmer. FT-IR Spectroscopy Attenuated Total Reflectance (ATR) Technological Note, 2005.

Chapter 3 Overview

A popular route to the synthesis of nanoparticulate sulfides is the solvothermal decomposition of transition metal dithiocarbamates. These single source precursors are typically dissolved in a coordinating solvent and heated rapidly. The coordinating solvent acts as a heat sink and capping agent but its role in each decomposition process is less understood. In this chapter, it is shown through *ex situ* XAS that the coordinating solvent has significant effect on the starting material of the decomposition reaction through coordination to the transition metal centre. Case studies shown here are zinc dimethyl, and nickel and iron diisobutyl dithiocarbamates in oleylamine and hexylamine.

Chapter 3

XAS of the Solvent effects on the local structure of transition metal dithiocarbamates

3.1 Introduction

This chapter investigates the interaction of the coordinating solvent oleylamine with transition metal (TM) dithiocarbamate complexes. TM dithiocarbamates¹ are commonly used as single source precursors for the synthesis of nanoparticulate TM sulfides owing to their stability, availability, and versatility.^{2,3,4} The decomposition is commonly carried out in the coordinating solvent oleylamine owing to its advantages as a cheap solvent with a high boiling point.⁵ Oleylamine acts as a heat sink in the reaction process and a capping agent for the final product. Its role in the decomposition is considered innocent and few studies have been conducted to investigate an alternative hypothesis. Those which have, present theories rather than clear evidence.^{6,7} The results of this chapter show that oleylamine has significant effects on each of the studied dithiocarbamate complexes: bonding between the primary amine and the metal center is shown, coupled with modifications to geometry as well as changes to existing metal-dithiocarbamate bond lengths. Consequences of these interactions have knock on effects on the decomposition process, discussed further in Chapter 4.

Dithiocarbamate ligands ($R_2NCS_2^-$) have been shown to form organometallic complexes with a wide range of metals, and adopt various geometries. R groups are wide ranging, and characteristics of complexes including solubility, volatility, and decomposition are altered depending on the choice of R group. The charge that is shared between the 2 sulfur atoms results in a degree of lability; many of the observations noted in this chapter may be attributed to this quality.

Structures of the three TM dithiocarbamate complexes studied here are well known in the solid state. Zinc bis- dimethyl dithiocarbamate ($Zn(Me_2NCS_2)_2$) exists as a dimeric structure sharing two bridging dithiocarbamate ligands, and possessing one terminal ligand.⁸ A fifth interaction is noted between zinc and a sulfur atom directly bonded to the neighbouring zinc, thus resulting in a distorted trigonal bipyramidal geometry. Gas phase electron diffraction shows a monomeric structure in the gas

phase⁹ and the same is predicted for the complex in solution. The nickel bis-diisobutyl dithiocarbamate $\text{Ni}(\text{iBu}_2\text{NCS}_2)_2$ is observed as a square planar complex by bonding to two chelating dithiocarbamate ligands, and iron tris-diisobutyl dithiocarbamate $\text{Fe}(\text{iBu}_2\text{NCS}_2)_3$ adopts a distorted octahedral geometry and a full coordination sphere with three chelating dithiocarbamate ligands. While the final aim and objective of this thesis is on chemistry related to the iron sulfide greigite, which is made from the iron dithiocarbamate, three metal dithiocarbamate complexes have been chosen for investigation in the next two chapters. This is because the iron case is rather complex and a more basic understanding is needed. The zinc and nickel dithiocarbamates are ideal to gain a basic understanding of solvent interactions and subsequent decomposition processes because these metal centres are stable at 2+ with unmistakable orbital characteristics. It is also an ongoing aim of the group to dope iron sulfide with nickel and zinc and therefore this work is important in the long-run.

Interactions between amines and dithiocarbamate complexes have been extensively recorded in the past for a number of TM dithiocarbamates. In particular, literature describing the coordination of 2,2-bipyridine and 1,10-phenanthroline to zinc and cadmium dithiocarbamates is extensive. In both cases, the diamines are coordinated in cis formation due to the rigidity of the diamine ligands.¹⁰⁻¹² The monodentate ligand piperidine was shown to bind to the zinc center with a Zn-N bond distance of typically 2.07 Å creating a five coordinate complex.¹³⁻¹⁵ A similar five coordinated complex is formed with the addition of dibutyl and diisodobutyl amines to the zinc dithiocarbamate complex.¹⁶ The structures are usually determined in the solid state by crystallographic and MAS-NMR methods; although a few studies in solution have also been interpreted using NMR¹⁷ and EXAFS.¹⁸

In the following section, the local structure of each TM dithiocarbamate complex is investigated by XAS in three environments. First, the solid state EXAFS structure is compared to XRD derived data to establish the precision of the technique for characterisation of these complexes. Next, each TM dithiocarbamate complex is investigated in solution with a non-coordinating and a coordinating solvent. In this way, changes resulting from the loss of crystal structure constraints can be distinguished from changes arising specifically from coordinating effects of

oleylamine. XAS is particularly appropriate for these systems which comprise of a single metal environment, short range order, and low dilution, when dissolved.

3.2 Method

3.2.1 Samples Synthesis and Preparation

3.2.1.1 Synthesis of $Zn(Me_2NCS_2)_2$

A solution containing $NaS_2CN(CH_3)_2$ (2.8642 g, 20 mmol) in water (50 mL) was added dropwise to a solution of $ZnCl_2$ (1.3630 g, 10 mmol) in water (50 mL), resulting in a white precipitate. The mixture was vigorously stirred for 2 hrs, filtered, washed with water, and evaporated to dryness. The white powder was dissolved in dichloromethane (100 mL) and stirred with magnesium sulfate for 30 mins, filtered and dried.

3.2.1.2 Synthesis of $NaS_2CN(C_4H_9)_2$

CS_2 (17.3 mmol, 1.04 ml) was added dropwise to a mixture of tBu_2NH (17.3 mmol, 3.00 ml), $NaOH$ (17.3 mmol, 0.6918 g), distilled H_2O (50 ml), and stirred overnight. Water was removed resulting in an off-white crystalline powder.

3.2.1.3 Synthesis of $Ni(tBu_2NCS_2)_2$

A solution containing $NaS_2CN(C_4H_9)_2$ (4.5474 g, 20 mmol) in water (50 mL) was added dropwise to a solution of $NiCl_2 \cdot 6H_2O$ (2.3771 g, 10 mmol) in water (50 mL), resulting in a green precipitate. The mixture was vigorously stirred for 2 hrs, filtered, washed with water, and evaporated to dryness. The green powder was dissolved in dichloromethane (100mL) and stirred with magnesium sulfate for 30 mins, filtered and dried.

3.2.1.4 Synthesis of $Fe(tBu_2NCS_2)_3$

A solution containing $NaS_2CN(C_4H_9)_2$ (6.8211 g, 30 mmol) in water (75 mL) was added dropwise to a solution of $FeCl_3 \cdot 6H_2O$ (2.7030 g, 10 mmol) in water (75 mL), resulting in a black precipitate. The mixture was vigorously stirred for 2 hrs, filtered, washed with water, and evaporated to dryness. The black powder was dissolved in dichloromethane (100mL) and stirred with magnesium sulfate for 30 mins, filtered and dried.

3.2.1.5 Sample Preparation

Oleylamine (technical grade, 70 %), xylene (≥ 99 %), were purchased from Sigma Aldrich Ltd and used as supplied. Hexylamine (99 %) was purchased from Sigma Aldrich Ltd and distilled before use. Dodecane (99 %) was purchased from Fisher Scientific UK and used as supplied. Solutions were made at 5 mM concentrations.

3.2.2 Sample Environment

Solids were pelletized with polyvinylpyrrolidone and placed in holders provided by the beamline. Dissolved dithiocarbamate complexes were held between two Kapton windows in a liquid cell, described later in section 5.2.2.

3.2.3 Measurements

XAS spectra were acquired at the zinc K-edge (9659eV), nickel K-edge (8333eV), and iron K-edge (7112eV). Details of the measurements are given in Table 3.1.

Table 3.1: Acquisition mode and k-range details of XAS measurements taken for TM dithiocarbamates in different environments.

XAS Measurements			
Description	Environment	Transmission /Fluorecence	k-Range
Zn(Me ₂ NCS ₂) ₂	<i>Solid (12)</i>	Transmission	14 Å ⁻¹
	Dissolved in <i>xylene (13)</i>	Fluorescence	11 Å ⁻¹
	Dissolved in <i>oleylamine (14)</i>	Fluorescence	12 Å ⁻¹
Ni(ⁱ Bu ₂ NCS ₂) ₂	<i>Solid (1)</i>	Transmission	12 Å ⁻¹
	Dissolved in <i>dodecane (2)</i>	Fluorescence	9 Å ⁻¹
	Dissolved in <i>oleylamine (3)</i>	Fluorescence	12 Å ⁻¹
	Dissolved in <i>hexylamine (4)</i>	Fluorescence	12 Å ⁻¹
Fe(ⁱ Bu ₂ NCS ₂) ₃	<i>Solid (7)</i>	Transmission	11 Å ⁻¹
	Dissolved in <i>dodecane (8)</i>	Fluorescence	9 Å ⁻¹
	Dissolved in <i>oleylamine (9)</i>	Fluorescence	11 Å ⁻¹

3.2.4 Beamline

XAS data was acquired mainly on the Dutch-Belgian EXAFS beamline, BM26A.¹⁹ Monochromatic radiation was supplied by a double Si(111) crystal, ion chambers were used to measure incident and transmitted beam intensities (I_0 and I_t), and fluorescence was measured using a 9 element germanium solid state detector. Data for zinc dimethyl dithiocarbamate solid and the iron diisobutyl dithiocarbamate dissolved in oleylamine were acquired at B18 of the Diamond Light Source.²⁰ The beamline is also equipped with a Si(111) monochromator, ion chambers, and 9 element germanium solid state detector.

3.2.5 Data Processing

XAS data was normalized and background subtracted using Horae Athena software.²¹ Detailed EXAFS analyses were performed on Excurve Version 9.273.²² Amplitude factors values for each edge were derived from reference foil data except for the zinc K-edge where zinc oxide was used owing to known problems of using zinc foil.

3.3 Results

3.3.1 Zinc Dithiocarbamate

The dimethyl derivative of zinc dithiocarbamate, zinc bis-dimethyl dithiocarbamate $\text{Zn}(\text{Me}_2\text{NCS}_2)_2$ was investigated as a solid (**12**), dissolved in the non-coordinating solvent xylene (**13**), and coordinating solvent oleylamine (**14**). $\text{Zn}(\text{Me}_2\text{NCS}_2)_2$ is dimeric in the solid state. According to XRD, it has a unique structure that is distinguished from other R-group zinc dithiocarbamate complexes by two bridging dithiocarbamate ligands located on the same side of the zinc centre, thus resulting in a dimer of boat conformation. The additional complexity in solid state results in non-degenerate bond distances.⁸ The complex is known to be monomeric in the gas phase with 4 equivalent Zn-S distances of 2.35 Å.⁹

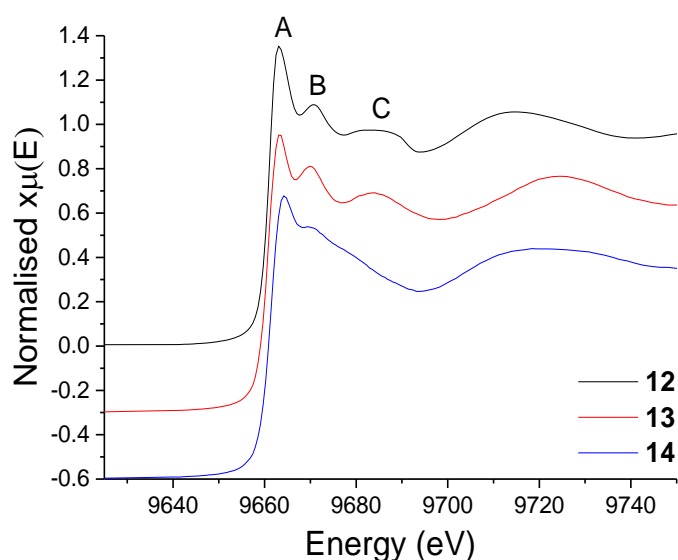


Figure 3.1: XANES spectra of $\text{Zn}(\text{Me}_2\text{NCS}_2)_2$ solid (**12**), dissolved in xylene (**13**), and dissolved in oleylamine (**14**).

The XANES spectrum of **12** shown in Figure 3.1 exhibits a straight edge jump followed by a multi-featured region including white line intensity **A**, peak **B**, and peak **C**. As expected for similar zinc(II) sulfide complexes, edge position remains exact at ca. 9661 eV for the three complexes. The spectrum of **13** is comparable to **14** with similar features after the edge position. Some differences appear, for example the ratio between **A** and **B**, and the shape of **C** differ, however, overall there is a significant resemblance. The spectrum of **13** is far more distinct – in this case peaks **B** and **C** are absent suggesting significant changes in the local structure.

Table 3.2: Results of EXAFS fittings for $\text{Zn}(\text{Me}_2\text{NCS}_2)_2$ as a solid and dissolved in xylene and oleylamine. Unrefined coordination numbers are indicated by *.

<i>Ex situ</i> XAS							
Sample	Scatter	<i>N</i>	$R_{\text{XRD}} (\text{\AA})$	$R_{\text{EXAFS}} (\text{\AA})$	$\sigma^2 (\text{\AA}^2)$	Reduced χ^2	<i>R-factor</i>
$\text{Zn}(\text{Me}_2\text{NCS}_2)_2$ solid (12)	S	4*	2.31 - 2.43	2.35 ± 0.01	0.011 ± 0.001	2×10^{-6}	20
	C	1*	2.77	2.71 ± 0.04	0.011 ± 0.001		
	S	1*	3.03	2.86 ± 0.02	0.011 ± 0.001		
	C	2*	3.02	2.86 ± 0.02	0.011 ± 0.001		
$\text{Zn}(\text{Me}_2\text{NCS}_2)_2$ in xylene (13)	S	4*	-	2.34 ± 0.01	0.011 ± 0.001	3×10^{-5}	26
	C	2*	-	2.73 ± 0.04	0.011 ± 0.001		
$\text{Zn}(\text{Me}_2\text{NCS}_2)_2$ in oleylamine (14)	N	1.3	-	2.06 ± 0.02	0.020 ± 0.001	3×10^{-4}	26
	S	4*	-	2.28 ± 0.03	0.020 ± 0.001		

EXAFS of **12** can be modelled in close agreement with the XRD derived crystal structure of $\text{Zn}(\text{Me}_2\text{NCS}_2)_2$.⁸ Four Zn-S distances at 2.35 Å arise from bonding interaction of the zinc centre to the terminal bidentate dithiocarbamate ligand (XRD distance 2.312(6) Å and 2.333(6) Å), and with bridging ligands (XRD distances at 2.373(6) Å and 2.429(6) Å). A fifth Zn-S distance is detected in **12** at 2.86 Å. This is a typical feature of dimeric zinc dithiocarbamates and arises in $\text{Zn}(\text{Me}_2\text{NCS}_2)_2$ at 3.036(6) Å according to XRD (Table 3.2, Figure 3.2a-b). The discrepancy between the XRD and EXAFS derived values at the longer distance may arise due to not taking multiple scattering into consideration.

In xylene, as expected EXAFS can be fit to a monomeric structure. **13** is fit to 4 Zn-S interatomic distances at 2.35 Å. This agrees well with the monomeric crystallographic structure of zinc bis- dibenzyl dithiocarbamate which is also found to contain 2 sets of bond distances with 2 Zn-S at 2.33 Å and 2 Zn-S at 2.36 Å,²³ and the gas phase monomeric structure which contains 4 Zn-S bond distances at 2.34 Å (Figure 3.3).⁹ A further 2 Zn-C interatomic distances are found in **13** at 2.73 Å, a

value similar to the 1 Zn-C distance at 2.74 Å from the terminal dithiocarbamate ligand of **12**. Moreover, amplitude of the EXAFS increases from that of **12**, attributed to a more ordered structure (Table 3.2, Figure 3.2c-d).

In oleylamine, the structure is modified by the coordination of at least one oleylamine ligand to the metal centre. 1.3 Zn-N distances are discovered at 2.06 Å with a 10 % error. In addition, 4 Zn-S are shown at 2.28 Å. The Zn-N interatomic distance of 2.06 Å is similar to those noted in literature (typically 2.07 Å for monodentate amine ligands^{13-15,24}). The Zn-S distance of 2.28 Å is slightly shorter than literature reports which list Zn-S distances above 2.30 Å.²⁵ FTs showing zinc and copper dithiocarbamates in amine solvents have previously been shown visually to decrease in average bond distance as is observed in this current study.¹⁸ The Debye-Waller factor is considered high for the ambient temperature and is most likely a result of the dynamic nature of the five-coordinated complex which can interchange between trigonal bipyramidal and square based pyramidal owing to similar energies and low activation barriers (Table 3.2, Figure 3.2e-f). The interatomic distance variation based on the Debye-Waller factor is 0.1 Å.

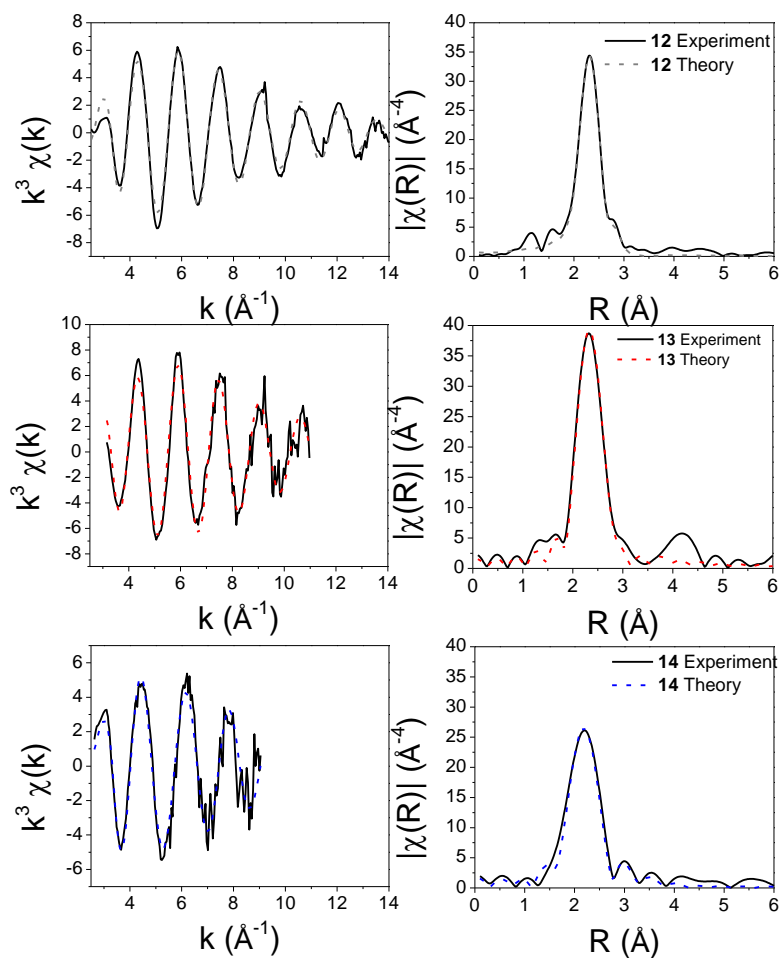


Figure 3.2: a. EXAFS and b. FT of $\text{Zn}(\text{Me}_2\text{NCS}_2)_2$ solid (12), c. EXAFS and d. FT of $\text{Zn}(\text{Me}_2\text{NCS}_2)_2$ dissolved in xylene (13), and e. EXAFS and f. FT of $\text{Zn}(\text{Me}_2\text{NCS}_2)_2$ dissolved in oleylamine (14).

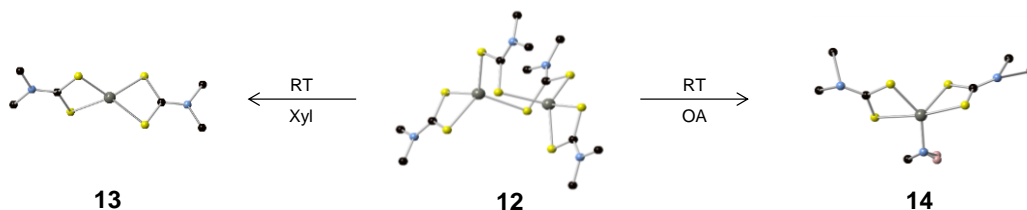


Figure 3.3: Pictorial representation of 12, 13, and 14. Images were created on CrystalMaker® Software Ltd by modifying a crystal structure file of zinc dimethyl dithiocarbamate.

3.3.2 Nickel Dithiocarbamate

Nickel bis-diisobutyl dithiocarbamate $\text{Ni}(\text{}^i\text{Bu}_2\text{NCS}_2)_2$ was investigated as a solid (1), and dissolved in non-coordinating solvent dodecane (2), and coordinating solvent oleylamine (3). Investigations were also performed both by XAS and UV-Vis on

$\text{Ni}(\text{tBu}_2\text{NCS}_2)_2$ dissolved in hexylamine (**4**), another coordinating solvent, and UV-vis data was compared with that of $\text{Ni}(\text{tBu}_2\text{NCS}_2)_2$ dissolved in hexane (**15**), the non-coordinating equivalent.

The complex is found in a square planar geometry owing to d^8 character of the nickel centre. While many nickel dithiocarbamates form stacked dimers, the diisobutyl derivative is found in monomeric form as a result of bulky R groups. The local structure is much simpler than the zinc complex studied above with four equivalent Ni-S bond distances of 2.20 Å, making the material an ideal structure to investigate in greater detail, with respect to understanding the solvothermal decomposition process.

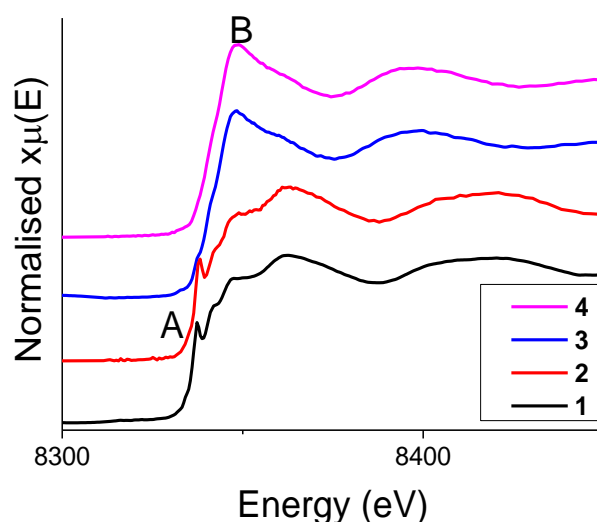


Figure 3.4: XANES spectra of $\text{Ni}(\text{tBu}_2\text{NCS}_2)_2$ solid (**1**), dissolved in dodecane (**2**), dissolved in oleylamine (**3**), and dissolved in hexylamine (**4**).

The XANES spectrum of $\text{Ni}(\text{tBu}_2\text{NCS}_2)_2$ solid **1** can be identified by a sharp feature at the edge position (ca. 8337 eV) labelled **A** and a major peak at ca. 8349 eV marked **B** in Figure 3.4. Feature **A** is common for linear and square planar geometries and arises from a 1s to 4p transition that occurs simultaneously with ligand to metal transfer, thus reducing the energy at which the transition occurs.^{18,26–28} Feature **B** is the white line intensity associated with the classic 1s to 4p transition and multiple scattering. The spectrum of **2** is identical to **1**, with equivalent features and unchanged edge position. While **3** also shares the same edge position, indicating persisting 2+ oxidation state of the nickel center, the spectrum displays significant

changes. The sharp spectral feature **A** located at the edge position of **1**, is unobserved for **3**. Instead, the featured edge is replaced by a well-defined white line intensity at **B**. The disappearance of **A** indicates the replacement of the square planar geometry, and increase in white line intensity points to the development of octahedral geometry.

XANES of **4**, $\text{Ni}(\text{iBu}_2\text{NCS}_2)_2$ in hexylamine, exhibits the same transformation as **3** thus confirming that the effects observed with oleylamine is similar to the effects of other amines. **4** was also investigated by UV-vis spectroscopy against $\text{Ni}(\text{iBu}_2\text{NCS}_2)_2$ dissolved in the non-coordinating solvent hexane (**15**). The substantial differences observed between the two spectra further confirm changes in the coordination environment (Figure 3.5). The peak at 330nm on **15** is associated with metal to ligand charge transfer.²⁹ This is not fully observed in **4**. Instead, 2 peaks are observed at 260 and 300nm indicating clear changes in local environment.

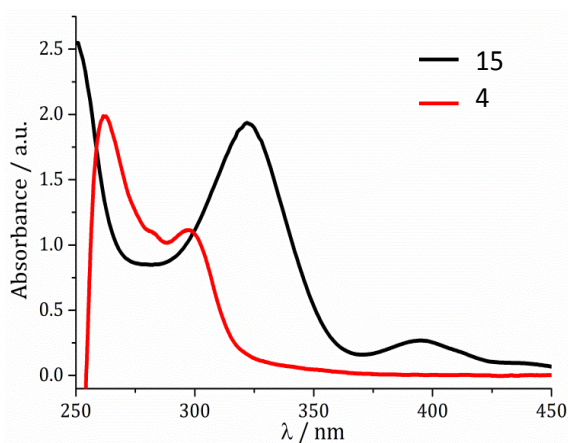


Figure 3.5: UV-vis spectra of $\text{Ni}(\text{iBu}_2\text{NCS}_2)_2$ dissolved in hexane (**15**) and hexylamine (**4**).

Table 3.3: Results of EXAFS fittings for Ni(ⁱBu₂NCS₂)₂ as a solid and dissolved in dodecane, oleylamine, and hexylamine. Unrefined coordination numbers are indicated by *.

<i>Ex situ</i> XAS							
Sample	Scatter	<i>N</i>	<i>R</i> _{XRD} (Å)	<i>R</i> _{EXAFS} (Å)	σ^2 (Å ²)	Reduced <i>chi</i> ²	<i>R</i> -factor
Ni(ⁱ Bu ₂ NCS ₂) ₂ solid (1)	S	4*	2.20	2.20 ± 0.01	0.007 ± 0.001	2 x 10 ⁻⁶	24
	C	2*	2.68	2.69 ± 0.02	0.006 ± 0.001		
	N	2*	4.00	4.33 ± 0.02	0.010 ± 0.001		
Ni(ⁱ Bu ₂ NCS ₂) ₂ in dodecane (2)	S	4*	-	2.21 ± 0.01	0.007 ± 0.001	1 x 10 ⁻⁶	27
	N	2*	-	2.05 ± 0.02	0.006 ± 0.001		
Ni(ⁱ Bu ₂ NCS ₂) ₂ in oleylamine (3)	S	2*	-	2.37 ± 0.02	0.008 ± 0.001	3 x 10 ⁻⁶	22
	S	2*	-	2.51 ± 0.02	0.009 ± 0.002		
	S	2*	-	2.51 ± 0.02	0.009 ± 0.002		
Ni(ⁱ Bu ₂ NCS ₂) ₂ in hexylamine (4)	N	2*	-	2.03 ± 0.02	0.006 ± 0.001	1 x 10 ⁻⁵	37
	S	2*	-	2.32 ± 0.02	0.009 ± 0.001		
	S	2*	-	2.47 ± 0.02	0.006 ± 0.002		

EXAFS of **1** reveals good agreement with XRD data³⁰; 4 Ni-S distances are observed at 2.20 Å and 2 Ni-C distances exist at 2.69 Å while XRD derived bond distances include 4 Ni-S between 2.1936(5) and 2.2095(6) Å and 2 Ni-C distances at 2.6842(14) Å (Table 3.3, Figure 3.7a-b).³⁶ EXAFS of **2** produces a comparable result to **1** with 4 Ni-S interatomic distances at 2.21 Å, and 2 Ni-C distances at 2.68 Å (Table 3.3, Figure 3.7c-d). The discrepancy between the XRD and EXAFS derived value for the interatomic distance of the third shell is most likely caused by not taking multiple scattering effects into consideration.

Like the XANES, EXAFS of **3** is greatly varied from the known structure of **1**. According to EXAFS analysis, the complex acquires a full coordination sphere through the addition of 2 Ni-N bonds at 2.05 Å between the nickel center and oleylamine. In addition, increased bond distances are observed for existing nickel-dithiocarbamate interactions; 2 Ni-S distances are found at an average of 2.37 Å and 2 Ni-S distances appear at 2.51 Å (Table 3.3, Figure 3.7e-f). EXAFS of **4** reveals the same trend, although bonds are shown to be slightly shorter than in **3**; 1 Ni-N interaction is observed at 2.03 Å while 2 sets of Ni-S bonds are found at 2.32 Å and 2.47 Å (Table 3.3, Figure 3.7g-h).

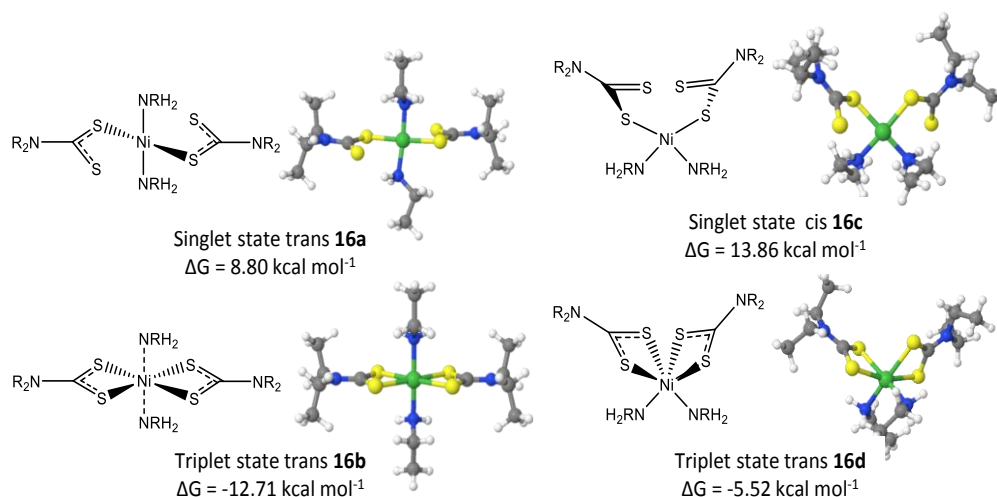


Figure 3.6: Possible conformations of $\text{Ni}(\text{Bu}_2\text{NCS}_2)_2(\text{C}_2\text{H}_4)_2\text{N}$ according to DFT, including two singlet (**16a** and **16c**) and two triplet (**16b** and **16d**) states in *cis* and *trans* geometry.

Although geometry could not be determined by EXAFS, DFT calculations performed by the computational group of the CO₂ consortium, and published by Hollingsworth *et al.*³¹ on the interaction of ethylamine to the nickel diethyl dithiocarbamate complex (**16**) provided some insight. DFT calculations were performed with the B3PW91 hybrid functional³² with a Pople basis set 6-31G(d,p).³³ Solvent effects were introduced *via* a continuum dielectric constant around the molecules with the PCM model³⁴ and the suite of programs, Gaussian 09 Rev C, was used.³⁵ It uncovered 4 main configurations, of which the *trans* bonded triplet state **16b** was shown to be most stable with a Gibbs free energy of $-12.71 \text{ kcal mol}^{-1}$. The alternative – the *cis* bonded triplet state **16d** – was also shown to display relative stability with a negative Gibbs free energy of $-5.52 \text{ kcal mol}^{-1}$. It is likely that both structures coexist in an equilibrium which tends towards the *trans* bonded form. The singlet states containing monodentate ligands were shown to be energetically unfavourable (Figure 3.6).

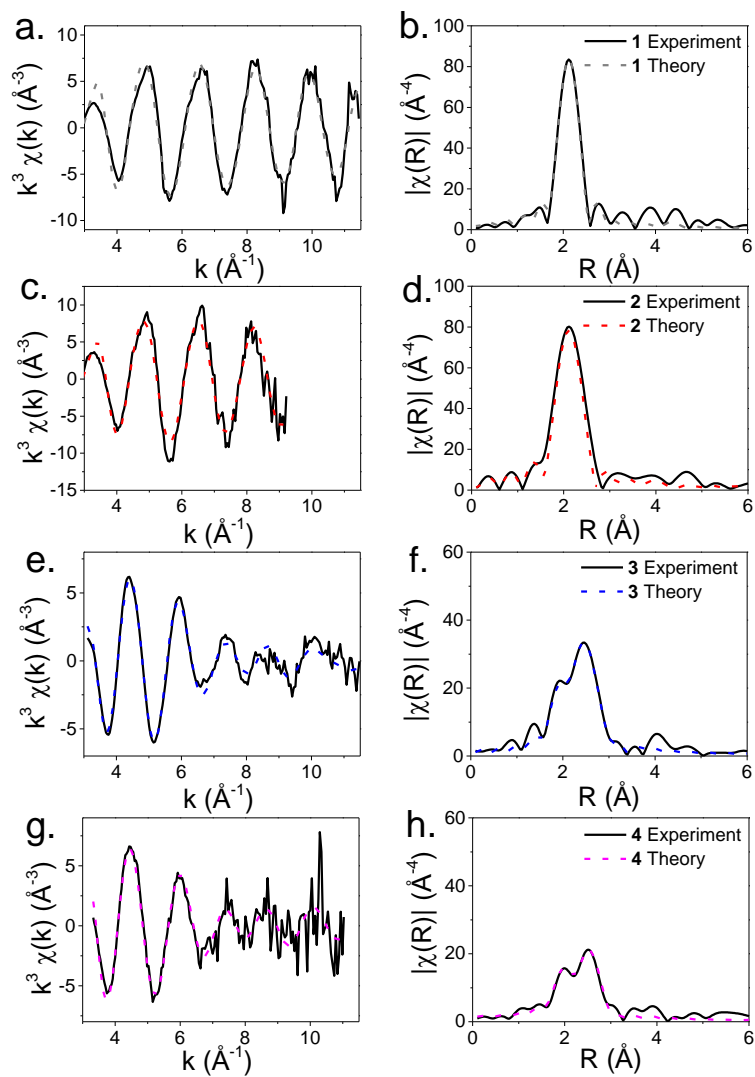


Figure 3.7: a. EXAFS and b. FT of $\text{Ni}(\text{Bu}_2\text{NCS}_2)_2$ solid (1), c. EXAFS and d. FT of $\text{Ni}(\text{Bu}_2\text{NCS}_2)_2$ dissolved in dodecane (2), e. EXAFS and f. FT of $\text{Ni}(\text{Bu}_2\text{NCS}_2)_2$ dissolved in oleylamine (3), and g. EXAFS and h. FT of $\text{Ni}(\text{Bu}_2\text{NCS}_2)_2$ dissolved in hexylamine (4).

3.3.3 Iron Dithiocarbamate

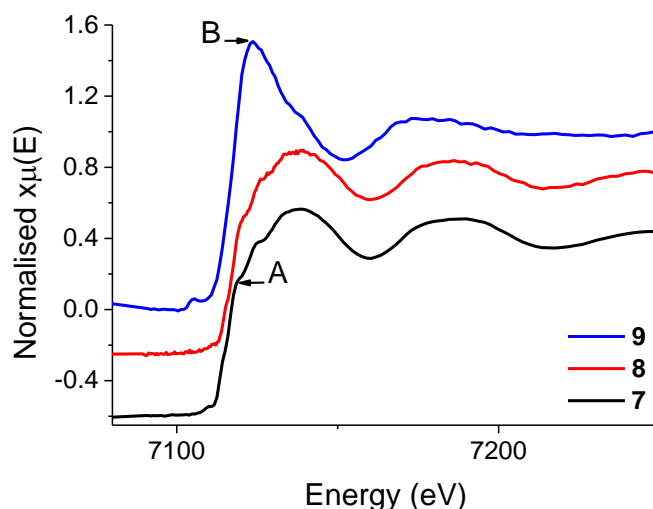


Figure 3.8: XANES spectra of $\text{Fe}(\text{i-Bu}_2\text{NCS}_2)_3$ solid (**7**), dissolved in dodecane (**8**), and dissolved in oleylamine (**9**).

XAS data was taken of $\text{Fe}(\text{i-Bu}_2\text{NCS}_2)_3$ as a solid (**7**), dissolved in oleylamine (**9**) and dissolved in dodecane (**8**), shown in Figure 3.8. XANES shows that while spectra of **7** and **8** are identical, significant differences are observed between the spectra of **7** and **9**. White line intensity belonging to **9**, labelled **B** at ca. 7124 eV, is more prominent than in **7**, while a shoulder present on **7**, ca. 7119 eV, labelled **A**, and associated with the p-orbital contribution of sulfur to the 4s-orbital of iron, is reduced on **9**. The differences are suggestive of changes to the local iron environment. UV-vis spectra of $\text{Fe}(\text{i-Bu}_2\text{NCS}_2)_3$ dissolved in dodecane (**8**) and hexylamine (**17**), shown in Figure 3.9, reveal differences between the structures in coordinated and uncoordinated solvents, again indicating changes to local structure.

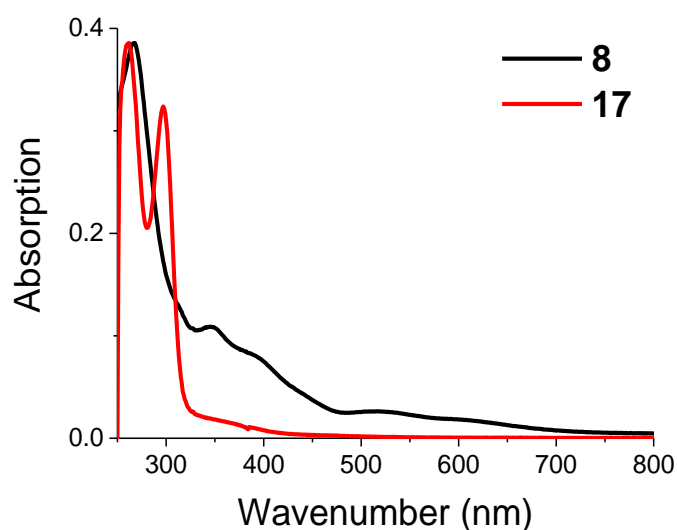


Figure 3.9: UV-vis spectra of $\text{Fe}(\text{iBu}_2\text{NCS}_2)_3$ dissolved in dodecane (8) and hexylamine (17).

This result is surprising given that the iron center of iron tris-isobutyl dithiocarbamate is fully coordinated in the solid state. Changes observed in the XANES of **9** must occur via the weakening or breakage of existing dithiocarbamate bonds. EXAFS analysis confirms this suspicion.

Table 3.4: Results of EXAFS fittings for $\text{Fe}(\text{iBu}_2\text{NCS}_2)_3$ as a solid and dissolved in dodecane, and oleylamine. Unrefined coordination numbers are indicated by *.

Ex situ XAS							
Sample	Scatter	N	$R_{\text{XRD}} (\text{\AA})$	$R_{\text{EXAFS}} (\text{\AA})$	$\sigma^2 (\text{\AA}^2)$	Reduced χ^2	R-factor
$\text{Fe}(\text{iBu}_2\text{NCS}_2)_3$ solid (7)	S	6*	2.29	2.30 ± 0.01	0.011 ± 0.001	2×10^{-6}	17
	C	3*	2.78	2.79 ± 0.02	0.011 ± 0.001		
	N	3*	4.09	4.09 ± 0.05	0.012 ± 0.002		
$\text{Fe}(\text{iBu}_2\text{NCS}_2)_3$ in dodecane (8)	S	6*	-	2.31 ± 0.02	0.013 ± 0.002	2×10^{-6}	18
	C	3*	-	2.71 ± 0.02	0.013 ± 0.002		
$\text{Fe}(\text{iBu}_2\text{NCS}_2)_3$ in oleylamine (9)	N	2*	-	1.89 ± 0.02	0.006 ± 0.001	9×10^{-6}	36
	S	3*	-	2.21 ± 0.09	0.008 ± 0.001		
	C	3*	-	2.69 ± 0.08	0.006 ± 0.002		
	S	3*	-	3.08 ± 0.07	0.013 ± 0.002		

According to single crystal X-ray diffraction, **7** adopts a distorted octahedral geometry. EXAFS of **7** is in exact agreement with XRD data showing 6 Fe-S interatomic distances at 2.30 Å, 3 Fe-C interactions at 2.79 Å, and 3 Fe-N distances at 4.09 Å (Table 3.4, Figure 3.10a-b). According to XRD, bonding of the iron centre to three bidentate dithiocarbamate ligands is shown by 6 Fe-S bond distances between 2.2824(15) and 2.2899(3) Å, 3 Fe-C distances at 2.7786(4) Å, and 3 Fe-N distances at 4.0928(6) Å.³⁰ Comparisons can be made between the bond distance here, and those reported previously by EXAFS that demonstrated bond distance

change of solid iron tris N,N-ethylphenyl dithiocarbamate between 7 K and 330 K and attributed this to spin crossover, reporting 2.30 Å and 2.44 Å for low spin and high spin Fe-S bond distances respectively.³⁶

EXAFS of **8** is similar to XRD and EXAFS of **7** with increased disorder as is expected in solution. Here, the 6 Fe-S bonds are present at 2.31 Å. The structure remains in a distorted octahedral geometry with 3 bidentate ligands as indicated by 3 Fe-C distances at 2.71 Å (Table 3.4, Figure 3.10c-d).

EXAFS of **9** is significantly different from that of **7** or **8**. The bidentate ligands are no longer fully bound. Instead each ligand is singly bonded to the iron centre by a covalent Fe-S bond while the detached sulfur remains in close proximity; EXAFS reveals 3 Fe-S interatomic distances at an average of 2.21 Å and 3Fe-S distances at 3.08 Å. In addition, 2 Fe-N interatomic distances, arising from the introduction of iron-oleylamine interactions, emerge at 1.89 Å (Table 3.4, Figure 3.10e-f). Given that the cluster is no longer fully coordinated, it can be inferred that the unbound sulfur of each dithiocarbamate ligand forms long range interactions, in equilibrium, with the iron centre. This would explain the highly specific Fe-S interatomic distance of 3.08 Å detected by EXAFS. In reality, it would seem that the EXAFS portrays an averaged structure that may involve several interchanging conformations including the structure containing one bidentate and two monodentate dithiocarbamate ligands, and the structure containing 3 rather than 2 oleylamine ligands (Figure 3.11). The spin state of the iron centre is difficult to determine and is further discussed in the next chapter.

For the iron dithiocarbamate fits, data ranges were variable depending on the acquisition settings on beamtime which were decided based on time pressures and macros built for the proceeding in situ data acquisitions. Data for the iron dithiocarbamate in oleylamine was fit up to 11 Å⁻¹ despite oscillations decreasing after 8 Å⁻¹. This is because of the “beating effect” which sees oscillations become more destructively interfered at high k owing to the presence of two different and distinctive bond distances in the first shell.³⁷ The lower oscillations are in this case contains a lot of information on the structure of the system and should not be discounted.

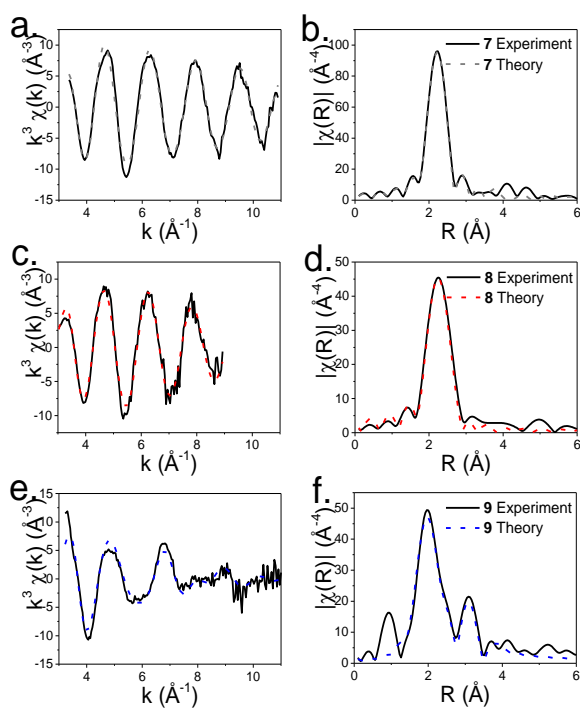


Figure 3.10: a. EXAFS and b. FT of $\text{Fe}^{\text{I}}(\text{Bu}_2\text{NCS}_2)_3$ solid (7), c. EXAFS and d. FT of $\text{Fe}^{\text{I}}(\text{Bu}_2\text{NCS}_2)_3$ dissolved in dodecane (8), and e. EXAFS and f. FT of $\text{Fe}^{\text{I}}(\text{Bu}_2\text{NCS}_2)_3$ dissolved in oleylamine (9).

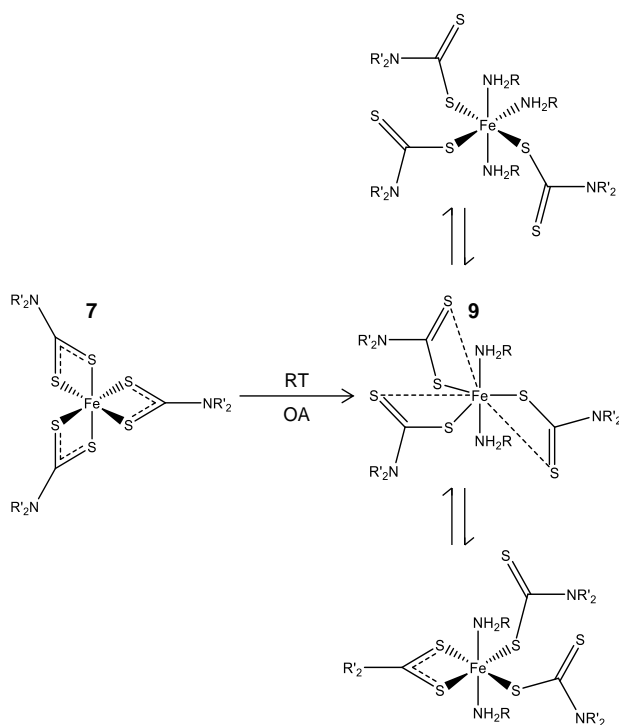


Figure 3.11: Pictorial representation of 7, and 9.

3.4 Conclusion

In this chapter, the effect of oleylamine on the coordination environment of TM dithiocarbamate complexes was investigated using EXAFS analysis. The oleylamine, being an electron donor, and in large excess, was found to form bonds with each system.

Many changes that occurred to the $\text{Zn}(\text{Me}_2\text{NCS}_2)_2$ upon dissolution were attributed to the dimer-monomer transition. For $\text{Zn}(\text{Me}_2\text{NCS}_2)_2$, the local structure of the TM centre in oleylamine was shown to include a zinc-oleylamine interaction, as well as signs of the monomeric form with zinc-dithiocarbamate bond distances changing in length. Two Zn-S distances were shown to decrease significantly, while the Zn-oleylamine distance was shorter than those typically reported in literature.

In $\text{Ni}(\text{Bu}_2\text{NCS}_2)_2$, the interaction of 2 oleylamine molecules with the nickel centre was observed, most likely in *trans* arrangement according to DFT calculations. Existing nickel-dithiocarbamate bonds were shown to lengthen both experimentally by EXAFS, and computationally by DFT. Of the three metal dithiocarbamate complexes, $\text{Ni}(\text{Bu}_2\text{NCS}_2)_2$ was least affected by dissolution in non-coordinating solvent thus demonstrating the stability of the square planar conformation of the d^8 metal centre. The effect was not limited to oleylamine: the primary amines hexylamine was shown to induce the same level of change.³¹

$\text{Fe}(\text{Bu}_2\text{NCS}_2)_3$ also exhibited significant restructuring as a result of interaction with oleylamine. Here, the existing chelating dithiocarbamate ligands were forced to monodentate as interaction with 2 oleylamine molecules were introduced. $\text{Fe}(\text{Bu}_2\text{NCS}_2)_3$ in dodecane demonstrated the expected six coordinated structure with slightly increased disorder. Later in Chapter 4, the continued change in the Fe-S bond disorder is seen as a function of temperature.

The consequences of these interactions, and others not detected by EXAFS have knock on effects on the decomposition process, discussed in Chapter 4.

3.5 Acknowledgements

The dithiocarbamate complexes used for the decomposition reactions were synthesised by Anna Roffey and Nathan Hollingsworth who also performed single crystal XRD analysis on nickel and iron diisobutyl dithiocarbamate. Results are published in the thesis of Anna Roffey.³⁰ UV-vis experiments of the nickel dithiocarbamate were carried out by Anna Roffey, and DFT calculations were performed by Maxime Mercy. These results are published in a paper about the decomposition of nickel dithiocarbamate.³¹

3.6 References

- (1) Hogarth, G. Karlin, K. D., Ed.; John Wiley & Sons, Inc.: Hoboken, NJ, USA, 2005; pp. 71–561.
- (2) Afzaal, M.; Malik, M. A.; O'Brien, P. *J. Mater. Chem.* **2010**, *20*, 4031.
- (3) Han, W.; Gao, M. *Cryst. Growth Des.* **2008**, *8*, 1023–1030.
- (4) O'Brien, P.; Walsh, J. R.; Watson, I. M.; Hart, L.; Silva, S. R. P. *J. Cryst. Growth* **1996**, *167*, 133–142.
- (5) Mourdikoudis, S.; Liz-marzan, L. M. *Chem. Mater.* **2013**, *25*, 1465–1476.
- (6) Gelling, I. R. *Ruuber Chem. Technol* **1974**, *46*, 524.
- (7) Jung, Y. K.; Kim, J. Il; Lee, J. K. *J. Am. Chem. Soc.* **2010**, *132*, 178–184.
- (8) Klug, H. *Acta Crystallogr.* **1966**, *21*, 536–546.
- (9) Hagen, K.; Holwill, C. J.; Rice, D. A. **1989**, 3239–3242.
- (10) Thirumaran, S.; Ramalingam, K.; Bocelli, G.; Cantoni, A. *Polyhedron* **1999**, *18*, 925–930.
- (11) Manohar, A.; Venkatachalam, V.; Ramalingam, K.; Thirumaran, S.; Bocelli, G. *J. Chem. Crystallogr.* **1998**, *28*, 861–866.
- (12) Lai, C. S.; Tiekink, E. R. T. *Appl. Organomet. Chem.* **2003**, *17*, 197–198.
- (13) Ivanov, a. V.; Zaeva, a. S.; Gerasimenko, a. V.; Rodina, T. a. *Russ. J. Coord. Chem.* **2008**, *34*, 688–698.
- (14) Malik, A. M.; Motevalli, M.; O'Brien, P. *Polyhedron* **1999**, *18*, 1259–1264.
- (15) Ivanov, A. V.; Forsling, W.; Antzutkin, O. N.; Novikova, E. V. *Russ. J. Coord. Chem.* **2001**, *27*, 158–166.
- (16) Ivanov, A. V.; Zaeva, A. S.; Novikova, E. V.; Gerasimenko, A. V.; Forsling, W. *Russ. J. Coord. Chem.* **2007**, *33*, 233–243.
- (17) Arul Prakasam, B.; Ramalingam, K.; Bocelli, G.; Cantoni, A. *Polyhedron* **2007**, *26*, 4489–4493.
- (18) Mazalov, L. N.; Bausk, N. V; Larionov, S. V; Branch, S. *J. Struct. Chem.* **2001**, *42*, 784–793.

- (19) Nikitenko, S.; Beale, A. M.; van der Eerden, A. M. J.; Jacques, S. D. M.; Leynaud, O.; O'Brien, M. G.; Detollenaere, D.; Kaptein, R.; Weckhuysen, B. M.; Bras, W. *J. Synchrotron Radiat.* **2008**, *15*, 632–640.
- (20) Dent, A. J.; Cibin, G.; Ramos, S.; Smith, A. D.; Scott, S. M.; Varandas, L.; Pearson, M. R.; Krumpa, N. A.; Jones, C. P.; Robbins, P. E. *J. Phys. Conf. Ser.* **2009**, *190*, 012039.
- (21) Ravel, B.; Newville, M. *J. Synchrotron Radiat.* **2005**, *12*, 537–541.
- (22) Binsted, N. EXCURV98: CCLRC Daresbury Laboratory Computer Program, 1998.
- (23) Decken, A.; Gossage, R. a.; Chan, M. Y.; Lai, C. S.; Tiekink, E. R. T. *Appl. Organomet. Chem.* **2004**, *18*, 101–102.
- (24) Mei, L.; Ming, T. H.; Rong, L. Q.; Jie, S.; Zhong, Y. S.; Liang, L. X. *J. Chem. Sci.* **2009**, *121*, 435–440.
- (25) Sing Lai, C.; Tiekink, E. R. T. *Appl. Organomet. Chem.* **2003**, *17*, 255–256.
- (26) Bair, R.; Goddard, W. *Phys. Rev. B* **1980**, *22*, 2767–2776.
- (27) Kryuchkova, N. A.; Parygina, G. K.; Tarasenko, O. A.; Trubina, S. V. *J. Struct. Chem.* **2008**, *49*, 19–39.
- (28) Noh, D.-Y.; Mizulno, M.; Kim, D.-K.; Yoon, J.-B.; Choy, J.-H. *Polyhedron* **1997**, *16*, 1351–1355.
- (29) Oktavec, D.; Siles, B.; Stefanec, J. *Collect. Czechoslov. Chem. Commun.* **1980**, *45*, 791–799.
- (30) Roffey, A. Dithiocarbamate Complexes as Single Source Precursors to Metal Sulfide Nanoparticles for Applications in Catalysis, University College London, 2014.
- (31) Hollingsworth, N.; Roffey, A.; Islam, H.; Mercy, M.; Roldan, A.; Bras, W.; Wolthers, M.; Catlow, R.; Sankar, G.; Hogarth, G.; de Leeuw, N. *Chem. Mater.* **2014**, *26*, 6281–6292.
- (32) Becke, A. D. *J. Chem. Phys.* **1993**, 5648.
- (33) Ditchfield, R.; Hehre, W. J.; Pople, J. A. *J. Chem. Phys.* **1971**, *54*, 724.
- (34) Scalmani, G.; Frisch, M. J. *J. Chem. Phys.* **2010**, 132.
- (35) Frisch, M. J.; Trucks, G. W.; Schlegel, H. B.; Scuseria, G. E.; Robb, M. A.; Cheeseman, J. R.; Montgomery Jr., J. A.; Vreven, T.; Kudin, K. N.; Burant, J. C.; Millam, J. M.; Iyengar, S. S.; Tomasi, J.; Barone, V.; Mennucci, B.; Cossi, M.; Scalmani, G.; Rega, N.; Petersson, G. A.; Nakatsuji, H.; Hada, M.; Ehara,

M.; Toyota, K.; Fukuda, R.; Hasegawa, J.; Ishida, M.; Nakajima, T.; Honda, Y.; Kitao, O.; Nakai, H.; Klene, M.; Li, X.; Knox, J. E.; Hratchian, H. P.; Cross, J. B.; Bakken, V.; Adamo, C.; Jaramillo, J.; Gomperts, R.; Stratmann, R. E.; Yazyev, O.; Austin, A. J.; Cammi, R.; Pomelli, C.; Ochterski, J. W.; Ayala, P. Y.; Morokuma, K.; Voth, G. A.; Salvador, P.; Dannenberg, J. J.; Zakrzewski, V. G.; Dapprich, S.; Daniels, A. D.; Strain, M. C.; Farkas, O.; Malick, D. K.; Rabuck, A. D.; Raghavachari, K.; Foresman, J. B.; Ortiz, J. V.; Cui, Q.; Baboul, A. G.; Clifford, S.; Cioslowski, J.; Stefanov, B. B.; Liu, G.; Liashenko, A.; Piskorz, P.; Komaromi, I.; Martin, R. L.; Fox, D. J.; Keith, T.; Al-Laham, M. A.; Peng, C. Y.; Nanayakkara, A.; Challacombe, M.; Gill, P. M. W.; Johnson, W.; Chen, B.; Wong, M. W.; Gonzalez, C.; Pople, J. A. Gaussian 09, Revision C 01, Gaussian Inc., Pittsburgh PA, 2009.

- (36) McGrath, C. M.; O'Connor, C. J.; Sangregorio, C.; Seddon, J. M. .; Sinn, E.; Sowrey, F. E.; Young, N. a. *Inorg. Chem. Commun.* **1999**, 2, 536–539.
- (37) Bauchspieß, K. R. *Phys. B Condens. Matter* **1995**, 208–209, 185–186.

Chapter 4 Overview

A popular route to the synthesis of nanoparticulate sulfides is the solvothermal decomposition of transition metal dithiocarbamates. These single source precursors are typically dissolved in a coordinating solvent and heated rapidly. In chapter 3, it was shown that the coordinating solvent coordinates to the transition metal centre of the zinc dimethyl, and nickel and iron diisobutyl dithiocarbamate case studies at room temperature prior to decomposition. In this chapter *in situ* XAS is used to show that the coordinating solvent subsequently has significant effect on the decomposition process through coordination to the transition metal centre and reaction with the dithiocarbamate backbone.

Chapter 4

***In situ* XAS of the solvothermal decomposition of transition metal dithiocarbamate complexes**

4.1 Introduction

In this chapter, solvothermal decomposition of the three transition metal (TM) dithiocarbamate complexes, examined in Chapter 3, are investigated. Each decomposition mechanism is understood by solving the structure of stable intermediates in the decomposition process using XANES and EXAFS. Full mechanistic pathways are suggested where a combination of techniques was possible. Particular attention is given to the role of the coordinating solvent in each decomposition mechanism, and the non-innocent nature of the solvent soon becomes apparent.

Monodisperse nanoparticles are routinely synthesised by the solvothermal decomposition of single source precursors (SSPs).¹ In a typical decomposition, a SSP is dissolved in a coordinating solvent at low concentrations, heated up to a specific temperature rapidly, and held for a number of hours. During the process decomposition occurs to form the relevant nanoparticulate species. Low concentration of SSP prevent aggregation and growth of resulting nanoparticles while the solvent acts as a heat sink for the reaction and capping agent for the final product. The popularity of the technique can be attributed to its cost effectiveness, ease of use, and versatility. Decompositions are performed using reflux apparatus, and oleylamine is often the solvent of choice on account of its high boiling point and capping ability.² Significant effort is directed to the design and synthesis of the SSP as this must decompose efficiently to the desired phase pure and monodisperse nanoparticulate materials, while maintaining stability prior to decomposition.

A widely used method for the formation of nanoparticulate sulfide materials is the solvothermal decomposition of transition metal (TM) dithiocarbamate complexes.³ The complexes act as SSPs due to pre-existing metal-sulfur bonds from the interaction with bidentate dithiocarbamate ligands. The solvothermal decomposition of cadmium dithiocarbamate complexes is extensively documented as a popular route to the formation of CdS semiconductors in various morphologies⁴⁻⁷ while in

the same field decomposition of zinc dithiocarbamate species allows the formation of nanoparticulate ZnS in both cubic zinc blend sphalerite and hexagonal wurtzite phases^{4,6,7}. The synthesis of MnS is reported from the decomposition of manganese diethyldithiocarbamate in an aqueous solution containing hydrazine⁸ and the synthesis of the important semiconductor PbS is shown by injecting lead dithiocarbamate SSPs into hot hexadecylamine, TOPO, oleylamine, and decylamine – each solvent displaying varied morphology of resulting particles.⁹ Synthesis of pyrrhotite and greigite phases of iron sulfide are also reported by decomposition of iron dithiocarbamates in oleylamine¹⁰, and the pure phase synthesis of pyrite is reported through the decomposition of iron diethyldithiocarbamate in water.¹¹

While the method is employed extensively to synthesize monodisperse sulfide nanoparticles, little is understood about solvothermal decomposition of TM dithiocarbamate complexes with regards to mechanism and the role of particular components in a typical reaction. Clearly, the role of the alkyl backbone, concentration, solvent, and temperature are deemed to be important by trial and error, but how and why these parameters impact a reaction can be investigated further. There are many questions that have not been conclusively answered. For example, given the wide range of metal centers, oxidation states, and coordination, is there a common pathway that results in decomposition of the complexes? In addition, some phases are repeatedly synthesized while others are highly elusive using this method, is this dictated by phase stability or are there underlying mechanistic factors? The role of the solvent must also be questioned– while changing the solvent can bring about dramatic differences in final product, the solvent is generally considered to be innocent in the decomposition process, acting only as a heat sink and capping agent.

Past literature has extensively described the interaction of coordinating ligands to metal dithiocarbamate complexes.^{12–18} Despite this, little consideration is given to the phenomena when using TM dithiocarbamates as SSPs. In the previous chapter, zinc bis- dimethyl, nickel bis-, and iron tris- diisobutyl dithiocarbamates were dissolved in oleylamine and non-coordinating solvents. The structure of each dissolved species was determined by XAS. Interactions between oleylamine and the TM center were observed in all cases. $\text{Zn}(\text{Me}_2\text{NCS}_2)_2$ was shown to become

monomeric in solution with one zinc-oleylamine interaction resulting in a distorted trigonal bipyramidal geometry. In the case of $\text{Ni}(\text{Bu}_2\text{NCS}_2)_2$, oleylamine was found to interact above and below the plane of the complex, and in $\text{Fe}(\text{Bu}_2\text{NCS}_2)_3$, bidentate ligands were shown to become monodentate with the lengthening of one iron-sulfur interaction on each ligand, and addition of two iron-oleylamine interactions. Far fewer changes were observed in the non-coordinating solvents, and dithiocarbamate complexes kept their overall structure.

The presence of oleylamine interactions prior to the decomposition process makes the possibility of its continued influence on the decomposition highly likely.

In this chapter the solvothermal decomposition of zinc bis- dimethyl, nickel bis-, and iron tris- diisobutyl dithiocarbamate complexes are investigated by heating each in oleylamine *in situ* on an EXAFS beamline. Of the three case studies, one (nickel) has been published¹⁹ and the others are in various stages of publication. The nickel dithiocarbamate decomposition is used to explain common mechanisms in the three decomposition groups.

4.2 Method

4.2.1 Sample Synthesis and Preparation

Details of the chemicals used and syntheses of most of the dithiocarbamate complexes are given in the previous chapter. Synthetic procedures for materials not mentioned in the previous chapter are given below.

4.2.1.1 Synthesis of $\text{Ni}(\text{Hex}(\text{H})\text{NCS}_2)_2$

CS_2 (1.80 mL, 30 mmol) was added dropwise to a solution of n-hexylamine (4 mL, 30 mmol) in MeOH (30 mL) and cooled in an ice bath to 3° C. A solution of NaOH (1.20 g, 30 mmol) in water (ca. 5 mL) was added dropwise to the solution and the reaction was stirred for 3 hrs. A solution of $\text{NiCl}_2 \cdot 6\text{H}_2\text{O}$ (3.56 g, 15 mmol) in water (20 mL) was then added dropwise over 2 minutes, producing a green precipitate. The mixture was stirred for 30 minutes, filtered, washed with water (3 x 30 mL) and evaporated to dryness. The green powder was then dissolved in dichloromethane (100 mL) and stirred with magnesium sulfate for 30 minutes, filtered, and dried *in vacuo*.

4.2.1.2 Synthesis of $S_2(iBu_2NCS)_2$

Reagent iBu_2NH (2.62 mL, 15 mmol) was added to NaOH (0.60 g, 15 mmol) in water (50 mL). CS_2 (0.90 mL, 15 mmol) was added to the mixture dropwise, and the mixture stirred overnight. An solution of $K_3[Fe(CN)_6]$ (4.94 g, 15 mmol) in water (20 mL) was added dropwise to the mixture and stirred vigorously for 2 hrs. The solution was filtered, washed with water (1 x 20 mL) and dried *in vacuo*. The resulting solid was crushed, washed with water (3 x 30 mL) and dried *in vacuo* to produce a white powder.

4.2.1.3 Laboratory synthesis of NiS/Ni_3S_4

$Ni(iBu_2NCS_2)_2$ (0.1 mmol, 0.0467 g) was heated in oleylamine (20 mL) for 1 hr under reflux at 150° C. This produced a black precipitate dispersed into the solvent. The mixture was allowed to cool over 1 hr, then washed and centrifuged with MeOH (3 x 60 mL). The resulting black powder was dispersed into $CHCl_3$ (100 mL), then filtered and dried *in vacuo*.

4.2.2 Measurements

XAS measurements were acquired at the zinc K-edge (9659 eV), nickel K-edge (8333 eV), and iron K-edge (7112 eV). Scans lasting 12-15 minutes were acquired sequentially during each reaction process and temperature was recorded at the start of each measurement. Where applicable, the reaction was repeated to acquire higher k range EXAFS up to 14 \AA^{-1} at temperatures of interest. Reactions and experimental conditions are tabulated below. Owing to noise above 11 \AA^{-1} , data was typically analysed up to 14 \AA^{-1} .

Table 4.1: *In situ* experiments carried out on the zinc, nickel, and iron K-edges.

Zinc K-edge				
Description	Precursor	Solvent	Temperature Profile	k-Range
Decomposition of 14	Zn(Me ₂ NCS ₂) ₂ (5mM)	Oleylamine	Room temperature to 94° C at 1° C/min	9 Å ⁻¹
Nickel K-edge				
Description	Precursor	Solvent	Temperature Profile	k-Range
Decomposition of 3	Ni ⁱ (Bu ₂ NCS ₂) ₂ (5mM)	Oleylamine	Room temperature to 150° C at 1° C/min	10 Å ⁻¹ Repeat to 14 Å ⁻¹ at 26, 118, 123, and 150° C
Decomposition of 2	Ni ⁱ (Bu ₂ NCS ₂) ₂ (5mM)	Dodecane	Room temperature to 150° C at 1° C/min	11 Å ⁻¹
Decomposition of 5	Ni(Hex(H)NCS ₂) ₂ (5mM)	Dodecane	Room temperature to 150° C at 1° C/min	11 Å ⁻¹
Decomposition of 3 (rapid)	Ni ⁱ (Bu ₂ NCS ₂) ₂ (5mM)	Oleylamine	Rapid ramp between room temperature and 150° C, hold at 150° C, and cool naturally	11 Å ⁻¹
Iron K-edge				
Description	Precursor	Solvent	Temperature Profile	k-Range
Decomposition of 8	Fe ⁱ (Bu ₂ NCS ₂) ₃ (5mM)	Dodecane	Room temperature to 170° C at 1° C/min	10 Å ⁻¹
Decomposition of 9	Fe ⁱ (Bu ₂ NCS ₂) ₃ (5mM)	Oleylamine	Room temperature to 190° C at 1° C/min	10 Å ⁻¹ Repeat to 14 Å ⁻¹ at 26, 59, 67, and 125° C
Decomposition of 10	Fe ⁱ (Bu ₂ NCS ₂) ₃ (5mM) and S ₂ ⁱ (Bu ₂ NCS) ₂ (20mM)	Oleylamine	Room temperature to 140° C at 1° C/min	10 Å ⁻¹
Decomposition of 11	Fe ⁱ (Bu ₂ NCS ₂) ₃ (20mM)	Oleylamine	Room temperature to 140° C at 1° C/min	10 Å ⁻¹

4.2.3 Cell

The *in situ* cell used for measurements was developed at UCL for synchrotron based experiments on liquid samples (Figure 4.1). The reaction chamber at the center of the cell can hold 400 µL of solution with a variable path length between 2 and 4 mm; measurements acquired for the following experiments were performed with a 4 mm path length. The reaction mixture was sealed between two 127 µm Kapton windows and the cell was placed at a 20° angle at the sample stage thus permitting both transmission and fluorescence measurements and minimizing beam clipping at the cell edges (Figure 4.2). For *in situ* measurements, the cell was connected to a temperature controller that was programmed accordingly for each reaction. A calibration of the temperature inside the reaction chamber was performed prior to on-

line measurements to account for heat loss between heating elements embedded in the solid brass casing, and the central reaction chamber.

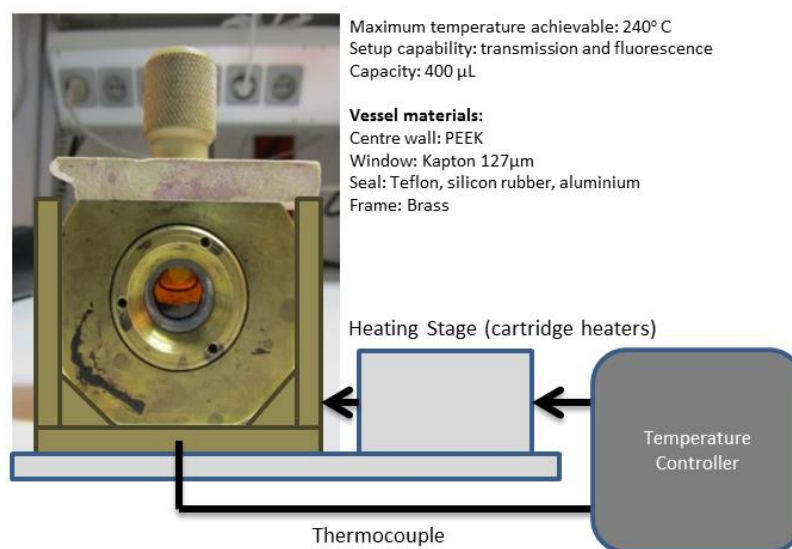


Figure 4.1: Illustration and specifications of the reaction cell used for solvothermal decomposition reactions. The brass cell is connected to a temperature controller that regulates temperature at the base of the cell. The reaction centre and seal is built with several high boiling point materials for stability during reactions.

4.2.4 Beamline

XAS data was acquired on the Dutch-Belgian EXAFS beamline, BM26A. Monochromatic radiation was supplied by a double Si(111) crystal. All *in situ* measurements were acquired in fluorescence using the 9 element germanium solid state detector, although transmission data was also collected but not used from ion chambers before and after the *in situ* sample cell.

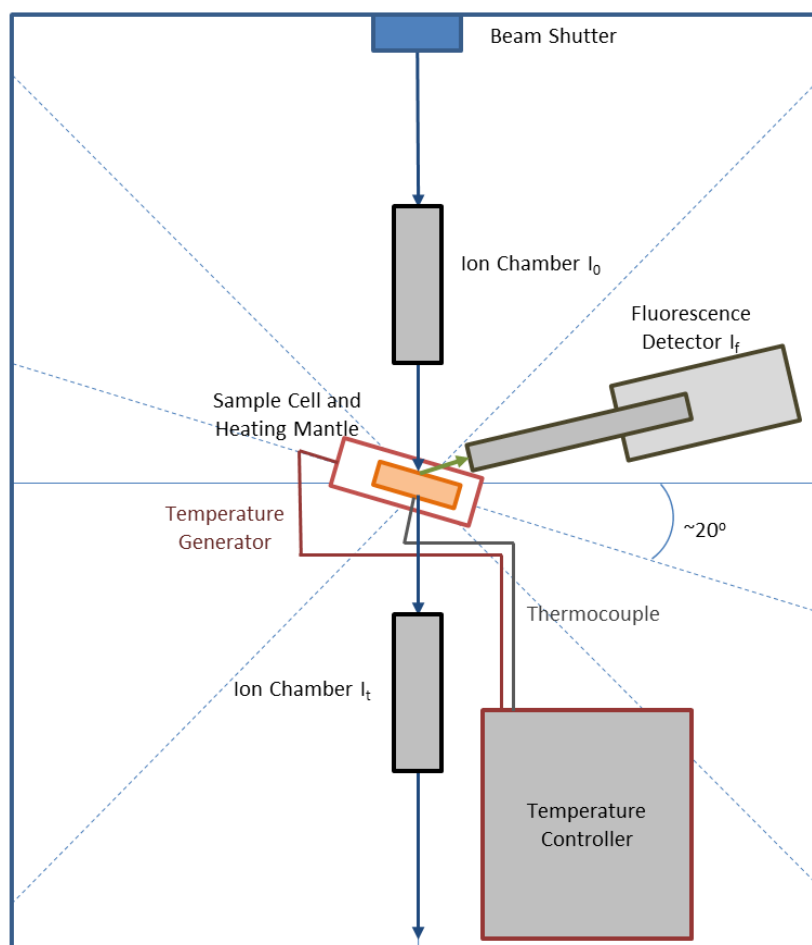


Figure 4.2: Set up of experimental hutch at the Dutch-Belgian EXAFS beamline. The beamline is equipped with both ion chambers (I_0 and I_t) and fluorescence detector for transmission and fluorescence measurements. The reaction cell is held at a 20° angle from the perpendicular line to the beam.

4.2.5 Processing

XAS data was normalized and background subtracted using Horae Athena software.²⁰ Detailed EXAFS analyses were performed on Excurve Version 9.273.²¹ Amplitude factors values for each edge were derived from reference foil data except for the zinc K-edge where zinc oxide was used.

4.3 Results and Analysis

4.3.1 Zinc Dithiocarbamate Decomposition

The solvothermal decomposition of zinc dithiocarbamates result in the formation of zinc sulfide (wurtzite) nanotubes according to literature.²² The distinctive geometry of the resulting particles suggests a highly directional particle growth mechanism. The *in situ* decomposition of **14** also results in the formation of wurtzite nanoparticles according to XRD (Figure 4.3); one sharp peak is assigned to the (002) orientation and indicative of crystallinity along this direction; other peaks are smaller and broader possibly indicating smaller crystallite size or more amorphousness in these orientations.^{23,24} TEM of these particles reveals wire or tube formation (Figure 4.4).

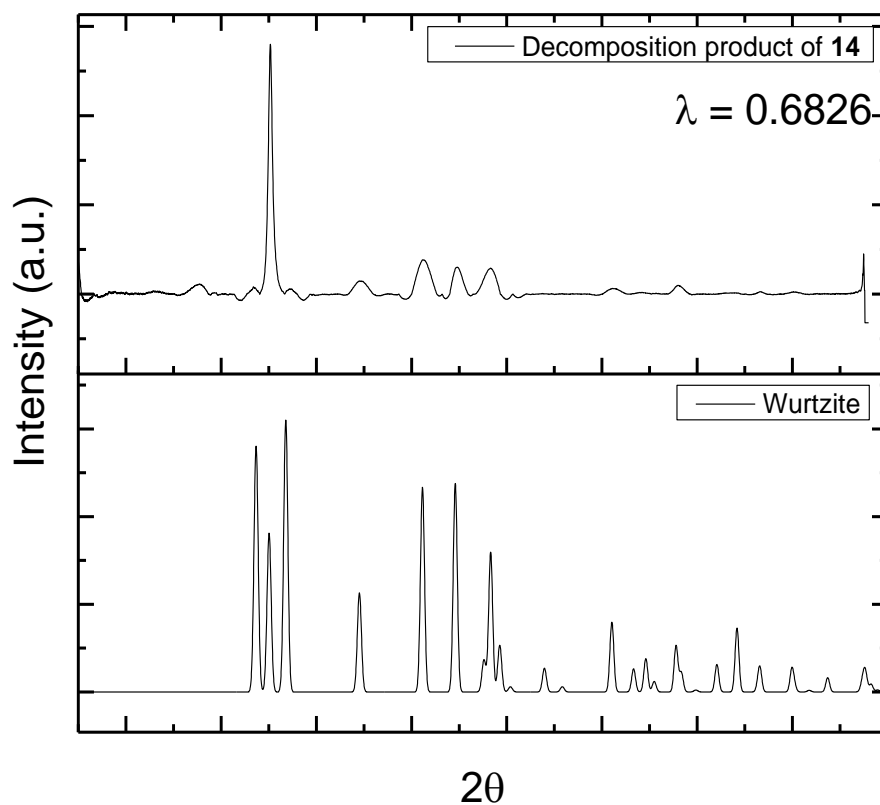


Figure 4.3: XRD of the solvothermal decomposition of **14** in oleylamine reveals a good match to the literature structure of wurtzite. The model wurtzite XRD was produced from CrystalDiffract from the CrystalMaker® software Ltd using a wurtzite crystal file available with the software. XRD of the decomposition product of **14** was acquired at the Swiss-Norwegian beamline, station A.²⁵

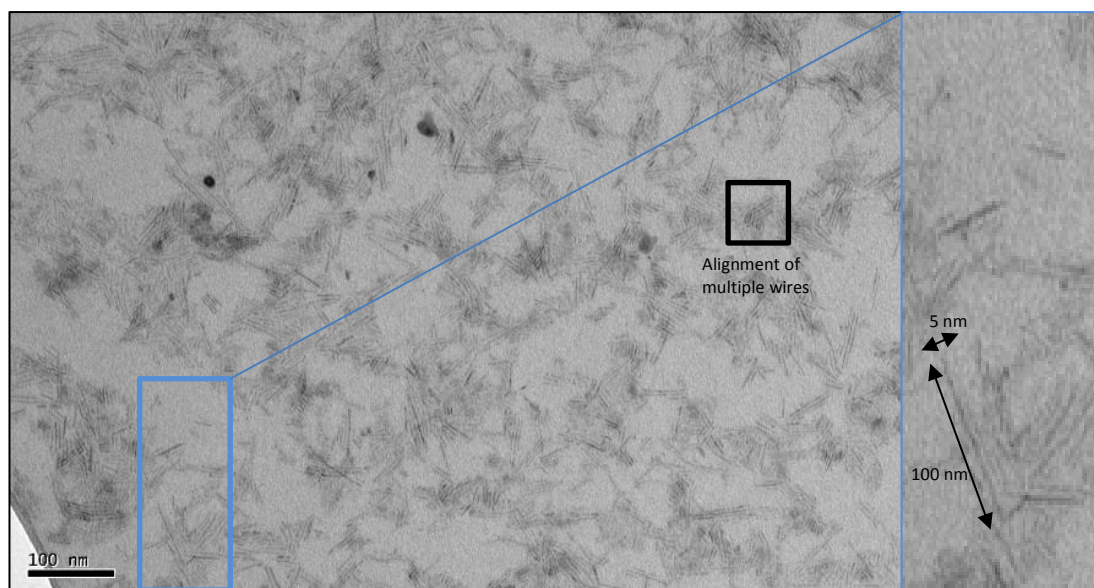


Figure 4.4: TEM of the final ZnS nanoparticles formed during the *in situ* experiment of the decomposition of **14** in oleylamine. Particles are shaped nanowires. The nanowires align in rows owing to secondary interactions.

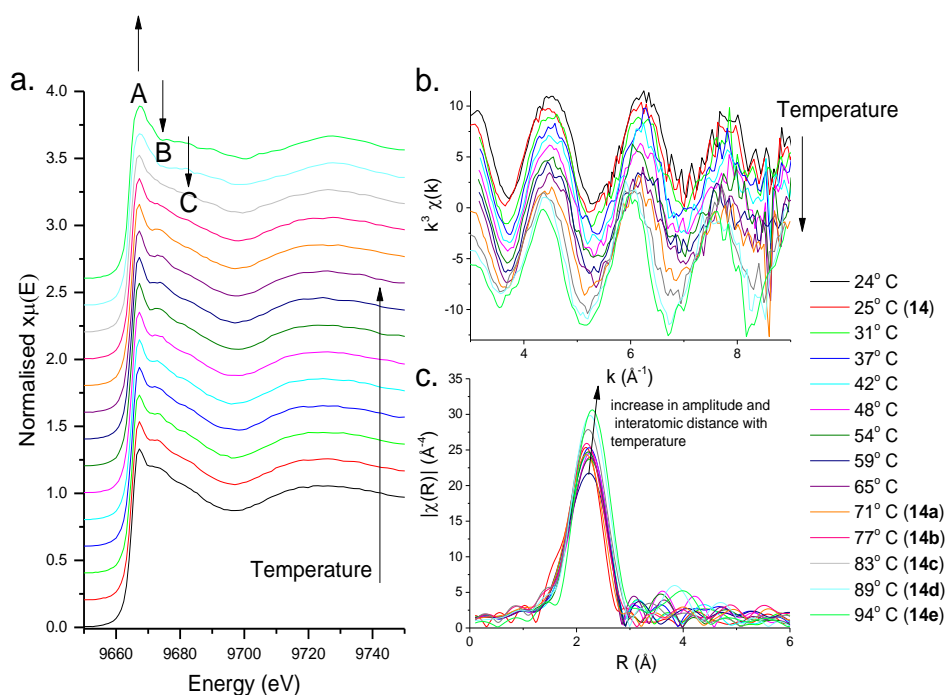


Figure 4.5: *In situ* a. XANES spectra, b. EXAFS and c. FT of the solvothermal decomposition of $\text{Zn}(\text{Me}_2\text{NCS}_2)_2$ in oleylamine (**14**) up to 94°C at a ramp rate of 1°C/min.

XANES of the decomposition process of **14** is given in Figure 4.5. This shows that the structure in oleylamine is stable up to 71°C. Above this temperature, the peak previously labelled **B** decrease significantly, along with a slight reduction in **C**. The

edge position remains remarkably constant as a result of stable oxidation state, while slight drop in white line intensity indicates a decrease in overall coordination.

EXAFS and FT suggest changes as well. In the previous chapter, oleylamine bound zinc dimethyl dithiocarbamate (**14**) was fitted to 1 Zn-N distance at 2.06 Å, and 4 Zn-S distances at 2.28 Å, with a high level of disorder possibly as a result of the dynamic behaviour of the five coordinated zinc complex in solution. At 71° C (**14a**), the structure fits to a lower coordination number of bound oleylamine with 0.8 Zn-N distances at 2.06 Å, in addition 4 Zn-S interatomic distances are shown at 2.29 Å and disorder is slightly reduced. By 83° C (**14c**), there are 0.6 Zn-N interatomic distances at 2.06 Å, and 4 Zn-S interatomic distances at 2.32 Å with again a lower disorder. Between **14a** and **14c**, at 77° C (**14b**), zinc-oleylamine coordination is 0.7 Zn-N at 2.06 Å, and 4 Zn-S interatomic distances are present at 2.30 Å with disorder lower than that of **14a** and higher than that of **14c**, suggesting that a gradual change occurs between 71 and 83° C. Clearly, the fraction of the five coordinated species decreases and is replaced by the tetrahedral dithiocarbamate complex with increasing temperature. This indicates the presence of an equilibrium that favours the four coordinated form with increasing temperature (Figure 4.6). At 89° C (**14d**), the 4 Zn-S distances remain at 2.32 Å and zinc-oleylamine interactions are no longer detected. A further lengthening of the 4 Zn-S interatomic distances to 2.33 Å occurs at 94° C (**14e**). EXAFS data analyses are shown in Table 4.2 and Figure 4.5. The Zn-S interatomic distance of 2.33 Å (with an error of ± 0.03 Å) is similar to the 4 Zn-S distances found in both wurtzite²⁶ and sphalerite²⁷ at 2.3415(5) Å and 2.3445(4) Å respectively according to XRD. The synthesis of the wurtzite phase is confirmed by XRD, and wire or tube morphology is confirmed by TEM (Figure 4.3-4).

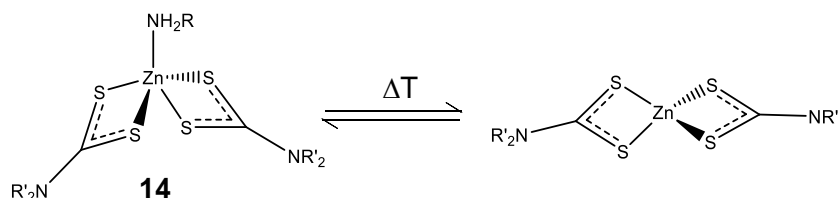
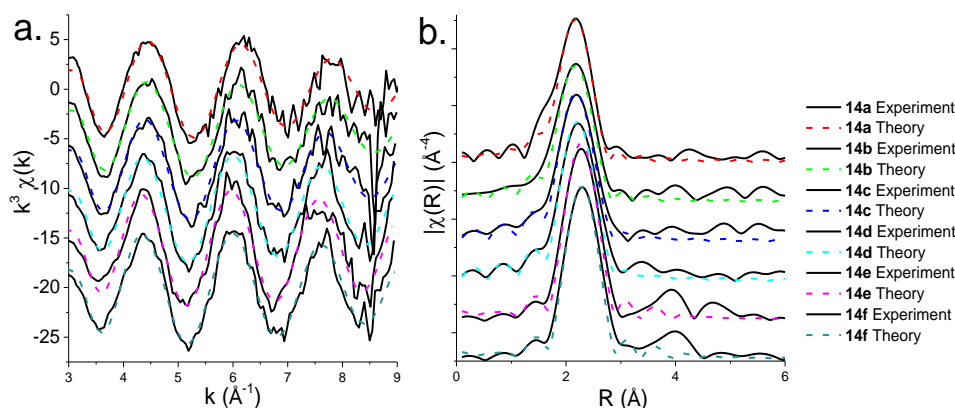


Figure 4.6: Equilibrium demonstrating the dissociation of oleylamine from the zinc centre as a function of increasing temperature.

Table 4.2: Results of EXAFS fitting for the *in situ* decomposition of 14. Unrefined coordination numbers and bond distances are indicated by *.

Decomposition of 14 : Zn(Me ₂ NCS ₂) ₂ in oleylamine						
Sample	Scatter	<i>N</i>	<i>R</i> _{EXAFS} (Å)	2σ ² (Å ²)	Reduced <i>chi</i> ²	<i>R</i> -factor
Zn(Me ₂ NCS ₂) ₂ in oleylamine at 71° C (14a)	N	0.8	2.06 ± 0.02	0.019 ± 0.002	7 x 10 ⁻⁷	27
	S	4*	2.29 ± 0.03	0.019 ± 0.002		
Zn(Me ₂ NCS ₂) ₂ in oleylamine at 77° C (14b)	N	0.7	2.06 ± 0.02*	0.016 ± 0.002	6 x 10 ⁻⁷	27
	S	4*	2.30 ± 0.03	0.016 ± 0.002		
Zn(Me ₂ NCS ₂) ₂ in oleylamine at 83° C (14c)	N	0.6	2.06 ± 0.02*	0.013 ± 0.002	5 x 10 ⁻⁷	23
	S	4*	2.32 ± 0.03	0.013 ± 0.002		
Zn(Me ₂ NCS ₂) ₂ in oleylamine at 89° C (14d)	S	4*	2.32 ± 0.03	0.009 ± 0.002	6 x 10 ⁻⁷	28
Zn(Me ₂ NCS ₂) ₂ in oleylamine at 94° C (14e)	S	4*	2.33 ± 0.03	0.009 ± 0.002	6 x 10 ⁻⁷	26

**Figure 4.7: a. EXAFS and b. FT fits for the solvothermal decomposition of Zn(Me₂NCS₂)₂ in oleylamine (14) at 25° C (14a), 71° C (14b), 77° C (14c), 83° C (14d), 89° C (14e), and 94° C (14f).**

The decomposition takes place in two steps. Firstly, the oleylamine that forms interactions with the zinc dithiocarbamate dissociates with increasing temperature. Next decomposition into a sulfide occurs suddenly. This is consistent with amide-exchange which is described in section 4.3.2.3 for nickel dithiocarbamate decomposition.^{19,28} Several points can be made about the structure of the dithiocarbamate complex during the decomposition process. Firstly, the five coordinated structure is highly fluxional. This is most likely as a result of the disorder caused by the high rate of rearrangement that the complex undergoes between stable geometries. With increasing temperature, disorder is shown to decrease. This is not intuitive. The most likely reason for this is the decrease in five coordinated species as more oleylamine becomes unbound, resulting in the ordered four coordinated monomeric zinc dithiocarbamate structure. The decrease in static disorder caused by the five coordinated structure has a greater effect than the increase

in thermal disorder caused by increase in temperature. The sulfide is formed at 89° C; spectra of **14c** and **14d** are similar, and distinctive from the zinc dithiocarbamate XANES.

4.3.2 Nickel Dithiocarbamate Decomposition

The nickel dithiocarbamate decomposition process was studied in great detail by the group.¹⁹ This is because nickel is well-behaved: while XANES of the zinc model is subtle and the iron model is complicated by redox properties and spin states, the nickel system provides informative spectra; each geometry that it adopts is distinct owing partly to the interaction of ligands with unfilled orbitals and predictable redox properties. The system can also be analysed by other methods including UV-vis, and DFT. The first part of this section takes into account the changes in local structure according to XANES and EXAFS. Where XANES and EXAFS have been insufficient to understand changes, a wide range of alternative techniques have been used in an attempt to fully understand the decomposition mechanism in its entirety, described in the second part of this section. In addition, the structure of the final product is understood in greater detail – with an initial hypothesis that the cooling process may contribute to the phase of the final product as well as decomposition temperature.

4.3.2.1 Decomposition of $\text{Ni}(\text{iBu}_2\text{NCS}_2)_2$ in oleylamine

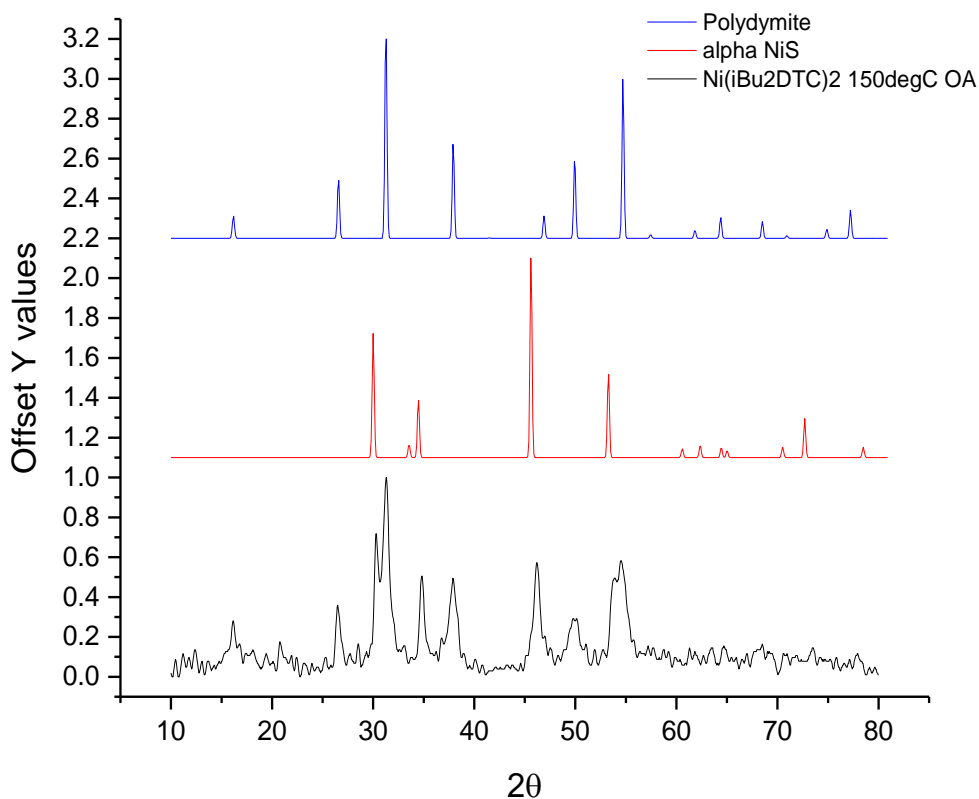


Figure 4.8: XRD of the reaction product of the decomposition of $\text{Ni}(\text{iBu}_2\text{NCS}_2)_2$ in oleylamine (3) up to 150° C in laboratory reaction conditions, plotted with polydymite and alpha-NiS for comparison.

The solvothermal decomposition of $\text{Ni}(\text{iBu}_2\text{NCS}_2)_2$ in oleylamine results in the formation of a mixture of hexagonal nickel sulfide (NiS) and polydymite (Ni_3S_4) according to XRD (Figure 4.8).

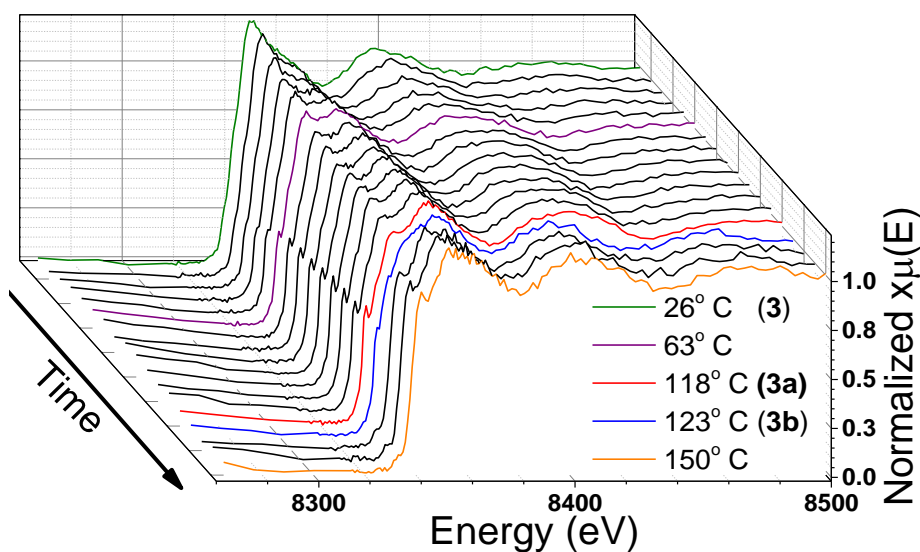


Figure 4.9: *In situ* XANES spectra of the solvothermal decomposition of $\text{Ni}(\text{Bu}_2\text{NCS}_2)_2$ in oleylamine (**3**) up to 150°C at a ramp rate of $1^\circ\text{C}/\text{min}$.

In situ XANES of the solvothermal decomposition of $\text{Ni}(\text{Bu}_2\text{NCS}_2)_2$ in oleylamine is shown in Figure 4.9. The decomposition occurs in a two-step process: first, spectra transform gradually between room temperature (green) and 118°C (red). The high white line intensity, previously labelled **B** on the spectrum of **3** in section 3.3.2, and associated with a fully coordinated nickel centre, decreases from the onset until it reaches a minimum at 118°C . Conversely, the sharp spectral feature **A** - identified on square planar systems **1** and **2** - emerges gradually, first appearing at 63°C (purple) and then becoming fully distinguishable by 118°C . The spectrum at 118°C bares significant resemblance to the structure of **1** and **2** the solid dithiocarbamate complex, and the complex dissolved in dodecane. This suggests that the square planar form is dominant at this temperature. By 123°C (blue), spectra undergo an abrupt change that remains constant up to 150°C (orange).

Table 4.3: Results of EXAFS fitting for the *in situ* decomposition of 3. Unrefined coordination numbers are indicated by *.

Decomposition of 3: Ni(ⁱ Bu ₂ NCS ₂) ₂ in oleylamine								
Sample	Scatter	<i>N</i>	<i>R</i> _{XRD} (Å)	<i>R</i> _{EXAFS} (Å)	σ ² (Å ²)	Reduced <i>chi</i> ²	<i>R</i> -factor	
Ni(ⁱ Bu ₂ NCS ₂) ₂ in oleylamine at 118° C (3a)	S	4*	-	2.20 ± 0.01	0.006 ± 0.001	1 × 10 ⁻⁶	26	
	C	2*	-	2.68 ± 0.01	0.006 ± 0.001			
Decomposed Ni(ⁱ Bu ₂ NCS ₂) ₂ in oleylamine at 123° C (3b) -Modelled to 0.30:0.70 Ni ₃ S ₄ :hexagonal NiS-	S	0.9*	2.15	2.18 ± 0.04	0.017 ± 0.003	6 × 10 ⁻⁵	40	
	S	4.6*	2.32-2.39	2.30 ± 0.02	0.017 ± 0.003			
	Ni	0.6	2.67	2.69 ± 0.02	0.010 ± 0.001			

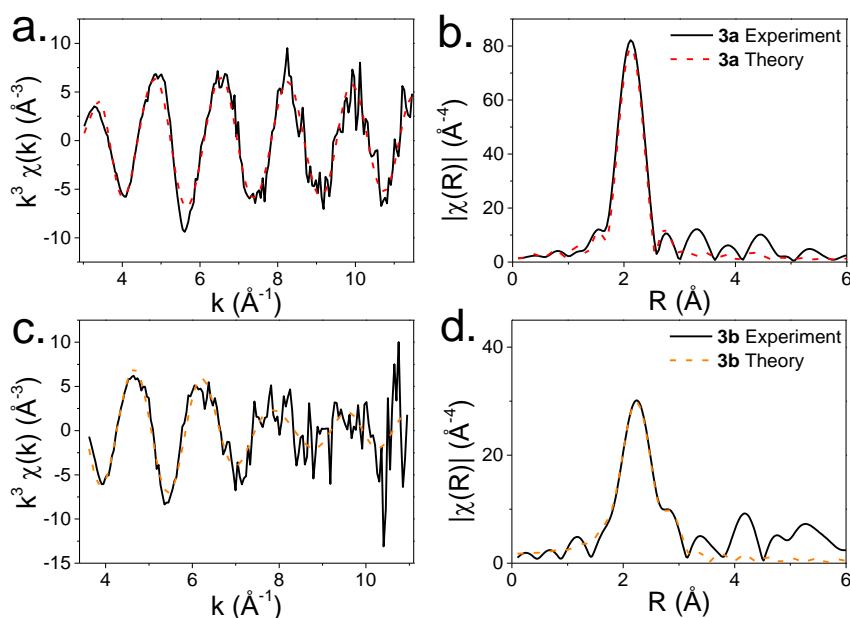


Figure 4.10: a. EXAFS and b. FT of Ni(ⁱBu₂NCS₂)₂ in oleylamine at 118° C (3a**), and c. EXAFS and d. FT of Ni(ⁱBu₂NCS₂)₂ in oleylamine after decomposition at 150° C (**3b**).**

According to EXAFS performed in the previous chapter, the reaction mixture at the start of the decomposition in oleylamine (**3**) consists of a solution containing Ni(ⁱBu₂NCS₂)₂(C₁₈H₃₅NH₂)₂: the nickel dithiocarbamate is modified by additional bonding between nickel and 2 oleylamine. The structure at 118° C (**3a**) on the other hand, can be modelled to the original square planar complex showing 4 Ni-S bonds at 2.20 Å and 2 Ni-C distances at 2.68 Å, identical to the structure of **1** and **2** (Table 4.3, Figure 4.10a-b).

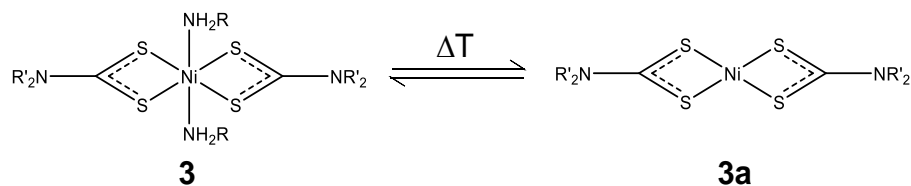


Figure 4.11: Equilibrium demonstrating the dissociation of oleylamine from the nickel centre as a function of increasing temperature.

Between 26° C and 118° C, spectra consist of a combination of both oleylamine bound (octahedral) and square planar structures at varied ratios. This is confirmed by linear combination fitting (LCF) using **3** and **2** as model compounds for the octahedral and square planar geometries respectively. The results shown in Figure 4.12 indicate a gradual emergence of square planar and decline of octahedral species. Up to 85° C the process is constant. Between 85 and 105° C, the ratios of species remain stable, before another short surge in the amount of square planar species up to 118° C. Results indicate that the oleylamine bound octahedral and unbound square planar forms exist in an equilibrium which favours square planar with increasing temperature (Figure 4.11). The short period that the square planar species exists before an abrupt transformation at 123° C suggests that this form is unstable at temperatures higher than 118° C. Example LCF analyses are provided in Figure A1.1, Appendix 1.

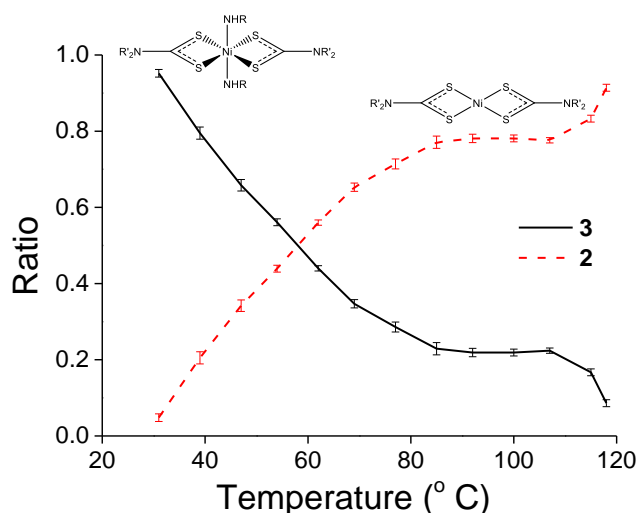


Figure 4.12: Linear combination fitting of *in situ* XANES spectra of **3 between 26 and 118° C demonstrating that the fully coordinated structure of **3** at room temperature becomes more like the square planar structure of **2** with increasing temperature.**

By 123° C (**3b**), the dithiocarbamate complex has decomposed. The XRD of this structure synthesised in the laboratory in oleylamine showed a mixture of polydymite (Ni₃S₄) and hexagonal nickel sulfide (NiS) (Figure 4.8). Modelling EXAFS at 123° C also suggests the presence of these two sulfide phases, polydymite and hexagonal NiS, at a ratio of 0.7:0.4. Polydymite is an inverse spinel structure containing both tetrahedral (t) and octahedral (o) sites at a ratio of 1:2 and interatomic distances of 2.1507(1) Å and 2.3142(1) Å respectively.²⁹ Hexagonal NiS contains 6 Ni-S interatomic distances at 2.3929 (3) Å and 2 distinctly short Ni-Ni distances at 2.6710(3) Å.³⁰ For the EXAFS model, the Ni-S interatomic distances of polydymite (2.32 Å) and hexagonal NiS (2.39 Å) were grouped. The first shell EXAFS at 123° C can be modelled to 0.9 Ni_(t)-S distances at 2.18 Å, 4.6 Ni-S distances at 2.30 Å, and 0.6 Ni-Ni distances at 2.69 Å (Table 4.3, Figure 4.10c-d). To obtain these results, coordination number of the short Ni-Ni distance was optimised as a variable parameter while the remaining coordination numbers were fixed according to this variable. Bond distance and disorder optimization was also performed. The process was repeated several times in order to obtain a best fit.

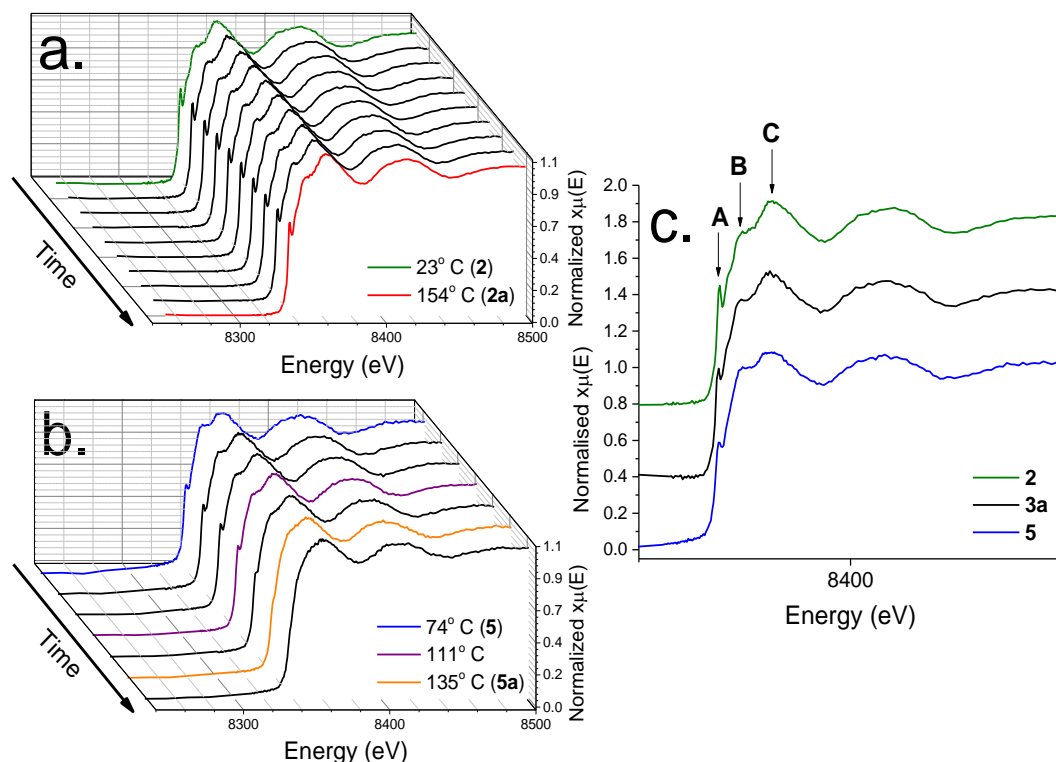
4.3.2.2 Decomposition of $\text{Ni}(\text{iBu}_2\text{NCS}_2)_2$ and $\text{Ni}(\text{Hex}(\text{H})\text{NCS}_2)_2$ in dodecane

Figure 4.13: a. *In situ* XANES spectra of the solvothermal decomposition of $\text{Ni}(\text{iBu}_2\text{NCS}_2)_2$ in dodecane (**2**) up to 154° C at a ramp rate of 1° C/min, b. *in situ* XANES spectra of the solvothermal decomposition of $\text{Ni}(\text{Hex}(\text{H})\text{NCS}_2)_2$ in dodecane (**5**) up to 135° C at a ramp rate of 1° C/min, and c. comparison of spectra of **2** and **5** against spectra of **3a**.

In contrast to the decomposition in oleylamine, the square planar $\text{Ni}(\text{iBu}_2\text{NCS}_2)_2$ remains intact during the solvothermal treatment in dodecane and the decomposition does not occur. *In situ* XANES of the heating of $\text{Ni}(\text{iBu}_2\text{NCS}_2)_2$ in dodecane (Figure 4.13a) shows that the spectrum of **2a** at 154° C is identical to **2** at room temperature.

Referring back to the decomposition in oleylamine, **3a** also adopts a square planar local structure identical to **2** and **2a** according to EXAFS. The difference between **2a** and **3a** however is that **2a** remains stable above 123° C while **3a** is decomposed soon after its formation, at 123° C. Further to this, heating in tertiary amine trihexylamine and secondary amine dihexylamine shows no evidence of decomposition.¹⁹ Only heating in primary amine results in the successful decomposition of the complex but first shell EXAFS analysis falls short of explaining how this occurs. A hypothesis that satisfies this finding is termed transamination and refers to amide-exchange whereby the carbon backbone of the dithiocarbamate ligand is exchanged with the

solvent amine. The formation of a secondary amine on one or both of the dithiocarbamate ligands results in the destabilization of the square planar species at elevated temperatures thus causing decomposition (Figure 4.14).¹⁹ While amide exchange with secondary amines are reported³¹, and observed in these investigations through ¹³C NMR of exchange between dihexylamine and Ni(¹Bu₂NCS₂)₂, transamination with primary amines is more difficult to isolate and characterise.

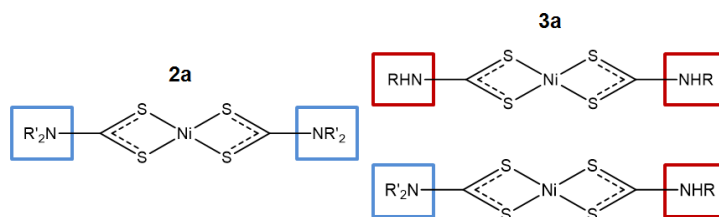


Figure 4.14: Predicted structures of 2a and 3a. While 2a contains tertiary amine R groups, 3a is likely to fully or partly contain secondary amine R groups which result in the destabilisation of the complex.

The theory is tested by decomposing a nickel dithiocarbamate complex Ni(Hex(H)NCS₂)₂ (**5**) in a non-coordinating solvent. The structure of **5** is analogous to the predicted structure of **3a** and consists of a secondary amine backbone with hexylamine R groups attached to the end of each dithiocarbamate ligand. *In situ* XANES of its decomposition in dodecane reveals stability of the structure up to 111° C. Decomposition of the complex occurs between 123 and 135° C (Figure 4.13b). The experiment is designed to bypass the transamination step, and the positive result in the non-coordinating solvent provides strong evidence that the secondary amine backbone is vital for the decomposition process. The decomposition of **5** was also carried out in a solventless environment and was shown to form sulfide according to TGA; on the other hand, heating **3** in the solid state resulted in sublimation of the complex rather than sulfide formation. DFT calculations were performed with the B3PW91 hybrid functional³² with a Pople basis set 6-31G(d,p),³³ and the PCM model³⁴ using the Gaussian 09 Rev C suite of programs³⁵, and summarised by Hollingsworth *et al.*¹⁹ DFT of the amide-exchange of Ni(Ethyl₂NCS₂)₂ (**16**) with ethylamine suggests that the process occurs in two equally energetically demanding steps. As a result, the amide-exchange is likely to result in both Ni(Ethyl₂NCS₂)(Ethyl(H)NCS₂) (**16e**) and Ni(Ethyl(H)NCS₂)₂ (**16f**) species.

On closer inspection of the XANES of the square planar structures of **2**, **3a**, and **5** (Figure 4.13c), the largely similar features reveal slight variation: feature **A** is sharper and more prominent in **2** than **3a** and **5**, feature **B** is higher in **5** than **3a** and **2**. The weakening of feature **A**, coupled with the increase in **B** suggest that **3a** and **5** are not purely square planar and contain some octahedral species. For **3a**, this is established by linear combination fitting (Figure 4.12) in which the percentage of square planar complex does not reach 100 before the decomposition of the complex. The synthesis process of **5** could explain the presence of octahedral impurities; the hexylamine used for the synthesis can possibly interact with the metal centre.

4.3.2.3 Decomposition Mechanism of Nickel Dithiocarbamates

The final decomposition process of the dithiocarbamate complex was investigated by DFT using functionals and basis sets described above (section 4.3.2.2), and following the intrinsic reaction coordinate (IRC) for the transition states to confirm connection between reactant and product. Figure 4.15 illustrates the process starting with the mixed Ni(Ethyl₂NCS₂)(Ethyl(H)NCS₂) **16e**. Decomposition is initiated *via* a transition state where the proton of the secondary amide binds to a sulfur on the dithiocarbamate backbone resulting in a dithiocarbamate isomer (**16g**). Ethylisothiocyanate is then lost and results in the formation of Ni(Ethyl₂NCS₂)SH (**16h**) which dimerizes in a highly exothermic reaction (**16i**). In the decomposition of the doubly amide-exchanged **16f**, the resultant dimer has the form of **16k** which has unstable dithiocarbamate ligands. This dimer can undergo further loss of isothiocyanate to form further “sticky” -SH ends (Figure 4.16). In slight contrast, the dimer of the singly amide-exchanged species **16i** consists of stable dithiocarbamate ligands that can only be eliminated by substitution with the solvent, which is in excess.

Evidence for the two routes is found experimentally by ¹³C NMR and mass spectrometry (MS). The organic bi-product hexylisothiocyanate is detected by ¹³C NMR and MS during the decomposition of Ni(Hex(H)NCS₂)₂ in dodecane. The decomposition of Ni(ⁱBu₂NCS₂)₂ in hexylamine also yields n-hexylthiourea according to UV-Vis, NMR, and MS as well as n-hexylisothiocyanate. The reaction of the latter with the solvent hexylamine can explain the presence of the

alkylthiourea. When $\text{Ni}(\text{Bu}_2\text{NCS}_2)_2$ is decomposed in oleylamine, both oleylamine-thiorurea and thiuram monosulfide are observed by MS suggesting again, a slightly changed reaction process.¹⁹ The origin of this is justified by the slower rate of amide-exchange of the longer chain amine which can drive the reaction through Route 1; isobutyl thiuram monosulfide is formed by the reaction of two $[\text{Bu}_2\text{NCS}_2]^-$, the bi-product going from **16i** to **16j**.

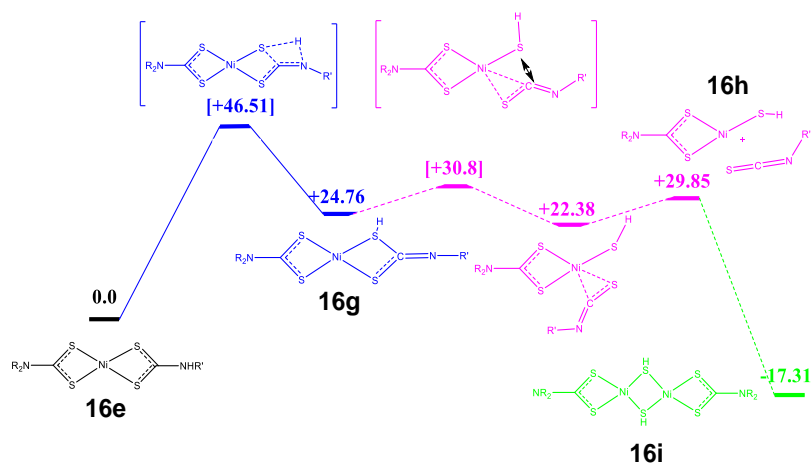


Figure 4.15: DFT modelling of the decomposition of $\text{Ni}(\text{Ethyl}_2\text{NCS}_2)(\text{Ethyl}(\text{H})\text{NCS}_2)$ (**16e**) via the loss of ethylisothiocyanate.

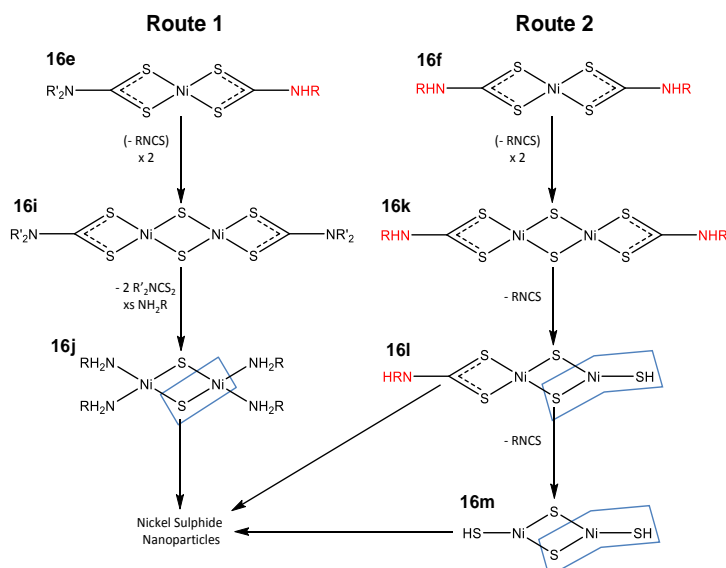


Figure 4.16: Reaction products of the side product alkylisothiocyanate which are detected by ^{13}C NMR and MS. R = hexyl/oleyl, R' = isobutyl.

In summary, the solvothermal decomposition can be defined in three stages. For decomposition to occur, it is vital that a secondary amide is present on the backbone of the dithiocarbamate ligands. If this is not the case, decomposition must occur in a primary amine. The amine involved in the decomposition readily coordinates to the nickel centre above and below the plane of the complex. Dissociation of the axial amine ligands occurs with increasing temperature. A separate process, and one which is vital for the decomposition, sees the primary amine replace the amide backbone, thus resulting in a secondary amide. The hydrogen incorporated into the backbone initiates the decomposition by reacting with a dithiocarbamate sulfur which results first in a dithiocarbamate, and then $(R'_2NCS_2)NiSH$ or $(R(H)NCS_2)NiSH$ intermediates that dimerize. After dimerization, growth is facile.

Comparisons can be drawn between this reaction and the one of zinc dimethyl dithiocarbamate. Oleylamine interaction with the zinc centre was also noted at room temperature and shown to dissociate as a function of increasing temperature. The decomposition process to zinc sulfide is rapid. Both observations are similar to the nickel. The decomposition mechanism of nickel dithiocarbamate may not be specific to just this case study. The amide-exchange of the dithiocarbamate backbone is likely to be a universal requirement and applicable to the zinc dithiocarbamate study. Indeed a similar pathway was predicted by others for zinc dithiocarbamate.²⁸

4.3.2.4 Decomposition of Ni(ⁱBu₂NCS₂)₂ in oleylamine - after decomposition**Table 4.4: Results of EXAFS fitting for the *in situ* decomposition of 3 (rapid ramp, hold and cool). Unrefined coordination numbers are indicated by *.**

Decomposition of 3: Ni(ⁱ Bu ₂ NCS ₂) ₂ in oleylamine - rapid ramp and cool							
Sample	Scatter	<i>N</i>	<i>R</i> _{XRD} (Å)	<i>R</i> _{EXAFS} (Å)	σ^2 (Å ²)	Reduced <i>chi</i> ²	<i>R</i> -factor
Decomposed Ni(ⁱ Bu ₂ NCS ₂) ₂ in oleylamine at 150° C (3c) (held for 1hr)							
	S	0.7*	2.15	2.13 ± 0.05	0.017 ± 0.002	2 x 10 ⁻⁶	29
	S	4.9*	2.32-2.39	2.31 ± 0.01	0.017 ± 0.002		
-Modelled to	Ni	0.9	2.67	2.67 ± 0.02	0.010 ± 0.002		
0.55:0.45 Ni ₃ S ₄ :hexagonal NiS-							
Decomposed Ni(ⁱ Bu ₂ NCS ₂) ₂ in oleylamine at 60° C (3d) (during cooling)							
	S	0.7*	2.15	2.15 ± 0.04	0.014± 0.002	3 x 10 ⁻⁶	29
	S	5.0*	2.32-2.39	2.31 ± 0.01	0.014± 0.002		
-Modelled to	Ni	1	2.67	2.67 ± 0.02	0.010± 0.002		
0.50:0.50 Ni ₃ S ₄ :hexagonal NiS-							
Decomposed Ni(ⁱ Bu ₂ NCS ₂) ₂ in oleylamine at 40° C (3e) (during cooling)							
	S	0.6*	2.15	2.15 ± 0.04	0.014± 0.002	3 x 10 ⁻⁶	32
	S	5.2*	2.32-2.39	2.31 ± 0.01	0.014± 0.002		
-Modelled to	Ni	1.2	2.67	2.67 ± 0.02	0.010± 0.002		
0.44:0.56 Ni ₃ S ₄ :hexagonal NiS-							
Decomposed Ni(ⁱ Bu ₂ NCS ₂) ₂ in oleylamine at room temperature (3f) (after rapid ramp)							
	S	0.5*	2.15	2.15 ± 0.04	0.014± 0.001	3 x 10 ⁻⁶	30
	S	5.3*	2.32-2.39	2.31 ± 0.01	0.014± 0.001		
-Modelled to	Ni	1.2	2.67	2.67 ± 0.02	0.010± 0.002		
0.39:0.61 Ni ₃ S ₄ :hexagonal NiS-							
<i>Ex situ</i> XAS of 6: Laboratory synthesised nickel sulfide							
Sample	Scatter	<i>N</i>	<i>R</i> _{XRD} (Å)	<i>R</i> _{EXAFS} (Å)	σ^2 (Å ²)	Reduced <i>chi</i> ²	<i>R</i> -factor
Decomposed Ni(ⁱ Bu ₂ NCS ₂) ₂ in oleylamine at 150° C in laboratory (6)							
	S	1*	2.15	2.15 ± 0.02	0.010± 0.001	4 x 10 ⁻⁶	26
	S	4.5*	2.32-2.39	2.31 ± 0.01	0.010± 0.002		
	Ni	0.5	2.67	2.70 ± 0.02	0.010± 0.002		
	Ni	1.5*	3.35	3.29 ± 0.02	0.009± 0.002		
-Modelled to	Ni	1.5*	3.44	3.44 ± 0.02	0.009± 0.002		
0.25:0.75 Ni ₃ S ₄ :hexagonal NiS-							
	S	3*	3.95	3.90 ± 0.03	0.011± 0.003		
	Ni	2.4*	3.93	3.90 ± 0.03	0.011± 0.003		

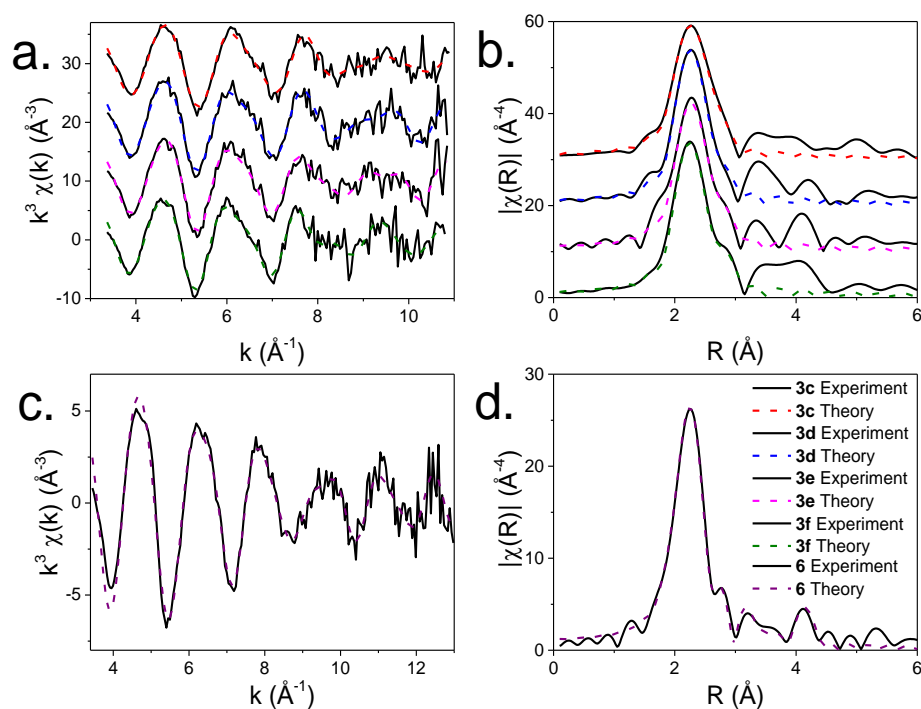


Figure 4.17: a. EXAFS and b. FT of $\text{Ni}(\text{iBu}_2\text{NCS}_2)_2$ in oleylamine at 150°C for an hour (3c), and during cooling at 60°C (3d), 40°C (3e), and 26°C (3f), and c. EXAFS and d. FT of the product of $\text{Ni}(\text{iBu}_2\text{NCS}_2)_2$ in oleylamine decomposition in laboratory at 150°C (6).

In order to imitate realistic laboratory conditions, XAS data was collected for the decomposition product formed in oleylamine during an hour of heating at 150°C and during the cooling process. As mentioned earlier in section 4.3.2.1, XRD confirms that a mixture of polydymite and hexagonal NiS are formed upon decomposition of nickel diisobutyl dithiocarbamate. The amount of mixed phase seems unpredictable, being highly sensitive to heating and cooling rates, this is most likely as a result of the close thermodynamic stabilities of the two phases. Given the confirmation of a mixed phase system by XRD, the EXAFS here is modelled to mixtures. As in section 4.3.2.1, the ratios of mixtures is determined by the short Ni-Ni distance found in hexagonal NiS and all other coordination parameters are defined according to this. Shells have been grouped according to similarities in distances as described earlier. The outcome of this experiment is to understand the effect of cooling rates on the ratio of the phases. After an hour, EXAFS of the structure at 150°C (3c) reveals a mixture of Ni_3S_4 and hexagonal NiS at a ratio of 0.55:0.45. Modelling of 3c

indicates 0.7 Ni_(t)-S interatomic distances at 2.13 Å, 4.9 Ni-S distances at 2.31 Å, and 0.9 Ni-Ni distances at 2.67 Å.

During the cooling stage, at 60° C, the composition of the mixture **3d** changes to 0.5:0.5 of Ni₃S₄ and hexagonal NiS. Modelling reveals 0.7 Ni_(t)-S interatomic distances at 2.15 Å, 5.0 Ni-S distances at 2.31 Å, and 1 Ni-Ni distance at 2.69 Å.

Further changes occur to the composition ratio by 40° C (**3e**), EXAFS indicates a mixture of Ni₃S₄ and hexagonal NiS at 0.44:0.56. Modelling shows 0.57 Ni_(t)-S interatomic distances at 2.15 Å, 5.2 Ni-S distances at 2.31 Å, and 1.2 Ni-Ni distances at 2.67 Å.

EXAFS of **3f** (at room temperature, 26° C) indicates that the material maintains a mixed phase with a ratio of 0.61:0.39 Ni₃S₄ to hexagonal NiS. Data is modelled to 0.5 Ni_(t)-S interatomic distances at 2.15 Å, 5.3 Ni-S distances at 2.31 Å, and 1.2 Ni-Ni distance at 2.67 Å. All analyses are shown in Table 4.4 and Figure 4.17a-b.

XRD of the final decomposition product from a laboratory synthesis in oleylamine indicates the formation of a mixture containing Ni₃S₄ and hexagonal NiS. EXAFS modelling is indicative of the existence of the mixture at a ratio of 0.75:0.25. Through EXAFS, the structure is defined by an average coordination of 1 Ni_(t)-S distance at 2.15 Å, 4.5 Ni-S distances at 2.31 Å, and a further 0.5 Ni-Ni distance at 2.70 Å. Longer distances of the 2nd shell are also fit based on the ratios derived from the first shell (Table 4.4, Figure 4.17c-d).

The laboratory decomposition products can be hugely varied. Typically, hexagonal NiS is the main product for decomposition in oleylamine, and Ni₃S₄ is the product in hexylamine but this is not always guaranteed. Based on the EXAFS results, 2 phases remain in coexistence and the reaction product may be better directed with a thorough regulation of the cooling process.

4.3.3 Iron Dithiocarbamate Decomposition

The decomposition of iron dithiocarbamate is complicated by redox processes. To begin with, the iron centre of iron tris-diisobutyl dithiocarbamate is in a 3+ oxidation state whereas the iron sulfide nanoparticles produced from its decomposition contain predominantly or exclusively iron(II) species. Reduction of iron(III) clearly forms a

key step in the decomposition, yet there are no examples of this process being observed or acknowledged. Literature of xanthates is clearer on the subject. A notable paper describes Mössbauer results of a solution containing a xanthate in pyridine: the reduction of Fe(III) to Fe(II) is observed simultaneously to the release of the xanthate equivalent of thiuram disulfide according to UV-vis.³⁶ Spin states must also be considered and can have significant effect on bond distances as demonstrated by XRD³⁷⁻⁴⁰ and EXAFS⁴¹⁻⁴⁴ as well as reactivity. Additional complexity arises from the relationships between the many phases of iron sulfides. Iron dithiocarbamate decomposition alone is reported to result in the successful synthesis of greigite, pyrrhotite¹⁰, and pyrite¹¹ of variable morphologies.

Here the iron diisobutyl dithiocarbamate complex is decomposed under conditions that result in either pyrrhotite or greigite structures. The decomposition of iron dithiocarbamate in oleylamine at low dilutions results in the formation of pyrrhotite. The addition of thiuram disulfide (TDS) results in the formation of greigite. The decomposition of a highly concentrated solution also forms greigite. All three reaction mechanisms are investigated. Firstly the dynamic nature of the iron dithiocarbamate complex is understood through a high temperature study in dodecane.

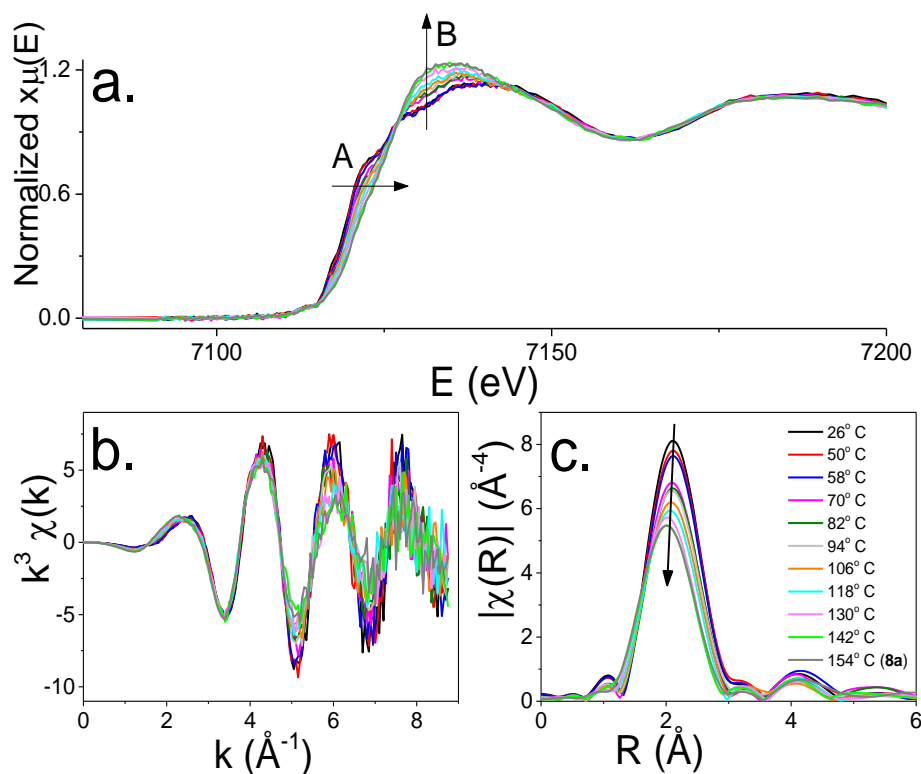
4.3.3.1 Decomposition of $\text{Fe}(\text{iBu}_2\text{NCS}_2)_3$ in dodecane

Figure 4.18: a. *In situ* XANES spectra, b. *in situ* EXAFS, and c. and *in situ* FT of the solvothermal treatment of $\text{Fe}(\text{iBu}_2\text{NCS}_2)_3$ in dodecane (**8**) up to 154°C at a ramp rate of $1^\circ\text{C}/\text{min}$.

The solvothermal treatment of $\text{Fe}(\text{iBu}_2\text{NCS}_2)_3$ in dodecane (**8**) demonstrates that the iron dithiocarbamate structure is more dynamic, and therefore perhaps more inclined to modification in solution, prior to decomposition, than initially realised.

Table 4.5: Results of EXAFS fitting for the *in situ* treatment of **8**. Unrefined coordination numbers are indicated by *.

Decomposition of 8 : $\text{Fe}(\text{iBu}_2\text{NCS}_2)_3$ in dodecane						
Sample	Scatter	N	R_{EXAFS} (\AA)	$2\sigma^2$ (\AA^2)	Reduced χ^2	R -factor
$\text{Fe}(\text{iBu}_2\text{NCS}_2)_3$ in dodecane at 58°C (8a)	S	6*	2.32 ± 0.02	0.015 ± 0.002	2×10^{-6}	22
	C	3*	2.74 ± 0.02	0.015 ± 0.002		
$\text{Fe}(\text{iBu}_2\text{NCS}_2)_3$ in dodecane at 82°C (8b)	S	6*	2.32 ± 0.02	0.021 ± 0.002	2×10^{-6}	26
	C	3*	2.74 ± 0.02	0.021 ± 0.002		
$\text{Fe}(\text{iBu}_2\text{NCS}_2)_3$ in dodecane at 106°C (8c)	S	6*	2.32 ± 0.02	0.023 ± 0.002	2×10^{-6}	29
	C	3*	2.73 ± 0.02	0.023 ± 0.003		
$\text{Fe}(\text{iBu}_2\text{NCS}_2)_3$ in dodecane at 130°C (8d)	S	6*	2.30 ± 0.02	0.026 ± 0.002	2×10^{-6}	29
	C	3*	2.73 ± 0.02	0.026 ± 0.003		
$\text{Fe}(\text{iBu}_2\text{NCS}_2)_3$ in dodecane at 154°C (8e)	S	6*	2.30 ± 0.02	0.027 ± 0.002	2×10^{-6}	34
	C	3*	2.75 ± 0.02	0.027 ± 0.003		

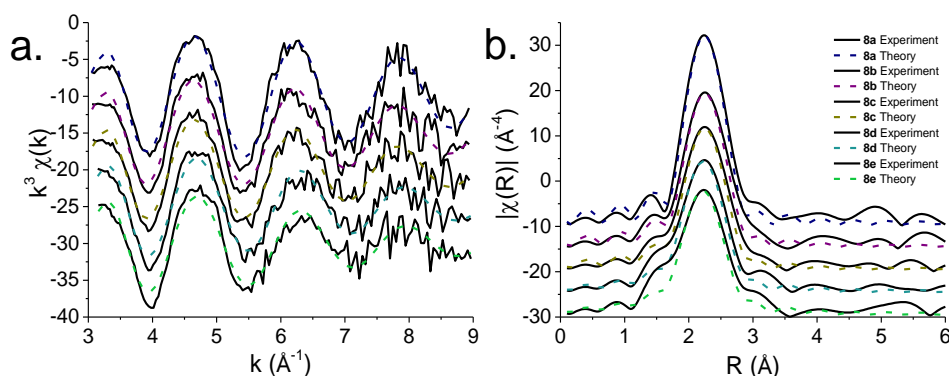


Figure 4.19: a. EXAFS and b. FT of $\text{Fe}(\text{ᵀBu}_2\text{NCS}_2)_3$ in dodecane.

At room temperature, EXAFS of **8** in dodecane reveals the slight lengthening of the 6 Fe-S bonds to 2.32 Å as compared to solid **7** which has 6 Fe-S bonds at 2.30 Å with a $2\sigma^2$ of 0.013 Å², a higher value than expected at room temperature (shown in Chapter 3). Modelling of the same material at 58° C (**8a**), 82° C (**8b**), and 106° C (**8c**) reveals a further increase in Debye-Waller factor with the same bond distance. By 130° C, average bond length is slightly shortened to 2.30 Å, but $2\sigma^2$ continues to increase; by 154° C, $2\sigma^2$ has a value of 0.027 Å² (Table 4.5, Figure 4.19). Anharmonicity is expected to result in a higher average bond distance with increasing temperature, this is not seen. This may be because the system is a highly labile one and the highest temperature investigated is still rather low for any obvious bond distance increase to be detected. *In situ* XANES show changes occurring gradually with the shoulder feature labelled **A** decreasing, and white line intensity **B** simultaneously increasing (Figure 4.18). **A** is related to the 1s to 4s transition: sulfur ligands contribute p-character to the 4s-orbital, thus making the transition more allowed. Typically, as the orbital loses p character, the transition becomes less allowed. **B** is harder to interpret, however, its gradual increase may indicate a shift to lower coordination or less sulfur character. During the solvothermal treatment of **8** up to 154° C, decomposition of the dithiocarbamate complex is not observed; 3 Fe-C bond lengths persist between 2.73 and 2.75 Å up to high temperatures.

Results point to the highly dynamic nature of the iron dithiocarbamate complex. The level of disorder observed in this system is not observed in the nickel dithiocarbamate system. It can be suggested that the disorder results from the wide bond length distribution of the dithiocarbamate ligands to the metal centre which is

averaged over time. Based on the Debye-Waller factor at 154° C, bond length varies by 0.12 Å. This shortening and lengthening may contribute to the ease with which other ligands such as oleylamine can be inserted into the complex as shown in the previous chapter. Another conclusion that can be drawn by the *in situ* EXAFS analysis of **8** is that the dithiocarbamate complex remains in a low spin state. All bond distances remain degenerate and at an average bond length close to the typical value of a low spin system.

4.3.3.2 Decomposition of $\text{Fe}(\text{iBu}_2\text{NCS}_2)_3$ in oleylamine – pyrrhotite synthesis

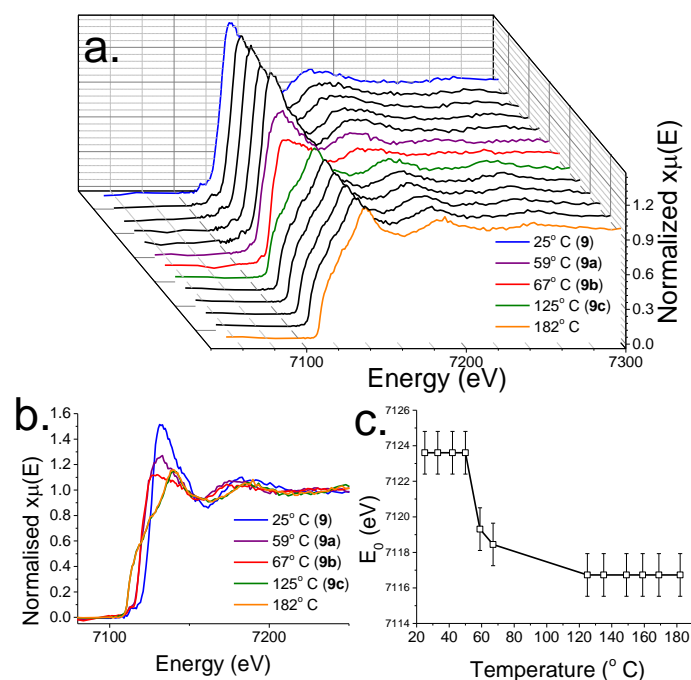


Figure 4.20: a. *In situ* XANES spectra of the solvothermal decomposition of $\text{Fe}(\text{iBu}_2\text{NCS}_2)_3$ in oleylamine (9) up to 182° C at a ramp rate of 1° C/min, b. XANES spectra of the same decomposition highlighting temperatures of interest, and c. plot of edge position calculated as value at half spectral maximum against temperature.

The decomposition of $\text{Fe}(\text{iBu}_2\text{NCS}_2)_3$ in oleylamine (9) is used for the formation of pyrrhotite (Fe_7S_8), characterised by XRD.⁴⁵ According to the *in situ* XANES shown in Figure 4.20a-b, the decomposition of **9** occurs in a three step process. The starting material is established as a complex containing 2 oleylamine and 3 monodentate dithiocarbamate ligands (described in the previous chapter). This structure is stable

up to 59° C. Reduction of the iron(III) centre takes place at 59° C (**9a**) indicated by a shift in edge position of approximately 6 eV (Figure 4.20c). Data is lost between 67° C (**9b**) and 125° C (**9c**) due to severe inhomogeneity of the reaction mixture – this in itself hints at the formation of inorganic sulfide; inhomogeneity arising from the immiscibility of inorganic material in organic solvent often leads to decline in data quality. At 125° C, the edge position is shifted to lower energy again by approximately 2 eV. The shift is suggestive of either further reduction of remaining iron(III) species, or significant changes to the coordination environment. The sulfide species **9c** remains unchanged up to the final acquisition at 182° C. The spin state of iron in the solid state structure **7** was shown to be low spin, however, spin in the modified system **9** is difficult to determine by EXAFS bond distances. Typically, introduction of amine systems should increase orbital splitting, thus resulting in a low spin complex. On the other hand, the reactivity at 60° C, which is a low temperature, suggests a lack of crystal field stabilisation which is characteristic of high spin iron(III) complexes.

Table 4.6: Results of EXAFS fitting for the *in situ* decomposition of **9. Unrefined coordination numbers are indicated by *.**

Decomposition of 9 : Fe(^t Bu ₂ NCS ₂) ₃ in oleylamine						
Sample	Scatter	<i>N</i>	<i>R</i> _{EXAFS} (Å)	2σ ² (Å ²)	Reduced <i>chi</i> ²	<i>R</i> -factor
Fe(^t Bu ₂ NCS ₂) ₃ in oleylamine at 59° C (9a)	N	2*	1.91 ± 0.02	0.008± 0.001	1 x 10 ⁻⁵	42
	S	2*	2.26 ± 0.05	0.006± 0.001		
	S	2*	2.45 ± 0.02	0.006± 0.002		
	C	2*	2.85 ± 0.08	0.007± 0.002		
Fe(^t Bu ₂ NCS ₂) ₃ in oleylamine at 67° C (9b)	S	2*	2.21 ± 0.03	0.006± 0.001	5 x 10 ⁻⁵	58
	S	2*	2.44 ± 0.04	0.008± 0.002		
	C	2*	2.78 ± 0.08	0.010± 0.002		
Fe(^t Bu ₂ NCS ₂) ₃ in oleylamine at 125° C (9c) (modelled to Fe ₇ S ₈)	S	6*	2.36 ± 0.01	0.008± 0.002	1 x 10 ⁻⁶	29

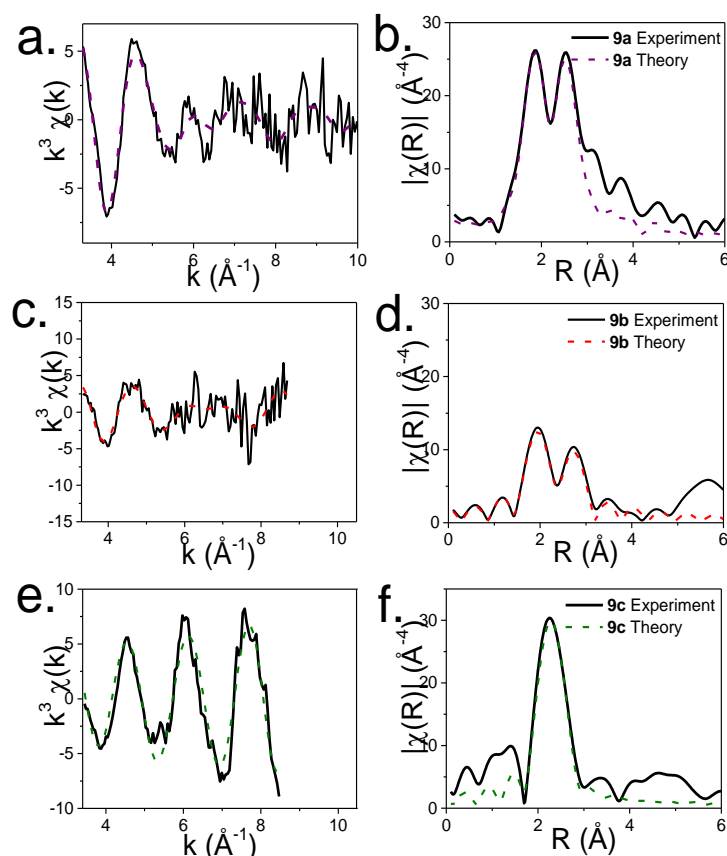


Figure 4.21: a. EXAFS and b. FT of $\text{Fe}(\text{ᵀBu}_2\text{NCS}_2)_3$ in oleylamine at 59° C (9a), c. EXAFS and d. FT of $\text{Fe}(\text{ᵀBu}_2\text{NCS}_2)_3$ in oleylamine at 67° C (9b), and e. EXAFS and f. FT of $\text{Fe}(\text{ᵀBu}_2\text{NCS}_2)_3$ in oleylamine at 125° C (9c).

Modelling EXAFS of **9a** reveals that the reduction shown in the XANES spectrum is coupled with the expulsion of one dithiocarbamate ligand. The new structure contains two bidentate dithiocarbamate ligands and two iron-oleylamine interactions. 2 Fe-S bonds exist at 2.23 Å, 2 Fe-S bonds are present at 2.46 Å, and 2 Fe-C distances are shown at 2.85 Å. Two Fe-N bonds from iron-oleylamine interactions persist at 1.91 Å (Table 4.6, Figure 4.21a-b). Based on the results, reduction of the metal centre seems to be caused by an intramolecular electron-transfer that results in the expulsion of a dithiocarbamate ligand. Two expelled ligands form thiuram disulfide *via* oxidative coupling. Analogies can be drawn between the structure of **9a** to that of nickel(II) dithiocarbamate in oleylamine (**3**). *Trans* geometry is assumed based on calculations on **3**.

At 67° C the structure of the complex is further transformed. EXAFS of **9b** is modelled without iron-oleylamine interactions. Interactions instead include 2 Fe-S

distances at 2.21 Å and 2 Fe-S distances at 2.44 Å as well as 2 Fe-C interactions at 2.78 Å which represent two bidentate ligands (Table 4.6, Figure 4.21c-d). **9b** is similar to the structure of **3a**, nickel bis dithiocarbamate at 118° C before decomposition. The transformation of **9a** to **9b** is analogous to the transition of **3** to **3a** in the nickel dithiocarbamate decomposition. Other possible similarities in the decomposition pathway are therefore plausibly the amide-exchange of the dithiocarbamate backbone by oleylamine. This occurs for the nickel dithiocarbamate at **3a** and initiates the decomposition process according to DFT.¹⁹

Between 67° C and 125° C data is lost due to initial decomposition. When the material reappears at 125° C, EXAFS of **9c** suggests the formation of an iron sulfide which is most likely amorphous or nanoparticulate as XRD of sulfides synthesized between 125 and 180° C do not show diffraction peaks in the laboratory.^{10,45} 6 Fe-S interatomic distances are shown at 2.37 Å, within the range of expected pyrrhotite distances of between 2.36 and 2.53 Å according to XRD⁴⁶ (Table 4.6, Figure 4.21e-f). EXAFS analysis was only possible by lowering the amplitude factor to 0.47 - much lower than the typical value of ~0.70 - this suggests self-absorption issues in the newly formed material, owing to the high concentration of iron in the agglomerated system. The amorphous structure remains unchanged up to 182° C. A pictorial representation of the intermediate structures in the reaction scheme is given in Figure 4.22. Pyrrhotite diffraction peaks emerge after 180° C according to XRD of the laboratory decomposition of the system.^{10,45} The higher temperatures were unfortunately not attainable with this *in situ* setup and therefore the transformation to the crystalline phase to be observed. *Ex situ* XANES of the pyrrhotite synthesized in the laboratory at 230° C (**9d**) was acquired and showed a significantly different spectrum to the amorphous iron sulfide isolated between 125 and 180° C (Figure 4.23). This confirms that there is a further transformation in the decomposition process.

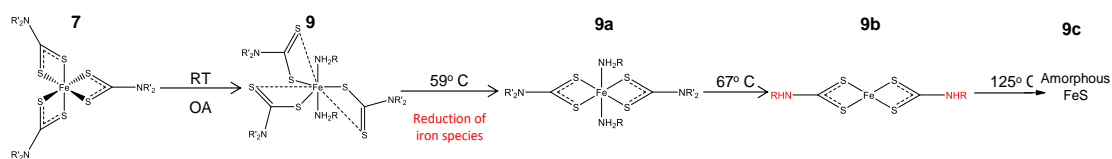


Figure 4.22: Predicted structures of stable intermediates in the decomposition pathway of 9.

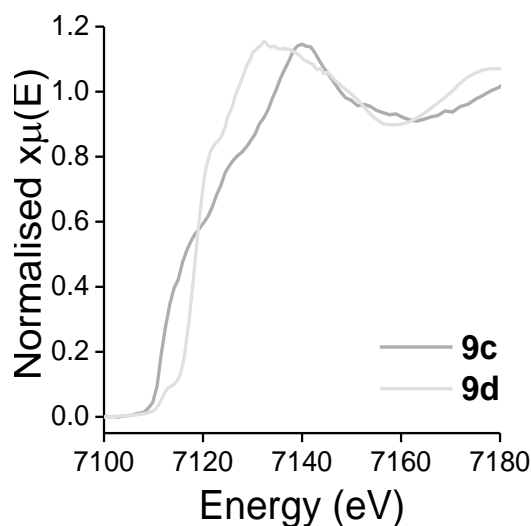


Figure 4.23: XANES spectrum of 9 decomposed up to 180°C (9c), and at 230°C (9d). 9c was acquired in situ at 180°C, while 9d was acquired ex situ at room temperature. Despite different experimental conditions, the significant difference in XANES spectra indicate two different local structures. 9c is suggested to be amorphous FeS as it does not have any diffraction peaks, while 9d is characterised by XRD as pyrrhotite Fe_7S_8 .⁴⁵

4.3.3.3 Decomposition of $\text{Fe}(i\text{Bu}_2\text{NCS}_2)_3$ (high concentration) in oleylamine – greigite synthesis

Decomposition of iron tris-diisobutyl dithiocarbamate in oleylamine at a high concentration results in the formation of greigite (Fe_3S_4) according to XRD.⁴⁵ The resulting greigite contains a significant Fe(III) component and a higher ratio of sulfur compared to pyrrhotite. XANES of the decomposition is shown in Figure 4.24.

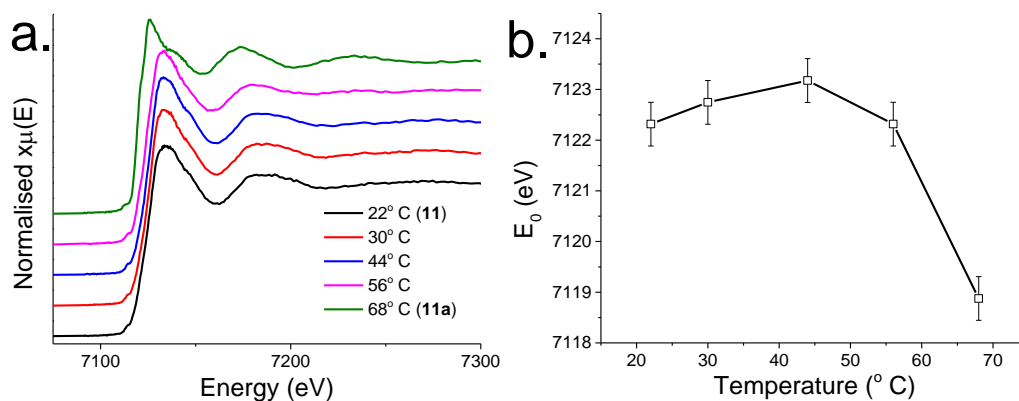


Figure 4.24: a. *In situ* XANES spectra of the solvothermal decomposition of $\text{Fe}(\text{iBu}_2\text{NCS}_2)_3$ at high concentration in oleylamine (**11**) up to 68°C at a ramp rate of $1^\circ\text{C}/\text{min}$ (inhomogeneity after this temperature prevented further successful data acquisition), and b. plot of edge position calculated as value at half spectral maximum against temperature.

The initial iron dithiocarbamate-oleylamine species (**11**) is a mixture of dissolved complex similar to **9** and undissolved complex with the structure of **7** or **8**. LCF of **11** fit against **9** and **8** reveals a ratio of 53:47 (Figure 4.25). Owing to the number of scatter paths required to fit this data (including Fe-N and 3 Fe-S from the structures of **9** and **8**), and the short k-range, EXAFS was not fit. The LCF provides enough evidence of a mixture of dissolved and undissolved iron dithiocarbamate within the reaction mixture. **11** remains stable and unchanged up to 68°C .

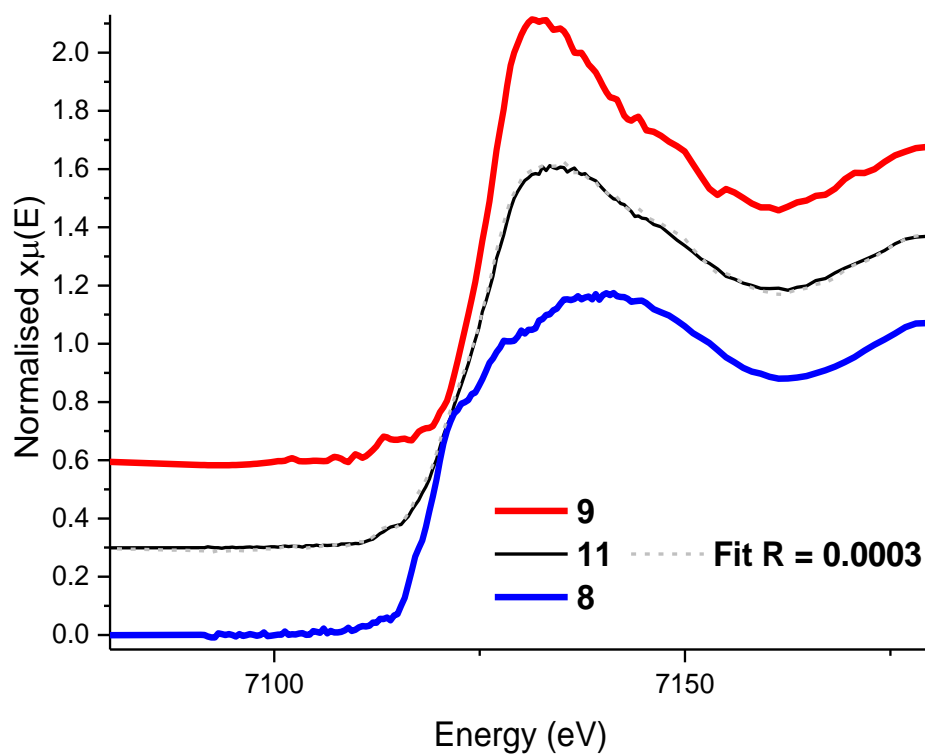


Figure 4.25: LCF fit of $\text{Fe}(\text{iBu}_2\text{NCS}_2)_3$ at high concentration in oleylamine (11) at room temperature. The XANES is fit to XANES of 9 (oleylamine interacted $\text{Fe}(\text{iBu}_2\text{NCS}_2)_3$) and 8 (species void of oleylamine interaction, representing here the undissolved constituent of the reaction mixture).

At 68° C, reduction occurs with a 6 eV shift in the edge position (**11a**). While the shift is the same as that of **9** to **9a**, the spectrum of **11a** differs significantly from the spectrum of **9a** with a sharper white line intensity labelled **B** and a defined curve at **C** (Figure 4.26). EXAFS modelling of **11a** was inconclusive owing to a number of possible first shell fits and a short k-range. The XANES of **11a** is similar to the XANES of **10a** and is discussed in the next section. After 68° C, the experiment could no longer be monitored due to deteriorated data quality. While the *in situ* data for this decomposition falls short of answering the absolute question of mechanism, it is an important step to understanding the determination of phase. Both this reaction, and reaction **10** described in section 4.3.3.4, result in the formation of the inverse spinel greigite. Data of the decompositions suggest that the phase determination may begin at the reduction step of the decomposition.

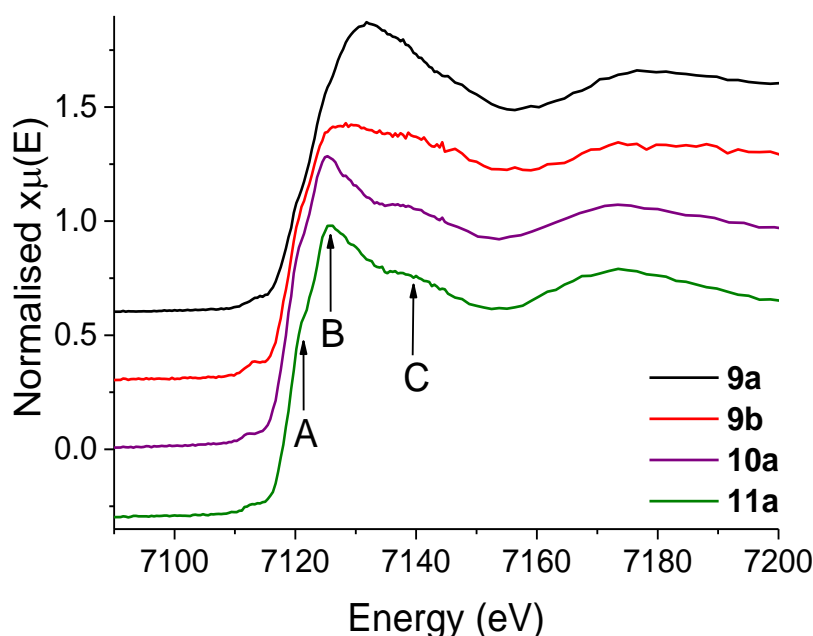


Figure 4.26: Plot of XANES spectra for 9a, 9b, 10a, and 11a, to highlight similarities and differences between the first intermediate structure formed after reduction of the iron centre.

4.3.3.4 Decomposition of $\text{Fe}(\text{iBu}_2\text{NCS}_2)_3$ and $\text{S}_2(\text{iBu}_2\text{NCS})_2$ in oleylamine – greigite synthesis

Addition of thiuram disulfide (TDS) to the reaction mixture of iron tris-diisobutyl dithiocarbamate in oleylamine has the same effect as increasing concentration in the reaction mixture, and the formation of pure greigite is highly favoured.⁴⁵ Thiuram disulfide can be considered as an oxidizing agent since the resulting greigite contains

a significant Fe(III) component. It is also considered a sulfur source owing to the higher ratio of sulfur in the resulting nanoparticles compared to pyrrhotite. The exact role of the thiuram disulfide, and the process by which the alternative phase is favored, is not fully understood.

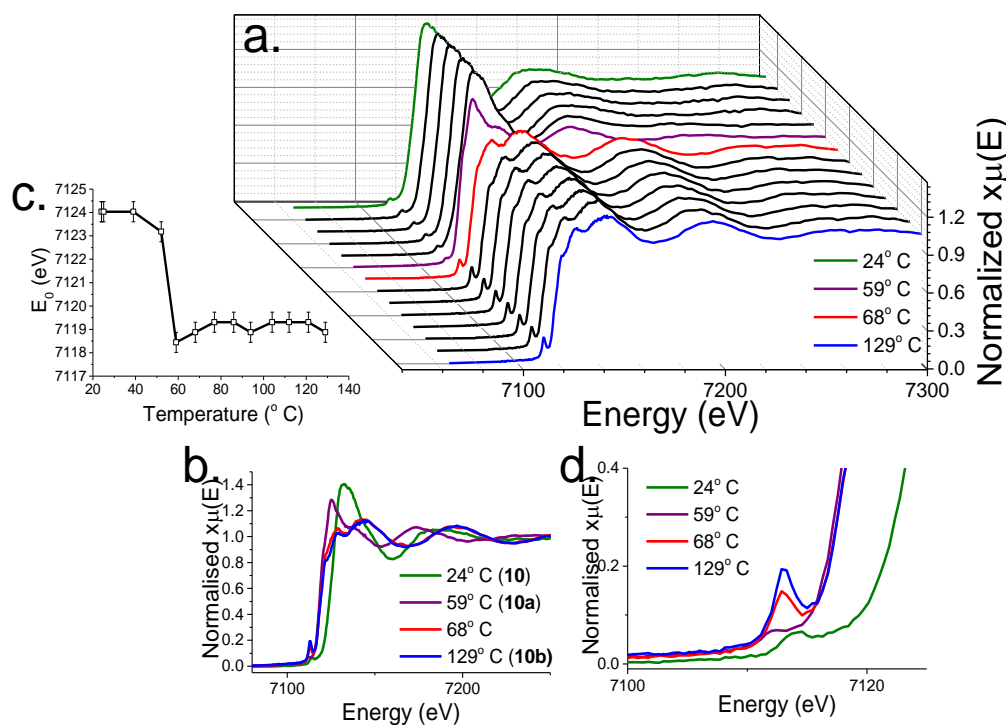


Figure 4.27: a. *In situ* XANES spectra of the solvothermal decomposition of $\text{Fe}^{\text{I}}(\text{Bu}_2\text{NCS}_2)_3$ with $\text{S}_2^{\text{I}}(\text{Bu}_2\text{NCS})_2$ in oleylamine (10) up to 129° C at a ramp rate of 1° C/min, b. XANES spectra of the same decomposition highlighting temperatures of interest, c. plot of edge position calculated as value at half spectral maximum against temperature, and d. zoomed image of spectra at pre-edge position showing pre-edge peaks at 68 and 129° C indicating tetrahedral geometry.

According to the *in situ* XANES shown in Figure 4.27a-b, the decomposition of **10** takes place in a similar number of steps to the decomposition of **9**, but diverges from the original mechanism at higher temperatures. At room temperature, the spectrum of **10** is identical to **9**, and like **9**, **10** is stable up to 59° C. At 59° C (**10a**), reduction of the iron(III) centre occurs, shown by a shift in edge position of 6 eV (Figure 4.27c). According to XANES, **10a** is identical to **11a**, three key features on the spectra are labelled **A**, **B**, and **C** (Figure 4.26). At 68° C, a material is formed in which the iron species adopts a geometry other than octahedral or square planar – this is indicated by the presence of a small pre-edge peak that arises from the 1s to

3d transition which is more allowed for tetrahedral and non-octahedral geometries (Figure 4.27d). The structure remains unchanged up to 129° C.

Table 4.7: Results of EXAFS fitting for the *in situ* decomposition of 10. Unrefined coordination numbers are indicated by *.

Sample	Scatter	N	R_{EXAFS} (Å)	$2\sigma^2$ (Å ²)	Reduced χ^2	R -factor
Fe(ⁱ Bu ₂ NCS ₂) ₃ in oleylamine with thiuram disulfide at room temperature (10)	N	2*	1.89 ± 0.02	0.007 ± 0.001	5 × 10 ⁻⁶	19
	S	3*	2.22 ± 0.09	0.006 ± 0.001		
	C	3*	2.69 ± 0.05	0.006 ± 0.002		
	S	3*	3.09 ± 0.07	0.008 ± 0.001		
Fe(ⁱ Bu ₂ NCS ₂) ₃ in oleylamine with thiuram disulfide at 129° C (10b)	S	5*	2.25 ± 0.01	0.006 ± 0.001	6 × 10 ⁻⁶	18
	Fe	1*	2.77 ± 0.01	0.006 ± 0.001		
	Fe	1*	3.22 ± 0.02	0.006 ± 0.002		
	Fe	1*	3.44 ± 0.02	0.006 ± 0.002		

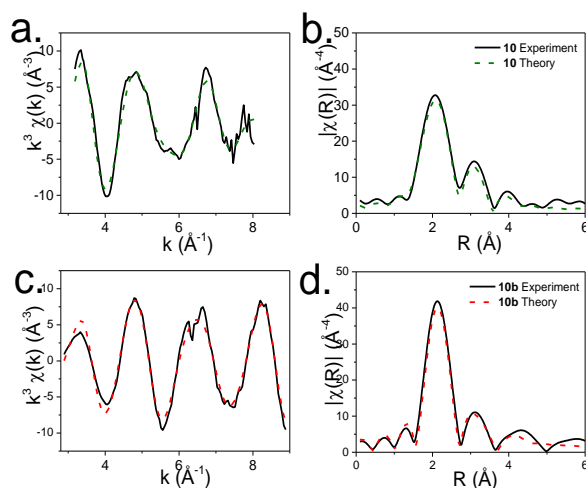


Figure 4.28: a. EXAFS and b. FT of Fe(ⁱBu₂NCS₂)₃ with S₂(ⁱBu₂NCS)₂ in oleylamine at 24° C (10), and c. and d. at 129° C (10b).

From EXAFS, the starting material (**10**), containing the dithiocarbamate complex and four times the concentration of thiuram disulfide in oleylamine, is identical to the structure of **9**, with 2 Fe-N bonds at 1.89 Å, 3 Fe-S bonds at 2.22 Å, and 3 Fe-S distances at 3.09 Å (Table 4.7, Figure 4.28a-b). Combined with XANES results, thiuram disulfide is shown not to have an effect on the immediate iron environment at room temperature, that is distinguishable by XAS.

At 60° C (**10a**) reduction of the iron(III) species takes place. EXAFS is noisy and modelling is not possible as a result, however, it is reasonable to assume that the species here is the same as the reduced species in the decomposition of **11** (**11a**)

based on identical XANES spectra (Figure 4.27). The structure of **10a** is discussed after fitting **10b**.

At 68° C, the cluster **10b** bears some resemblance to the structure of cubane (Figure A2.1, Appendix 2), and EXAFS modelling shows that in this case, the cubane may be stabilized by bidentate dithiocarbamate ligands (see Figure 4.30); a structure reportedly characterized by XRD before and therefore known to exist.⁴⁷ According to EXAFS, 5 Fe-S bonds are located at 2.25 Å. The second shell is fit separately and reveals 3 Fe-Fe interactions (Table 4.7, Figure 4.28c-d). The combination of distances may indicate a cubane-like complex. While more shells including the Fe-C interaction of the dithiocarbamate ligand, and the furthest Fe-S of the cubane could not be added due to a limited k-range; the most convincing argument for the nature of this species is the similarity of the XANES region to a known cubane structure (Figure A2.3, Appendix 2). Edge position shows signs of shifting positively by approximately 1eV after the initial reduction (Figure 4.27c); this may go some way to understanding the average oxidation state of these cubane-like species which can contain all 3+, all 2+, or a mixture of 3+ and 2+ iron species. The complex is well-dispersed in the solvent medium, and remains unchanged up to 129° C.

Given the similarity between the decomposition pathways of **10** and **11**, it can be strongly suggested that **11a** continues to form a cubane complex like **10b**. The structures of **11a** and **10a** must be such that they promote the formation of an Fe₄S₄ complex. It is therefore likely that structure is dimeric thus leading easily to tetrameric. A possible structure is suggested in the proposed reaction scheme shown in Figure 4.30. It is possible for a dimer to be formed without breaking dithiocarbamate bonds present after reduction.

Although the cubane to greigite conversion could not be captured by XAS in either reaction, the formation of greigite from a cubane type structure is documented⁴⁸ and both of the decompositions at high concentration and with thiuram disulfide are shown to result in greigite from XRD characterization of laboratory decompositions.⁴⁵ In addition, the building blocks of greigite are commonly referred to as “cubane-type” due to the Fe₄S₄ clusters present in the unit cell⁴⁹ and cubanes may be considered nanoparticulate greigite. The XANES of the cubane **10b** and the laboratory synthesized greigite **18** (Chapter 5, Section 5.3.1) are different to each

other suggesting unique structures, although, with some similar features including edge position, they could be considered as related structures (Figure 4.29).

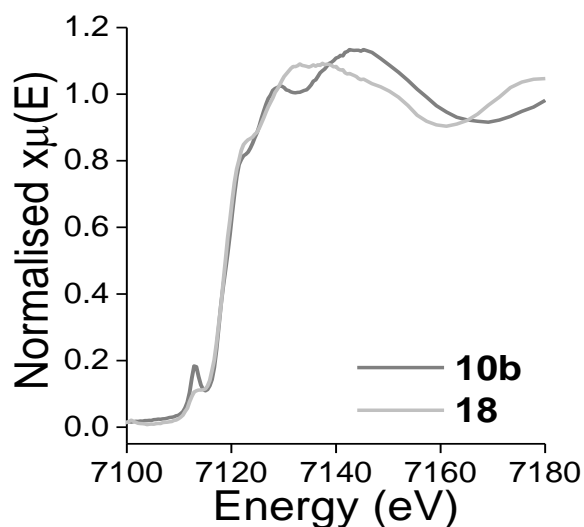


Figure 4.29: XANES spectrum of 10 decomposed up to 129° C (10b), and at 240° C (18). 10b was acquired *in situ* at 129° C, while 18 was acquired *ex situ* at room temperature.

Amide-exchange – which is likely to be key to the decomposition of the dithiocarbamate complexes according to investigations on the nickel K-edge described earlier- is plausible here: amide exchange of the dithiocarbamate ligands terminal to the cubane, with oleylamine, is expected to result in the destabilization of the dithiocarbamate ligands and create structures such as $(\text{Fe}_4\text{S}_4(\text{SH})_4)$ or Fe_4S_4 . Growth of the sulfide from this point is facile. A higher decomposition temperature compared to that of the intermediate dimer **9b** in the decomposition of **9**, could possibly explain the emergence of greigite; at higher temperatures, access to more thermodynamically stable phases such as greigite is possible.

A reaction scheme based on the analyses is given in Figure 4.30.

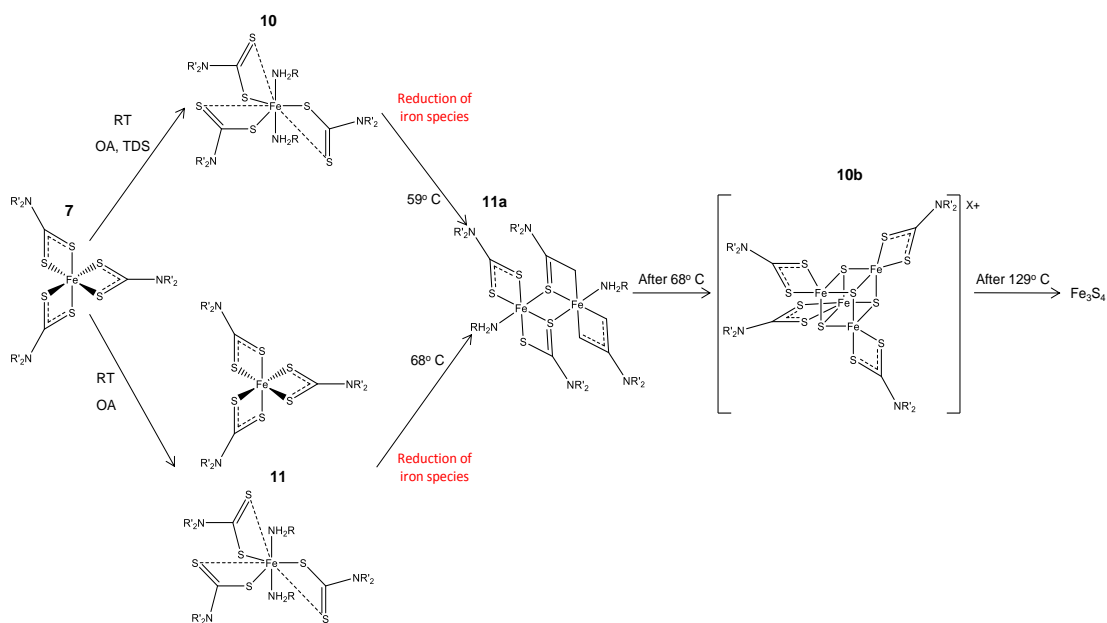


Figure 4.30: Solved structures of stable intermediates in the decomposition of 10 and 11. While not all structures are solved in either decomposition, a significant similarity is found between them and therefore, the full pathway can be hypothesised.

4.4 Discussion

Coordination to the metal center of the dithiocarbamate complexes has already been discussed in Chapter 3. It may be possible that the direct interaction of amine with the metal centers have little or no effect on the decomposition process, while the alternative amine interaction on the carbon backbone – amide-exchange - is exclusively responsible for the decomposition process. The onset of the first process is clear from EXAFS, and amide-exchange is difficult to pinpoint by most methods. When and how rapidly amide-exchange occurs is not fully understood. What is clear is that the amide-exchanged complex is unstable and decomposition becomes imminent upon its formation. Amines bound to the metal center may have an effect on growth direction as it is not always completely dissociated before decomposition occurs. It is reasonable to conclude that all the metal decompositions commence through the same amide-exchanged pathway.

The zinc dithiocarbamate was shown to monomerize upon dissolution in xylene. In coordinating solvent oleylamine, the complex was shown to form one interaction; this resulted in a five coordinated structure with high disorder. With increasing temperature oleylamine gradually dissociates resulting in a four coordinated structure with lower disorder. By 89° C, the zinc dithiocarbamate complex decomposes and results in the formation of zinc sulfide. This is confirmed by TEM which shows the formation of sulfide nanotubes.

In nickel dithiocarbamate, a similar trend is seen. Oleylamine is bound twice to the nickel center, above and below the plane of the complex according to DFT. Between room temperature and 118° C, the oleylamine dissociates. Transamination is predicted by DFT and proved by NMR, MS, and UV-Vis. This causes destabilization and the complex decomposes at 123° C suddenly.

Coordination of oleylamine to the iron center of iron dithiocarbamate results in monodentate dithiocarbamate ligands at room temperature which has an effect on its stability. This may be a result of spin – the typically low spin complex becomes high spin and therefore more reactive; or it may be the result of the monodentate dithiocarbamate ligands having no resonance forms. Iron within the complex is reduced to iron (II) at 60° C by intramolecular electron transfer and expulsion of a

dithiocarbamate ligand; the resulting complex bears resemblance to the nickel dithiocarbamate coordinated to oleylamine with two bidentate dithiocarbamate ligands. Between 60 and 70° C, the bound oleylamine dissociate. Rapid decomposition is observed and an amorphous sulfide is formed by 125° C which later goes on to form pyrrhotite (after 180° C).

In high concentrations, the structure becomes dimeric upon reduction. The same process is found in the decomposition at normal concentrations with thiuram disulfide. At 70° C, the dimer then forms a cubane structure stabilized by four terminal dithiocarbamate ligands. This remains stable up to at least 130° C. Transamination of the dithiocarbamate ligands is predicted to initiate decomposition and growth of iron sulfide particles via the same mechanism described for nickel dithiocarbamate.

4.5 Acknowledgements

All dithiocarbamate complexes and related molecules used for the decomposition reactions were synthesised by Anna Roffey and Nathan Hollingsworth, XRD of the zinc sulfide nanowires was taken by Phil Patterson of the Swiss-Norwegian beamline during in-house time, UV-vis measurements of the nickel dithiocarbamate were taken by Anna Roffey, ¹³C NMR and MS were acquired and analysed by Nathan Hollingsworth, and DFT calculations were performed by Maxime Mercy.

4.6 References

- (1) Afzaal, M.; Malik, M. A.; O'Brien, P. *J. Mater. Chem.* **2010**, *20*, 4031.
- (2) Mourdikoudis, S.; Liz-marzan, L. M. *Chem. Mater.* **2013**, *25*, 1465–1476.
- (3) Hogarth, G. Karlin, K. D., Ed.; John Wiley & Sons, Inc.: Hoboken, NJ, USA, 2005; pp. 71–561.
- (4) Malik, M. A.; Saeed, T.; O'Brien, P. *Polyhedron* **1993**, *12*, 1533–1538.
- (5) Lazell, M.; O'Brien, P. *Chem. Commun.* **1999**, 2041–2042.
- (6) Nyamen, L. D.; Rajasekhar Pullabhotla, V. S.; Nejo, A. A.; Ndifon, P.; Revaprasadu, N. *New J. Chem.* **2011**, *35*, 1133.
- (7) Ajibade, P. a.; Onwudiwe, D. C.; Moloto, M. J. *Polyhedron* **2011**, *30*, 246–252.
- (8) Wang, T. X.; Chen, W. W. *Chem. Eng. J.* **2008**, *144*, 146–148.
- (9) Nyamen, L. D.; Rajasekhar Pullabhotla, V. S. R.; Nejo, A.; Ndifon, P. T.; Warner, J. H.; Revaprasadu, N. *Dalton Trans.* **2012**, *41*, 8297–8302.
- (10) Han, W.; Gao, M. *Cryst. Growth Des.* **2008**, *8*, 1023–1030.
- (11) Chen, X.; Wang, Z.; Wang, X.; Wan, J.; Liu, J.; Qian, Y. *Inorg. Chem.* **2005**, *44*, 951–954.
- (12) Thirumaran, S.; Ramalingam, K.; Bocelli, G.; Cantoni, A. *Polyhedron* **1999**, *18*, 925–930.
- (13) Manohar, A.; Venkatachalam, V.; Ramalingam, K.; Thirumaran, S.; Bocelli, G. *J. Chem. Crystallogr.* **1998**, *28*, 861–866.
- (14) Lai, C. S.; Tiekink, E. R. T. *Appl. Organomet. Chem.* **2003**, *17*, 197–198.
- (15) Ivanov, a. V.; Zaeva, a. S.; Gerasimenko, a. V.; Rodina, T. a. *Russ. J. Coord. Chem.* **2008**, *34*, 688–698.
- (16) Malik, A. M.; Motevalli, M.; O'Brien, P. *Polyhedron* **1999**, *18*, 1259–1264.
- (17) Ivanov, A. V.; Forsling, W.; Antzutkin, O. N.; Novikova, E. V. *Russ. J. Coord. Chem.* **2001**, *27*, 158–166.
- (18) Ivanov, A. V.; Zaeva, A. S.; Novikova, E. V.; Gerasimenko, A. V.; Forsling, W. *Russ. J. Coord. Chem.* **2007**, *33*, 233–243.
- (19) Hollingsworth, N.; Roffey, A.; Islam, H.; Mercy, M.; Roldan, A.; Bras, W.; Wolthers, M.; Catlow, R.; Sankar, G.; Hogarth, G.; de Leuw, N. *Chem. Mater.* **2014**, *26*, 6281–6292.
- (20) Ravel, B.; Newville, M. *J. Synchrotron Radiat.* **2005**, *12*, 537–541.
- (21) Binsted, N. EXCURV98: CCLRC Daresbury Laboratory Computer Program, 1998.
- (22) Barrelet, C. J.; Wu, Y.; Bell, D. C.; Lieber, C. M. *J. Am. Chem. Soc.* **2003**, *125*, 11498–11499.
- (23) Wang, Y.; Zhang, L.; Liang, C.; Wang, G.; Peng, X. *Chem. Phys. Lett.* **2002**, *357*, 314–318.
- (24) Van Heerden, J. L.; Swanepoel, R. *Thin Solid Films* **1997**, *299*, 72–77.

- (25) Beamline specs
<http://www.esrf.eu/UsersAndScience/Experiments/CRG/BM01/bm01-a>.
- (26) Dirksen, A.; Nieuwenhuizen, P. J.; Hoogenraad, M.; Haasnoot, J. G.; Reedijk, J. *J. Appl. Polym. Sci.* **2001**, *79*, 1074–1083.
- (27) Rabadanov, M. K.; Loshmanov, A. A.; Shaldin, Y. V. *Crystallogr. Reports* **1997**, *42*, 592–602.
- (28) Jung, Y. K.; Kim, J. Il; Lee, J. K. *J. Am. Chem. Soc.* **2010**, *132*, 178–184.
- (29) Vaughan, D. J.; Craig, J. R. *Am. Mineral.* **1985**, *70*, 1036–1043.
- (30) Kuznetsov, V. G.; Eliseev, A. A. *J. Struct. Chem.* **1961**, *2*, 534–539.
- (31) Coucouvanis, D.; Fackler Jr., J. P. *Inorg. Chem.* **1967**, *6*, 2047.
- (32) Becke, A. D. *J. Chem. Phys.* **1993**, 5648.
- (33) Ditchfield, R.; Hehre, W. J.; Pople, J. A. *J. Chem. Phys.* **1971**, *54*, 724.
- (34) Scalmani, G.; Frisch, M. J. *J. Chem. Phys.* **2010**, *132*.
- (35) Frisch, M. J.; Trucks, G. W.; Schlegel, H. B.; Scuseria, G. E.; Robb, M. A.; Cheeseman, J. R.; Montgomery Jr., J. A.; Vreven, T.; Kudin, K. N.; Burant, J. C.; Millam, J. M.; Iyengar, S. S.; Tomasi, J.; Barone, V.; Mennucci, B.; Cossi, M.; Scalmani, G.; Rega, N.; Petersson, G. A.; Nakatsuji, H.; Hada, M.; Ehara, M.; Toyota, K.; Fukuda, R.; Hasegawa, J.; Ishida, M.; Nakajima, T.; Honda, Y.; Kitao, O.; Nakai, H.; Klene, M.; Li, X.; Knox, J. E.; Hratchian, H. P.; Cross, J. B.; Bakken, V.; Adamo, C.; Jaramillo, J.; Gomperts, R.; Stratmann, R. E.; Yazyev, O.; Austin, A. J.; Cammi, R.; Pomelli, C.; Ochterski, J. W.; Ayala, P. Y.; Morokuma, K.; Voth, G. A.; Salvador, P.; Dannenberg, J. J.; Zakrzewski, V. G.; Dapprich, S.; Daniels, A. D.; Strain, M. C.; Farkas, O.; Malick, D. K.; Rabuck, A. D.; Raghavachari, K.; Foresman, J. B.; Ortiz, J. V.; Cui, Q.; Baboul, A. G.; Clifford, S.; Cioslowski, J.; Stefanov, B. B.; Liu, G.; Liashenko, A.; Piskorz, P.; Komaromi, I.; Martin, R. L.; Fox, D. J.; Keith, T.; Al-Laham, M. A.; Peng, C. Y.; Nanayakkara, A.; Challacombe, M.; Gill, P. M. W.; Johnson, W.; Chen, B.; Wong, M. W.; Gonzalez, C.; Pople, J. A. Gaussian 09, Revision C 01, Gaussian Inc., Pittsburgh PA, 2009.
- (36) Saleh, R. Y.; Straub, D. K. *Inorg. Chem.* **1974**, *13*, 1559–1562.
- (37) Butcher, R. J.; Sinn, E. *J. Am. Chem. Soc.* **1976**, *98*, 2440–2449.
- (38) Butcher, R. J.; Sinn, E. *J. Am. Chem. Soc.* **1976**, *98*, 5159–5168.
- (39) Healy, P. C.; Sinn, E. *Inorg. Chem.* **1975**, *14*, 109–115.
- (40) Cukauskas, E. J.; Deaver, B. S.; Sinn, E. *J. Chem. Phys.* **1977**, *67*, 1257–1266.
- (41) McGrath, C. M.; O'Connor, C. J.; Sangregorio, C.; Seddon, J. M.; Sinn, E.; Sowrey, F. E.; Young, N. a. *Inorg. Chem. Commun.* **1999**, *2*, 536–539.
- (42) Healy, P. C.; White, A. H. *J. Chem. Soc. Dalton Trans.* **1972**, 1163.
- (43) Butcher, R. J.; Ferraro, J. R.; Sinn, E. *Inorg. Chem.* **1976**, *15*, 2077–2079.
- (44) Bereman, R. D.; Churchill, M. R.; Nalewajek, D. *Inorg. Chem.* **1979**, *18*, 3112–3117.
- (45) Roffey, A. Dithiocarbamate Complexes as Single Source Precursors to Metal Sulfide Nanoparticles for Applications in Catalysis, University College London, 2014.

- (46) Fleet, M. E. *Acta Crystallogr. Sect. B - Struct. Crystallogr. Cryst. Chem.* **1971**, B 27, 1864.
- (47) Liu, Q. T.; Huang, L. R.; Yang, Y.; Lu, J. X. *Kexue Tongboa* **1988**, 33, 1633.
- (48) Vanitha, P. V; O'Brien, P. *J. Am. Chem. Soc.* **2008**, 130, 17256–17257.
- (49) Rickard, D.; Luther, G. W. *Chem. Rev.* **2007**, 107, 514–562.

Chapter 5 Overview

The solvothermal decomposition of iron or iron and nickel diisobutyl dithiocarbamate in the presence of thiuram disulfide results in the formation of Fe_3S_4 or NiFe_2S_4 nanoparticles. These inverse spinel structures are formed as hexagonal sheets with 001 and 111 surfaces which are predicted to be electrocatalytically active. The oxidation of the systems in electrolyte during cyclic voltammetry – a process that is thought to reduce catalytic activity – is investigated by *in situ* XAS in this chapter.

Chapter 5

***In situ* XAS of Greigite and Violarite during Electrocatalytic Processes with Carbon Dioxide**

5.1 Introduction

Research into materials that catalytically activate carbon dioxide are of great interest. CO₂ is not only the most common product of the oxidation processes of hydrocarbons and therefore readily available in high purity, but its increasing presence in the atmosphere presents a problem for global atmospheric temperatures. Therefore tapping into the immense reserve can provide a positive environmental impact as well provide opportunities in industry.

CO₂ activation is challenging. The molecule is classically non-polar with two nucleophilic ends and an electrophilic carbon at the centre; although resonance forms of the molecule result in polarisation in the form of ⁺O≡C-O⁻ and ⁻O-C≡O⁺.¹ The reduction of CO₂ to CO₂⁻ requires a large over potential, owing to the change in the geometry of the linear molecule required to activate it.² For this reason, it is thermodynamically demanding to synthesise most small organic molecules from CO₂ without electrocatalytic help; methanol and methane are the most easily synthesised products with negative Gibbs free energy but require a highly acidic environment (to add 6H⁺ and 8H⁺ respectively) as well as a negative overpotential. Experimentally, major products synthesised in uncatalysed electrochemical reactions of CO₂ are formic acid and oxalic acid, and CO in proton deficient media.

Electrocatalysis is a popular route to activating CO₂. Activation of the CO₂ molecule can be induced by changing its chemical properties through binding to a metal centre. There are three major binding modes of CO₂ which are demonstrated in Figure 5.1. The “side on” coordination η^2 -CO₂ is stabilised by π back donation. The C coordination η^1 -CO₂ is also stabilised by π back donation and is more common for electron rich metal centres. The final binding mode, “end on” coordination η^1 -OCO, consists of oxygen coordination through electrostatic interactions.

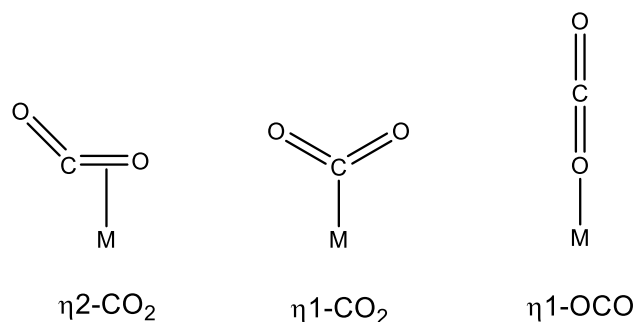


Figure 5.1: Binding modes of CO₂ onto metals.

Metal-ligand systems are particularly effective at activating CO₂. The insertion of CO₂ can result in the formation of organic molecules. An example is the insertion of CO₂ into a metal hydride which results in the formation of carbon monoxide and metal hydroxide. Most electrocatalytic reactions of CO₂ follow through a carbon monoxide intermediate.

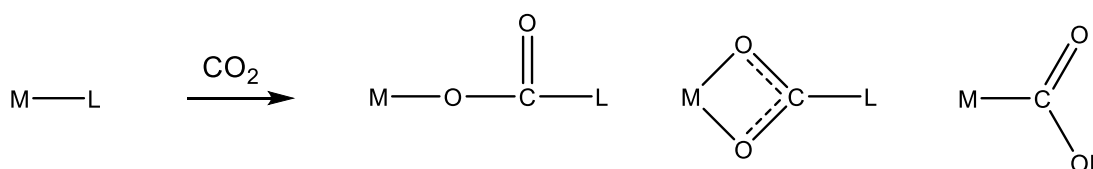


Figure 5.2: Insertion of CO₂ into metal-ligand complexes.

Both homogeneous and heterogeneous electrocatalysts have been reported in the literature.³ Transition metal organometallic complexes are extensively used in homogeneous CO₂ catalysis, acting as redox mediators in the CO₂ reduction process. Transition metals include nickel^{4,5}, cobalt⁴⁻⁸, iron^{5,6}, ruthenium⁹, and rhenium¹⁰, which have either square planar or octahedral coordination to polydentate ligands such as porphyrins^{6,7} phthalocyanines^{4,5,8}, and pyridines.^{8,10} Heterogeneous CO₂ activators include a range of metal and alloyed electrodes.¹¹⁻¹⁵ Most common products from these catalysts are formic acid^{11-14,16} and CO^{5,17}, although methane¹⁵, ethylene¹⁸, and methanol¹⁹ have all been reported. Copper is of particular interest due to its ability to catalyse the production of a range of hydrocarbons and alcohols including propanol.²⁰

Popular iron sulfide world hypotheses postulate the use of iron sulfide materials as catalysts for the activation of CO₂.²¹⁻³⁰ Iron sulfides are naturally synthesised in several environments including hydrothermal deep sea vents.^{31,32} According to the general hypothesis, the chemical activation of dissolved CO₂ is achieved by the

binding of the molecule to iron sulfide surfaces. Some hypotheses suggest that the morphologically porous systems create natural ionic gradients that mimic an electrochemical circuit, thus electrochemically aiding the catalytic process.^{27–30} Overall, hypotheses also suggest that the synthesis of longer chain organic molecules is possible by growth of the organic molecule by further CO₂ activation while it is still bound to the sulfide surface in an autocatalytic process.³³

Evidence for electrocatalytically driven CO₂ activation and utilization on iron sulfide surfaces is described by Roldan *et al.*³⁴ One of the most significant challenges of iron sulfide utilisation is the air and moisture sensitivity of sulfides. In aerobic conditions, they are easily converted to oxides, and iron(II) components are oxidised to iron(III). The use of the solvothermal decomposition methods investigated in Chapter 4 permitted the synthesis of heavily protected iron sulfide nanoparticles. The TEM of a relevant material, hexagonal shaped greigite sheets, show surface structures that are in exact agreement with the calculated surface structure of pure greigite. These particles demonstrate a delay in oxidation thus allowing facile handling and transportation prior to electrochemical tests.

Electrochemical experiments show the synthesis of small organic molecules on the surface of carbon loaded greigite nanoparticles in three carbon rich pH buffer solutions. Formic acid is made in all three pH's, with the highest rate of productivity at pH 6.5, and lowest rate at pH 4.5. Acetic acid is the second most prevalent product, formed again in all three pH buffer solutions, with the highest occurrence at pH 6.5 and lowest at pH 4.5. Methanol is the third notable reaction product; it is found at pH 6.5 and 4.5 but not at pH 10.5. Finally, pyruvic acid is formed only at pH 6.5 (Figure 5.3). Acetic acid requires a slightly more complex reaction route as two carbon dioxide molecules must be activated in close proximity to each other on the surface of the iron sulfide. Methanol is synthesised only at low pH's because it requires substantial reduction and 6H⁺ to synthesise. The presence of pyruvic acid is intriguing as its 3C chain suggests that an autocatalytic process may exist as predicted by Origins of Life hypotheses.^{21–30}

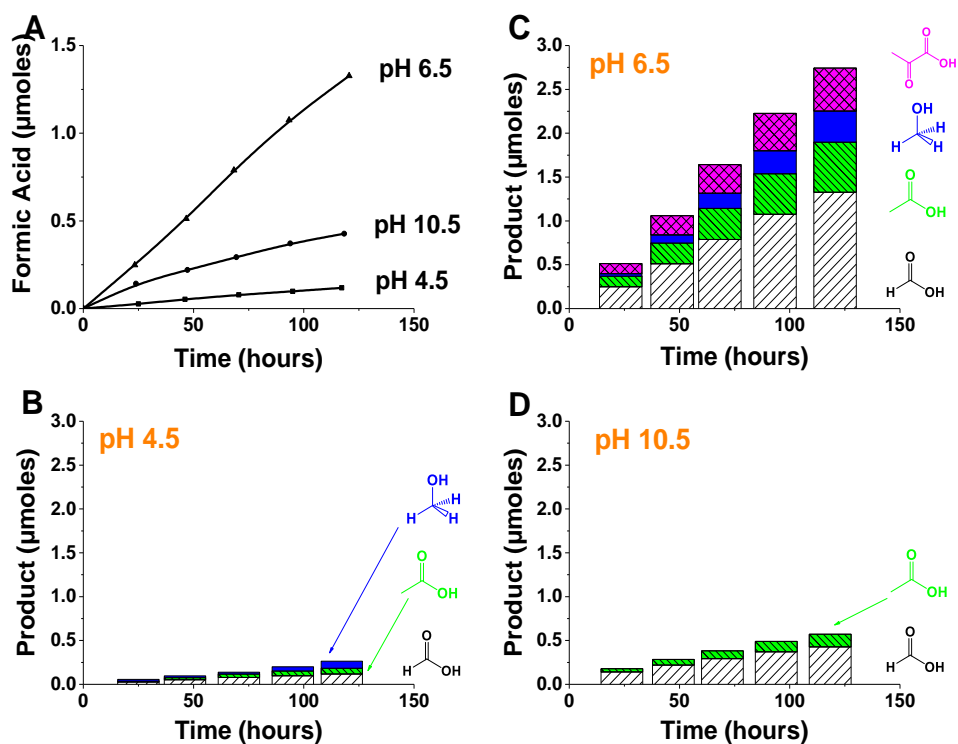


Figure 5.3: Electrocatalytic reaction products of CO₂ on carbon loaded greigite at **B.** pH 4.5, **C.** pH 6.5, and **D.** pH 10.5, and **A.** formation rate of formic acid at the three pH buffer solutions. Figure reproduced produced with permission of Roldan *et al.*³⁴

It is important to note that the low turnover numbers for the reaction products suggest an inefficient reaction system. There are several implications to this. Firstly, high turnover frequencies are not necessarily a requirement for origins of life hypotheses, given the timescales involved in the evolutionary processes. The essence of the theory and a reason for its popularity is that rather than an efficient process occurring on a reactive surface, a process is able to occur on a system that is constantly formed in hydrothermal vents, and therefore statistics of the synthesis of organic products from carbon dioxide are improved. The second point is to consider the suitability of the setup and whether this exploits the reactive system for maximum efficiency or if early degradation of the system as a result of environment leads to the low turnover numbers. Complications arise from the fact that the major competing reactions with CO₂ reduction are water dissociation (the process describing water breaking into H⁺ and OH⁻)³⁵ and water splitting (the process in which water reacts to become O₂ and H₂)³⁶ – both provide a source of hydrogen needed for the formation of small organic molecules from CO₂.

The aim of this chapter is to understand the structural integrity of the greigite nanoparticles during electrochemical cycles. The first way to do this is to understand natural processes (without the aid of, for example, electrochemistry) that affect iron sulfides at various pH environments. Literature is extensive on this topic and sheds light onto some of the observations here. An investigation of the cyclic voltammetry traces and what redox processes each of the features corresponds to is essential. The chosen *in situ* methods for this investigation were XAS and Attenuated transmission reflectance infra-red (ATR-IR) spectroscopy. The combination of the techniques allowed insight into local changes in the iron environment, as well as changes in water and sulfur species, and in some cases carbon species, as a function of potential.¹ The explanation of effects observed in this data is however vital to understanding effects seen in XAS; together they provide a comprehensive view of the evolution of the system and therefore are referred to repeatedly in the text. Appendix 3 provides CV data (Figure A3.1) and ATR-IR data (Figure A3.2-5). For both *in situ* techniques, novel *in situ* cells were produced. Details of these are also provided in the main text and in Appendix 3. The results for greigite will be compared briefly to those of violarite, a system that does not produce any reaction products.

5.2 Method

5.2.1 Sample

5.2.1.1 Synthesis of carbon loaded greigite 18

$\text{Fe}(\text{Bu}_2\text{NCS}_2)_3$ (0.1 mmol, 0.0670 g), $\text{S}_2(\text{Bu}_2\text{NCS})_2$ (0.4 mmol, 0.0946 g), and mesoporous carbon (0.266 g) were heated in oleylamine (20 mL) for 1 hr under reflux at 240° C. This produced a black precipitate. The mixture was cooled for 1 hr, then washed and centrifuged with MeOH (3 x 60 mL). The resulting black powder was dispersed into CHCl_3 (100 mL), then filtered and dried *in vacuo*.

5.2.1.2 Synthesis of violarite 22

$\text{Fe}(\text{Bu}_2\text{NCS}_2)_3$ (0.1 mmol, 0.0670 g), $\text{Ni}(\text{Bu}_2\text{NCS}_2)_2$ (0.1 mmol, 0.0467 g) were heated in oleylamine (20 mL) for 1 hr under reflux at 240° C. This produced a black precipitate. The mixture was cooled for 1 hr, then washed and centrifuged with

¹ The CV traces and ATR-IR measurements were performed by another student of the CO₂ consortium and is unreported in thesis or paper format at time of publishing this thesis.

MeOH (3 x 60 mL). The resulting black powder was dispersed into CHCl_3 (100 mL), then filtered and dried *in vacuo*.

5.2.1.3 Buffer solutions

The pH 6.8 buffer solution was made by the addition of KH_2PO_4 (0.1 M, 13.61 g) and K_2HPO_4 (0.1 M, 17.42 g) to deionised water (1 dm^3). The pH 4.5 phosphate buffer solution was made by the addition of KH_2PO_4 (0.2 M, 27.21 g) to deionised water (1 dm^3). The pH 10.5 carbonate buffer solution was made by the addition of K_2CO_3 (0.2 M, 27.64 g) to deionised water (1 dm^3). A pH meter was used to check and adjust pH.

5.2.1.4 Standards

The oxyhydroxide (**21**) was made by drying uncapped iron sulfide in air on a glass slide and was characterised by XRD as a mixture of goethite and lepidocrocite (Figure A4.2, Appendix 4). Iron(III) oxide, haematite (powder, $<5\mu\text{m}$, $\geq 99\%$, **23**) was purchased from Sigma Aldrich Ltd. A pellet was made using haematite (7 mg) and polyvinyl pyrrolidone (90 mg), provided by the beamline. Iron(III) chloride, $\text{FeCl}_3 \cdot 6\text{H}_2\text{O}$ (ACS reagent grade, 97%, **24**) and iron(III) sulfate hydrate, $\text{Fe}_3(\text{SO}_4)_2 \cdot x\text{H}_2\text{O}$ (97%) were purchased from Sigma Aldrich Ltd. Both were dissolved in deionised water and sealed in capillaries under anaerobic conditions.

5.2.2 Electrochemical Cell

The electrochemical cell (Figure 5.4) was designed to perform EXAFS measurements in fluorescence on the surface of an electrode. The cell body, carved out of Teflon, limits experimental error from unwanted contact with conductive walls. The body of the cell can hold up to 10 cm^3 of electrolyte. At the front of the cell, an inverted cone shaped Teflon ring holds a 40 μm Kapton window in place with silicon rubber. The material is thin enough to limit further fluorescence loss since there is significant loss due to an electrolyte layer. The working electrode is a 1 cm diameter carbon rod. The rod is drop coated with chloroform dispersed sample at one end, and the remainder of the rod is covered with insulating tape so that contact with electrolyte occurs only at the sample. The electrode is held horizontally with a screw system at the back of the cell which allows the electrode's distance from the window to be adjusted. The flexibility of the screw system allows the optimum set up to be achieved so that the electrode can be pushed as close to the window as

possible without restricting the movement of electrolyte thus causing severe resistance. A silver chloride reference electrode and a platinum wire counter electrode - are held perpendicular to the working electrode and are inserted into the cell via custom made holes on the cell cover. Swagelok adaptors present on the cover are used for gas inlet and outlet. The inlet is attached to tubing which allows gas to be bubbled directly into the electrolyte. The cover is screwed onto the cell to create an airtight environment. Finally, the cell is held in an aluminium cell holder that can be screwed into a variety of sample stages; cell alignment is needed only once and the cell is steady when connected to the potentiostat circuitry. This means the cell is aligned once and is steady when connected to the potentiostat.

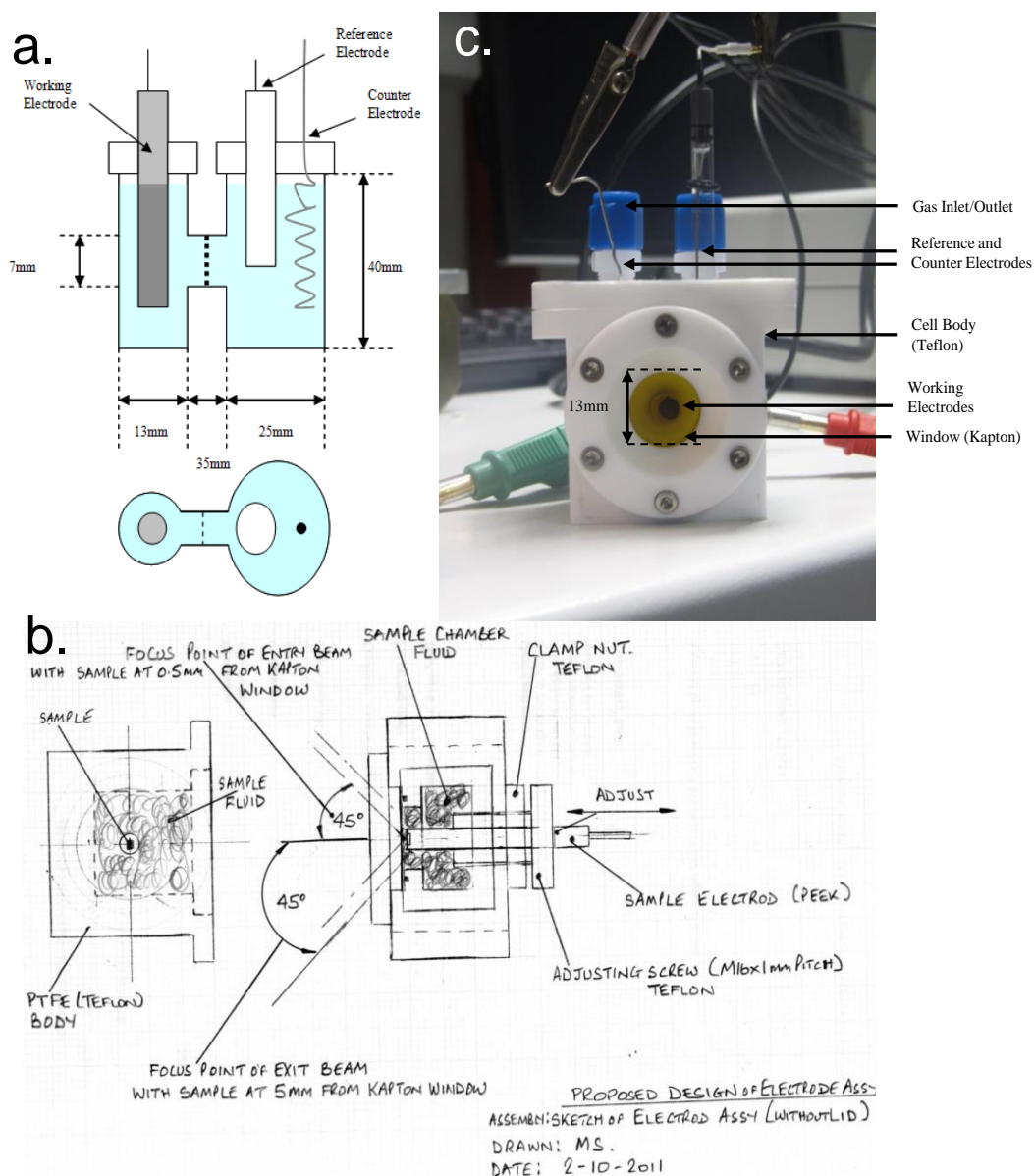


Figure 5.4: a. Design of electrochemical cell used in laboratory measurements, b. Design of *in situ* electrochemical cell used for XAS measurements (drawn by Mike Sheehy), and c. Labelled image of *in situ* electrochemical cell.

5.2.3 Preparation of Experiment

The experimental conditions for XAS acquisition are not as strict as those for tracking product formation; with this, very small product quantities are measured whereas by XAS, much larger bulk changes are observed. In order to degas and for carbon dioxide enrichment of the system for product testing, the electrolyte is bubbled with N_2 and CO_2 which are first purified through a separate bubbler to

remove dissolved organic contaminants. The electrode supported sample is then inserted into the degassed buffer solution. The emphasis of these experiments is to analyse the supernatant and headspace for organic products and so the counter electrode is held in a separate chamber partitioned by a thin membrane to prevent oxidation of reduced products at the counter electrode.

XAS measurements were performed in order to understand bulk structural changes of the sulfide structure during electrochemistry. The gasses were bubbled directly into the electrolyte, and electrodes were held within the same chamber. Typically, the loaded electrode was screwed halfway into the cell so that the back of the cell was sealed before the electrolyte was poured in. The cell was then sealed from the top, and tapped to insure dispersion of any bubbles caught on the sample. The working electrode was moved forward as close to the window as feasible (about 0.5mm distance from the window), and the reference and counter electrodes were inserted. When the setup was complete the cell was placed in line with the beam and connected to the potentiostat.

5.2.4 *In situ* Acquisition

After taking spectra at open potential, a step profile was programmed onto the potentiostat to run at stationary potentials for an hour each. The potentials were chosen as they corresponded to features of the cyclic voltammogram (CV) offline (Figure A3.1, Appendix 3), and also represented a variety of potentials within the loop. For greigite, the CV was performed over two cycles at potentials of -0.25 V, -0.8 V, -1.0 V, +0.4 V, -0.5 V, -0.8 V, -1.0 V, and +0.4 V versus Ag/Ag⁺. Each experiment lasted approximately 8 hrs. For violarite, one cycle was performed using stationary potentials at -0.25 V, -0.8 V, -1.0 V, +0.4 V, and -0.5 V. Violarite measurements lasted 5 hrs.

XAS measurements were acquired at the iron K-edge (7112 eV), and for violarite, the experiment was repeated with fresh sample on the nickel K-edge (8333 eV). XAS measurements were set so that each acquisition lasted *ca.* 20 minutes, thus providing three scans at each potential. A k range of 11 Å⁻¹ was possible in this time frame.

5.2.5 Beamline

XAS data was acquired on the Dutch-Belgian EXAFS beamline, BM26A. Monochromatic radiation was supplied by a double Si(111) crystal. All *in situ* measurements were acquired in fluorescence mode using the 9 element germanium solid state detector.

5.2.6 Data Analysis

XAS data was normalized and background subtracted using Horae Athena software.³⁷ Detailed EXAFS analyses were performed on Excurve Version 9.273.³⁸

5.2.7 Sulfur K-edge

Ex situ sulfur K-edge XAS measurements were taken of carbon loaded greigite before and after a CV run in a pH 6.8 phosphate buffer solution bubbled with N₂. The measurements were performed to understand if significant structural changes occurred at the sulfur sites of greigite, and if probing these changes using the method could be useful for future investigations.

5.2.7.1 Sample

To obtain the greigite sample after electrochemistry (**18b**), a used electrode was removed from the electrolyte and dried inside a glove bag under anaerobic conditions. The dried carbon electrode was then scraped into a glass vial and sealed in nitrogen. For the unused greigite sample (**18**), carbon loaded greigite was used as supplied. The unused and spent greigite were loaded evenly onto carbon tape and placed in a vacuum chamber prior to S K-edge acquisition.

5.2.7.2 Standards

Solvothermal synthesis of carbon loaded hexagonal greigite nanoparticles (**18**) is described in section 5.2.1.1. Mineral pyrite from the Huanzala mines (**26**) was donated by Utrecht University Geosciences Department. The pyrite was previously ground down from bulk in a glove box and stored in a sealed glass container with nitrogen. Sodium sulfite, Na₂SO₃ (≥ 98%) and iron(II) sulfate heptahydrate, FeSO₄·7H₂O (ACS reagent grade, ≥ 99%) were purchased from Sigma Aldrich Ltd and used as purchased.

5.2.7.3 *Beamlines and Acquisition*

Fluorescence and total electron yield (TEY) data of the electrochemical samples and oxidised sulfur species were collected at XMaS, ESRF, and data for the sulfide standards was collected at LUCIA, Soleil. XMaS is equipped with a number of monochromators, of which a thin Si (111) phase plate is optimised for sub 3 keV operations. A Vortex® multi-cathode single element solid-state detector was used for fluorescence measurements, and drain current was measured simultaneously. At Soleil, a double crystal Si (111) monochromator was employed for the measurements. A 4-elements silicon drift diode was used to measure fluorescence and drain current was measured simultaneously. All measurements were performed in vacuum.

5.3 Results and Discussion

Carbon loaded greigite (**18**), and violarite (**22**) were investigated in this electrochemical experiment. Both were made using the solvothermal decomposition of iron or iron and nickel dithiocarbamates in oleylamine. For the synthesis of carbon loaded greigite, iron dithiocarbamate was decomposed in the presence of mesoporous carbon by 10 weight % while the violarite was used pure due to instability of the carbon loaded product. The solvothermal decomposition product is ideal in this experiment for a number of reasons. Firstly, it is repelled by water and therefore does not dissolve into the aqueous electrolyte. Secondly, it is capped and therefore does not react with the electrolyte unless induced by an external current. Finally, the decomposition produces well defined surfaces that can be modelled theoretically for CO₂ activation parallel to experiment. Carbon loading is preferred due to the increased electrical contact from the conductive medium and the even dilution and dispersion preferred for EXAFS.

It is important to note that compared to structures and processes investigated *in situ* in Chapter 4, the system here is complicated by several considerations. Previously, cluster chemistry of systems with short range structure was investigated, for which EXAFS presented an ideal technique. In this chapter, the evolution of the structure of two inverse spinel systems is investigated. The structure of greigite in its simplest form contains 2 iron sites – four coordinated tetrahedral and six coordinated octahedral, there are also two oxidation states, one of which (3+) is found in both

octahedral and tetrahedral geometry. In addition, the solvothermal decomposition results in 50-100nm particles, and the surface therefore has significant effect on the overall EXAFS spectrum. There are more than 14 iron sites on the two most prominent surfaces of the nanoparticles according to DFT (Appendix 5), these can be grouped into two sites (tetrahedral and octahedral), adding to the already existing sites in the bulk. While the tetrahedral bond distances of bulk and surface have been grouped for simplification, the bulk and surface octahedral sites are very different and therefore are considered separately. Once electrochemistry begins, EXAFS is further complicated owing to an increased number of bond types and distances within the first shell. Phase change from interaction with water species must be taken into account: this is usually conversion of the sulfide to an oxyhydroxide, and then oxide in some cases. The Fe-O bond distance from oxidation processes must be considered against the three sets of Fe-S in the first shell of the inverse spinels. The supernatant between the sample and window, and any dissolved species within it, must also be considered. The contribution of dissolved species cannot be considered quantitatively as the electrolyte is dynamic. With a smaller cell volume, this may not be an issue as equilibrium is reached much quicker. In this work, more emphasis is placed on linear combination fitting of the XANES region. Through this, oxyhydroxides and oxides are more distinguishable from each other, although this presents some limitations with respect to data interpretation due to large errors. Examples of LCF analyses from each set of results are shown in Figure A6.1-5, Appendix 6.

The reactive behaviour of the system with carbon dioxide is undetected by EXAFS on the iron k-edge owing to the low efficiency of the reaction process and competition with other processes involving water of which there is great excess.

5.3.1 Greigite

The nanoparticulate greigite structure (**18**) was solved *ex situ* using EXAFS. While greigite is well understood by XRD, the variation of the EXAFS for the nanoparticulate structure and in particular contribution from surface bond distances was first established. Surface bond distances were obtained from computational studies, while bulk distances are known from XRD literature. The best fits were judged by the reduced chi squared value, and the drift of the interatomic distances

from their expected values. The bulk tetrahedral Fe-S bond distance of greigite is 2.15 Å. The value of the tetrahedral Fe-S bond distance of the most prominent surface of the nanoparticles is 2.24 Å. The surface octahedral bond distance is 2.33 Å while the bulk octahedral bond distance is 2.46 Å. With a Δk of 9, the maximum bond distance resolution is 0.17; the surface and bulk distances are therefore grouped into tetrahedral and octahedral distances with DW factor as an indicator of bond distance variation due to thermal and static disorder. To avoid the use of too many variable parameters, a range of fixed coordination numbers were tried based of tetrahedral to octahedral on the surface and in the bulk – the two vary slightly. In the best fit, EXAFS was modelled to 1.5 tetrahedral Fe-S at 2.18 Å, and 3.7 octahedral Fe-S at 2.38 Å. 0.3 Fe-O distances at 2.01 Å were implemented into the calculation to improve fitting and indicated a slight oxidation of the system (Table 5.1, Figure 5.5). This calculation was published by Roldan *et al.*³⁴ According to TEM, the dimension of the hexagonal particles range from between 50 to 100 nm in diameter and 10 nm in depth. Therefore, if surface depth is approximately 1 nm, the ratio of bulk to surface can be calculated at between 4.2:1 and 4.6:1 (Appendix 8). The bond distances according to the EXAFS from fluorescence XAS reflect the significant contribution of the surface.

Table 5.1: Best fit for greigite nanoparticles with fixed coordination numbers.

Model	Scatter	N	R_{THEORY} (Å)	R_{EXAFS} (Å)	σ^2 (Å ²)	Reduced χ^2	R -factor
Greigite nanoparticles	O	0.3	-	1.99 ± 0.06	0.007 ± 0.003	5×10^{-5}	40
	S	1.5	2.15-2.24	2.20 ± 0.02	0.014 ± 0.002		
	S	3.7	2.33-2.46	2.38 ± 0.01	0.014 ± 0.002		

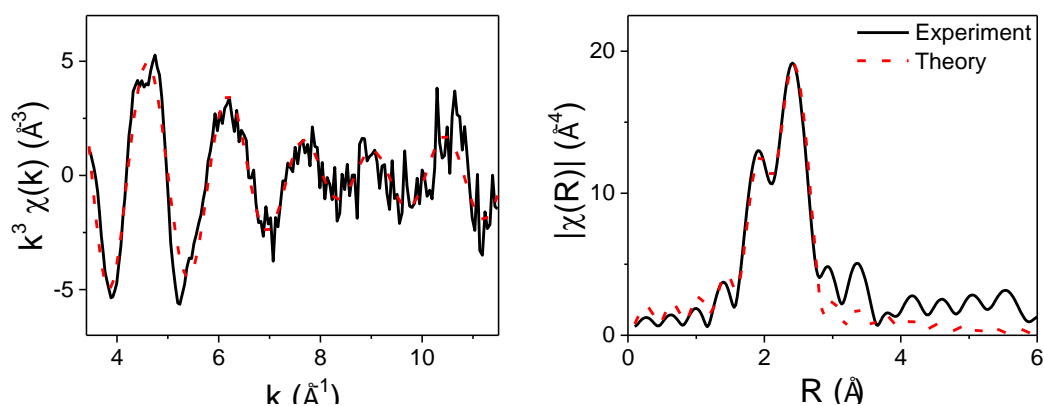


Figure 5.5: EXAFS and FT of greigite nanoparticles.

5.3.2 Greigite in phosphate buffer bubbled with N₂ at pH 6.8

From the onset it is clear that oxyhydroxides and oxides have a crucial role in this investigation as it is shown that sulfide converts to oxyhydroxide electrochemically and in the presence of water. The most common oxyhydroxide is ferrihydrite. This is an amorphous system with the approximate formula $\text{Fe}(\text{OH})_8 \cdot 4\text{H}_2\text{O}$. Here, the oxyhydroxide, determined from LCF and XRD is a mixture of goethite and lepidocrocite. Goethite, or $\alpha\text{-FeOOH}$, the room temperature crystalline form of oxyhydroxide. Related to this is the alpha oxide haematite, or $\alpha\text{-Fe}_2\text{O}_3$. The $\beta\text{-FeOOH}$ akaganeite is an oxyhydroxide which occurs when trace impurities are present, the most frequent impurity being chloride ions, but also including sulfates. The high temperature form of the crystalline oxyhydroxides is lepidocrocite, $\gamma\text{-FeOOH}$, which is closely linked to the oxide crystal structure maghemite $\gamma\text{-Fe}_2\text{O}_3$.³⁹ The oxide magnetite exists with both 3+ and 2+ iron centres. This oxide is significant because it is an inverse spinel, and the oxide analogue of greigite which is studied in this chapter. The only iron oxide to contain purely iron (II) centres is wustite, FeO – this is naturally quite unstable, converting to iron (III) oxide readily in aerobic atmosphere.³⁹ According to literature, the amorphous oxyhydroxide, ferrihydrite, is the most common oxidation product of iron sulfides (in particular pyrite) in aqueous environments in nature.^{40,41} The multistep process resulting in oxyhydroxide formation is controlled by many factors;⁴¹ It is suggested that initial presence of ferrihydrite can lead to accelerated oxidation of pyrite. This accelerated oxidation is not limited to the presence of ferrihydrite, with report of manganese dioxide and nitrates having a similar effect.⁴² Moreover, increased acidity of water as a result of pyrite oxidation, due to the formation of sulfates, leads to other iron containing products being formed.⁴⁰ In other literature, a study of mackinawite in air over six months yielded results showing the gradual formation of magnetite through a greigite - and possibly goethite - intermediate.⁴³ Mackinawite disk-like particles heated in air showed the formation of magnetite adlayers of ten micrometer depths. The rate of magnetite formation was limited in this case by the migration of iron from the sulfide core to the magnetite interface.⁴⁴ The observation that amorphous ferrihydrite is predominantly formed from iron sulfides in aqueous conditions, and increasingly more crystalline oxidation products including goethite and haematite are formed in drier conditions was noted by Nordstrom.⁴⁵ The result here of the formation of crystalline oxyhydroxides from the aerobic drying of iron sulfide is

therefore logical. The presence of lepidocrocite is however less intuitive given that this is the high temperature variation of oxyhydroxide.

Investigating the evolving structure of the greigite system under electrochemical conditions was approached by first performing linear combination fitting of the material at different potentials in electrolyte. The standards used in the linear combination fitting included a range of iron species, particularly oxides, oxyhydroxides and dissolved iron species in 3+ and 2+ oxidation states (Figure A9.1, Appendix 9). Input parameters for EXAFS were derived from the linear combination fitting results at each potential. Bond distance was kept constant, and parameters including coordination were refined. Where it was not possible to keep ideal bond distances, the bond distances were refined separately. Particular attention was given to bond distances from the common oxyhydroxide goethite for which three distances exist in the first shell. These were taken as one average. While coordination number and average bond distances from EXAFS analysis are shown in this chapter, full output parameters are provided in Appendix 10.

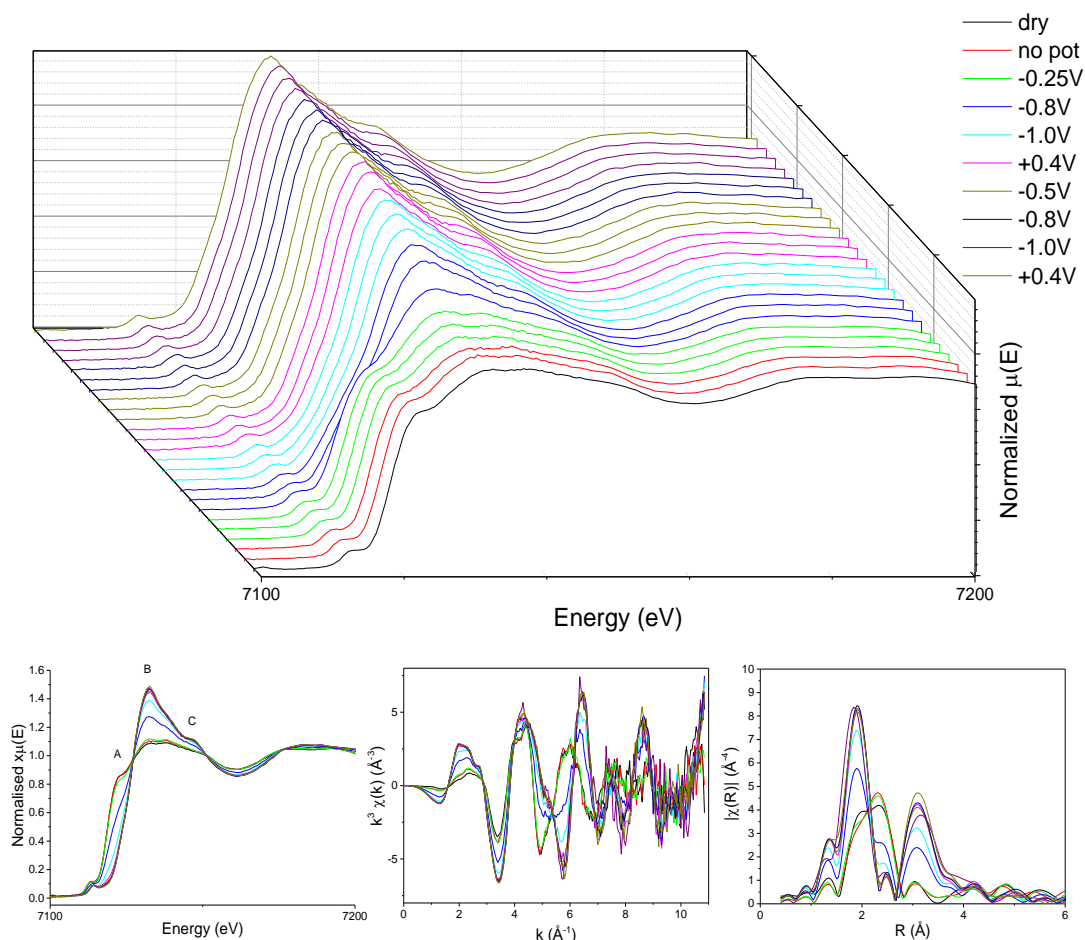


Figure 5.6: a. *in situ* XANES spectra during two CV loops of carbon loaded greigite in a pH 6.8 buffer solution bubbled with N_2 (18a), and merged b. XANES spectra, c. EXAFS, and d. FT at each potential in the loop.

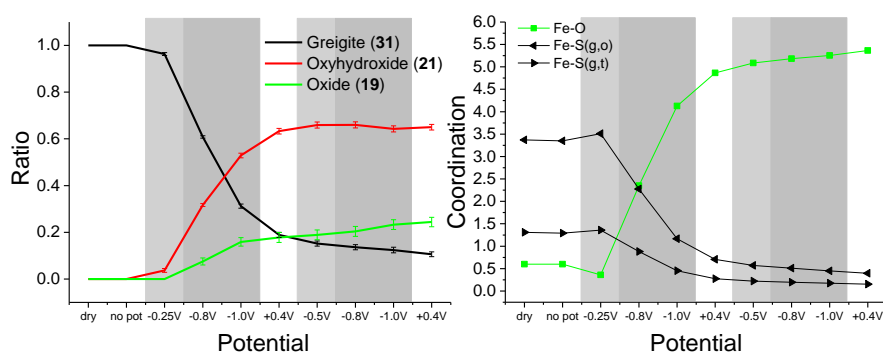


Figure 5.7: a. Linear combination fitting and b. coordination numbers derived from EXAFS modelling of carbon loaded greigite in a pH 6.8 buffer solution bubbled with N_2 (18a) at each potential in the loop.

The first system studied electrochemically was the greigite structure in a pH 6.8 phosphate buffer solution degassed with N_2 (18a). The structure of greigite is shown

to be stable at this pH, with little change in the spectra upon immersion in the buffer solution. When potential is applied at -0.25 V, the structure remains stable, with few changes occurring in the XANES. Rapid oxidation of the greigite structure to oxyhydroxide begins when potential is set to -0.8 V and continues at a constant rate at -1.0 V. The process only slows down when the cycle is taken to a positive potential at +0.4 V. The ratio of oxyhydroxide remains constant through the second cycle. Instead, a growing presence of the iron oxide haematite is observed towards the end of the first cycle. This is most likely formed from the oxyhydroxide as the surface oxidation matures. EXAFS analysis reveals the same pattern. The coordination number of Fe-O, a bond distance that encompasses both oxyhydroxide and oxide, reaches a maximum of 5.4. The oxidation state of the iron species is not shown to change dramatically, rather, the shoulder related to the 1s to 4s transition which is more allowed in sulfides due to more electron donation from the p orbitals of the soft sulfur ligands, gradually disappears to create spectra that are more characteristic of oxides (Figure 5.6 and 5.7). While haematite is detected, bond distances of haematite are very similar to those of magnetite, an inverse spinel oxide analogous to greigite. Its formation on the surface as an intermediate should not be discounted. Oxyhydroxide and haematite are both 3+ species. It is unclear whether only the iron(III) component of the greigite that reacts to form the oxides or if iron(II) is also affected. The ratio at the end of the two cycles between oxide type phases and greigite is 0.8:0.2. This means that at least 80 % of the system is in a 3+ state whereas prior to oxide formation the total 3+ component is 33 %. The CV of the greigite in pH 6.8 buffer solution contains several features of interest. The cycle range covers the potential for water dissociation and water splitting. This is noticed in the ATR-IR spectra where at -0.8V an increase in -OH stretch at 3000 cm⁻¹ is coupled with a decrease in -OH stretch with hydrogen bonding at 3400 cm⁻¹ (typical of water). This indicates a classic water dissociation from H₂O to OH⁻ and H⁺.³⁵ At -1.0 V, the intensity of this water stretch decreases significantly but with no increase in the -OH stretch suggesting that water is split and H₂ is formed as is expected at this potential.³⁶ Water dissociation at the surface of the greigite instigates rapid oxyhydroxide formation as seen by XANES, since OH⁻ groups are far more reactive and better surface binders than H₂O. The formation of oxyhydroxide is coupled with formation of IR-active sulfur species which are shown by IR to increase at negative potentials. At +0.4 V the opposite occurs. The IR-active sulfur species are reversed

according to ATR-IR. A halt in the formation of oxyhydroxide is also observed here thus tying the two processes together. By the next cycle, water dissociation and water splitting, and both sulfur species evolution and oxyhydroxide formation recommence.

Reversible oxidation and reduction is unobserved at the iron K-edge. This is in contrast to signals in the cyclic voltammogram and *in situ* ATR-IR which both indicate reversible processes related to potential involving the water and sulfur species only. The conclusion is that much of the phase change is driven by water and sulfur electrochemistry rather than iron redox properties. This is backed by ATR-IR data which shows the increase and decrease of peaks at the region belonging to oxidised sulfur species – unfortunately the IR region also corresponds to phosphate species and important questions must be asked about the role of the phosphate buffer solution on the surface. The iron is affected in an irreversible manner as a result of these ongoing reversible reactions – the formation of the oxyhydroxide and gradually the oxide does not seem reversible.

Proof-of-concept sulfur K-edge measurements were taken *ex situ* of carbon loaded greigite before and after a CV run in a pH 6.8 phosphate buffer solution degassed with N₂. S K-edge XAS is highly effective in identifying sulfur species owing to the large energy shift (up to 14 eV) as a result of sulfur oxidation states. The technique is also surface sensitive due to the small penetration depth of the low energy. The results revealed several pieces of information.

Interpretation of the XAS data requires comparison with spectra of standards. The first standard shown in Figure 5.8 is fresh hexagonal sheet greigite synthesised by the solvothermal decomposition of an iron dithiocarbamate precursor in oleylamine (**18**). The spectrum acts as a standard for S²⁻ with an edge jump at 2469 eV. There is also a broad feature between 2474 and 2482 eV which is characteristic of sulfide structures. The second standard is mineral pyrite extracted from the Huanzala mines of Peru (**26**) prepared and donated by Meleke Balk from the Paul Mason group of the Geosciences Department at Utrecht University, Netherlands. The pyrite was ground down to a powder in anaerobic conditions and stored under nitrogen for a year before the sulfur XAS was acquired. The pyrite is used as an S₂²⁻ standard with an edge jump at 2470 eV, although evidence of a small amount of SO₄²⁻ species is observed

at higher energies ca. 2482 eV. Iron sulfite, and iron sulfate are used as positively charged sulfur standards.

The carbon loaded greigite (**18**) shows a significant contribution from S_2^{2-} as well as S^{2-} species at its surface. Sulfide phases are known to transform over time to the most stable iron sulfide phase pyrite. The S_2^{2-} species is probably found closer to the surface which S k-edge is sensitive to since the Fe-S distance of pyrite at 2.26 Å is not observed on the more infiltrating Fe K-edge EXAFS of the same structure. The surface also shows traces of positively charged sulfur species. The spent greigite sample taken after being run through a CV (**18b**) has similar peaks at S^{2-} and S_2^{2-} , with a small decrease in S^{2-} species. Ratios of peaks in the positively charged sulfur region are more significantly changed. A large contribution from SO_4^{2-} is detected. As well as this, reduction in amount of sulfite species is observed.

Changes during *in situ* ATR-IR are much more pronounced than those shown in the static samples on sulfur K-edge XAS, there are processes which result in sulfurous peaks strengthening, shifting, and disappearing. There is clearly a change in the composition of the surface which may largely be temporary, and the key to isolating and understanding these changes is to watch the electrochemistry *in situ* by sulfur K-edge XAS, or to analyse the greigite structure as well as supernatant at each step of the electrochemical cycle in a pseudo *in situ* experiment.

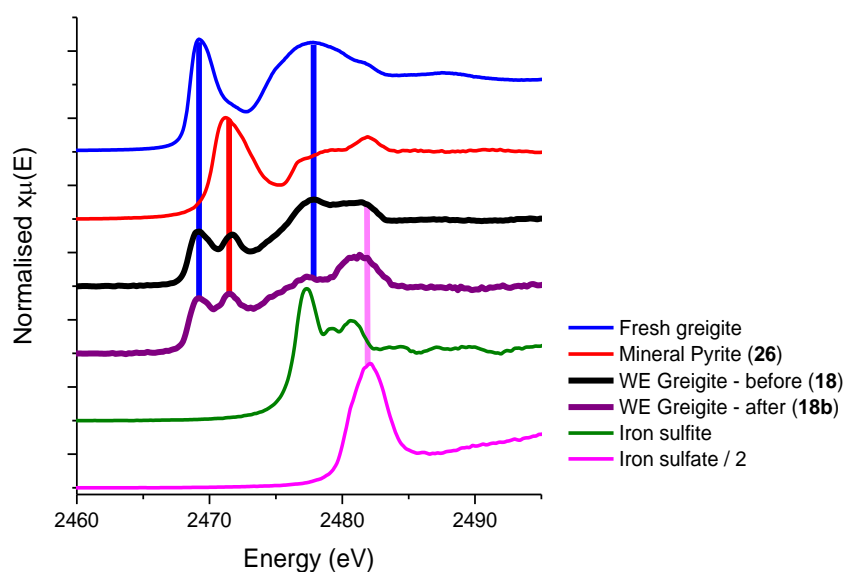


Figure 5.8: a. Sulfur k-edge XANES spectra of used (18b) and unused (18) carbon loaded greigite compared against freshly synthesised greigite, natural pyrite (26), iron sulfite, and iron sulfate.

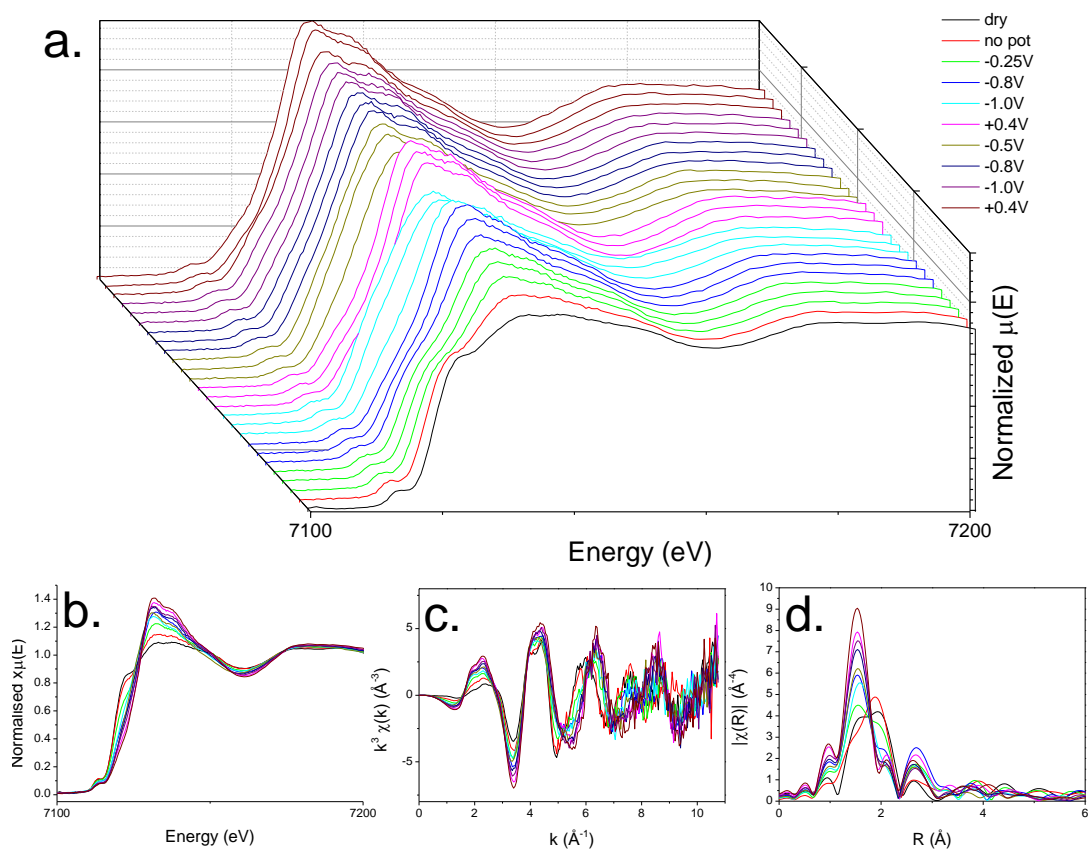
5.3.3 Greigite in phosphate buffer bubbled with N₂ at pH 4.5

Figure 5.9: a. *in situ* XANES spectra during two CV loops of carbon loaded greigite in a pH 4.5 buffer solution bubbled with N₂ (18c), and merged b. XANES spectra, c. EXAFS, and d. FT at each potential in the loop.

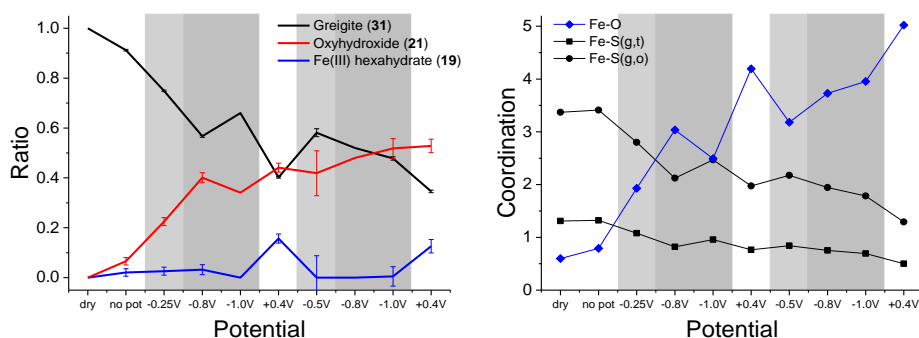


Figure 5.10: a. Linear combination fitting and b. coordination numbers derived from EXAFS modelling of carbon loaded greigite in a pH 4.5 buffer solution bubbled with N₂ (18c) at each potential in the loop.

The process at pH 4.5 (18c) is greatly varied from that at pH 6.8. At this pH, the greigite is unstable from the moment it is immersed in the electrolyte, and before potential is applied. During the cycle, three species are identified: greigite (18),

oxyhydroxide (**21**), and iron(III) hexahydrate (**19**) (Figure 5.9 and 5.10). Identification of the hexahydrate comes from XANES spectra that are similar to iron (III) sulfate or iron (III) chloride dissolved in water. The species is distinguished by a double peak at the white line intensity (Appendix 6).

Formation of oxyhydroxide occurs before potential is applied leading to the conclusion that the acidic environment has a significant effect on the protection provided by the capping agent. In acidic pH, the amine group of oleylamine may be easily protonated to NRH_3^+ . The loss of functionality arises from the fact that NRH_3^+ is more soluble in water than NRH_2 . This means that the surface of the greigite is effectively uncapped and therefore more exposed to the oxidative effects of the electrolyte. Formation of oxyhydroxide continues at a rapid rate between -0.25 V and -0.8 V. In the first cycle of the CV at pH 4.5, the initial flat region covers a much smaller potential range than at pH 6.8. This flat feature is an indication of surface protection (by oleylamine) which is far more effective at pH 6.5 than pH 4.5. By -0.8 V, the ratio of greigite to oxyhydroxide is 0.6:0.4, this is common for both pH 4.5 and pH 6.8. By ATR-IR, water dissociation is apparent once again with the H_2O stretch. At -1.0 V formation of oxyhydroxide seems to reverse: there is a drop in white line intensity and LCF suggests an increased ratio of greigite (Figure 5.9 and 5.10). This could be interpreted as a reversal of oxidation, but most likely, the highly negative potential instigates a breaking of the spent electrode surface to reveal a fresh under layer. This is likely given the rapid and violent H_2 production from water splitting at the surface of the electrode at this low pH as seen also by a significant drop in ATR-IR signal for the H_2O stretch.

The hexahydrate is first detected at +0.4 V but, according to LCF, quickly disappears by the next negative potential and reforms at +0.4 V of the second cycle. Oxyhydroxide formation continues over the second cycle. The 3+ dissolved iron species is not favourable and only exists at the positive potential, disappearing as soon as negative potentials are applied and possibly aiding the rapid formation of oxyhydroxide.

EXAFS reveals a similar story to LCF. The Fe-O distance encompasses all Fe-O species in the system including the hexahydrate. The Fe-O distance shows a much larger increase in coordination number at +0.4 V and a steady increase over the

second cycle indicating that the hexahydrate and/or the first shell of oxyhydroxide continue to be formed over the second cycle.

Compared to the smooth and gradual oxidation at pH 6.8, it is clear that the system at pH 4.5 is much more unstable and highly reactive to environmental changes.

5.3.4 Greigite in phosphate buffer bubbled with CO₂ at pH 6.8

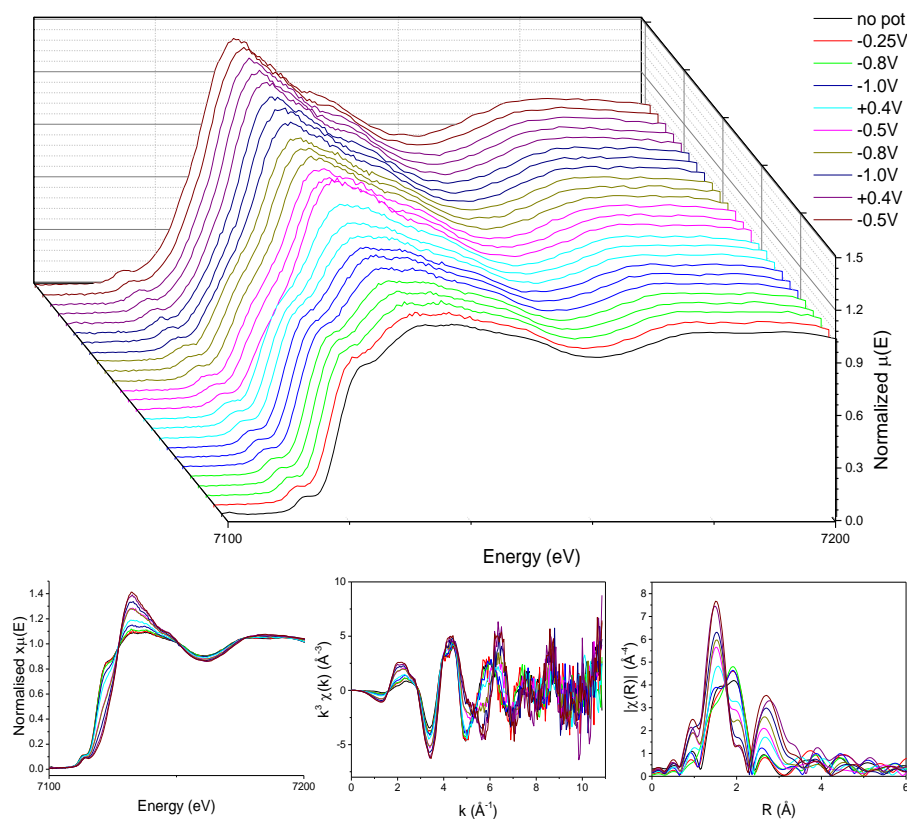


Figure 5.11: a. *in situ* XANES spectra during two CV loops of carbon loaded greigite in a pH 6.8 buffer solution bubbled with CO₂ (18d), and merged b. XANES spectra, c. EXAFS, and d. FT at each potential in the loop.

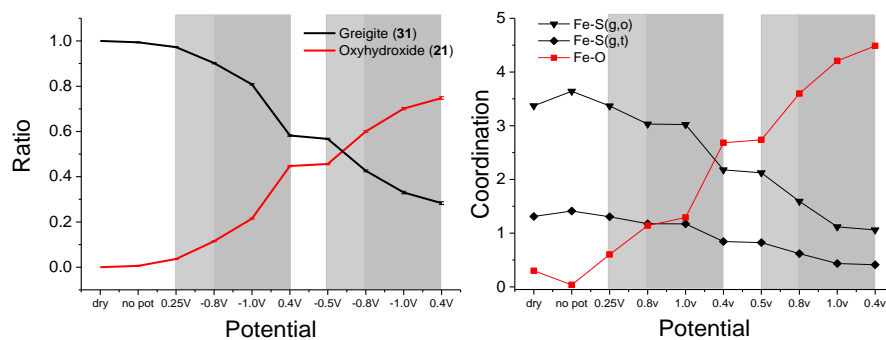


Figure 5.12: a. Linear combination fitting and b. coordination numbers derived from EXAFS modelling of carbon loaded greigite in a pH 6.8 buffer solution bubbled with CO₂ (18d) at each potential in the loop.

In situ electrochemical measurements of greigite in a pH 6.8 phosphate buffer solution bubbled with CO₂ (**18d**) are in contrast to the greigite in buffer solution bubbled with N₂. The CV, when compared to pH 6.8 buffer solution degassed with nitrogen, shows a much more suppressed trace classic of a passivated system. Water dissociation and water splitting occur far less according to ATR-IR, and the formation of oxyhydroxide is less over the two cycles. This ties in with the idea that CO₂ and H₂O compete for surface binding sites. As it has been shown so far, oxyhydroxide is a biproduct of the processes resulting from the interaction of the greigite surface with reactive water species in the presence of an external potential. At neutral pH, CO₂ exists primarily as HCO₃⁻, an effective surface binder that can potentially reduce the number of surface sites available for water binding. The system in this environment retains greigite type structure more successfully than without the presence of CO₂. It may be assumed that both species are in competition as adsorbates and the carbonate helps to partially passivate the surface of greigite thus reducing the rate of oxyhydroxide formation from water.

Before potential is applied, there is no change in the greigite. This confirms the stability of the structure and effectiveness of the capping agent. The structure is also stable at -0.25 V as expected. At -0.8 V and -1.0 V, the rate of oxyhydroxide formation is much slower than in the N₂ saturated buffer solution. At -0.8 V, 80 % of the greigite structure remains, compared to 30 % in N₂. The formation of oxyhydroxide gains momentum by -1.0 V (Figure 11 and Figure 12). Results of the first cycle suggest that the largest loss of greigite occurs at the potential where water splitting occurs.

Between +0.4 V and -0.5 V of the next cycle, reaction processes seem to be completely halted. This positive potential according to ATR-IR shows some carbonate activity with a small loss in the carbonate peak at 1396 cm⁻¹. By the next potential, oxyhydroxide formation continues slowly, subsiding towards the end of the cycle. The ratio of greigite to oxyhydroxide is 0.3:0.7 by the end of the second cycle (Figure 11 and Figure 12). This is the same composition as in the N₂ buffer solution after the first cycle, demonstrating a delay in oxyhydroxide formation and increased stability of the greigite. If the theory is correct that CO₂ slows the oxide formation, then hypothetically a third cycle would show similar characteristics to the

second cycle in N_2 with the reaction levelling off and the possible formation of haematite.

EXAFS of the experiment reveal the same results as LCF. A gradual formation of oxyhydroxide is shown over the two cycles, and a halt to the formation process is observed between +0.4V and -0.5V at the end of the first cycle.

5.3.5 Greigite in phosphate buffer bubbled with CO_2 at pH 4.5

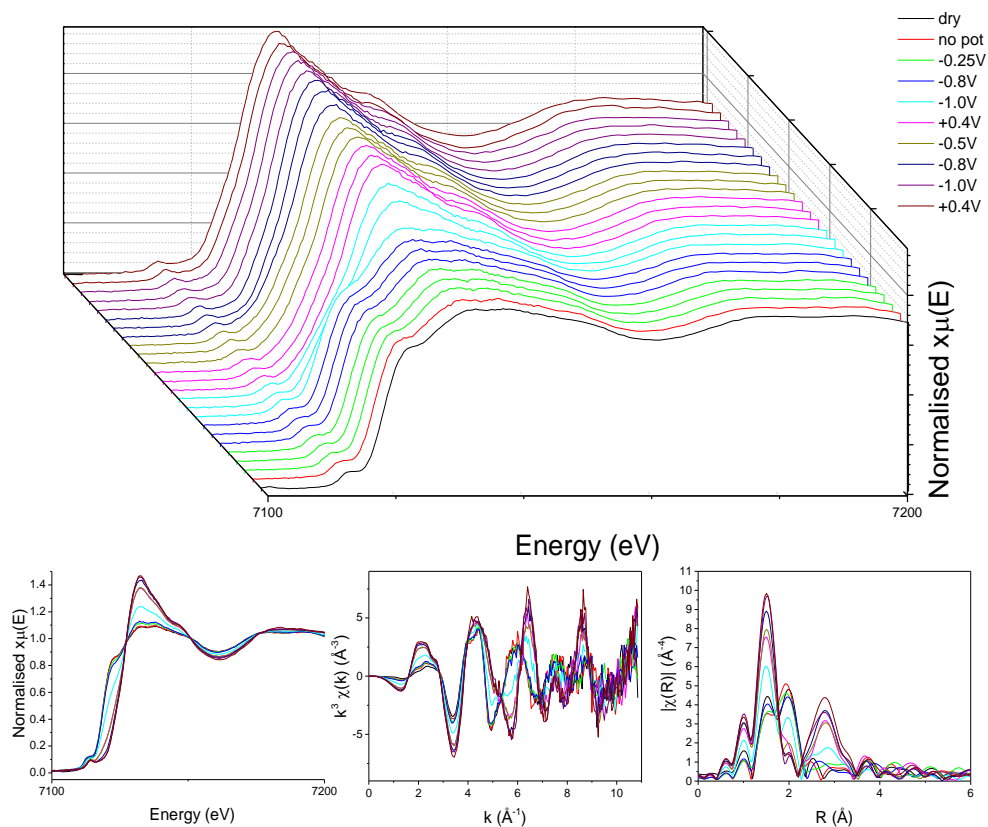


Figure 5.13: a. *in situ* XANES spectra during two CV loops of carbon loaded greigite in a pH 4.5 buffer solution bubbled with CO_2 (18e), and merged b. XANES spectra, c. EXAFS, and d. FT at each potential in the loop.

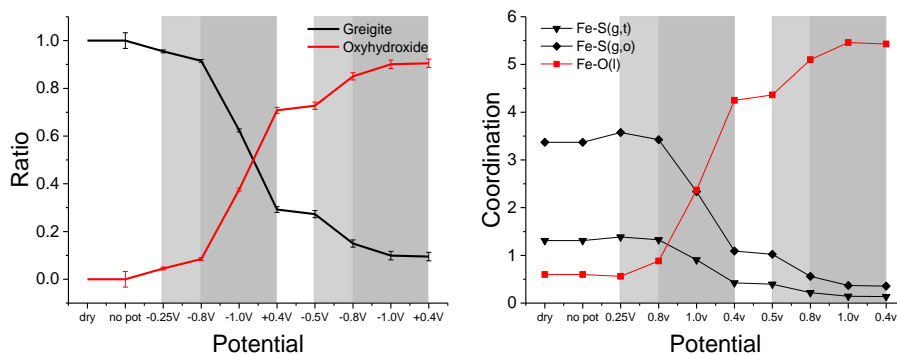


Figure 5.14: a. Linear combination fitting and b. coordination numbers derived from EXAFS modelling of carbon loaded greigite in a pH 4.5 buffer solution bubbled with CO₂ (18e) at each potential in the loop.

When the greigite is put into a pH 4.5 buffer solution bubbled with CO₂ (18e), it behaves surprisingly different to greigite in pH 4.5 buffer solution bubbled with N₂ (18c). The greigite is far less unstable and there is no evidence of dissolution of iron(III) to form iron(III) hexahydrate.

According to XAS, the structure is stable before potential is applied suggesting that the surface is protected. The oleylamine is either not protonated, but this is unlikely at low pH as shown for 18c, or the CO₂ passivates the electrode surface thus protecting it. CO₂ remains an uncharged and linear species at low pH with a small component of charged HCO₃⁻ present. In this form it is a weak surface binder. LCF produces a similar profile at pH 4.5 to pH 6.8 with CO₂, (18d) with recognisable features including stability at open potential, rapid oxyhydroxide formation at highly negative potentials and a halt in the process at the positive potential, followed by a continuation of greigite replacement with oxyhydroxide over the second cycle. The difference between the two pH buffer solutions is that whereas at pH 6.8, the formation of oxyhydroxide gains momentum by -1.0 V, at pH 4.5 the rapid formation begins earlier at -1.0 V. By the end of the first cycle 30 % of the greigite structure remains compared to 60 % remaining at pH 6.8. The final ratio of greigite at pH 4.5 is less than 0.1 (Figure 13 and Figure 14). The effects seen at pH 4.5 may be due to the small HCO₃⁻ constituent

EXAFS is in agreement with LCF analysis showing a gradual formation of oxyhydroxide that becomes rapid by the end of the first cycle, levels out between the positive and negative potential, and continues on the second cycle, gradually slowing

toward the end of the cycle. Trace formation of haematite may be possible according to EXAFS; when looking at the evolution of the bond distances, the Fe-O distance becomes shorter with time which could indicate its formation. Any haematite present in the structure is under the detection limit of LCF which can be fit with or without a small percentage of haematite with large errors.

It must be taken into consideration that saturation of the electrolyte with CO₂ leads to the formation of gaseous CO₂ bubbles which were observed to catch on the grooves of the electrode surface. It is likely that these bubbles could protect the surface from the effects of water before potential is applied and perhaps during the electrochemical cycle. This is only a problem for the *in situ* XAS cell which has a horizontal working electrode. In the electrochemical cell used for product detection, and the cell used for *in situ* ATR-IR, are vertical with the catalyst face down and therefore less prone to the same problem.

In summary, greigite in a pH 4.5 buffer solution bubbled with CO₂ is comparable to greigite in pH 6.8 buffer solution bubbled with CO₂. The process of oxyhydroxide formation at pH 4.5 however is much further accelerated than at pH 6.8. This may be owing to the overwhelming effects of the acidity on the system, particularly with regards to the defunctionalisation of the oleylamine capping agent. Alternatively, it may be the weaker binding ability of CO₂ at low pH, with a higher prevalence of the uncharged linear species rather than the charged HCO₃⁻. In reality, a combination of both effects probably contribute to the more advanced effects on greigite seen at pH 4.5 compared to pH 6.8. The system is also much more stable than greigite at the same pH in N₂. Apart from the protection by CO₂ bubbles at the start of the CV, delayed oxyhydroxide formation is also due to the CO₂ protection of the surface from the competing H₂O / H⁺ adsorption.

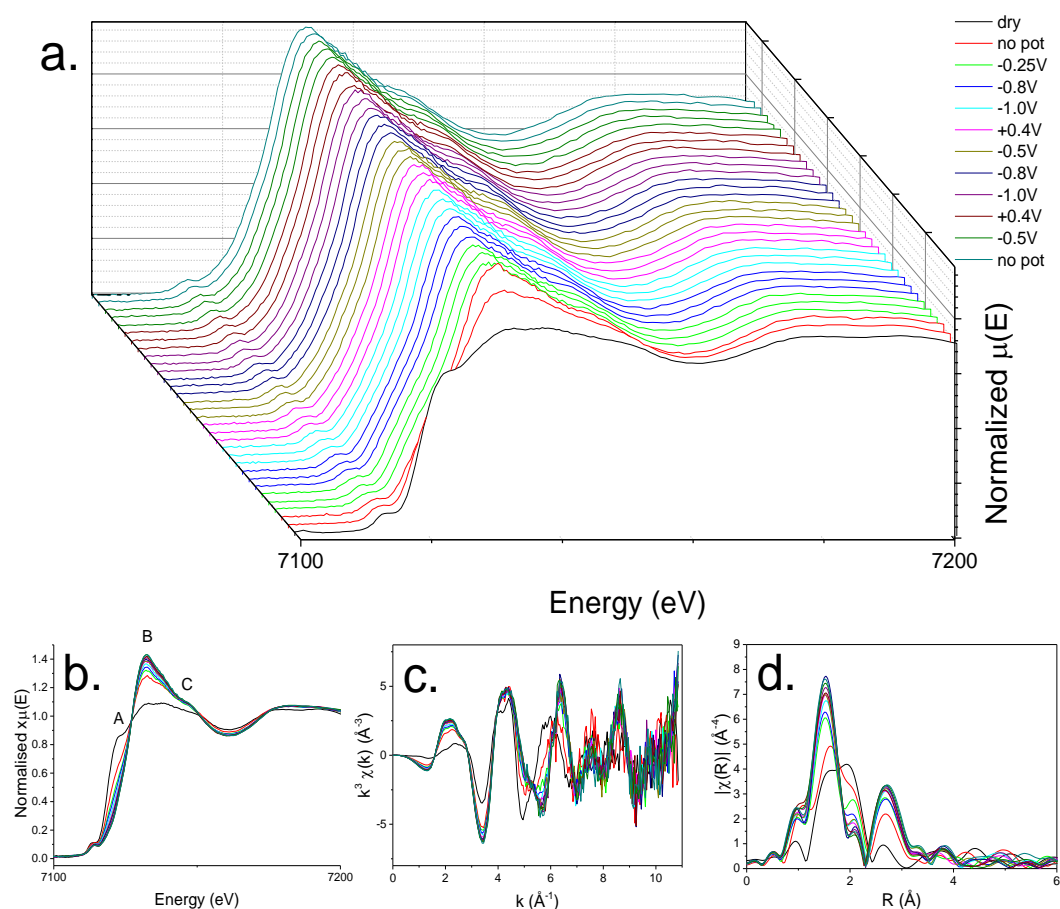
5.3.6 Greigite in carbonate buffer bubbled with N₂ at pH 10.5

Figure 5.15: a. *in situ* XANES spectra during two CV loops of carbon loaded greigite in a pH 10.5 carbonate buffer solution bubbled with N₂ (18f), and merged b. XANES spectra, c. EXAFS, and d. FT at each potential in the loop.

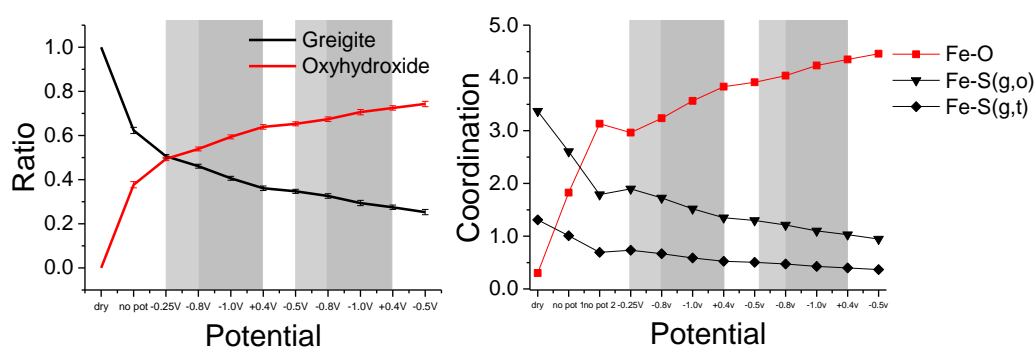


Figure 5.16: a. Linear combination fitting and b. coordination numbers derived from EXAFS modelling of the carbon loaded greigite in a pH 10.5 carbonate buffer solution bubbled with N₂ (18f) at each potential in the loop.

Given the stabilising effect of HCO₃⁻ on the pH 6.8 buffer solution, greigite in the pH 10.5 carbonate buffer solution degassed with N₂ (18f), which contains the doubly charged, and more strongly binding CO₃²⁻ species, is expected to be most stable. In

addition to prevalence of CO_3^{2-} , the capping agent is unlikely to be protonated and iron species are less likely to dissolve in high pH.

The observations however, contradict the expected results. The greigite is least stable in this buffer solution compared to any of the other solutions. Leaving the electrode in the electrolyte without potential over two scans is shown to result in the decrease of greigite by 50 %, replaced by oxyhydroxide. When potential is applied, oxyhydroxide continues to form at a slow rate until the end of the two cycles with no evidence of slowing down although there may be a slight arrest in the reaction process between +0.4 V and -0.5 V as is seen with carbon rich buffer solutions at other pHs. By the end of the two cycles, 30 % of the greigite structure remains. EXAFS fittings are in exact agreement with LCF results (Figure 5.15 and Figure 5.16). While OH^- rapidly binds to iron sites on the surface, the oxidation of sulfur sites requires reaction with H^+ species which are less available at high pH.

The reason for the instability before potential is applied is probably the large presence of highly reactive OH^- species at pH 10.5. The species rapidly binds to the surface of the greigite and creates a hydroxyl layer which contributes to the XANES spectrum. Once the initial surface is completely covered, the formation of oxyhydroxide is slow; between the start and the end of the two cycles, the ratio of oxyhydroxide increases from 0.5 to 0.7. According to ATR-IR, very little water dissociation occurs – this is possibly as a result of a lower number of surface sites available to water, a weaker surface binder than hydroxyl groups and also bicarbonate groups. Water splitting is also suppressed. The formation of oxidised sulfur species is not observed. At the positive potential, a large loss of the symmetric carbonate stretch at 1398 cm^{-1} is observed, proving that carbonate is in some way strongly interacted with the greigite surface and may contribute to its passivation. This is coupled by what seems to be the conversion of OH^- and H^+ to molecular water with a decrease in the OH^- stretch and increase in the H_2O stretch – although expected at the positive potential, the peak change is far more pronounced than in the other two pH's.

Overall, it seems that at high pH, two species – OH^- and CO_3^{2-} - play a major role in passivating the surface. Once they are attached to the surface, any other processes including small organic product formation and oxyhydroxide formation are slowed

down. The bicarbonate species is the source of carbon for any organic product synthesis on the surface of the greigite, however, its strong binding requires a high energy to move on the surface and or dissociate according to Roldan *et al.*³⁴

5.3.7 Bond distances during electrochemical cycle according to EXAFS

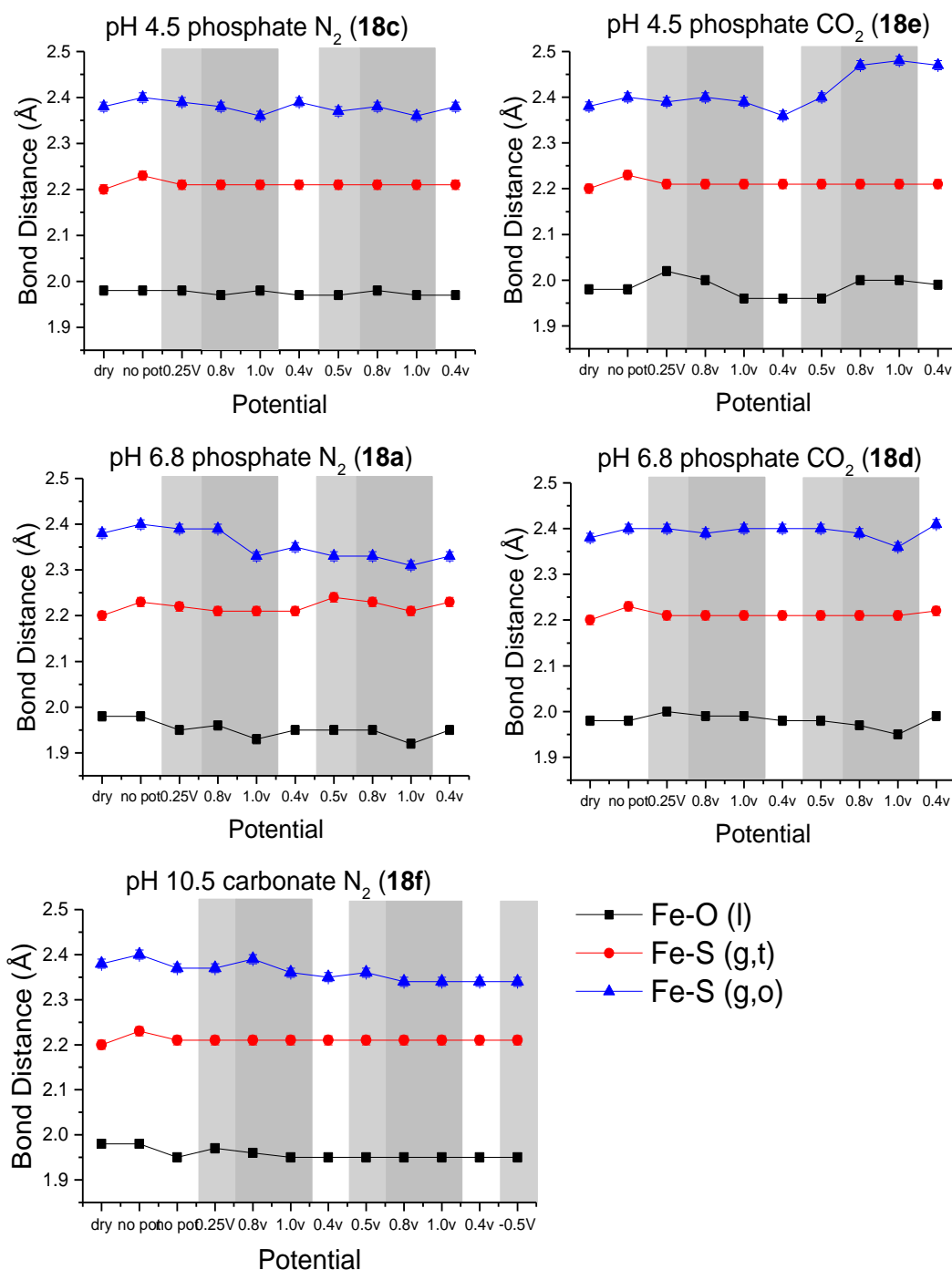


Figure 5.17: Evolution of bond distances according to EXAFS of the carbon loaded greigite structure from oxide formation during CV loops in the five buffer solutions.

Bond distances were optimised on each of the systems after optimising coordination. Therefore bond distance must be analysed for any trends. For the most part, bond distances are constant, there are however a few exceptions. Although the changes mentioned can signify important changes in the system, they are mostly within error.

5.3.8 Violarite in phosphate buffer bubbled with N_2 at pH 6.8

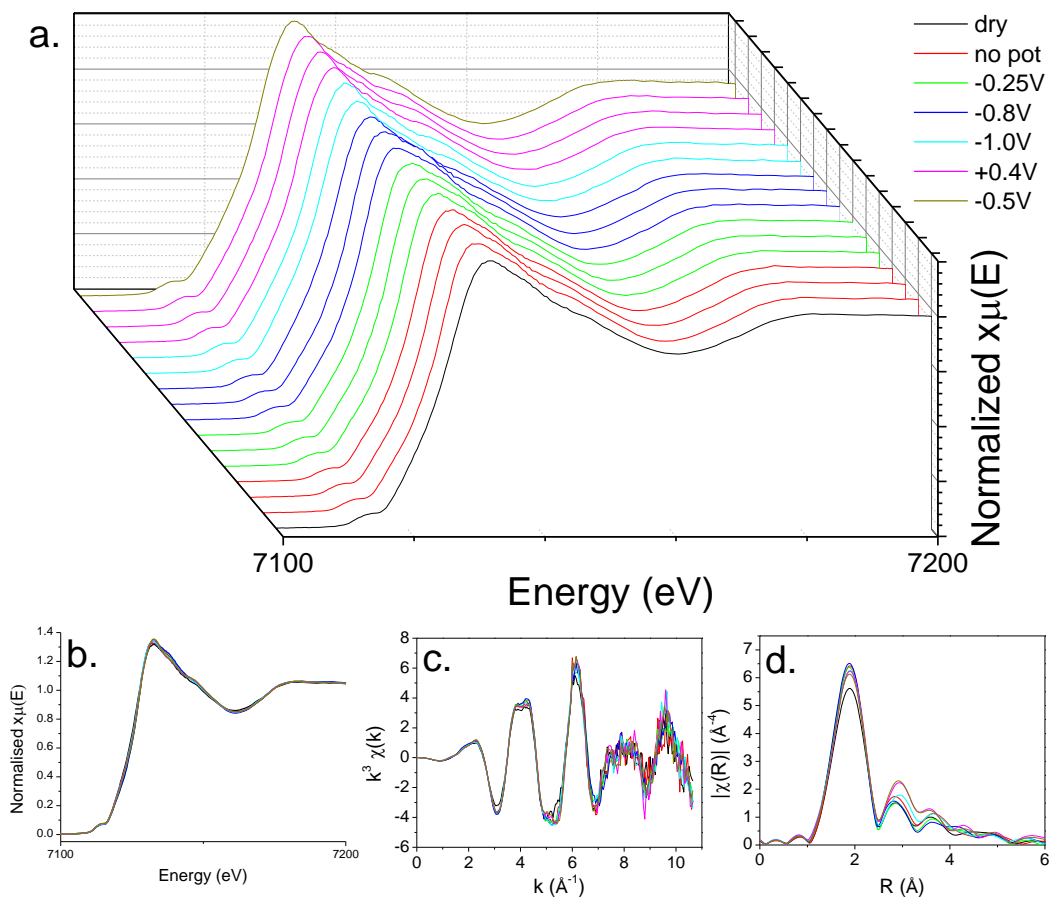


Figure 5.18: a. *in situ* XANES spectra during a CV loop of violarite on the iron K-edge in a pH 6.8 buffer solution bubbled with N_2 (22), and merged b. XANES spectra, c. EXAFS, and d. FT at each potential in the loop.

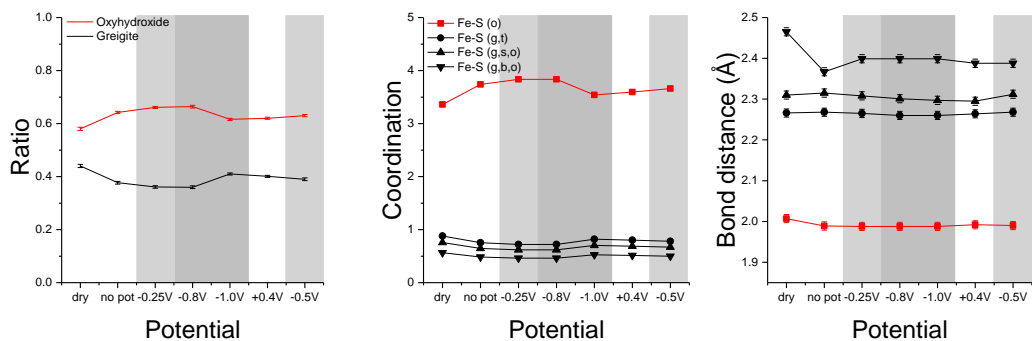


Figure 5.19: a. Linear combination fitting, and b. coordination numbers and c. bond distances derived from EXAFS modelling of violarite on the iron K-edge in a pH 6.8 buffer solution bubbled with N_2 (22) at each potential in the loop.

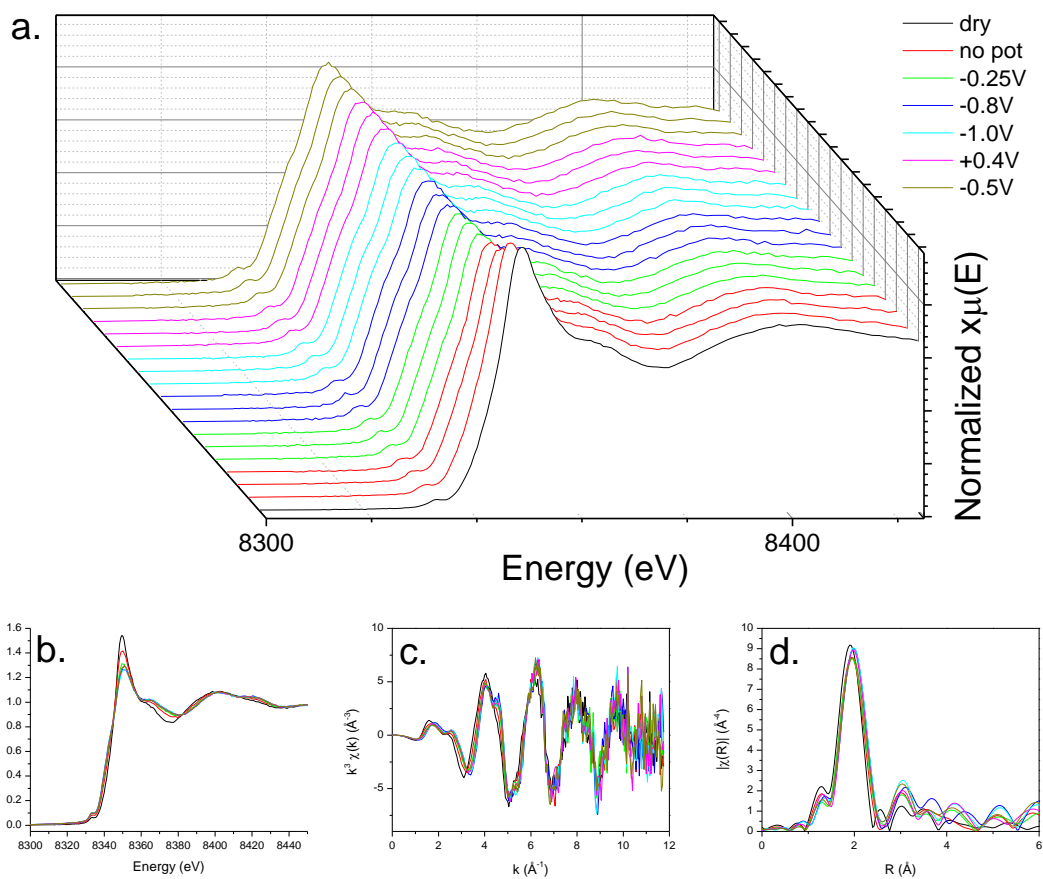


Figure 5.19: a. *in situ* XANES spectra during a CV loop of violarite on the nickel K-edge in a pH 6.8 buffer solution bubbled with N_2 (22), and merged b. XANES spectra, c. EXAFS, and d. FT at each potential in the loop.

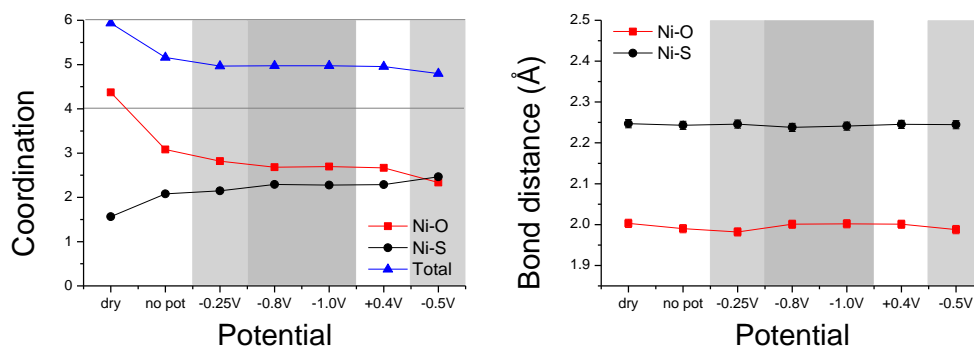


Figure 5.20: a. Coordination numbers and b. bond distances derived from EXAFS modelling of violarite on the nickel K-edge in a pH 6.8 buffer solution bubbled with N₂ (22) at each potential in the loop.

Violarite is a mixed phase inverse spinel sulfide: a third of all sites occupied by nickel(III) species and the remainder are occupied by iron(II). The inverse spinel is one of the few naturally occurring structures to stabilize nickel(III) which sits solely at octahedral B sites. The structure is synthesised by solvothermal decomposition of iron and nickel dithiocarbamates in oleylamine in the presence of thiuram disulfide to form hexagonal sheets similar to greigite made by the same method. Logically, the surface of the violarite has many similarities with the surface of greigite and the chemistry is theoretically analogous. Experimentally however, very little occurs on the violarite surface during electrochemistry. CV profiles are featureless despite the similar structure to greigite. Although there are reports of enhanced reaction by nickel doping in other systems,^{46–48} measurements to determine CO₂ conversion reaction capabilities offline have shown that the violarite is a very inefficient system.

To investigate further, *in situ* electrochemistry of one cycle was performed on both the iron and nickel K-edges in a pH 6.8 buffer solution bubbled with N₂. From the spectra at the iron K-edge, the reason for the lack of sensitivity to the CV is immediately apparent. The spectra show a highly oxidised system before electrochemistry is performed. According to LCF, the system contains only 44 % greigite type structure, and 56 % oxyhydroxide in the solid state. Throughout the electrochemical cycle, the ratio of greigite to oxyhydroxide is altered very little, maintaining an average ratio of 0.4:0.6. EXAFS reveals that the bond distances of the first shell are different to those of pure greigite. The tetrahedral bond distance is shown to be consistently longer at 2.26 Å, and the octahedral surface and bulk bond

distances are shorter in electrolyte at 2.31 Å and 2.39 Å respectively. Bond distances remain largely constant throughout the electrochemical cycle.

LCF of the nickel K-edge is not possible owing to difficulty in securing pure Ni(III) standards. However, the nickel K-edge is far easier to model in EXAFS than the iron K-edge because there is only one nickel site in the bulk. In a pure system, six equivalent Ni-S bond distances are expected in octahedral geometry. The XANES spectrum of the real system in the solid state looks like it has a significant contribution from oxygen in its first shell shown by a high white line intensity. EXAFS modelling confirms this: the average environment of the first shell is made up of 26 % Ni-S distances at 2.24 Å and 74 % Ni-O distances at 1.99 Å. The average coordination around the nickel centre is six, indicating that all the nickel remains largely in 3+ state and octahedral geometry. Upon contact with electrolyte and during the cycle, the large white line intensity decreases significantly. The percentage distribution by the end of the cycle is 51 % Ni-S and 49 % Ni-O. The average coordination decreases to 5, and edge position is also shifted to lower energies by 2 eV. All the evidence points towards the reduction of Ni(III) to Ni(II) and conversion of half the nickel centres from 6 coordinate to 4 coordinate geometry.

Violarite is extensively oxidized in the solid state despite oleylamine capping. The instability and easy oxidation compared to pure phase sulfides may arise from the instability of the nickel centre, in turn affecting the neighbouring iron environments. The nickel is much further oxidised than the iron sites according to the results above. The oxide formation is also irreversible, with electrochemistry resulting in the reduction of nickel(III) to stable nickel(II). The highly reactive surface is not necessarily destructive if it can be harnessed correctly – exposure to CO₂ and steam in anaerobic environments while the violarite is fresh, and re-oxidation of the nickel(II) to nickel(III) on the spent system could result in successful CO₂ reaction. The effect of the photon beam on nickel(III) species during XAS acquisition must also be considered. Previous studies have shown that nickel(IV) complexes can be photoreduced to nickel(II).⁴⁹

5.4 Conclusion

All CV and *in situ* ATR-IR data described in the text are provided in Appendix 3. In this chapter, greigite was investigated from the perspective of both *in situ* methods in

a thorough investigation performed by two students (one of whom is the author of this work). The use of these complimentary datasets allowed the processes of change of the system as a function of applied potential to be pieced together. There are further questions to be answered in this work which are most likely to be answered by computational methods.

There are several conclusions to be made from this work.

The aged surface of greigite is shown from the sulfur K-edge to gain an increasing presence of pyrite type sulfur species over time. The phase conversion of greigite to pyrite is well known in nature.^{41,42}

The capping agent of the greigite sheets plays an important role in passivating the surface until it is ready to be used electrocatalytically; the structure is stable while dry, with minimal oxidation on the surface, and is stable in electrolyte before potential is applied when the capping agent is finally repelled from the surface and other processes are allowed to occur. The capping agent is less able to perform its function at extreme pH conditions. At low pH, oleylamine is defunctionalised, while in high pH, the large presence of OH⁻ overwhelms the capping effect.

Water reactions on the surface of the greigite play a major role in the changes that are observed. Irreversible oxyhydroxide formation from water reactions is apparent, as are reversible oxidised sulfur species formation.

Oxide formation on the surface is not to be confused with oxidation of the iron centre. In all cases, the average oxidation state does not change abruptly as a result of potential, but rather over time as the amount of oxide builds up. We can deduce from observations from CV traces and ATR-IR, that the redox properties of the sulfur species are much more sensitive to potentials in the cycle and in line with redox processes of the water, suggesting that the two may be connected. Oxidised sulfur species are observed at the negative potential when water dissociation and water splitting occur. The reversibility of the redox chemistry is proven by ATR-IR. A key area for further research is the identification of stable sulfur intermediate species during the CV using sulfur K edge XAS.

The mechanism of oxide formation on greigite surfaces is not known, although it is commonly observed in acidic soils.⁴³ Mechanisms of aerobic and anaerobic oxidation of pyrite are much more thoroughly studied.⁴⁴⁻⁴⁶ pyrite oxidation is initiated at surface defect sites consisting of iron(III) species next to sulfur vacancies. Water binding at these sites initiates hydrolysis and hydrogen peroxide formation. OH radicals formed from the dissociation of hydrogen peroxide are thought to attack sulfide species on the pyrite surface, and induce oxidation to sulfate in a multistep process.⁴⁴⁻⁴⁶

Significant differences are noticed in the presence of CO₂ including the delayed formation of oxyhydroxides in both pH 4.5 and pH 6.8. The carbon species present in the solutions act as competitive adsorbates to water species. This indicates that the first step towards organic molecule synthesis, the binding of carbon dioxide to the reactive material, is an efficient process. Of all the pH buffer solutions, the greigite structure is most stable in the pH 6.8 solution in the presence of carbon dioxide. The highest turnover numbers are also found at this pH according to electrocatalytic studies.³⁴ This has important implications for the type of environment suggested in Origins of Life theories which range from acidic to high pH.

It can be assumed that the rapid formation of oxyhydroxide on the surface of the greigite is one of the largest factors preventing efficient carbon dioxide electrocatalysis. While water is required in the reactive process as a hydrogen source, its presence in excess results in rapid oxyhydroxide formation. The system must therefore be designed to reduce the amount of water to the minimum requirement in order to increase reaction efficiency. Ideas include use of non-aqueous electrolytes. Gas phase systems using water vapour or hydrogen are also possibilities, although performing electrocatalysis with gaseous electrolyte is complex. Possibility of sulfur replenishment to reverse oxide formation must also be considered. The violarite system is an interesting one to investigate. Although the surface is highly oxidised from the onset, thus reducing the reactive capabilities, nickel remains in a 3+ state. Its reduction over the cycle is the first observation of a change in oxidation state of a metal in any of the systems studied. While this process is interesting to observe, what it means for catalysis is unclear. There is certainly scope to explore the nickel

species in the system further under different conditions to understand if the reduction is reversible or relevant to catalysis.

5.5 Acknowledgements

Image 5.3 is taken from a paper published by Roldan *et al*³⁴ and consisted of organic products obtained from carbon loaded greigite in an electrochemical cell with aqueous carbon dioxide. The DFT calculated greigite surface structure was derived by Alberto Roldan Martinez and is found in the supplementary section of the same paper.³⁴ The carbon loaded greigite was synthesised by Husn Islam and Anna Roffey. The synthesis of this material is investigated in Chapter 4 of this thesis and also reported in the PhD thesis of Anna Roffey.⁵⁶ Violarite was synthesised by Anna Roffey and reported in the same thesis.⁵⁶ CV traces and ATR-IR measurements mentioned in the text were performed by Siti Nurul Azian Zakaria – this work is as of yet unpublished but clearly justified in Appendix 3. For future reference, Siti Zakaria will publish a thesis titled “Development of electrochemical and spectroscopic techniques in carbon dioxide conversion using iron-nickel sulfide nanoparticles” from Department of Chemistry, University College London. The *in situ* electrochemical cell was designed in collaboration with Andrew Smith, Katherine Holt, and Gopinathan Sankar, and built by Mike Sheehy. Standards used for linear combination fitting included samples belonging to Meleke Balk and Paul Mason of the Geosciences Department of Utrecht University.

5.6 References

- (1) Sullivan, B. P.; Krist, K.; Guard, H. E. *Electrochemical and Electrocatalytic Reactions of Carbon Dioxide*; Elsevier, 1992.
- (2) Amatore, C.; Saveant, J. M. *J. Am. Chem. Soc.* **1981**, *103*, 5021–5023.
- (3) Sánchez-Sánchez, C. M.; Montiel, V.; Tryk, D. A.; Aldaz, A.; Fujishima, A. *Pure Appl. Chem.* **2001**, *73*, 1917–1927.
- (4) Meshitsuka, S.; Ichikawa, M.; Tamaru, K. *J. Chem. Soc. Chem. Commun.* **1974**, 158.
- (5) Furuya, N.; Koide, S. *Electrochim. Acta* **1991**, *36*, 1309–1313.
- (6) Ogura, K.; Yoshida, I. *J. Mol. Catal.* **1988**, *47*, 51–57.
- (7) Nielsen, I. M. B.; Leung, K. *J. Phys. Chem. A* **2010**, *114*, 10166–10173.
- (8) Yoshida, T.; Kamato, K.; Tsukamoto, M.; Iida, T.; Schlettwein, D.; Woehrle, D.; Kaneko, M. *J. Electroanal. Chem.* **1995**, *385*, 209–225.
- (9) Boston, D. J.; Xu, C.; Armstrong, D. W.; Macdonnell, F. M. *J. Am. Chem. Soc.* **2013**, *135*, 16252–16255.
- (10) Sullivan, B. P.; Bolinger, C. M.; Conrad, D.; Vining, W. J.; Meyer, T. J. *J. Chem. Soc. Chem. Commun.* **1985**, 1414.
- (11) Azuma, M.; Hashimoto, K. *J. Electrochem. Soc.* **1990**, *137*, 1772–1778.
- (12) Hori, Y.; Wakebe, H.; Tsukamoto, T.; Koga, O. *Electrochim. Acta* **1994**, *39*, 1833–1839.
- (13) Furuya, N.; Yamazaki, T.; Shibata, M. *J. Electroanal. Chem.* **1997**, *431*, 39–41.
- (14) Ikeda, S.; Takagi, T.; Ito, K. *Bull. Chem. Soc. Jpn.* **1987**, *60*, 2517–2522.
- (15) Hara, K. *J. Electrochem. Soc.* **1997**, *144*, 539.
- (16) Mahmood, M. N.; Masheded, D.; Harty, C. J. *J. Appl. Electrochem.* **1987**, *17*, 1159–1170.
- (17) Yamamoto, T.; Tryk, D. A.; Fujishima, A.; Ohata, H. *Electrochim. Acta* **2002**, *47*, 3327–3334.
- (18) Cook, R. L.; MacDuff, R. C.; Sammells, A. F. *J. Electrochem. Soc.* **1990**, *137*, 607–608.
- (19) Summers, D. P.; Leach, S.; Frese, K. W. *J. Electroanal. Chem. Interfacial Electrochem.* **1986**, *205*, 219–232.
- (20) Hori, Y.; Murata, A.; Takahashi, R. *J. Chem. Soc. Faraday Trans. 1* **1989**, *85*, 2309.
- (21) Wächtershäuser, G. *Syst. Appl. Microbiol.* **1988**, *10*, 207–210.
- (22) Wächtershäuser, G. *Proc. Natl. Acad. Sci. U. S. A.* **1990**, *87*, 200–204.
- (23) Wächtershäuser, G. *Proc. Natl. Acad. Sci. U. S. A.* **1994**, *91*, 4283–4287.
- (24) Keller, M.; Blöchl, E.; Wächtershäuser, G.; Stetter, K. O. *Nature* **1994**, *368*, 836–838.
- (25) Drobner, E.; Huber, H.; Wächtershäuser, G.; Rose, D.; Stetter, K. O. *Nature*

- 1990**, 346, 742–744.
- (26) Blöchl, E.; Keller, M.; Wachtershäuser, G.; Stetter, K. O. *Proc. Natl. Acad. Sci. U. S. A.* **1992**, 89, 8117–8120.
- (27) Russell, M. J.; Daniel, R. M.; Hall, A. J.; Sherringham, J. A. *J. Mol. Evol.* **1994**, 39, 231–243.
- (28) Russell, M. J.; Hall, A. J. *J. Geol. Soc. London.* **1997**, 154, 377–402.
- (29) Russell, M. J.; Martin, W. *Trends Biochem. Sci.* **2004**, 29, 358–363.
- (30) Milner-White, E. J.; Russell, M. J. *Orig. Life Evol. Biosph.* **2005**, 35, 19–27.
- (31) Edmond, J. M.; Measures, C.; McDuff, R. E.; Chan, L. H.; Collier, R.; Grant, B.; Gordon, L. I.; Corliss, J. B. *Earth Planet. Sci. Lett.* **1979**, 46, 1–18.
- (32) Walker, J. C. *Mar. Geol.* **1986**, 70, 159–174.
- (33) Wächtershäuser, G. Barton, L. L.; Mandl, M.; Loy, A., Eds.; Springer Netherlands: Dordrecht, 2010; pp. 1–35.
- (34) Roldan Martinez, A.; Hollingsworth, N.; Roffey, A.; Islam, H. U.; Goodall, J. B.; Catlow, C. R. A.; Darr, J. A.; Bras, W.; Sankar, G.; Holt, K. B.; Hogarth, G.; de Leeuw, N. H. *Chem. Commun.* **2015**, 51, 7501–7504.
- (35) Burgot, J.-L. *Ionic Equilibria in Analytical Chemistry*; Springer Science & Business Media, 2012.
- (36) Gandia, L. M.; Arzamedi, G.; Dieguez, P. M. *Renewable Hydrogen Technologies: Production, Purification, Storage, Applications and Safety*; Newnes, 2013.
- (37) Ravel, B.; Newville, M. *J. Synchrotron Radiat.* **2005**, 12, 537–541.
- (38) Binsted, N. EXCURV98: CCLRC Daresbury Laboratory Computer Program, 1998.
- (39) Cornell, R. M.; Schwertmann, U. *The Iron Oxides: Structure, Properties, Reactions, Occurrences and Uses, Second Edition*; Wiley-VCH Verlag GmbH & Co., 2004.
- (40) Sullivan, P. J.; Reddy, K. J.; Yelton, J. L. *Environ. Geol. Water Sci.* **1988**, 11, 289–295.
- (41) Stumm, W.; Morgan, J. *Aquatic Chemistry*; Wiley-Inte.; New York, 1981.
- (42) Schippers, A.; Jørgensen, B. B. *Geochim. Cosmochim. Acta* **2002**, 66, 85–92.
- (43) Hunger, S.; Benning, L. G. *Geochem. Trans.* **2007**, 8, 1.
- (44) Asaki, Z.; Matsumoto, K.; Tanabe, T.; Kondo, Y. *Metall. Trans. B* **14**, 109–116.
- (45) Nordstrom, D. K. In *Acid Sulfate Weathering*; Kittrick, J. A.; Fanning, D. S.; Hosner, L. R., Eds.; Soil Science Society of America, 1982; pp. 37–56.
- (46) Kaneva, N. V.; Dimitrov, D. T.; Dushkin, C. D. *Appl. Surf. Sci.* **2011**, 257, 8113–8120.
- (47) Zou, Z.; Ye, J.; Sayama, K.; Arakawa, H. *Nature* **2001**, 414, 625–627.
- (48) Sharma, S. D.; Singh, D.; Saini, K. K.; Kant, C.; Sharma, V.; Jain, S. C.; Sharma, C. P. *Appl. Catal. A Gen.* **2006**, 314, 40–46.

- (49) Fackler, J. P.; Avdeef, A.; Fischer, R. G. *J. Am. Chem. Soc.* **1973**, *95*, 774–782.
- (50) Wang, Q.; Morse, J. W. *Mar. Chem.* **1996**, *52*, 99–121.
- (51) Rickard, D.; Luther, G. W. *Geochim. Cosmochim. Acta* **1997**, *61*, 135–147.
- (52) Ward, N. J.; Sullivan, L. A.; Fyfe, D. M.; Bush, R. T.; Ferguson, A. J. P. *Aust. J. Soil Res.* **2004**, *42*, 449–458.
- (53) Schoonen, M.; Elsetinow, A.; Borda, M.; Strongin, D. *Geochem. Trans.* **2000**, *1*, 23.
- (54) Borda, M. I. J. B.; Elsetinow, A. L. R. E.; Strongin, D. A. R. S.; Schoonen, M. A. A. S. *Geochemica Cosmochem. Acta* **2003**, *67*, 935–939.
- (55) Reedy, B. J.; Beattie, J. K.; Lowson, R. T. *Geochim. Cosmochim. Acta* **1991**, *55*, 1609–1614.
- (56) Roffey, A. *Dithiocarbamate Complexes as Single Source Precursors to Metal Sulfide Nanoparticles for Applications in Catalysis*, University College London, 2014.

Chapter 6

Conclusions and Future Work

6.1 Summary

The use of XAS in conjunction with XRD is a powerful technique for characterising crystalline and amorphous or nanoparticulate components of a system.¹ In addition, the use of synchrotron techniques permits flexibility in sample environment which means classically unstable products can be measured in preferred sample environments.²

TM dithiocarbamates act as single source precursors that decompose to form metal sulfides. In the next chapter, the effects of oleylamine on the coordination environment of TM dithiocarbamate complexes were investigated using XAS. The oleylamine, being an electron donor, and in large excess, was found to form bonds with each dithiocarbamate system. In the case of $\text{Fe}(\text{Bu}_2\text{NCS}_2)_3$, significant restructuring was also exhibited as a result of oleylamine interaction.

These interactions have huge consequences on the solvothermal decomposition process which are discussed in the following chapter. Coordination of oleylamine results in destabilisation of TM dithiocarbamate complexes, particularly $\text{Fe}(\text{Bu}_2\text{NCS}_2)_3$ which undergoes reduction, expulsion of a dithiocarbamate ligand, and then decomposition – none of these effects are seen in dodecane. The actual decomposition step is thought to occur due to transamination which sees oleylamine replace the tertiary amine on the dithiocarbamate backbone to form a highly unstable structure.³ Transamination is difficult to pinpoint by most methods including XAS, therefore when and how rapidly transamination occurs is not fully understood. The unstable structure decomposes upon formation.

The addition of thiuram disulfide to the reaction mixture results in a change in decomposition mechanism and final structure allowing access to more exotic phases including the inverse spinel greigite.

It is the structural changes during electrocatalytic processes of this greigite material that were investigated in the final chapter. Oxide formation of the greigite surface was observed in a range of pH buffer solution with and without carbon dioxide

present. Of all the pH buffer solutions, the greigite structure was most stable at pH 6.8, especially in the presence of carbon dioxide. The highest turnover numbers of catalytic products are also found at this pH according to electrocatalytic studies. The capping agent of the greigite nanoparticles plays an important role in passivating the surface until it is made redundant electrocatalytically or by exposure to extreme pH conditions. Significant differences are noticed in the presence of CO₂ including the delayed formation of oxyhydroxides since the binding of carbon dioxide to the catalytic material is a competing process to water binding. The formation of oxyhydroxide probably prevents efficient electrocatalytic carbon dioxide reduction.

6.2 Future work

The TM dithiocarbamate decomposition is versatile. By altering concentration, and in the presence of thiuram disulfide, the decomposition was recently shown to form pyrite at temperatures exceeding greigite formation. This sheds further light onto the role of thiuram disulfide on achieving more sulfur rich, oxidised species. Building a cell that can reach higher temperatures is high priority for liquid systems since capillaries often fail in this.

The electrochemical setup is such that of the two competing surface reactions - with water or carbon dioxide – reactions with water are overwhelmingly favoured, and a thick oxyhydroxide layer is formed. This results in a core shell system which would not be disadvantageous if the outer shell was known to be an affective catalyst. Rust is however a poor catalyst while structures such as haematite are more active – in fact, in the neutral pH, where traces of haematite are detected, catalytic products are more abundant. Tailoring the conditions in order to achieve a haematite surface layer is one option to improve catalytic activity. The other option is to perform gas phase catalysis with water vapour. This levels the probability of reaction between the two inorganic compounds and the greigite surface although if carbon dioxide reduction can occur without a large overpotential in these systems is yet to be established. The final option is the use of non-aqueous electrolyte such as an ionic liquid. This is currently being undertaken in an ongoing project with Queens University, Belfast, although ionic liquids are already very good at binding with carbon dioxide and creating the much needed change in symmetry required to reduce it: ionic liquids have been shown to produce catalytic products using the most inert electrodes.^{4,5}

It is only fitting to conclude with a final note on how this work has related to Origin of Life hypotheses. The project chose a route which was inspired by the work of Russel, Martin, and Hall⁶ which suggested the electrocatalytic activation of carbon dioxide. The alternative hypothesis, postulated by Wächtershäuser,⁷ was for the most part ignored because rather than suggesting a catalytic cycle, it suggested irreversible oxidation of iron sulfides to the iron disulfide pyrite. A small change in the relative ratios of sulfide to disulfide species seen in the sulfur K-edge XANES of greigite before and after an electrochemical cycle indicates that Wächtershäuser may have been right. This is only one proof-of-concept dataset and further investigation is needed.

6.3 References

- (1) Sankar, G.; Thomas, J. M.; Catlow, R. *Top. Catal.* **2000**, *10*, 255–264.
- (2) <http://www.esrf.eu/Instrumentation/sample-environment>.
- (3) Hollingsworth, N.; Roffey, A.; Islam, H.; Mercy, M.; Roldan, A.; Bras, W.; Wolthers, M.; Catlow, R.; Sankar, G.; Hogarth, G.; de Leeuw, N. *Chem. Mater.* **2014**, *26*, 6281–6292.
- (4) Rosen, B. A.; Salehi-Khojin, A.; Thorson, M. R.; Zhu, W.; Whipple, D. T.; Kenis, P. J. A.; Masel, R. I. *Science (80-.)*. **2011**, *334*, 643–644.
- (5) Yang, H.; Gu, Y.; Deng, Y.; Shi, F. *Chem. Commun. (Camb)*. **2002**, 274–275.
- (6) Russell, M. J.; Daniel, R. M.; Hall, A. J.; Sherringham, J. A. *J. Mol. Evol.* **1994**, *39*, 231–243.
- (7) Wächtershäuser, G. Barton, L. L.; Mandl, M.; Loy, A., Eds.; Springer Netherlands: Dordrecht, 2010; pp. 1–35.

Appendices

Appendix 1

LCF analysis of the solvothermal decomposition of $\text{Ni}(\text{iBuNCS}_2)_2$

The graph below displays example LCF analysis of the *in situ* data during the solvothermal decomposition of nickel diisobutyl dithiocarbamate in oleylamine. Fits relate to the ratios of oleylamine interacted (octahedral) and non-interacted (square planar) species of nickel dithiocarbamate. The standards used were the nickel dithiocarbamate solution in oleylamine at room temperature, and the nickel dithiocarbamate solution in dodecane at room temperature. The oleylamine mixture contains octahedral complexes consisting of two bidentate dithiocarbamate ligands and two oleylamine ligands. The dodecane solution contains dissolved square planar nickel dithiocarbamate complexes. With increasing room temperature, the octahedral complex in the reaction mixture is shown to become gradually more square planar. Fits are good with acceptable R-factors.

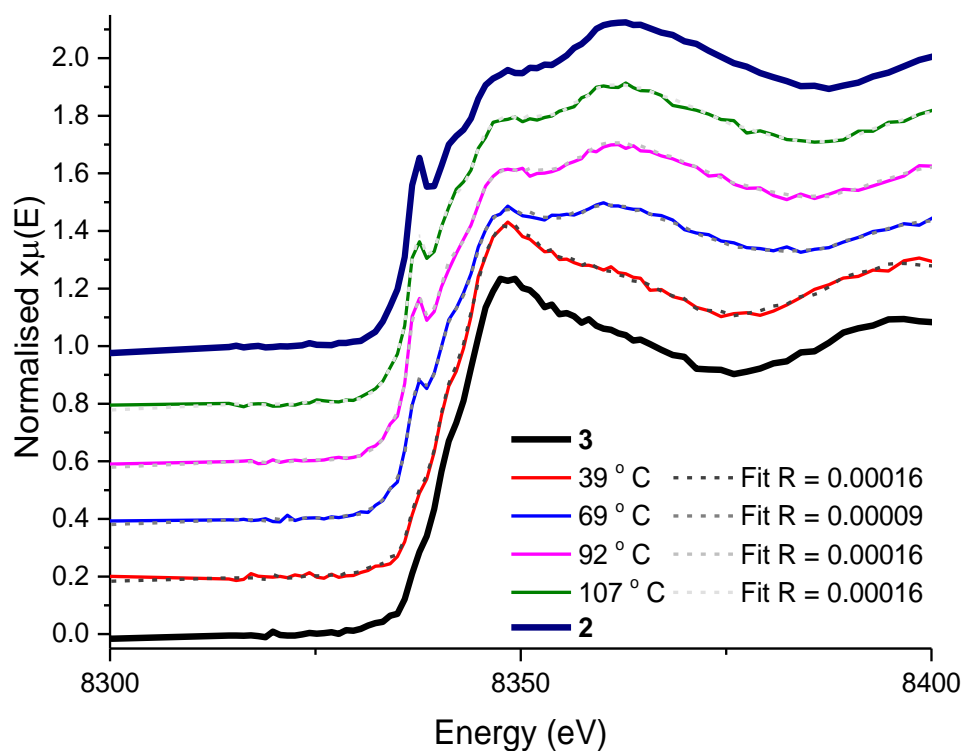


Figure A1.1: Example LCF analysis of solvothermal decomposition of 3.

Appendix 2

The structure of synthetic cubane

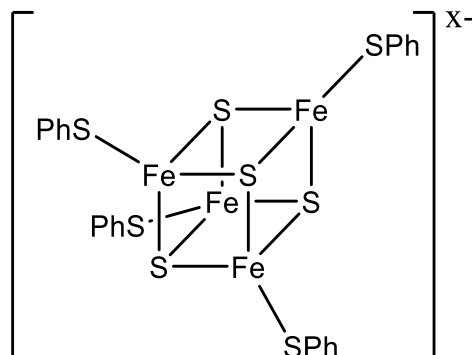


Figure A2.1: Chemical structure of a synthetic cubane stabilized by phenyl groups.

The synthesis of greigite nanospheres from the solvothermal decomposition of a cubane precursor¹ generates significant interest in the area of iron sulfide synthesis. The results are noteworthy because the cubane cluster is considered a bridge between biological catalysts and Origins of Life hypotheses. Cubanes form the metal sites of bacterial ferredoxin proteins²⁻⁴ and also serve as building blocks for inverse spinel sulfides.⁵

Here, XAS is used to understand the cubane structure.

Method

The cubane $[\text{N}^n\text{Bu}_4]_2[\text{Fe}_4\text{S}_4(\text{SPh})_4]$, bis(tetra-*n*-butylammonium) tetrakis [benzenethiolato- μ_3 -sulfido-iron] (**25**), was synthesised using the method reported by Christou⁶, and developed from the original synthesis methods of Holm.^{7,8} XRD of the cubane structure were taken on a single crystal Bruker Smart XRD and refined using the SHELXTL program suite (private communication, Dr. Nathan Hollingsworth). 7-8 mg of the cubane was pelletized with 90 mg of boron nitride. The XAS measurement of **25** was performed in transmission. The iron K-edge (7112eV) measurements were performed at BM26A, ESRF. Ion chambers and a 9 element solid state germanium detector were used to acquire data. XAS data reduction and EXAFS modelling were performed on Horae Athena, and Excurve 9.273 respectively.^{9,10}

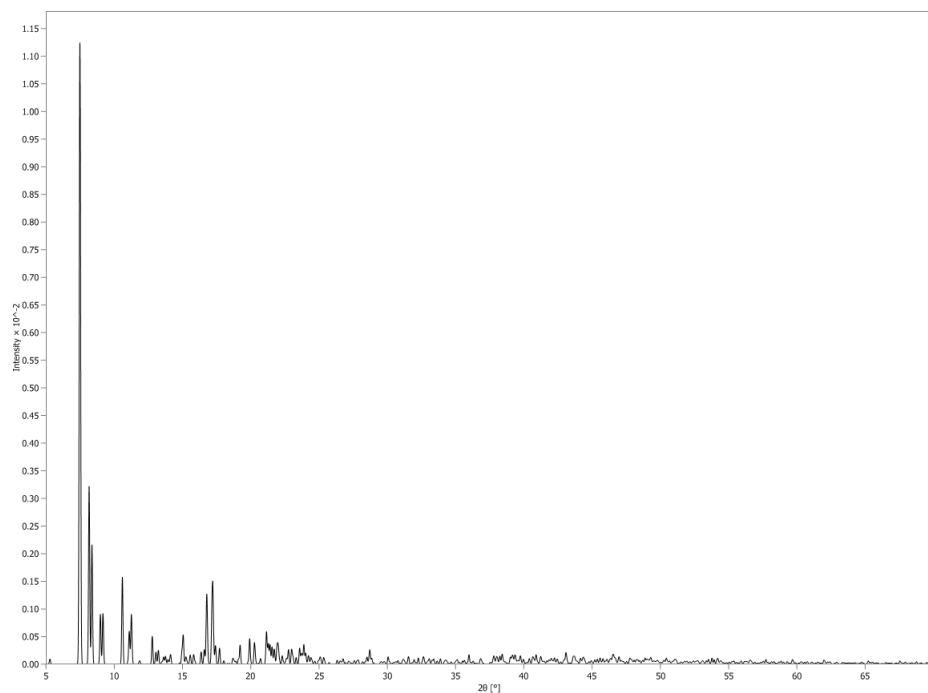
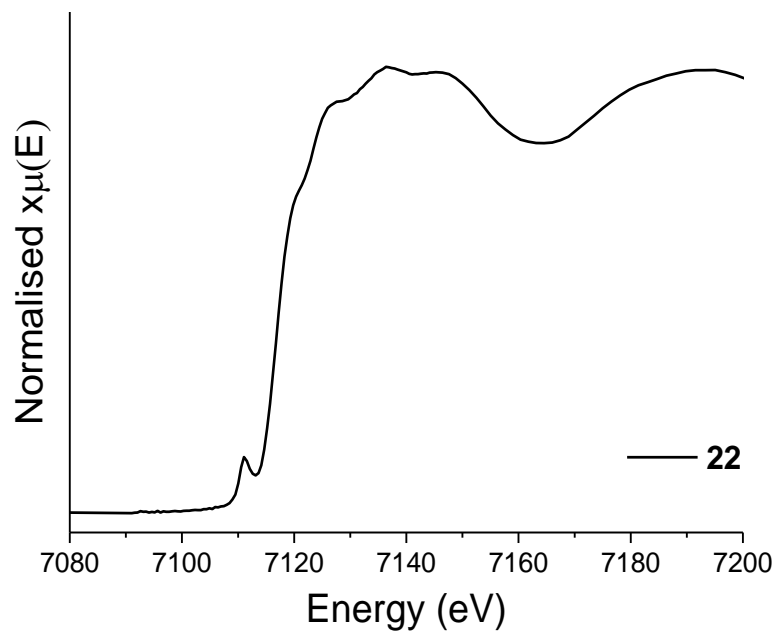
XRD**Figure A2.2: XRD of solid cubane structure (25).****XAS****Figure A2.3: XANES spectra of solid cubane structure (25).**

Table A2.1: Parameters derived from EXAFS modelling of the solid cubane. Unrefined coordination numbers are indicated by *.

Sample	Scatter	N	R_{XRD} (Å)	R_{EXAFS} (Å)	$2\sigma^2$ (Å ²)	R -factor
Cubane (25)	S	3*	2.26 - 2.27	2.25 ± 0.02	0.005	24
	S	1*	2.29 - 2.30	2.36 ± 0.06	0.005	
	Fe	1*	2.71 - 2.73	2.62 ± 0.03	0.010	
	Fe	2*	2.73 - 2.75	2.76 ± 0.03	0.010	
	S	1*	3.85 - 3.89	3.90 ± 0.05	0.010	

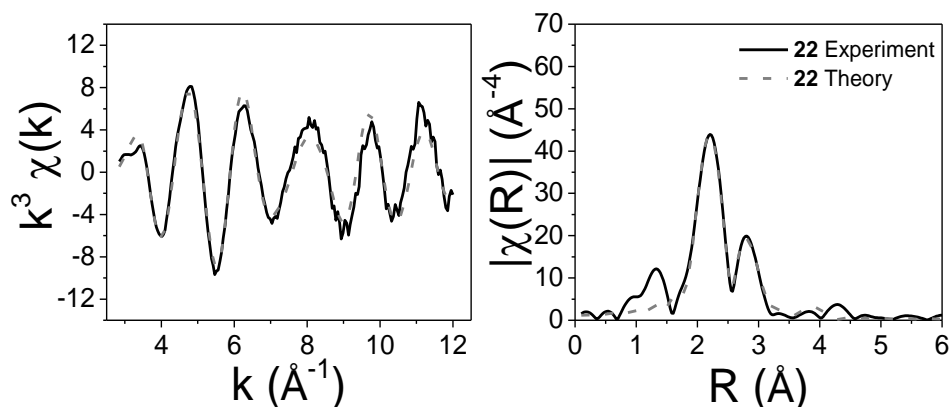


Figure A2.4: a. EXAFS and b. FT of solid cubane (25).

The cubane precursor (**25**), has a distinctive XANES profile shown in Figure 3.13, that includes a strong pre-edge peak from 1s to 3d transitions associated with the strained tetrahedral geometry of the iron. A shoulder arising from 1s to 4s transitions is also observed, corresponding to the presence of sulfur ligands.

The distinctive EXAFS profile of **25** is fit to 3 Fe-S distances at 2.25 Å, and one longer Fe-S distance at 2.36 Å. The second shell is fit to 3 Fe-Fe distances at 2.62 and 2.76 Å, and one long Fe-S distance at 3.90 Å (Table 3.4, Figure 3.14a-b). The combination of distances is unique to the cubane complex.

Appendix 3

CV traces of greigite with Ar and CO₂ saturated electrolyte

All CVs shown here were taken by **Siti Azian Zakaria**. CVs of greigite in phosphate buffer solutions saturated with argon or carbon dioxide at ~ pH 4 and pH 7. CV of greigite in carbonate buffer solution saturated with argon at pH 10.5. Instrumentation is mentioned in Chapter 2 (methodology chapter). Typically, the glass cell containing degassed buffer solution and three electrodes was sealed, and further bubbled throughout each experiment in order to maintain a controlled oxygen free environment. The working electrode is boron doped diamond, the reference electrode is silver/silver chloride, and the counter electrode is platinum. The in situ ATR-IR experiments were performed with a cell built onto the ATR-IR crystal. Here, the boron doped diamond electrode drop coated with greigite is pushed onto the crystal through buffer solution so that a small layer of buffer solution is found in between the greigite and the crystal, and electrochemical processes can occur. The cell in this case is also sealed and gasses controlled. IR-spectra are typically taken every five minutes and each potential, like the XAS experiments, is held for one hour. With the IR data, the first data is subtracted from the following data set and therefore graphs are constructed of “difference IR” spectra which show the evolution of peaks over time.

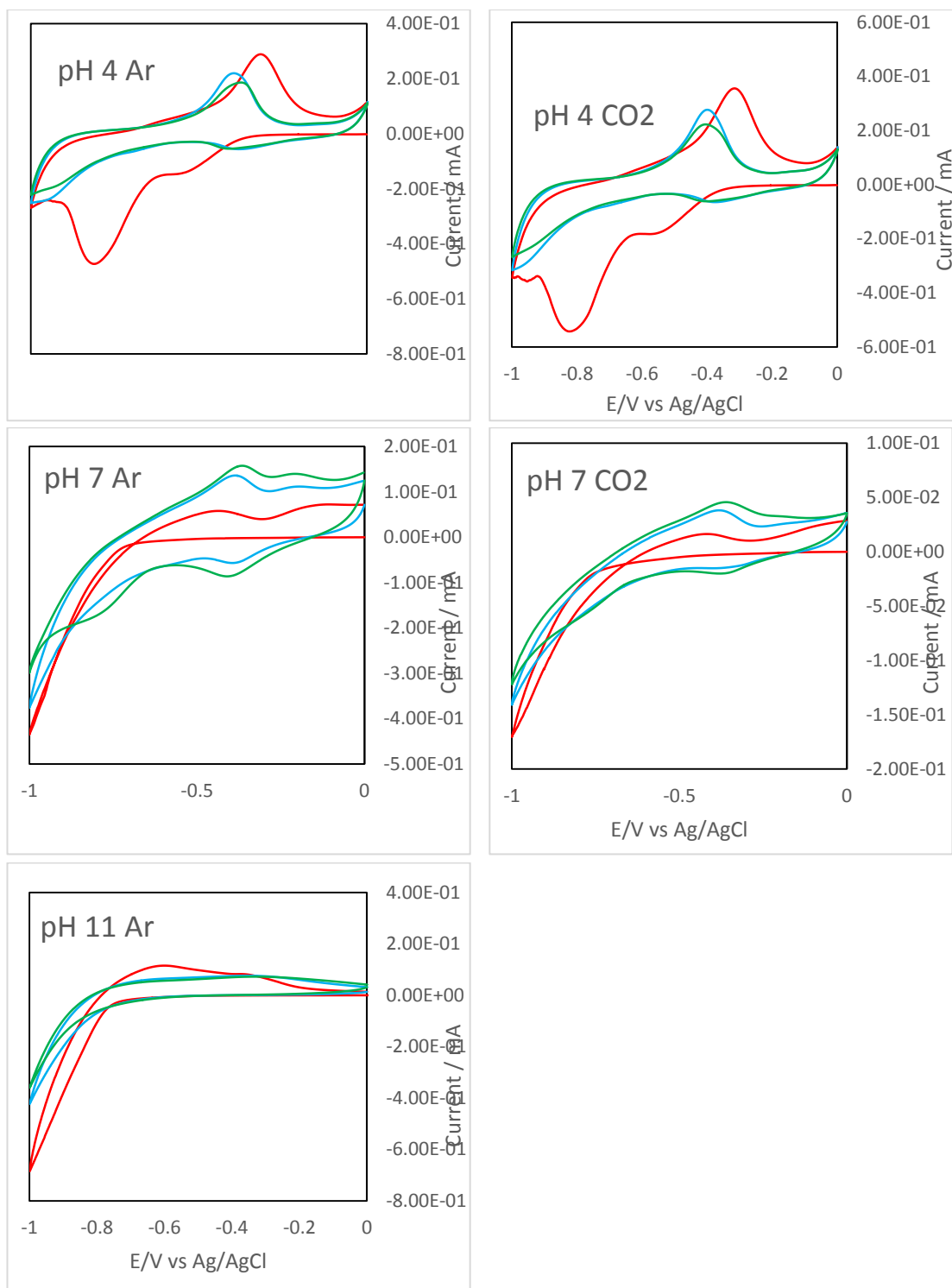


Figure A3.1: CV traces of greigite under different pH conditions with and without CO₂.

In situ ATR-IR data acquired using an electrochemical setup built onto an ATR crystal.

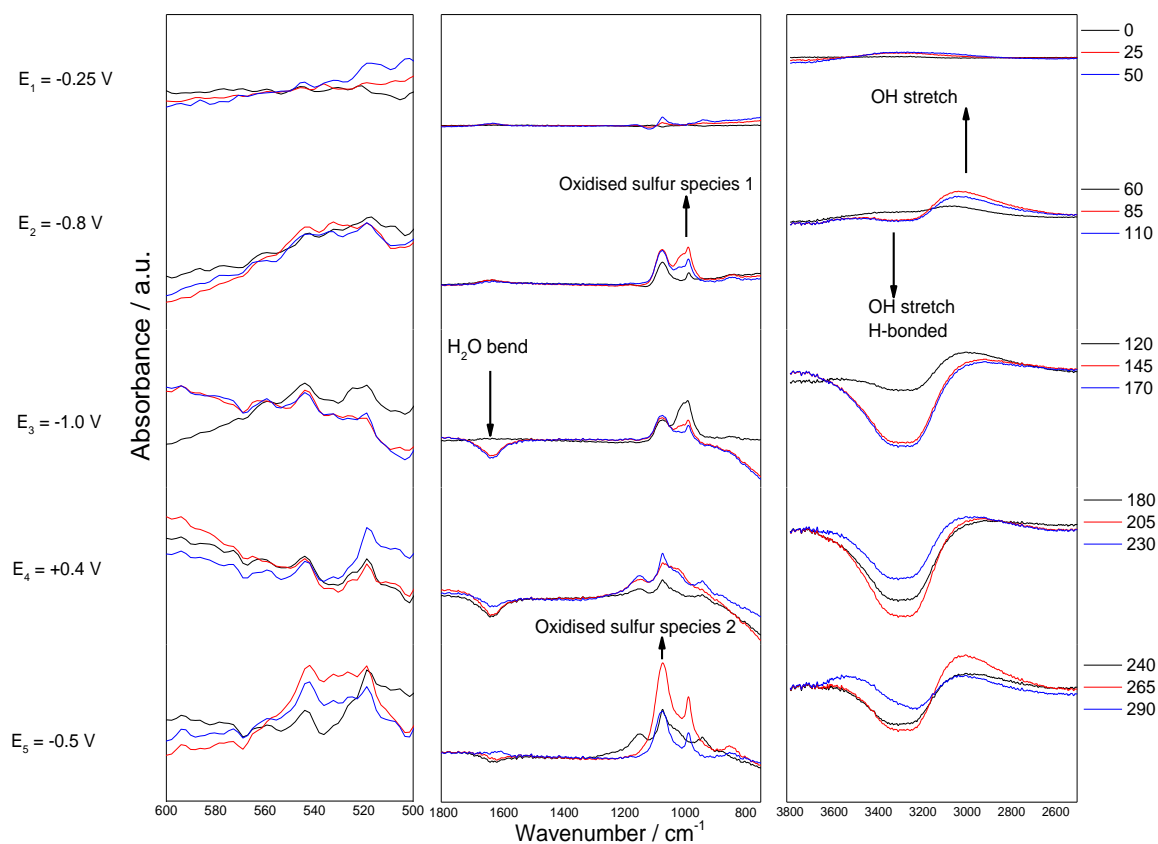


Figure A3.2: *In situ* difference ATR-IR spectra of the system in pH 7 buffer solution bubbled with argon.

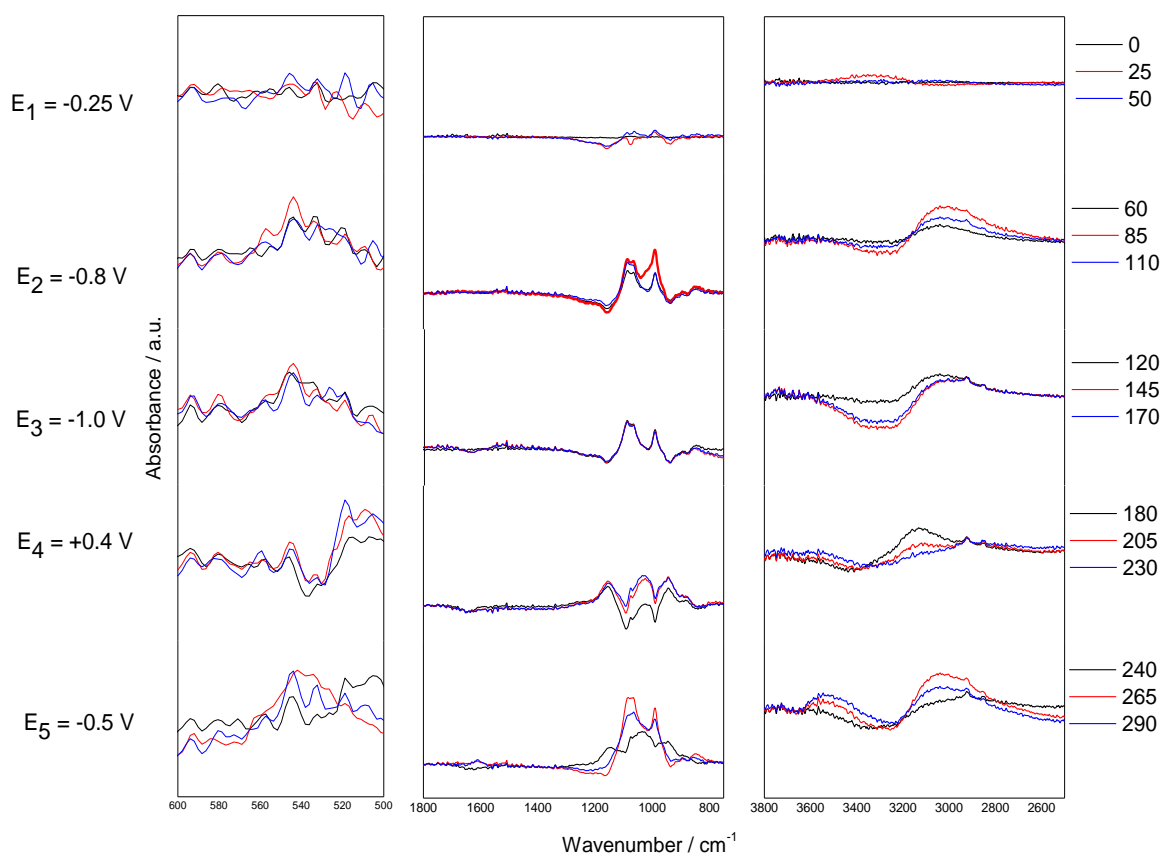


Figure A3.3: *In situ* difference ATR-IR spectra of the system in pH 7 buffer solution bubbled with carbon dioxide.

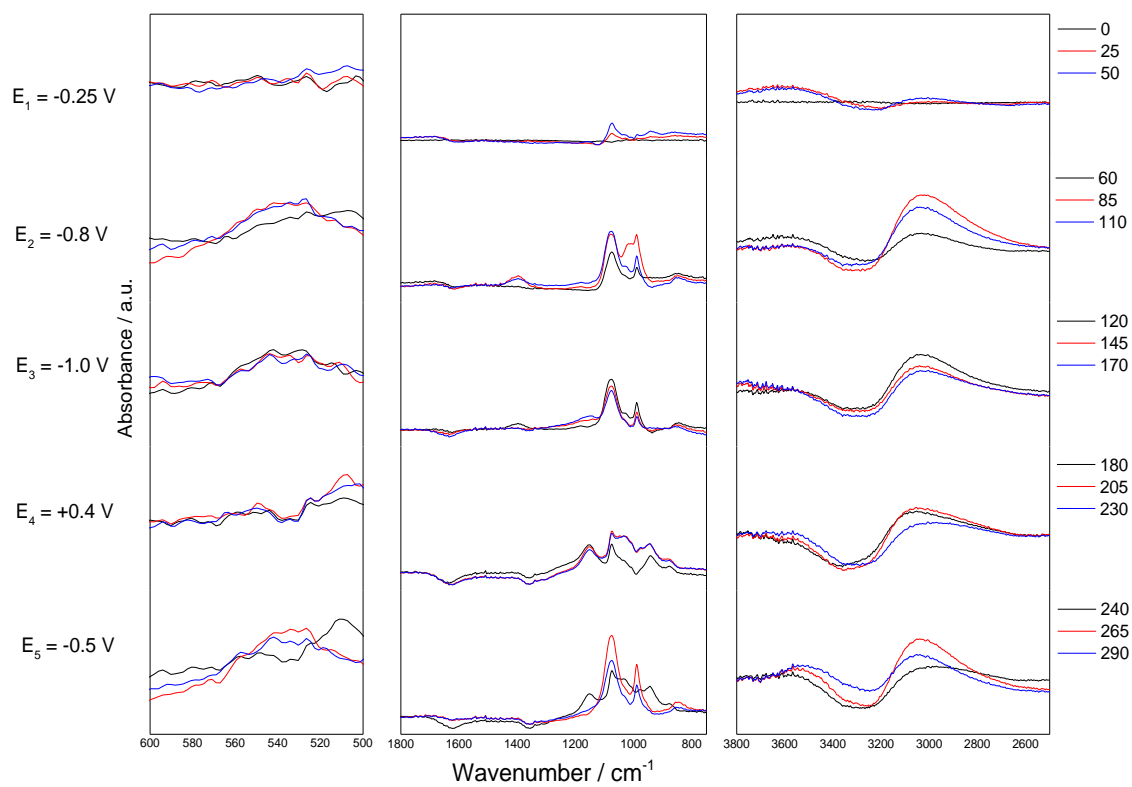


Figure A3.4: *In situ* difference ATR-IR spectra of the system in pH 4.5 buffer solution bubbled with argon.

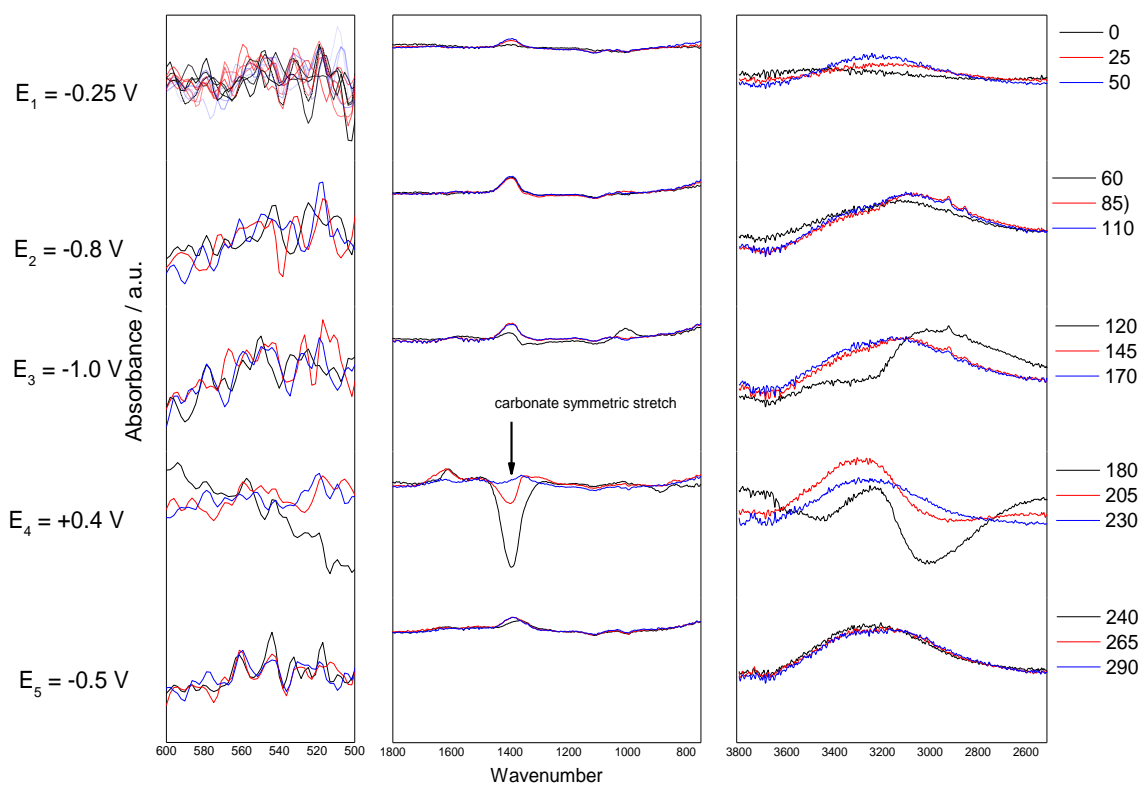


Figure A3.5: *In situ* difference ATR-IR spectra of the system in pH 10.5 buffer solution bubbled with argon.

Appendix 4

XRD and XAS of the oxyhydroxide

The displacement of iron and sulfide salts is the basis of many synthesis techniques.^{5,11,12} Varying pH, temperature, and concentration of reactants, results in access to different phases.⁵ Extreme anaerobic conditions must be met in order to prevent oxide formation owing to the sensitivity of the iron sulfide to oxygen. Extensive literature describes the common oxidation products of iron sulfides. This is investigated here.

Method

1. Preparation of iron(II) solution 19

A solution of iron(II) sulfate (0.1M) in degassed milliQ water (20cm³) was made in a glove bag filled with N₂. The solution was loaded into a capillary, sealed with araldite glue and removed from the glove bag.

2. Preparation of iron sulfide 20

The synthesis of the iron sulfide product and cell loading were performed in a glove bag filled with N₂. 200µL of **19** was loaded into the liquid cell. A solution of sodium sulfide (0.1M) was made in degassed milliQ water. 200 µL of the sodium sulfide solution was added dropwise to **19**. The cell was then sealed and removed from the glove bag.

3. Preparation of oxidised iron sulfide 21

For the structural identification of the common oxidation product of **20** (**21**), a fresh batch of **20** was synthesised within the glove bag using the stock solutions. 100µL of **20** was extracted and spread evenly over a glass slide. The glass slide was then dried in air.

4. XRD Acquisition

Sample **21** was analysed on a Bruker D4 diffractometer using a Cu source; the diffractometer was fitted with a post diffraction monochromator to reduce the effect of Fe fluorescence.

5. XAS Acquisition

Fluorescence measurements were taken of the samples on the iron K-edge (7112eV) at BM26A, ESRF using an incident beam ion chamber and a 9 element germanium solid state detector. XAS data reduction and EXAFS modelling were performed on Horae Athena and Excurve 9.273 respectively.^{9,10} Amplitude factors values for the iron K-edge derived from reference foil data.

Results

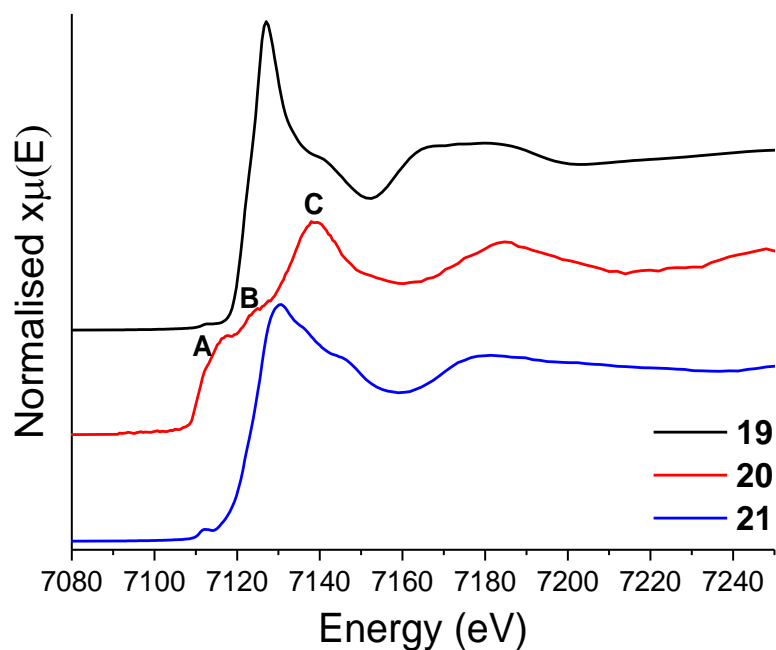


Figure A4.1: XANES spectra of dissolved iron (II) sulfate solution (19), iron sulfide formed from the displacement reaction (20), and the common oxidised product (21).

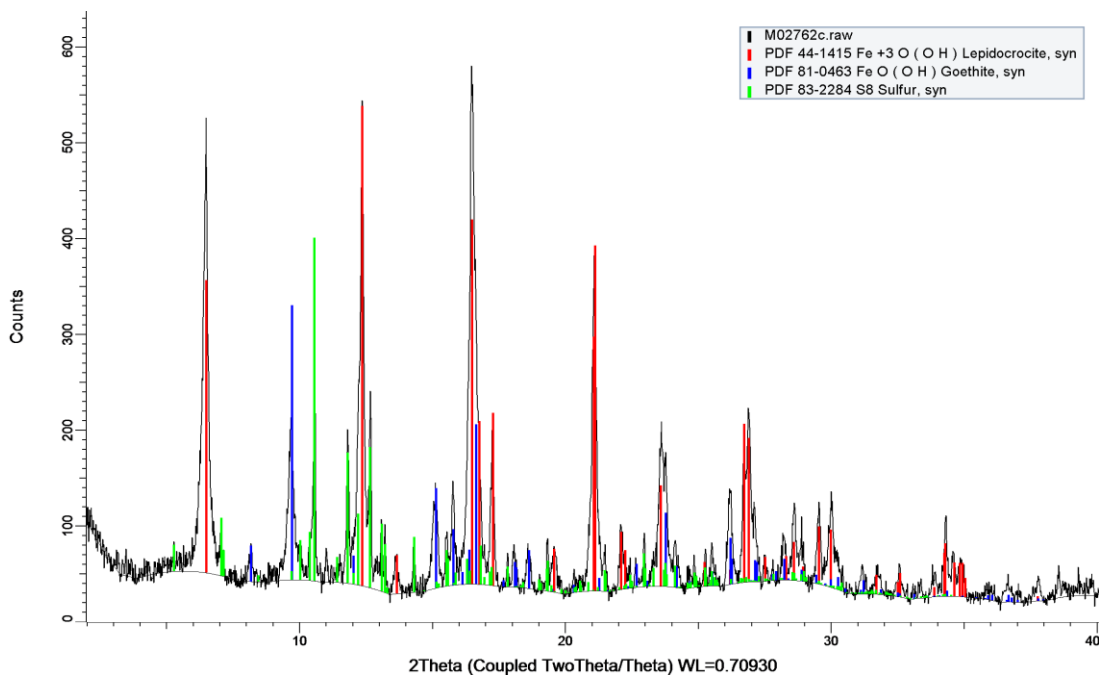


Figure A4.2: XRD of the room temperature oxidised product of 20 (21). Results are a match to a mixture of lepidocrocite (γ -FeO(OH)) and goethite (α -FeO(OH)) with excess crystallised sulfur present.

Aqueous iron (II) sulfate (**19**) has a XANES spectrum indicative of iron (II) in an octahedral geometry (Figure 3.1). The edge position of ca. 7121 eV is typical of iron (II) species while a sharp white line intensity indicates an ordered highly coordinated local structure. The distinctive XANES of **20** is identified for an amorphous iron sulfide complex (as shown in Chapter 5). When **20** is dried in air (**21**), a colour change occurs from black to orange suggesting oxidation. The edge position is shifted relative to **19** and **20** to ca. 7125 eV. This is indicative of a shift in oxidation state to iron (III). In addition, the high white line intensity is indicative of octahedrally coordinated oxygen ligands. XRD confirms the formation of oxyhydroxides goethite and lepidocrocite. An excess of crystalline sulfur is also detected – this is likely a biproduct of the oxyhydroxide formation from iron sulfide.

Appendix 5

DFT Calculated bond distances of the greigite surface

DFT calculations of greigite were performed by **Alberto Roldan Martinez**, UCL.

Surface was modelled with the following details: DFT-D plane-wave: VASP package; Exchange-correlation: GGA (PW91); Core electrons: PAW method, Hubbard; $U_{\text{Fe}}=1$ eV; Cut off: 600 eV; K-points: 4x4x4 & 5x5x1; Vacuum ~ 12 Å

Greigite (001) surface

Metal	Scatterer	N	Distances /Å	Average /Å
Fe _{Td} (7)	S	4	2.19 2.22 2.22 2.26	2.22
	Fe _{Td}	0		
Fe _{Td} (8)	S	4	2.19 2.19 2.33 2.33	2.26
	Fe _{Td}	2	2.61 2.61	2.61
Fe _{Oh} (24)	S	5	2.29 2.31 2.31 2.36 2.37	2.33

Greigite Fe₃S₄ (111) surface

Metal	Scatterer	N	Distances (Å)	Average (Å)
Fe _{Td} (7)	S	5	2.19; 2.20; 2.22; 2.62; 2.96	2.30
	Fe _{Td}	1	2.74	2.74
Fe _{Td} (8)	S	5	2.18; 2.18; 2.28; 2.57; 2.83	2.30
	Fe _{Td}	1	2.71	2.71
Fe _{Oh} (24)	S	7	2.15; 2.19; 2.20; 2.28; 2.49; 2.51; 2.53	2.34

Appendix 6

LCF analysis of the greigite during electrochemistry

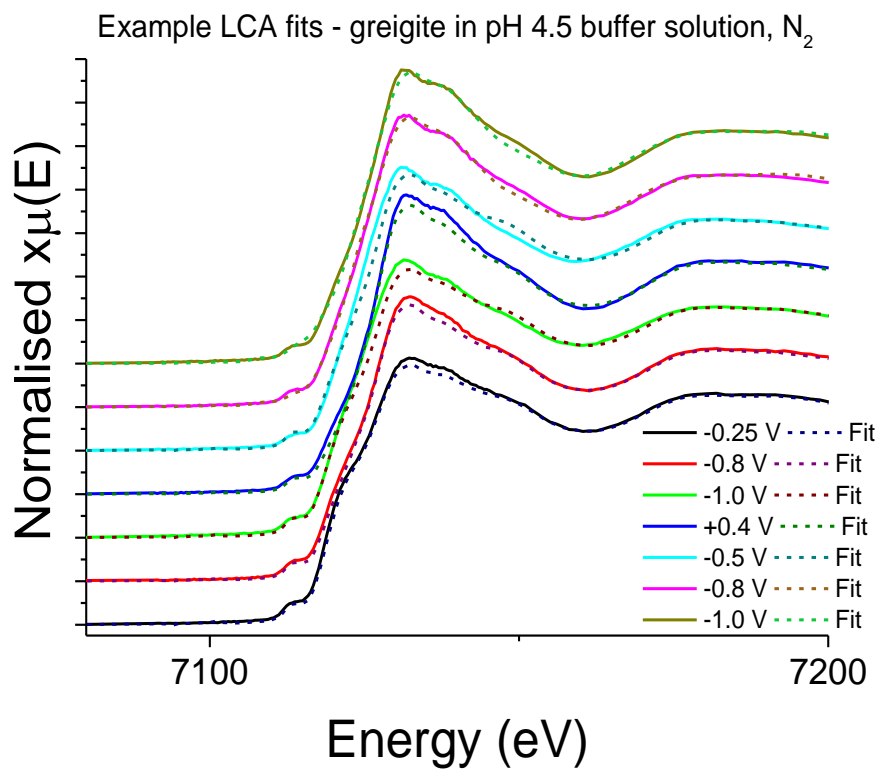


Figure A6.1: Example LCF analysis of the in situ XAS data of the electrochemical system of greigite in a pH 4.5 phosphate buffer solution bubbled with N₂.

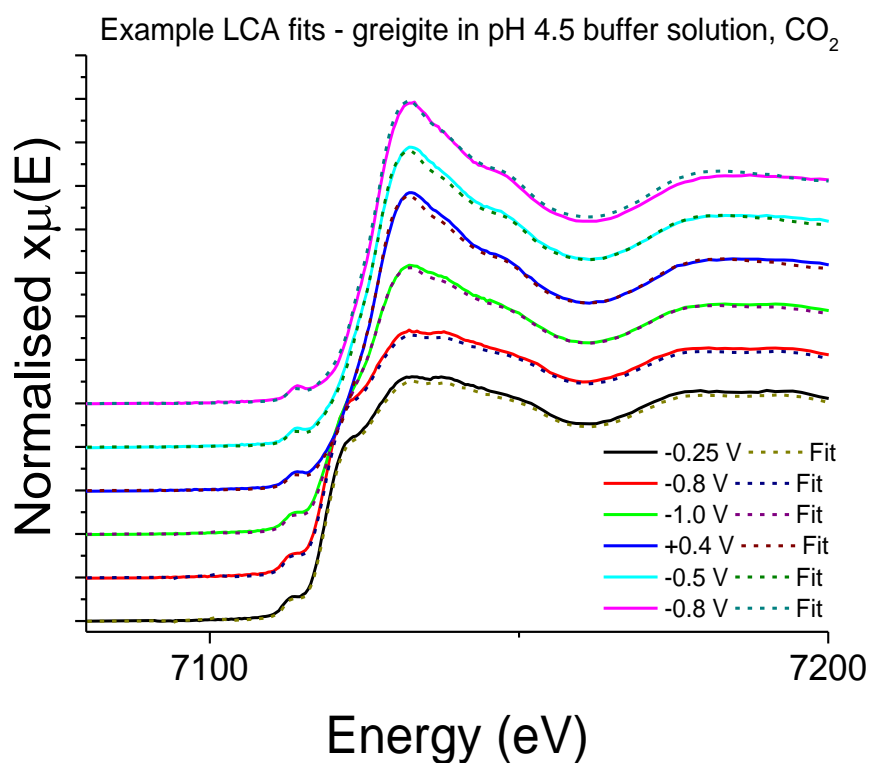


Figure A6.2: Example LCF analysis of the in situ XAS data of the electrochemical system of greigite in a pH 4.5 phosphate buffer solution bubbled with CO₂.

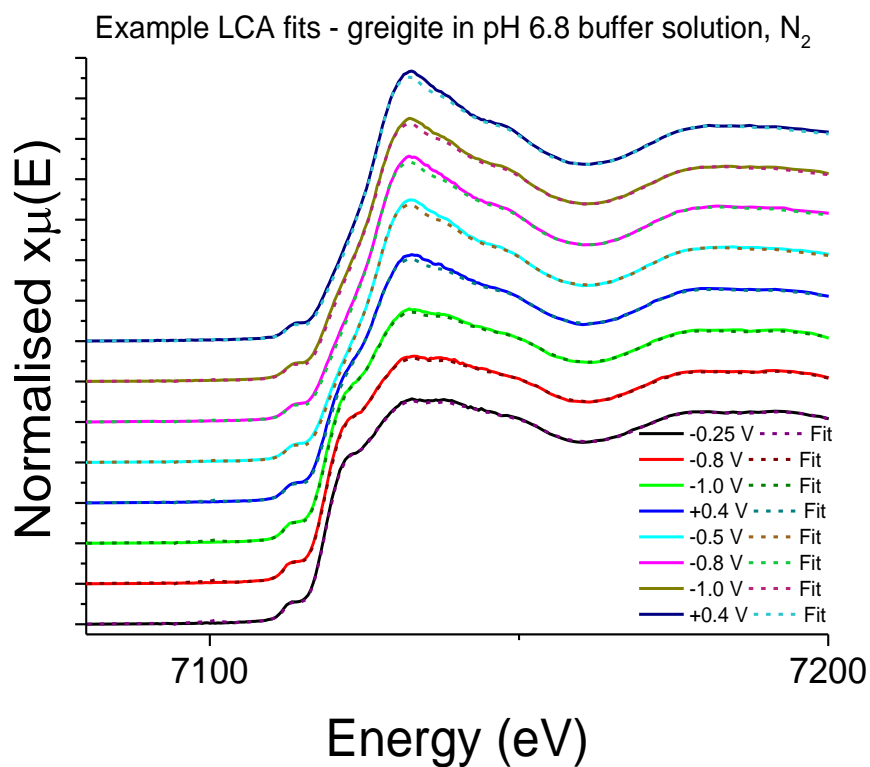


Figure A6.3: Example LCF analysis of the in situ XAS data of the electrochemical system of greigite in a pH 6.8 phosphate buffer solution bubbled with N₂.

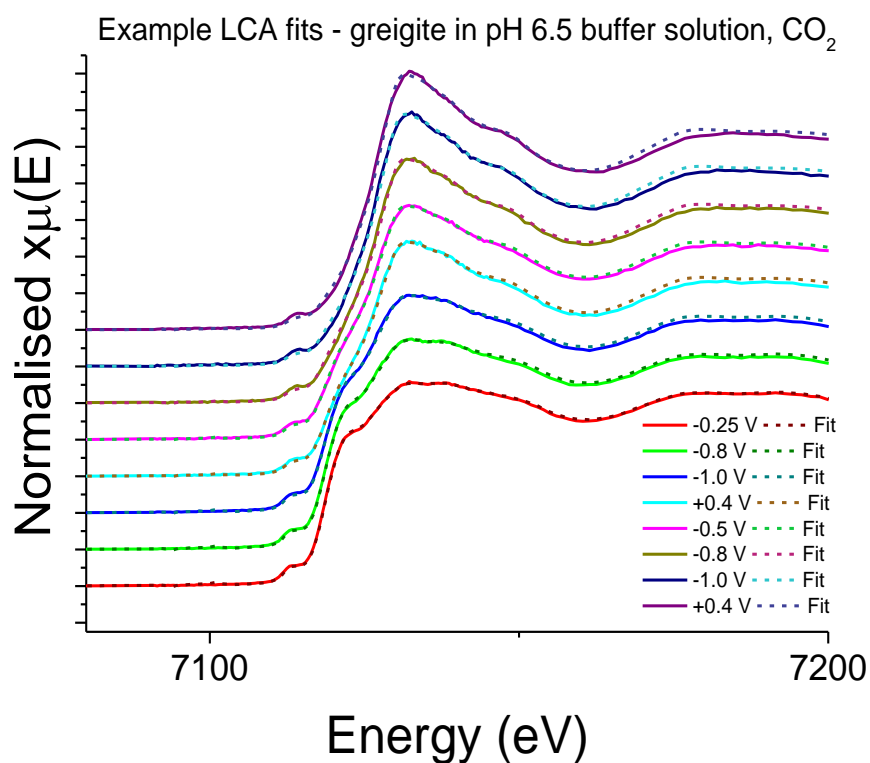


Figure A6.4: Example LCF analysis of the in situ XAS data of the electrochemical system of greigite in a pH 6.5 phosphate buffer solution bubbled with CO₂.

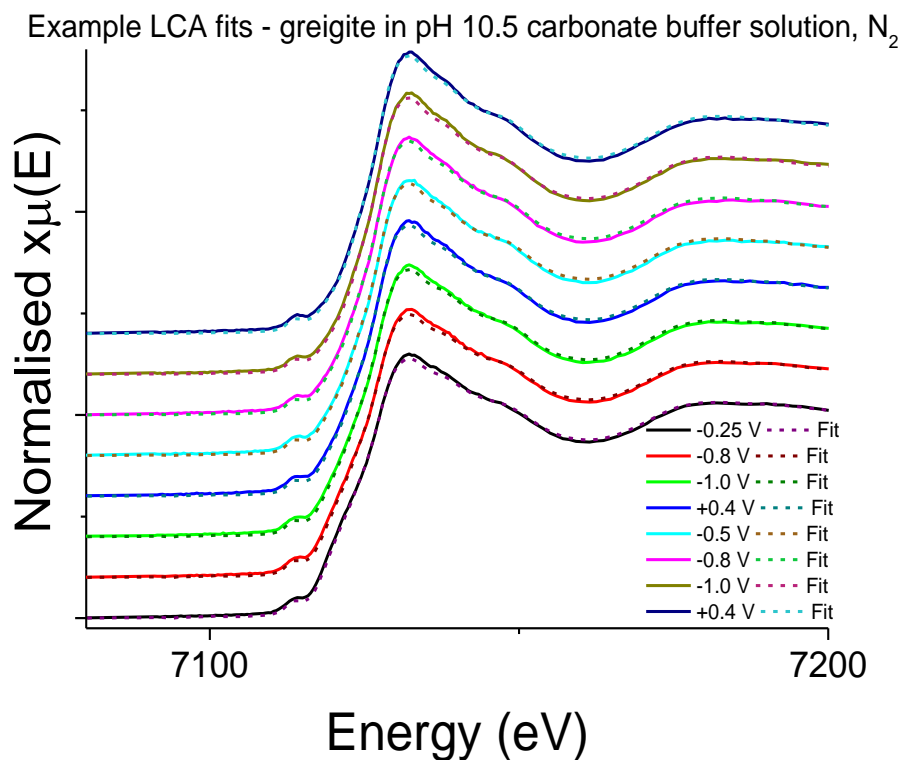


Figure A6.5: Example LCF analysis of the in situ XAS data of the electrochemical system of greigite in a pH 10.5 carbonate buffer solution bubbled with N₂.

Appendix 7

Coordination numbers for surface and bulk

The table shows calculations for coordination numbers used as input parameters in EXAFS calculations in section 5.3.1. Coordination number is calculated by distinguishing coordination number and ratio of each set of sites in the bulk and surface. The product of these is coordination number typically used in EXCURVE. This number is multiplied by “trial and error” ratios bulk to surface and used in the program.

				ratio per unit cell x coordination x volume ratio		
	N	ratio per unit cell	ratio per unit cell x coordination	0.5:0.5	0.4:0.6	0.3:0.7
BULK	4	0.333	1.333	0.667	0.533	0.400
	6	0.667	4.000	2.000	1.600	1.200
SURFACE	4	0.385	1.538	0.462	0.554	0.646
	5	0.615	3.077	0.923	1.108	1.292
Tetrahedral			4.410	1.436	1.456	1.477
Octahedral			11.385	3.785	3.742	3.698

Appendix 8

Surface to bulk ratio of a greigite nanoparticle

According to TEM analysis performed by **Anna Roffey**, the size distribution of **31**, carbon loaded greigite, is 50 – 100nm. The surface is assumed to be 1nm in depth. Calculation of average surface to bulk ratio are shown below.

$$\text{Area of hexagonal face: } (\text{radius}^2/2)*6 = [(50\text{nm}*50\text{nm})/2]*6 = 7500\text{nm}^2$$

$$\text{Bulk volume: } (\text{Area of hexagonal face})*10\text{nm} = 75000\text{nm}^3$$

$$\text{Area of sides: } \text{radius}*height*6 = 50\text{nm}*10\text{nm}*6 = 3000\text{nm}^2$$

$$\text{Surface area: } [(\text{Area of hexagonal face})*2] + (\text{Area of sides}) = [(7500\text{nm}^2)*2] + 3000\text{nm}^2 = 18000\text{nm}^2$$

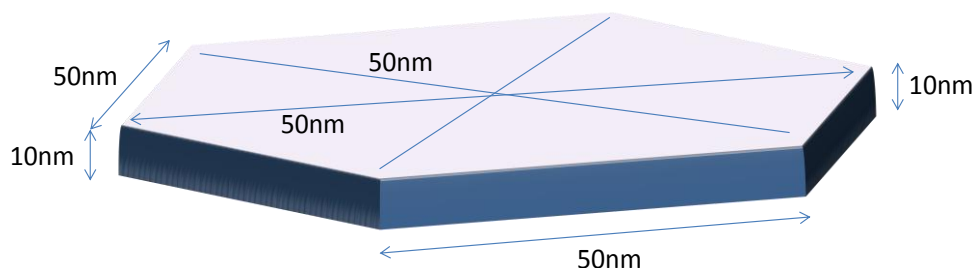
$$\text{Volume of crystal surface} \approx (\text{Surface area})*1\text{nm} = 18000\text{nm}^3$$

$$\text{Surface to bulk ratio: } [(\text{Volume of crystal surface})/(\text{Volume of crystal surface})]:[(\text{Bulk volume})/(\text{Volume of crystal surface})]$$

$$= 1:4.17$$

$$\% \text{ surface: } 19.4$$

$$\% \text{ bulk: } 80.6$$



$$\text{Area of hexagonal face: } (\text{radius}^2/2)*6 = [(50\text{nm}*50\text{nm})/2]*6 = 30000\text{nm}^2$$

$$\text{Bulk volume: } (\text{Area of hexagonal face})*10\text{nm} = 300000\text{nm}^3$$

$$\text{Area of sides: } \text{radius}*height*6 = 50\text{nm}*10\text{nm}*6 = 6000\text{nm}^2$$

$$\text{Surface area: } [(\text{Area of hexagonal face})*2] + (\text{Area of sides}) = [(7500\text{nm}^2)*2] + 3000\text{nm}^2 = 66000\text{nm}^2$$

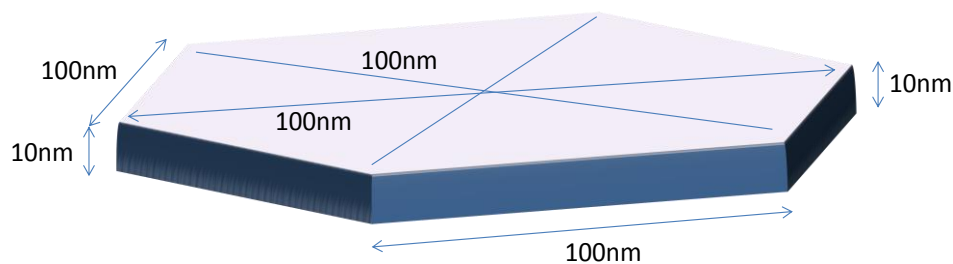
$$\text{Volume of crystal surface} \approx (\text{Surface area})*1\text{nm} = 66000\text{nm}^3$$

$$\text{Surface to bulk ratio: } [(\text{Volume of crystal surface})/(\text{Volume of crystal surface})]:[(\text{Bulk volume})/(\text{Volume of crystal surface})]$$

$$= 1:4.55$$

$$\% \text{ surface: } 19.4$$

$$\% \text{ bulk: } 80.6$$



Average Surface to bulk ratio: = 1:4.35.

Average % surface: 18.7. Average % bulk: 81.3

Appendix 9

Iron Standards and their XANES

The graph shows typical standard which are grouped into iron(II) (green), iron(III) (red), and sulfide, particularly pyrite (black). These spectra were taken by and belong to Meleke Balk, from the Geosciences Department at Utrecht University.

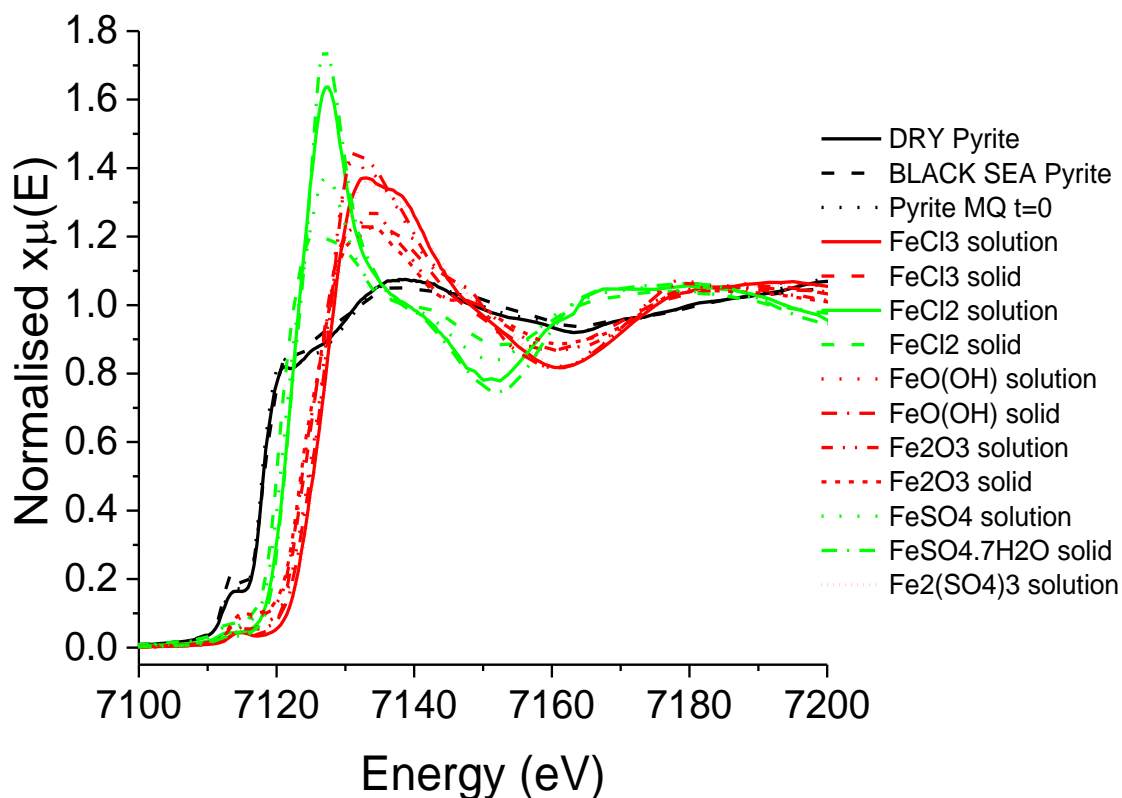


Figure A9.1: XANES of some iron standards.

Appendix 10

Output parameters of Chapter 5

Potential	Scatter	N	R_{EXAFS} (Å)	$2\sigma^2$ (Å ²)	R-factor
18					
Dry	O	0.3	1.98	0.007	40
	S	1.5	2.20	0.014	
	S	3.7	2.38	0.014	
18a					
no pot	O	0.6*	1.98	0.007	35
	S	1.3*	2.23	0.014	
	S	3.6*	2.40	0.014	
-0.25V	O	0.4*	1.95	0.007	35
	S	1.4*	2.22	0.014	
	S	2.0*	2.39	0.014	
-0.8V	O	2.6*	1.96	0.007	38
	S	0.9*	2.21	0.014	
	S	1.3*	2.39	0.014	
-1.0V	O	4.1*	1.93	0.010	20
	S	0.5*	2.21	0.014	
	S	1.2*	2.33	0.014	
+0.4V	O	4.8*	1.95	0.012	23
	S	0.3*	2.21	0.014	
	S	0.7*	2.35	0.014	
-0.5V	O	5.1*	1.95	0.012	21
	S	0.2*	2.24	0.014	
	S	0.5*	2.33	0.014	
-0.8V	O	5.2*	1.95	0.012	20
	S	0.2*	2.23	0.014	
	S	0.3*	2.33	0.014	
-1.0V	O	5.2*	1.92	0.012	25
	S	0.2*	2.21	0.014	
	S	0.3*	2.31	0.014	
-0.4V	O	5.2*	1.95	0.012	26
	S	0.2*	2.23	0.014	
	S	0.3*	2.33	0.014	
18c					
no pot	O	0.6*	1.98	0.007	35
	S	1.3*	2.23	0.014	
	S	3.6*	2.40	0.014	
-0.25V	O	2.0*	1.98	0.014	33
	S	1.1*	2.21	0.016	
	S	2.8*	2.39	0.016	
-0.8V	O	3.0*	1.97	0.012	30
	S	0.8*	2.21	0.017	
	S	2.1*	2.38	0.017	
-1.0V	O	2.5*	1.98	0.012	29
	S	0.9*	2.21	0.020	
	S	2.3*	2.36	0.020	
+0.4V	O	4.2*	1.97	0.011	27
	S	0.7*	2.21	0.020	
	S	1.8*	2.39	0.020	
-0.5V	O	3.2*	1.97	0.012	25
	S	0.8*	2.21	0.021	
	S	2.1*	2.37	0.021	
-0.8V	O	3.7*	1.98	0.011	24
	S	0.8*	2.21	0.018	
	S	1.9*	2.38	0.018	
-1.0V	O	4.0*	1.97	0.010	26

Potential	Scatter	N	R_{EXAFS} (Å)	$2\sigma^2$ (Å ²)	R-factor
	S	0.7*	2.21	0.019	
	S	1.8*	2.36	0.019	
+0.4V	O	5.1*	1.97	0.011	24
	S	0.5*	2.21	0.017	
	S	1.3*	2.38	0.017	
18d					
-0.25V	O	0.6*	2.00	0.009	31
	S	1.3*	2.21	0.014	
	S	3.4*	2.40	0.014	
-0.8V	O	1.1*	1.99	0.010	32
	S	1.2*	2.21	0.011	
	S	3.0*	2.39	0.011	
-1.0V	O	1.3*	1.99	0.006	31
	S	1.2*	2.21	0.012	
	S	3.0*	2.40	0.015	
+0.4V	O	2.7*	1.98	0.011	33
	S	0.8*	2.21	0.012	
	S	2.2*	2.40	0.012	
-0.5V	O	2.7*	1.98	0.010	29
	S	0.8*	2.21	0.014	
	S	2.1*	2.40	0.014	
-0.8V	O	3.6*	1.97	0.013	33
	S	0.6*	2.21	0.015	
	S	1.6*	2.39	0.015	
-1.0V	O	4.2*	1.95	0.011	32
	S	0.4*	2.21	0.012	
	S	0.6*	2.36	0.012	
+0.4V	O	4.5*	1.99	0.006	26
	S	0.4*	2.22	0.012	
	S	0.6*	2.41	0.012	
18e					
-0.25V	O	0.6*	2.02	0.007	33
	S	1.4*	2.21	0.017	
	S	2.1*	2.39	0.017	
-0.8V	O	0.9*	2.00	0.007	33
	S	1.3*	2.21	0.015	
	S	2.0*	2.40	0.015	
-1.0V	O	1.8*	1.96	0.010	25
	S	0.9*	2.21	0.018	
	S	1.3*	2.39	0.018	
+0.4V	O	4.3*	1.96	0.015	28
	S	0.4*	2.21	0.016	
	S	1.1*	2.36	0.016	
-0.5V	O	4.4*	1.96	0.013	23
	S	0.4*	2.21	0.013	
	S	1.0*	2.40	0.013	
-0.8V	O	5.1*	2.00	0.019	31
	S	0.2*	2.21	0.016	
	S	0.6*	2.47	0.016	
-1.0V	O	4.4*	2.00	0.016	30
	S	0.1*	2.21	0.014	
	S	0.4*	2.48	0.014	
+0.4V	O	4.4*	1.99	0.017	32
	S	0.1*	2.21	0.014	
	S	0.4*	2.47	0.014	
18f					
no pot 1	O	3.6*	1.95	0.010	41
	S	1.0*	2.21	0.014	

Potential	Scatter	N	R_{EXAFS} (Å)	$2\sigma^2$ (Å ²)	R-factor
	S	2.6*	2.37	0.014	
no pot 2	O	3.1*	1.97	0.010	35
	S	0.7*	2.21	0.014	
	S	1.8*	2.37	0.014	
-0.25V	O	3.0*	1.96	0.010	25
	S	0.7*	2.21	0.014	
	S	1.9*	2.39	0.014	
-0.8V	O	3.2*	1.95	0.010	25
	S	0.7*	2.21	0.014	
	S	1.7*	2.36	0.014	
-1.0V	O	3.6*	1.95	0.011	25
	S	0.6*	2.21	0.014	
	S	1.6*	2.36	0.014	
+0.4V	O	3.8*	1.95	0.010	23
	S	0.5*	2.21	0.013	
	S	1.4*	2.35	0.013	
0.5V	O	3.9*	1.95	0.011	24
	S	0.5*	2.21	0.012	
	S	1.3*	2.36	0.012	
0.8V	O	4.1*	1.95	0.010	23
	S	0.5*	2.21	0.013	
	S	1.2*	2.34	0.013	
-1.0V	O	4.2*	1.95	0.011	23
	S	0.4*	2.21	0.011	
	S	1.1*	2.34	0.011	
+0.4V	O	4.4*	1.95	0.013	26
	S	0.4*	2.21	0.008	
	S	1.0*	2.34	0.008	
-0.5V	O	4.5*	1.95	0.012	23
	S	0.4*	2.21	0.008	
	S	0.9*	2.34	0.008	

Appendix References

- (1) Vanitha, P. V.; O'Brien, P. *J. Am. Chem. Soc.* **2008**, *130*, 17256–17257.
- (2) Bruschi, M.; Guerlesquin, F. *FEMS Microbiol. Rev.* **1988**, *4*, 155–175.
- (3) Stephan, D. W.; Papaefthymiou, G. C.; Frankel, R. B.; Holm, R. H. *Inorg. Chem.* **1983**, *22*, 1550–1557.
- (4) Doukov, T. I.; Iverson, T. M.; Seravalli, J.; Ragsdale, S. W.; Drennan, C. L. *Science* **2002**, *298*, 567–572.
- (5) Rickard, D.; Luther, G. W. *Chem. Rev.* **2007**, *107*, 514–562.
- (6) Christou, G.; Garner, C. D. *J. Chem. Soc. Dalton Trans.* **1979**, *6*, 1093–1094.
- (7) Que, L.; Holm, R. H. *J. Am. Chem. Soc.* **1975**, *97*, 463–464.
- (8) Rao, P. V.; Holm, R. H. *Chem. Rev.* **2004**, *104*, 527–559.
- (9) Ravel, B.; Newville, M. *J. Synchrotron Radiat.* **2005**, *12*, 537–541.
- (10) Binsted, N. EXCURV98: CCLRC Daresbury Laboratory Computer Program, 1998.
- (11) Wolthers, M.; Van Der Gaast, S. J.; Rickard, D. *Am. Mineral.* **2003**, *88*, 2007–2015.
- (12) Hunger, S.; Benning, L. G. *Geochem. Trans.* **2007**, *8*, 1.